

Geochronology, mineral chemistry, isotope and microthermometry features of the Wunuer deposit, Inner Mongolia, China: a porphyry-hydrothermal-epithermal system

Xiejun Fan

Faculty of Earth Resources, China University of Geosciences, China

Abstract. The Wunuer Pb-Zn-Mo deposit is a newly explored polymetallic ore deposit located in the middle segment of the Great Xing'an Range, Inner Mongolia, NE China. Three stages of mineralization, composed of an early porphyry stage, an intermediate hydrothermal stage, and a later epithermal stage, have been identified. Sphalerite is the principal mineral in both hydrothermal and epithermal stages, and thus two generations of sphalerite are separated, which show distinct textural and chemical characteristics. Detailed study of the texture, chemistry, fluid inclusion and sulfur isotope characteristics of these two generations of sphalerite were carried out to reveal ore forming conditions of the hydrothermal and epithermal mineralization stages. In addition, granite porphyry zircon U-Pb concordia, hydrothermal stage hydrothermal zircon U-Pb concordia and epithermal stage sphalerite (Sp2) Rb-Sr isochron ages were determined to constrain the chronology of the system and the duration of the porphyry to hydrothermal and to epithermal transition.

The Wunuer Pb-Zn-Mo polymetallic deposit, located in the middle segment of the Great Xing'an Range, Inner Mongolia, NE China, is closely related to mesozoic volcanic-subvolcanic rocks (Fig. 1).

1 Brief introduction to deposit geology

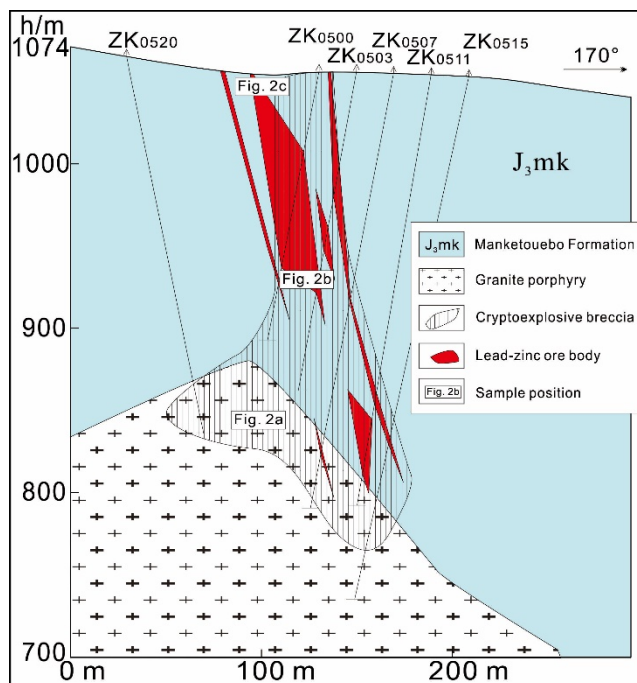


Figure 1. Geological section along exploration line 05 crosscutting the I₁ lead-zinc ore body.

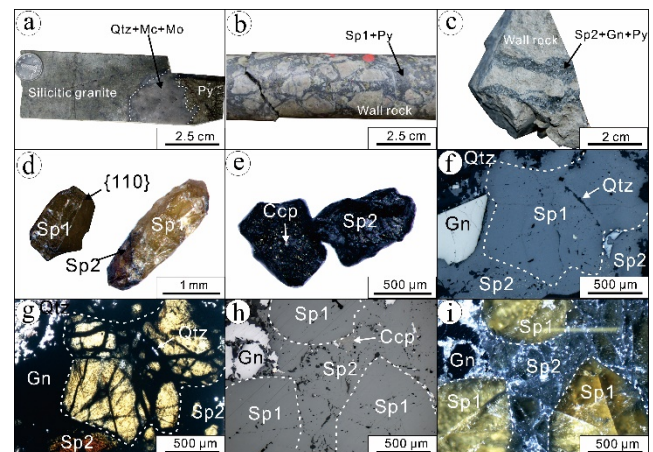


Figure 2. (a) Porphyry-stage molybdenite-muscovite-pyrite-bearing quartz veins. (b) Hydrothermal-stage Sp₁-bearing crypto-explosive breccia. (c) Epithermal-stage veined lead-zinc ore. (d) Translucent and euhedral first-generation sphalerite (Sp₁) granule, with rhombic dodecahedron structure {110}. (e) Black, opaque, and anhedral second-generation sphalerite (Sp₂) granule. (f) & (g) Reflected and transmitted light microphotographs, respectively, illustrating the textures of sphalerite: translucent, yellow sphalerite has been replaced by the opaque sphalerite both along crystal rims and fractures, accompanied by chalcopyrite, galena and quartz. (h) & (i) Reflected and internal reflection light microphotographs, respectively, illustrating the textures of sphalerite: the yellow sphalerite has been partly replaced by the opaque sphalerite which is accompanied by chalcopyrite, galena and quartz. Gn-galena; Ccp-chalcopyrite; Py-pyrite; Mo-molybdenite; Mc-muscovite; Qtz-quartz; Chl-chlorite; Ser-sericite.

Wall rocks in the Wunuer deposit area are dominated by Upper Jurassic Manketouebo Formation terrestrial volcanoclastic rocks, which were intruded by a late-Jurassic granite porphyry closely related to ore forming (Fig. 1). Porphyry-stage mineralization occurred mainly in the apical portions of the granite porphyry intrusion (Fig. 1), forming molybdenite-magnetite-hematite-pyrite-bearing quartz veins (Fig. 2a). Hydrothermal stage mineralization occurred mainly in crypto-explosive breccia of granite porphyry and wall rocks adjacent to intrusion (Fig. 1), forming sphalerite-bearing breccias (Fig. 2b). Epithermal-stage mineralization occurred principally in the wall rocks at the top of the deposit (Fig. 1) and comprises brecciated, veined and stockwork lead-

zinc ores (Fig. 2c). Therefore, two generations of sphalerite, with the first-generation sphalerite (Sp1) precipitated in hydrothermal stage and the second-generation sphalerite (Sp2) precipitated in epithermal stage, were identified. Generally, porphyry mineralization was usually accompanied by potassic, silicic, and fluorite-bearing alteration, hydrothermal stage mineralization was usually accompanied by chlorite-, sericite-, zircon- and rutile-bearing alteration, epithermal mineralization was mainly related to argillic, chlorite and carbonate alteration. The epithermal mineralization overprinted porphyry and hydrothermal mineralization, especially in the brecciated wall rocks near to the granite porphyry intrusion, where the hydrothermal stage sphalerite is widely replaced by the epithermal stage sphalerite.

Hydrothermal zircon, accompanied by sericite, pyrite, rutile and Sp1, is ubiquitous in hydrothermal stage mineralization. The occurrence of hydrothermal zircon is closely related to silicic, sericitic and chloritic alteration, generally in silicic granite porphyry (Fig. 3a, b), crypto-explosive breccias (Fig. 3c, d) and chlorite-bearing wall rocks (Fig. 3e, f).

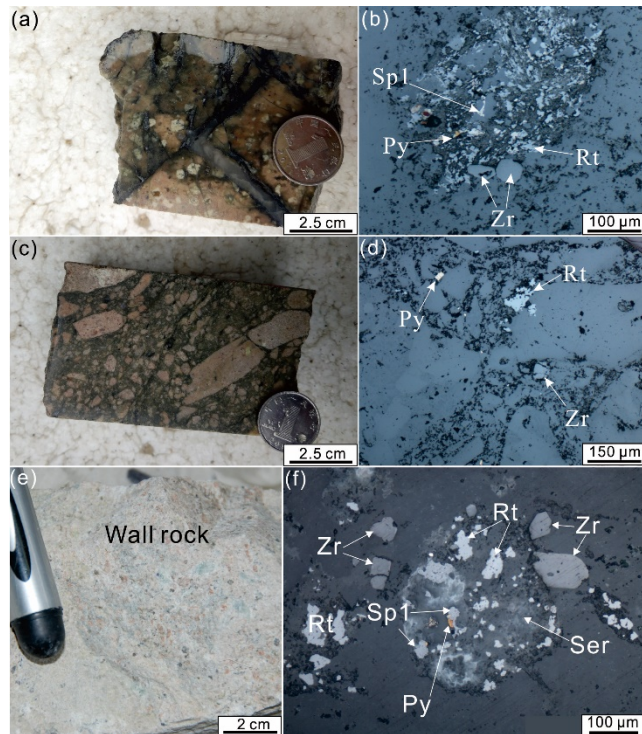


Figure 3. (a) Silicic porphyry granite. (b) Hydrothermal zircon accompanied by Sp1, rutile and pyrite in sample Fig. 3a. (c) Crypto-explosive breccia of granite porphyry. (d) Hydrothermal zircon accompanied by rutile and pyrite in sample Fig. 3c. (e) Chlorite-bearing wall rock. (f) Hydrothermal zircon accompanied by Sp1, sericite, rutile, and pyrite in sample Fig. 3e.

2 Ore forming conditions

2.1 Implications of sphalerite texture and chemistry

Two generations of sphalerite show different crystal texture, transparency, colour, mineral inclusions and

paragenetic relationship. The first-generation sphalerite (Sp1) is generally euhedral and light colored (yellow to brown in transmitted light), with rhombic dodecahedron structure (Fig. 2d). In general, this transparent sphalerite is free of mineral micro-inclusions, and is usually replaced by the second-generation sphalerite (Sp2) as well as by other sulfides along fractures or on crystal surfaces (Fig. 2d, f, h). The second-generation sphalerite (Sp2) is generally anhedral, opaque and black in colour (Fig. 2e, g, i). The black Sp2 contains abundant micro-inclusions, such as chalcopyrite “disease” (Fig. 2e, h).

These two generations of sphalerite have different chemical compositions. Element correlations, especially between Zn and Fe, Zn and Cu, Cu and Fe, and Cu and In, show different trends for Sp1 and Sp2. Fe shows negative linear correlation with Zn in both Sp1 and Sp2, but with a molar slope of -1 for Sp1, a molar slope of -1.8 for Sp2, respectively (Fig. 4a). Cu is limited in Sp1, but is elevated in Sp2 and shows a negative linear correlation with Zn with a molar slope of -1.98 (Fig. 4b), as well as shows a positive linear correlation with Cu with a molar slope of 0.96 (Fig. 4c). In is limited in Sp2, but is elevated in Sp2 and reaches to hundreds of ppm (Fig. 4d).

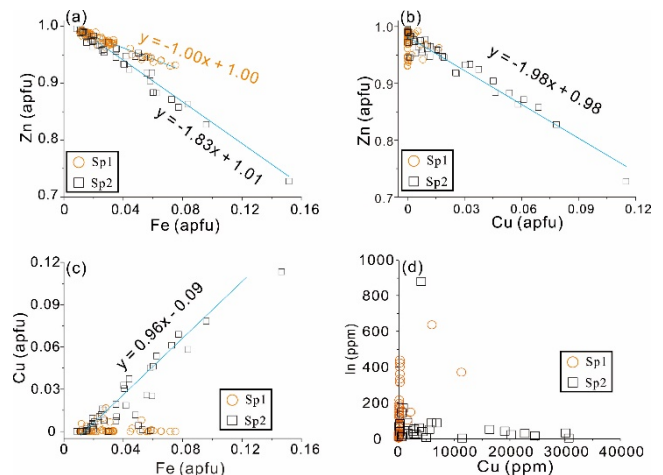


Figure 4. Binary plots of major element contents by EPMA and trace element contents by LA-ICP-MS for sphalerite from the Wunuer deposit.

2.2 Fluid inclusions

Primary fluid inclusions trapped in a quartz vein from the early porphyry stage preserve information on the conditions of potassic-silicic alteration condition. This stage was characterized by high temperature and moderate salinity fluids (Fig. 5). The first-generation sphalerite (Sp1) is transparent and hence is ideal for fluid inclusion studies. Primary fluid inclusions trapped in Sp1 imply a moderate temperature and low salinity fluid in hydrothermal stage mineralization (Fig. 5). Unfortunately, it was not possible to observe fluid inclusions in Sp2 as it is opaque. Thus, we studied primary fluid inclusions in quartz in apparent textural equilibrium with Sp2 to infer its conditions of precipitation. The fluid inclusions measured are characterized by low homogenization temperature and salinity (Fig. 5).

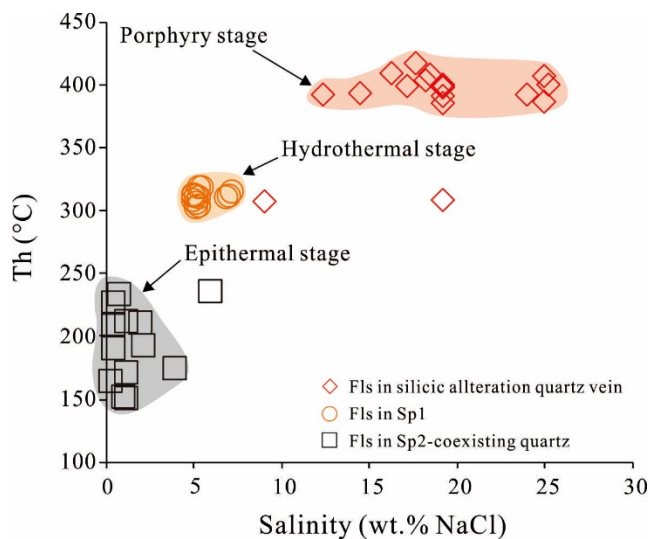


Figure 5. Total homogenization temperatures (Th) vs. salinities of fluid inclusions from Wunuer deposit.

3 Ore forming ages

3.1 Intrusion age

Magmatic zircons were hand-picked from a crushed sample of the ore-related granite porphyry intrusion, and were analyzed using LA-ICP-MS to obtain the zircon U-Pb age. As shown in Figure 6, the U-Pb concordia age implies that the granite porphyry was emplaced at 144.5 ± 0.6 Ma.

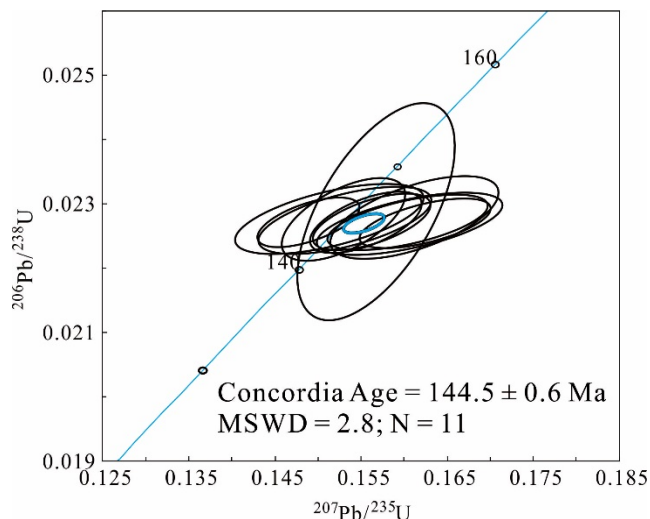


Figure 6. U-Pb concordia diagram of magmatic zircon from the granite porphyry causative intrusion from the Wunuer deposit.

3.2 Hydrothermal zircon concordia age

In-situ LA-ICP-MS analysis of hydrothermal zircon was conducted to constrain the age of hydrothermal activity. As shown in Fig. 7, the hydrothermal zircon U-Pb concordia age is 138.8 ± 1.1 Ma out of 10 samples.

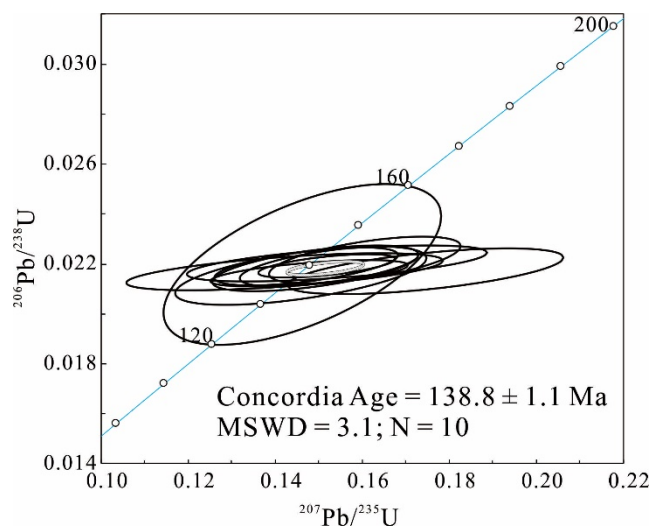


Figure 7. U-Pb concordia diagram of hydrothermal zircon from the Wunuer deposit.

3.3 Sphalerite Rb-Sr isochron age

Seven Sp2 samples from the Wunuer deposit were picked out to conduct Rb-Sr isotopic analyses and calculate the Rb-Sr isochron age. As shown in Fig. 8, the age obtained is 121 ± 2.3 Ma based on five out of seven analyses.

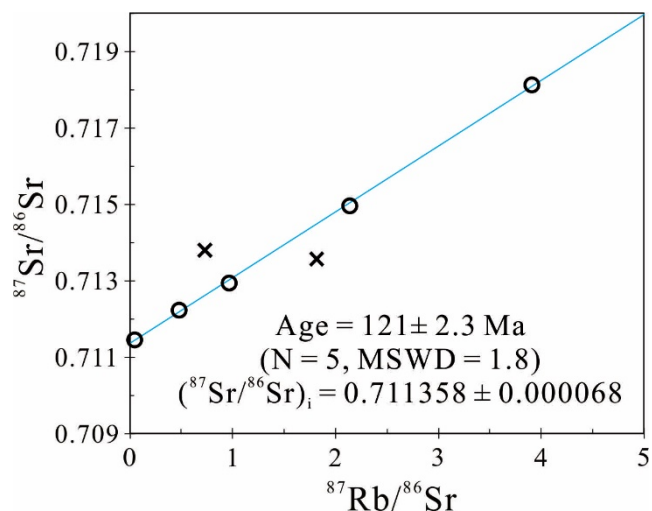


Figure 8. Rb-Sr isotopic isochron for Sp2 from the Wunuer deposit.

4 Sulfur source

In-situ sulfur isotope analysis of sphalerite was carried out using the LA-MC-ICP-MS technique. The two generations of sphalerite from the Wunuer deposit have similar sulfur isotope compositions, which range from 1.0‰ to 4.0‰ $\delta^{34}\text{S}_{\text{V-CDT}}$ (Fig. 9).

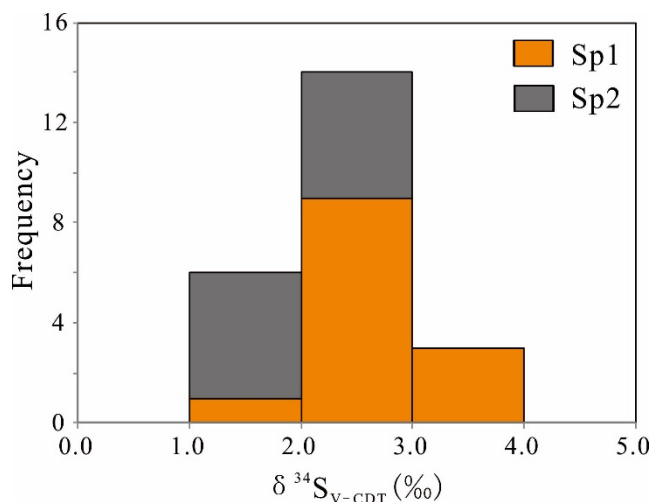


Figure 9. Frequency histogram of sulfur isotope compositions of sphalerite from the Wunuer deposit.

5 Discussion

The Wunuer deposit had successively sulfured three stages of mineralization, an early porphyry stage, an intermediate hydrothermal stage, and a later epithermal stage. And two generations of sphalerite, with the first-generation sphalerite (Sp1) precipitated in hydrothermal stage and the second-generation sphalerite (Sp2) precipitated in epithermal stage, were identified.

The negative linear correlation between Fe and Zn in Sp1, with a molar slope of approximately -1 (Fig. 4a), implies an isoivalent substitution of Fe²⁺→Zn²⁺ into crystal structure of Sp1. Negative linear correlations between Fe and Zn, Cu and Zn also exists in Sp2, both with a molar slope of approximately -2 (Fig. 4a, b). Fe in Sp2 shows a positive correlation with Cu, with a molar slope of approximately +1 (Fig. 4c). Therefore, it can be concluded that Cu, and most of Fe concentrated in Sp2 are mainly attribute to the ubiquitous chalcopyrite (CuFeS₂) inclusions in Sp2 (Bortnikov et al. 1991). Notably different Cu, In contents of Sp1 and Sp2 imply a Cu-depleted and In-rich fluid in hydrothermal stage, whereas a Cu-rich and In-depleted fluid in epithermal stage.

Fluid inclusion study reveals that from porphyry to hydrothermal and to epithermal mineralization, ore-forming fluids changed gradually from high temperature and moderate salinity to low temperature and low salinity (Fig. 5).

Magmatic zircon U-Pb concordia age of the ore-related granite porphyry, obtained as 144.5 ± 0.6 Ma (Fig. 6), can approximately represent the porphyry stage molybdenum-mineralization age. Hydrothermal zircons, formed during hydrothermal stage alteration, whose U-Pb concordia age (Fig. 7) thus can represent the hydrothermal stage zinc-mineralization age (121 ± 2.3 Ma). Rb-Sr isochron age of Sp2 (Fig. 8) implies that the epithermal stage lead-zinc-mineralization occurred at 121 ± 2.3 Ma (Yin et al. 2009).

Sp1 and Sp2 have similar positive sulfur isotope compositions (Fig. 9), which can be explained by the leaching of sulfur and potentially metals (Fe, Mo, Zn, Pb,

etc.) from the granite porphyry for both hydrothermal and epithermal stages of sphalerite mineralization (Ripley et al. 1999; Staude et al. 2011).

6 Conclusions

In the late Jurassic epoch (144.5 ± 0.6 Ma), felsic magma intruded and cooled to form the porphyry, and then induced the porphyry molybdenum-mineralization. Subsequently (138.8 ± 1.1 Ma), the high temperature and Cu-depleted fluids, which leached metal materials from the ore-forming related granite porphyry, induced the hydrothermal zinc-mineralization with the formation of Sp1. A long time after porphyry and hydrothermal mineralization (121 ± 2.3 Ma), low temperature and Cu-Pb-rich fluids resulted in the epithermal lead-zinc-mineralization with the formation of Sp2, galena and chalcopyrite. Finally, these three stages of mineralization composed the Wunuer porphyry-hydrothermal-epithermal system.

Acknowledgements

We acknowledge the financial support for the project from the Inner Mongolia Autonomous Region Geological Prospecting Fund Management Center [Grant number: NMKD2014-23]. We greatly acknowledge the fieldwork help of the Sixth Survey and Development Institute of Geology and Mineral in Inner Mongolia. Thanks to teacher Meijun Yang of WUT for helping me conduct the EPMA analyses.

References

- Bortnikov NS, Genkin AD, Dobrovol'Skaya MG, Muravitskaya GN, Filimonova AA (1991) The nature of chalcopyrite inclusions in sphalerite; exsolution, coprecipitation, or "disease"? *Econ Geol* 86:1070-1082. doi:10.2113/gsecongeo.86.5.1070
- Ripley EM, Park YR, Li C, Naldrett AJ (1999) Sulfur and oxygen isotopic evidence of country rock contamination in the Voisey's Bay Ni-Cu-Co deposit, Labrador, Canada. *Lithos* 47:53-68. doi: 10.1016/S0024-4937(99)00007-9
- Staude S, Göb S, Pfaff K, Ströbele F, Premo WR, Markl G (2011) Deciphering fluid sources of hydrothermal systems: A combined Sr- and S-isotope study on barite (Schwarzwald, SW Germany). *Chem Geol* 286:1-20. doi: 10.1016/j.chemgeo.2011.04.009
- Yin M, Li W, Sun X (2009) Rb-Sr isotopic dating of sphalerite from the giant Huize Zn-Pb ore field, Yunnan Province, Southwestern China. *Chinese J Geochem* 28:70-75. doi: 10.1007/s11631-009-0070-5

Hydrothermal alteration of granitic rocks and geophysical properties in “K-48-22-V” sheet in South Gobi, Mongolia

In-Joon Kim, Sang-Gun No*, Otgon-Erdene Davaasuren, Bum-Han Lee
Korea Institute of Geoscience and Mineral Resources

Abstract. The study area is located within the Gurvansayhan island arc terrane, Mongolia, which includes the Oyu Tolgoi, Kharmagtai, and Tsagaan suvarga porphyry type deposits. Intrusive rocks of the study area consist of granite, granite porphyry, acidic dyke, intermediate dyke, and aplite. In the study area chalcocopyrite, bornite and/or malachite bearing veins have been discovered in granite, granite porphyry, and aplite. Copper mineralization is mainly observed in granite which consists of quartz, alkali-feldspars, plagioclase, biotite and minor hornblende. The mineralization occurs as vein, breccia, disseminated, and fissure filling types. Alterations related to the Cu bearing veins were observed as alkali metasomatism, phyllic alteration, and prophylic alteration. The alterations were recognized by the changing color of the host granite due to the altered minerals such as alkali feldspar, epidote, and sericite. The chargeability obtained from the IP survey shows that there is a high anomaly point in the area where the content of Cu, Au, and Ag are high in the surface, especially in the underlying part bornite, covellite and chalcocite are observed.

1 Introduction

The “K-48-22-V” Cu area is located in the South Gobi region of Mongolia (Fig. 1), approximately 730 km south of the capital city of Ulaanbaatar and is in Omnogobi Province. The area has an average elevation of 1,345 m above sea level and relatively flat to gently undulating topography that is typical of the Gobi Desert of the southern Mongolia-Inner Mongolia plateau (Sung-Chiao, 1984). The term “Gobi” in Mongolian denotes all the deserts and semi deserts in the Mongolian plateau (Sung-Chiao, 1984), and locals use the term to refer to the windblown sand mounds around low bushes common in the region. The study area has been a subject of many systematic geological explorations since the last century. Expeditions of the Soviet Union have resulted in mapping and surveying of the region. Occurrences of copper and other minerals have been discovered during a 1:200,000 scale mapping expedition (Goldenberg et al., 1978), and identified as prospective. Many of the previous studies focused on Cu mineral areas and marked these areas as prospects.

Copper is one of the main metals produced in Mongolia. There are three primary belts across Mongolia where copper mineral deposits exist: South Mongolia, Central Mongolia and North Mongolian. The South Mongolian copper belt occupies nearly the entire area of the Gurvansayhan island arc terrane, and is a 600 km × 200 km arcuate belt that formed when Middle to Late

Palaeozoic volcanic and sedimentary rocks were intruded by Late Devonian and Carboniferous granitoids. The South Mongolian copper belt hosts most of the known porphyry and intrusion-related mineralization in the South Gobi region, including the giant Oyu Tolgoi copper-gold mine (2.4Bt @ 0.78% Cu & 0.33 g/t Au), the Tsagaan Suvarga copper molybdenum deposits (240 Mt @ 0.53% Cu & 0.018% Mo), Shuteen, Kharmagtai, and more than 45 additional deposits. The Early Mesozoic North Belt formed within a continental magmatic arc on the margin of the Siberian Craton. The arc developed in response to the closing of the Mongol-Okhotsk Sea and the subduction of the palaeo-Pacific ocean beneath the Siberian Craton. This belt hosts the giant Erdenet deposit (1.78Bt @ 0.62% Cu, 0.025% Mo), which is Mongolia’s largest producing porphyry copper-molybdenum deposit.

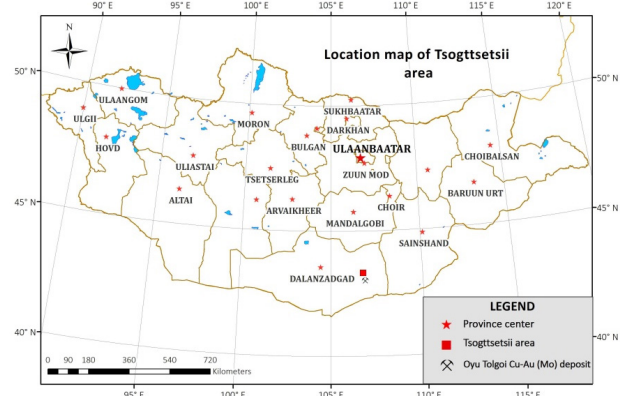


Figure 1. Location map of Tsogttsetsii area and Oyu Tolgoi Cu-Au (Mo) deposit.

2 Geological setting

The geology of the Tsogttsetsii area (Fig. 2) consists of the Lower Carboniferous Sainshand Khudag Formation which is the dominant formation in the southeastern and northeastern parts of the survey area and consists of andesite, andesite-basalt, basalt, and tuff with a total thickness of approximately 2000 m (Suetenko, 1973; Durante et al., 1976). The formation can be divided into an upper and lower series, and fossils of fauna and flora are locally observed. Goldenberg et al. (1978) reported a Lower Carboniferous age for the Sainshand Khudag Formation, based on fossils present within the strata. The Permian Argalant Formation, the lowest sequence in the survey area, consists of rhyolite, trachyrhyolite, basalt, ignimbrite, dacite, andesitedacite, tuff and tuffaleurolite, with a total thickness of 1800-1900 m. The Argalant Formation is cut through to the Sainshand Khudag

Formation. The Lower Cretaceous Bayanshiree Formation is present across most of the survey area and consists of red colored clay-sand, sandstone, conglomerate, gravelite, and aleurolite. This formation overlies an unconformity above Paleozoic and lower Mesozoic rocks rich in Uvurkhangai, South-Gobi, and East-Gobi and a sheeted discontinuity between the Bayanzag and Baruungoyot Formations. The multistage Permian intrusive complex is in the central and northern parts of the Tsogttsetsii area, and consists of granite, biotite- amphibole granite, hornblende-biotite, and granodiorite. Older, cross-cutting stocks and dikes are common in the survey area. Early dikes are possibly related to andesitic volcanism because the dikes intrude volcanic and volcano-sedimentary sequences of the Sainshand Khudag Formation. The dikes are monzodiorite and dacite porphyry, as well as rhyolite. Granodiorite and granite dikes that intruded later cut the Permian intrusive complex. Aplitic and andesitic dikes then intruded the granitic dikes. Based on regional tectonic constraints and the present-day erosion, two sets of faults (WNW trending and NW-trending) are recognized in the area. The W-NW trending lineaments are dikes, faults, and alteration zones (Otgon et al., 2016).

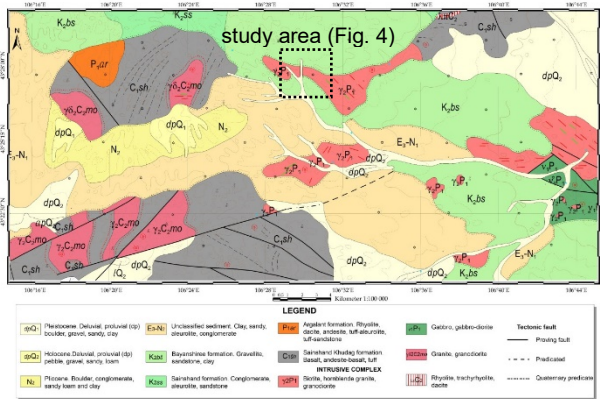


Figure 2. Geological map of the Tsogttsetsii area (modified after Jamiyandorj and Zoljargal, 2010).

3 Mineralization and alteration

Vein type is easily observed in field exploration. The veins are mainly extended in the NW-SE direction, and found within a rectangular area (500 m X 2km). The veins consist of different mineral assemblage such as magnetite + hematite + quartz + epidote + chalcocopyrite + bornite + pyrite and quartz + epidote + chalcocopyrite + pyrite (Fig. 3). The primary ore minerals containing copper are chalcocopyrite, malachite, bornite, and chrysocolla. In some samples, bornite has relatively high sulfur content.

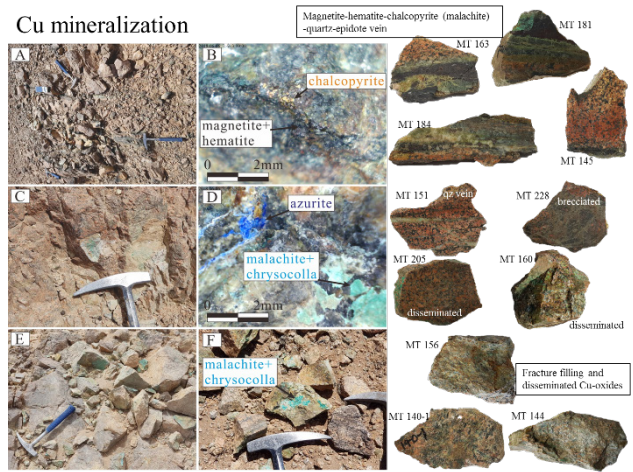


Figure 3. The Cu mineralization types from study area.

Alterations related with the Cu-bearing veins were observed as alkali metasomatism, phyllic alteration, and propylitic alteration (Fig. 4). The alterations were recognized by the changing the color of the host granite due to the altered minerals such as alkali feldspar, epidote, and sericite. The chargeability obtained from the IP survey shows that there is a high anomaly point in the area where the content of Cu, Au, and Ag are high in the surface, especially in the below part the bornite, covellite and chalcocite are observed.

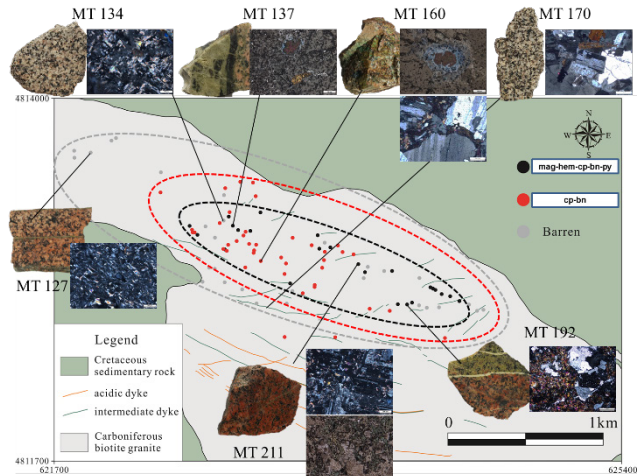


Figure 4. The alteration types associated with each Cu bearing veins.

The host granite has 10-10,000 (upper detection limit) ppm Cu, 4-64 ppb Au, and 0.5-23.9 ppm Ag (Fig. 5). High anomalies of Cu, Au, and Ag show similar NW-SE patterns on the anomaly map. The location points showing highest values of Cu, Au, and Ag are matched with the points of the bornite occurrences.

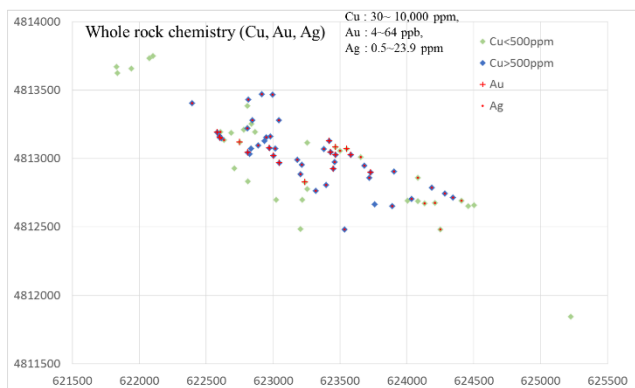


Figure 5. Whole rock chemistry (Cu, Au, Ag) from study area.

The chargeability obtained from the IP survey shows that there is a high anomaly point in the area (Fig. 6) where the content of Cu, Au, and Ag are high in the surface, especially in the below part the bornite, covellite and chalcocite are observed.

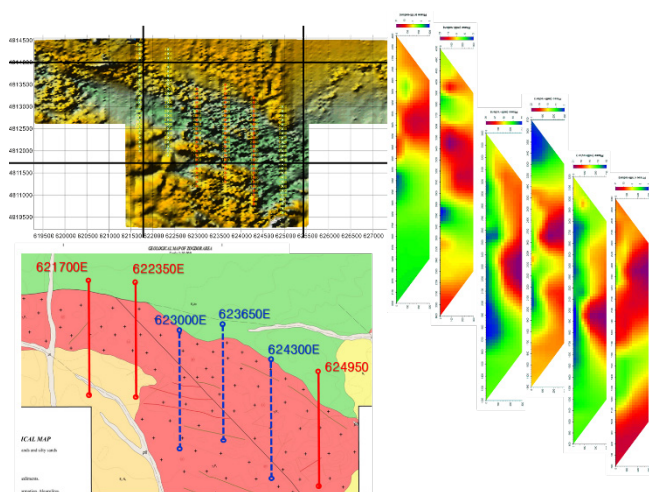


Figure 6. The chargeability map of study area.

4 Conclusion

We conclude that the mineral assemblages of the veins, along with the geochemical properties and alteration characteristics of the host rock, show that the study area has the potential for porphyry-related mineralization. Also, the results of chargeability surveys show NW-SE trending anomalies.

Acknowledgements

This research was supported by the Basic Research Project of the Korea Institute of Geoscience and Mineral Resources (Project No 19-3211-1) funded by the Ministry of Science, ICT and Future Planning of Korea.

References

Durante, M.V. and Zonenshein, P. (1976) Upper Paleozoic sediments and magmatism of Khan-Bogd area in South Mongolia. Bulletin of the Moscow Society of Naturalists Geological Series, 51, Moscow (in Russian).

Jamiyandorj, O. and Zoljargal, A. (2010) Geological map of Mongolia, Ikh luusiin uul sheet K-48-V (1:200,000 scale). Mineral Resources Authority of Mongolia (in Mongolian).
 Oteon, E.D., Lee, B.H., Kim, I. J., Ryoo, C.R., Heo, C.H (2016) Characteristics of the Copper Mineralization in Tsogttsetsii Area, Mongolia. J. Miner. Soc. Korea 29:23-34.
 Sung-Chiao, C. (1984) The sandy deserts and the gobi of China. In: El-Baz, F. (eds). Deserts and arid lands. The Netherlands, Martinus Nijhoff Publishers, 95-112.
 Goldenberg, V.I. and Sanjaadorj, D. (1978) Geological mapping scale 1 : 200000 on territory of Omnogovi, Dundgovi and Dornogovi aimaks. Ulaanbaatar, Ministry of Geology of Mongolia, open file Report No. 2724 (in Russian).
 Suetenko, O.D. (1973) Structure of Hercynian geosynclinal basin of southeastern Mongolia. Geotectonics, 3:167-182 (in Russian).

Constraining the relation of the Erdenet Porphyry Cu-Mo deposit to the Tsagaan Chuluut lithocap in Northern Mongolia

Leslie Logan, Albrecht Von Quadt, Thomas Driesner

Institute of Isotope Geochemistry and Mineral Resources, ETH Zurich, Zurich, Switzerland

Irena Peytcheva

Geological Institute, Bulgarian Academy of Science, Sofia, Bulgaria

Abstract. Erdenet porphyry Cu-Mo deposit is situated in the Central Asian Orogenic Belt, located north of the Tethyan tectonic domain, which formed as a result of multiple oceanic subduction events and collisions (Liu et al. 2015). Arc-magmatism resulted from the closure and subduction of the Mongol-Okhotsk Ocean under the Siberian Craton during the late Permian and early Triassic. The deposit is the second largest copper producer in Mongolia (26 million tons of ore per year) and is ~240 Ma (Watanabe and Stein 2000; Jiang et al. 2010; Kavalieris et al. 2017). Erdenet is spatially related to the Tsagaan Chuluut lithocap approximately 2 km NW of Erdenet open pit, however, recent $^{40}\text{Ar}/^{39}\text{Ar}$ dating on alunite from the lithocap suggests it is 16 Ma younger than the porphyry system (224 ± 2 Ma; Kavalieris et al. 2017). To constrain the relationship between the lithocap and Erdenet porphyry deposit and assess the future exploration potential of the region, new zircon U-Pb LA-ICP-MS and ID-TIMS age data, and trace element geochemistry were obtained on selected host and younger cross-cutting dikes in both the deposit and the lithocap.

1 Introduction

Magmatic-hydrothermal ore systems form from focused and expelled magmatic fluid as a result of progressive crystallization of hydrous silicate melt. When the fluids originate from a fertile magma chamber and carry metal complexes, the interaction of such fluids and volatiles with wall rocks and local meteoric water can create porphyry Cu (Au-Ag-Mo) deposits together with an important halo of characteristic alteration zones (Heinrich and Candela 2014). In the shallowest manifestations of such alteration zones, advanced argillic alteration commonly forms an erosion-resistant cap, termed lithocap, composed of quartz, alunite, and argillic minerals (Hedenquist and Taran 2013), which can also be hosts to high-sulfidation epithermal massive-sulfide or Au-Ag deposits.

Mongolia's second largest porphyry Cu deposit is the locally-owned Triassic age Erdenetiin Ovoo (referred to as Erdenet) porphyry Cu-Mo deposit in north central Mongolia which currently produces 530,000 tons of copper concentrate and 4,500 tons of molybdenum concentrate per year (Erdenet Mining Corporation 2017). Approximately 2 km northwest of Erdenet deposit, the Tsagaan Chuluut lithocap outcrops in the form of

resistant ridges of quartz-alunite and residual quartz. While a body of literature (mostly Russian and Asian) exists for Erdenet deposit from the last 40 years, only recently has the Tsagaan Chuluut lithocap been shown to be enigmatic in its relation to Erdenet porphyry (Kavalieris et al. 2017). Kavalieris et al. (2017) published a $^{40}\text{Ar}/^{39}\text{Ar}$ date on K-alunite from the lithocap indicating the timing of its formation was 223.5 ± 1.9 Ma, which is 16 Ma younger than the accepted age of the porphyry (~240 Ma; Watanabe and Stein 2000; Jiang et al. 2010; Kavalieris et al. 2017). This age discrepancy implies the fluid source for the Tsagaan Chuluut lithocap at 223.5 ± 1.9 Ma is not related to the fluids that formed the Erdenet porphyry intrusion at 240 Ma, which carries important economic and future exploration implications for the region. To further investigate whether the lithocap is related to either the adjacent Erdenet deposit or subjacent, still undiscovered porphyry mineralization, new zircon U-Pb laser ablation inductively coupled plasma mass spectrometry (LA-ICP-MS) and ion dilution thermal ionization mass spectrometry (ID-TIMS) age data, and trace element geochemistry were obtained on key geologic samples that bracket the timing of porphyry and lithocap formation.

2 Background

Erdenet porphyry Cu-Mo deposit is related to the formation of the Central Asian Orogenic Belt (CAOB), which extends from the present day Ural Mountains in the west to the Sea of Okhotsk in the east. The CAOB has a multi-phase tectonic history, including the subduction of the Mongol-Okhotsk Ocean (Liu et al. 2015) which drove the arc-magmatism responsible for the Erdenet porphyritic granodiorite that hosts the Cu-Mo mineralization. The Erdenet ore district is a 20 km long NW-SE trending line of ore prospects (Fig. 1a) which occur as magnetic-low anomalies in a reduced-to-pole magnetization map (Fig. 1b) due to the associated magnetite-destructive sericitic alteration. Notably, to the northwest of the currently mined Erdenet open pit, and running in the same trend as the other prospects in the district, is a hitherto unexploited magnetic-low anomaly (Power Station anomaly), which lies directly under a local Erdenet neighborhood. This is the closest magnetic-low anomaly to the Tsagaan Chuluut lithocap.

The currently accepted age data for Erdenet porphyry come from a Re-Os date on molybdenite (Watanabe and

Stein 2000), a U-Pb date on host quartz diorite zircons (Jiang et al. 2010), and a $^{40}\text{Ar}/^{39}\text{Ar}$ date on muscovite from the sericitic alteration zone exposed in

formation of the Tsagaan Chuluut lithocap (based on the porphyritic andesite dikes).

3 Results and discussion

3.1 Zircon geochronology – LA-ICP-MS

Weighted average $^{206}\text{Pb}/^{238}\text{U}$ ages give a first order approximation for the timing of the zircon crystallization in each of the respective samples (Table 1). The U-Pb data of the zircons of the pre-mineralization samples vary in age but are generally >250 Ma, in agreement with early stage magmatism in the region (Sotnikov et al. 2005). The syn-mineralization samples indicate protracted zircon crystallization, with weighted average ages around ~ 237 Ma, and within error of previously published dates for the deposit (Watanabe and Stein 2000; Jiang et al. 2010; Kavalieris et al. 2017). The post-mineralization samples bracket the timing of mineralization and alteration seen at Erdenet open pit and the Tsagaan Chuluut lithocap, respectively. Sample 376 (trachyandesite dike) gives a weighted average age of 240.3 ± 3.6 Ma, suggesting the dike could be coeval with the Erdenet magmatism. However, trace element discrimination diagrams and cathodoluminescent imaging argue that these zircons were not inherited from Erdenet porphyry rocks (Section 3.3). Sample 287 (porphyritic andesite dike) gives a weighted average age of 229.3 ± 3.4 Ma, and is within error of the alunite $^{40}\text{Ar}/^{39}\text{Ar}$ inverse isochron age of 224 ± 2 Ma from the lithocap (Kavalieris et al. 2017).

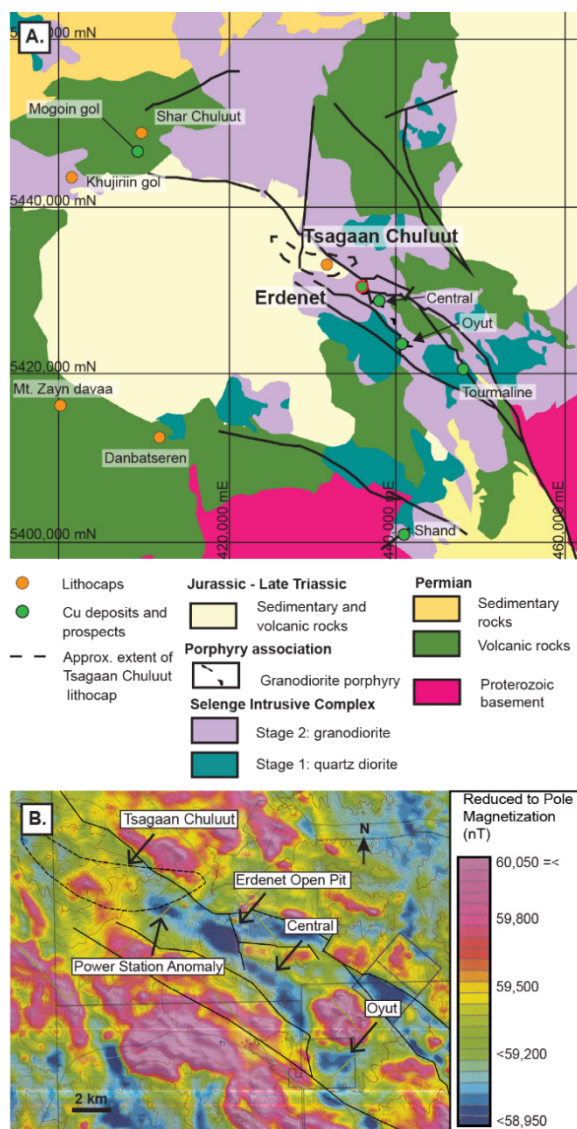


Figure 1. A. Schematic geologic map of Erdenet ore district showing locations of Cu deposits and prospects, lithocaps, and the location of Erdenet and Tsagaan Chuluut lithocap. Modified after Kavalieris et al. (2017). B. Reduced-to-pole magnetic map (nT) of the Erdenet ore district (JICA 1992). Porphyritic centers in the district occur as magnetic-low anomalies. Tsagaan Chuluut lithocap extent is outlined in both maps.

the open pit (Kavalieris et al. 2017). These dates bracket the timing of both intrusion and mineralization at ca. 240 Ma. The current study contributes new U-Pb LA-ICP-MS and first-time ID-TIMS zircon age data for pre-mineralization granodiorite host rocks, syn-mineralization porphyritic granodiorite, post-mineralization cross-cutting trachyandesite dikes in the open pit, and cross-cutting porphyritic andesite dikes in the lithocap. Samples were selected in order to bracket the latest timing of mineralization in the open pit (from the trachyandesite dikes) and compare it to the latest possible timing of

Table 1. Weighted average $^{206}\text{Pb}/^{238}\text{U}$ ages for Erdenet pre- syn- and post-mineralization samples based on LA-ICP-MS analysis and calculated using Isoplot (Ludwig 2003).

Sample	Rock Type	Relative Timing	$^{206}\text{Pb}/^{238}\text{U}$	Error*
245	QDi	Pre-min.	258.3	± 3.9
259	Gd	Pre-min.	255.7	± 3.8
379.3 EGGr	Gd	Pre-syn-min.	237.4	± 3.6
379.3 AP	Gd	Pre-syn-min.	237.7	± 3.6
380 EGGr	Gd	Pre-syn-min.	235.7	± 3.5
380 CPB	Gd brc	Pre-syn-min.	236.6	± 3.5
376	TA dke	Post-min.	240.3	± 3.6
287	An dke	Post-min.	229.3	± 3.4

Abbreviations: QDi: quartz diorite, Gd: granodiorite, brc: breccia, TA: trachyandesite, An: andesite, dke: dike, min: mineralization. *propagated systematic error (1.5%)

3.2 Zircon geochronology – ID-TIMS

Zircons from three samples were selected for further ID-TIMS U-Pb zircon analysis: an altered pre- to syn-mineralization porphyritic granodiorite (379.3 AP), a post-mineralization trachyandesite dike (376), and a porphyritic andesite dike (287) that cross-cuts the lithocap (Fig. 2). Results from the host granodiorite and cutting trachyandesite dike help constrain the latest

timing of porphyry mineralization in the open pit. While the results indicate the weighted average ID-TIMS age for the cross-cutting trachyandesite dike is older than the hosting (and mineralized) granodiorite, it is likely that analytical uncertainty and zircon grain selection causes this slight discrepancy. Though data is limited, utilizing the youngest zircons of both 376 (trachyandesite dike) and 379.3 AP (granodiorite), it can be suggested that at least 240,000 y passed at Erdenet porphyry deposit before the emplacement of the dike.

Zircons from the porphyritic andesite dike (287) that cross-cuts the lithocap show a weighted average ID-TIMS age of 230.219 ± 0.095 Ma (Fig. 2); importantly being older than and contradicting the currently published $^{40}\text{Ar}/^{39}\text{Ar}$ K-alunite age obtained for the lithocap (223.5 ± 1.9 Ma; Kavalieris et al. 2017). The lack of overlapping errors between the two ages suggests the $^{40}\text{Ar}/^{39}\text{Ar}$ age is not representative of the true timing of formation of the Tsagaan Chuluut lithocap and that the alunite measured for $^{40}\text{Ar}/^{39}\text{Ar}$ analysis did not remain in a closed isotopic system in its history. Additional microscopic and X-ray diffraction evidence from this study indicates plagioclase crystals in the porphyritic andesite samples have been altered to epidote, clays, and chlorite, corroborating that the dike and the lithocap were altered by relatively hot fluids after the dike's emplacement.

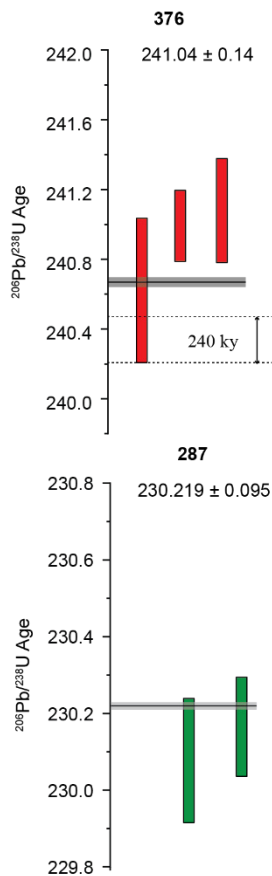


Figure 2. Weighted average $^{206}\text{Pb}/^{238}\text{U}$ ID-TIMS ages for the three selected Erdenet samples.

3.3 Zircon trace element geochemistry

Zircon trace element geochemistry was used to distinguish and compare the dated pre-, syn-, and post-

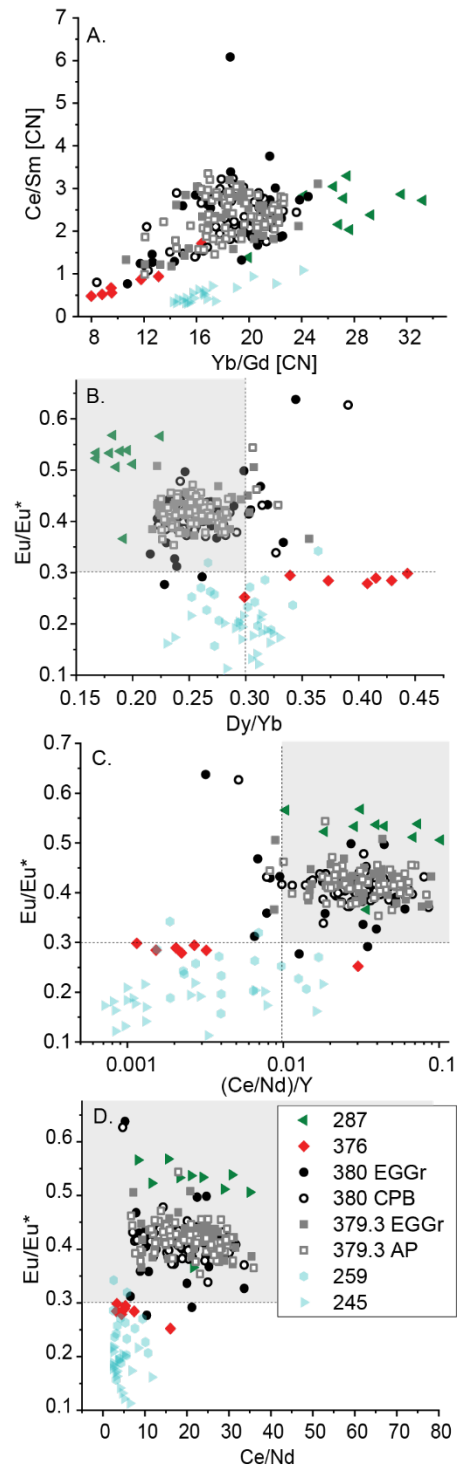


Figure 3. Trace element data showing the state of evolution of rocks at Erdenet. A. Sample 376, though post-dating the host porphyry rocks (gray and black symbols), shows least evolved signatures. B-D. Samples from fertile porphyry Cu deposits typically plot in gray zones (Lu et al. 2016). Note dike sample 287, which cross-cuts Tsagaan Chuluut plots in the same zones.

mineralization samples and to provide insight into the processes forming each rock type. In general, zircons from the trachyandesite dike that cross-cuts the Erdenet porphyry (376) shows least-evolved signatures (relative to the other analyzed samples) especially noted in the plot of Yb/Gd (chondrite normalized, CN) versus Ce/Sm (CN; Fig. 3a). This suggests that even though the U-Pb geochronology indicates the trachyandesite dike is approximately coeval with the granodiorite host rocks, it has significantly more primitive trace element signatures and therefore should be related to late-post-ore replenishment of the upper crustal magma chamber. Additionally, these primitive signatures discriminate these zircons from Erdenet porphyry rocks excluding the possibility that they were inherited from the late stage Erdenet magma. On the other hand, the cross-cutting dike in the lithocap (287) shows the most evolved signatures in trace elements comparisons. It has previously been shown that fertile porphyry Cu ± Mo ± Au deposits can be traced by Eu/Eu* (Eu/sqrt(Sm*Gd), CN values), Ce/Nd, Dy/Yb, and Y comparisons of zircon compositional data, with Eu/Eu* values >0.03, (Ce/Nd)/Y >0.01, Dy/Yb <0.3 (Lu et al. 2016). Using these values to compare Erdenet and Tsagaan Chuluut zircon data (Fig. 3b-d) reveals that the dike that cross-cuts the lithocap (287) has a fertile magma chamber signature, despite being ca. 10 Ma younger than Erdenet deposit. Importantly, this suggests that magmatism sourcing from a fertile magma chamber occurred 10 Ma after Erdenet deposit was formed, and these dikes may belong to a yet undiscovered porphyry deposit. Additionally, such magmatism may be an explanation for an isotopic resetting of the younger alunite ⁴⁰Ar/³⁹Ar age obtained by Kavalieris et al. (2017).

4 Implications

The recent ⁴⁰Ar/³⁹Ar alunite age published by Kavalieris et al. (2017) raises an important question about the relationship of Tsagaan Chuluut lithocap to the Erdenet porphyry Cu deposit with significant economic implications. The ²⁰⁶Pb/²³⁸U ID-TIMS youngest zircon age (230.079 ± 0.150 Ma) of the cross-cutting porphyritic andesite dike in the lithocap contradicts the 16 Ma younger ⁴⁰Ar/³⁹Ar alunite age and indicates the lithocap cannot be younger than ca. 230 Ma. However, zircon trace element geochemistry (Fig. 3) indicates the zircons from this dike source from a similar (and fertile) magma chamber as the Erdenet porphyry host rocks (²⁰⁶Pb/²³⁸U ID-TIMS youngest zircon age of 240.601 ± 0.395 Ma). The 10 Ma gap between these rocks suggests another similar and fertile magmatic system was occurring after the formation of Erdenet porphyry Cu-Mo deposit and may be related to the isotopic resetting and/or later formation of alunite in the Tsagaan Chuluut lithocap. Further geochronology and characterization of Tsagaan Chuluut lithocap is needed to fully assess the exploration potential of Erdenet ore district.

Acknowledgements

This project was carried out at and supported by the Institute of Isotope Geochemistry and Mineral Resources at ETH Zurich. The authors thank Erdenet Mining Corporation, Imants Kavalieris, and Bat-Erdene Khashgerel for their collaboration and guidance during the field work in this project.

References

- Erdenet Mining Corporation (2017) About Us. EMC. https://www.erdenetmc.mn/en/about_us/. Accessed 20 January 2018
- Hedenquist JW, Taran YA (2013) Modeling the formation of advanced argillic lithocaps: volcanic vapor condensation above porphyry intrusions. *Economic Geology* 108:1523–1540
- Heinrich CA, Candela PA (2014) Fluids and Ore Formation in the Earth's Crust. In: *Treatise on Geochemistry*. Elsevier, pp 1–28
- Japan International Cooperation Agency (1992) Report on the mineral exploration in the Uudam-tal area, Mongolian People's Republic (phase 1). Japanese International Cooperation Agency, Tokyo
- Jiang SH, Nie FJ, Su YJ, et al (2010) Geochronology and origin of the Erdenet Superlarge Cu-Mo deposit in Mongolia. *Acta Geoscientica Sinica* 31:289–306
- Kavalieris I, Khashgerel B-E, Morgan LE, et al (2017) Characteristics and ⁴⁰Ar/³⁹Ar Geochronology of the Erdenet Cu-Mo Deposit, Mongolia. *Economic Geology* 112:1033–1054. doi: 10.5382/econgeo.2017.4500
- Liu X, Xu J, Xiao W, et al (2015) The boundary between the Central Asian Orogenic belt and Tethyan tectonic domain deduced from Pb isotopic data. *Journal of Asian Earth Sciences* 113:7–15. doi: 10.1016/j.jseaes.2015.04.039
- Lu Y-J, Loucks RR, Fiorentini M, et al (2016) Chapter 13: Zircon Compositions as a Pathfinder for Porphyry Cu ± Mo ± Au Deposits. In: Richards JP (ed) *Society of Economic Geologists Special Publication 19 on Tethyan Tectonics and Metallogeny*. pp 329–347
- Ludwig KR (2003) *Isoplot/Ex—a geochronological toolkit for microsoft excel*. Berkeley Geochronol Centre Spec Publ 4:1–71
- Sotnikov VI, Ponomarchuk VA, Sorokin AA, Gimon VO (2005) Age boundaries of the formation of porphyry Cu-Mo deposits in framing structures of the Mongol-Okhotsk orogenic belt. *Transactions of the Russian Academy of Science* 403:522–525
- Watanabe Y, Stein HJ (2000) Re-Os ages for the Erdenet and Tsagaan Suvarga porphyry Cu-Mo deposits, Mongolia, and tectonic implications. *Economic geology* 95:1537–1542

Geology and ore-forming processes of Tiegelongnan giant porphyry-epithermal Cu deposit in Tibet, China

Bin Lin

MNR Key Laboratory of Metallogeny and Mineral Assessment, Institute of Mineral Resources, CAGS, Beijing, China

Abstract. Tiegelongnan is located in Bangongco-Nujiang metallogenic belt, Tibet. It is the largest porphyry-epithermal Cu deposit in Duolong ore cluster with over 2.0 Gt @ 0.53% copper. The deposit is hosted in the Jurassic sandstones (Sewa Formation), and is related to Cretaceous intermediated-felsic intrusions (diorite and granodiorite), covered and protected by post-ore andesitic volcanic rocks of the Abushan Formation (Fig. 1; Lin et al. 2017a). This study aims to reveal the alteration, mineralization, diagenesis and ore-forming processes of this giant deposit according to the detailed geological core-logging, geochronology and fluid inclusions.

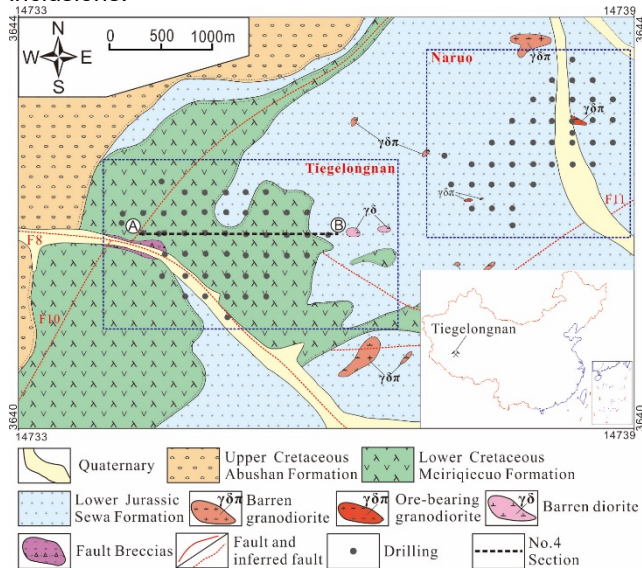


Figure 1. Geological map of Tiegelongnan (Lin et al., 2019).

1 Geology

Based on the detailed field geological survey, drilling logging and microscopy, two kinds of mineralization were identified, with the early porphyry mineralization overprinted by later epithermal mineralization (Lin et al. 2019). Veinlet, vein and disseminated pyrite, chalcopyrite, bornite and minor molybdenite, etc. were the typical mineralization in the deep and outer zones (Lin et al. 2017a). Potassic, prophylic, and phyllic were the main alteration styles and A, B, D veins occurred during the porphyry mineralization. Epithermal mineralization is mainly produced in the shallow parts of the system, superimposed onto the porphyry mineralization with disseminated and vein pyrite, enargite, bornite, covellite, digenite, spionkopite, yarrowite, djurleite and other Cu-S series minerals. The altered minerals are alunite, kaolinite and dickite, representing the advanced argillic

alteration. These altered minerals often occurred with high-sulfidation metal minerals as described above, in the N type veins (Fig. 2) (Lin et al. 2017b). The diagenesis and mineralization of Tiegelongnan deposit can be subdivided into: diagenetic stage, magmatic-hydrothermal stage (divided into porphyry mineralization substage and epithermal mineralization substage, furtherly), and supergene stage, according to characteristics of alteration and mineralization, the crosscutting relationship of veins.

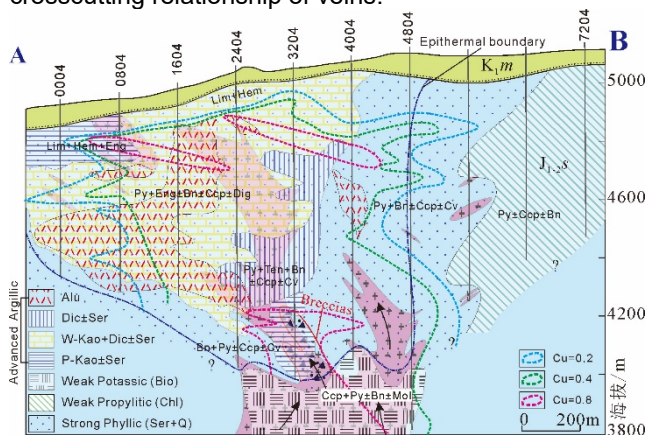


Figure 2. Mineralization and alteration zone of No.4 section of Tiegelongnan. Abbreviations: Alu-alunite, Bn-bornite, Bio-biotite, Ccp-chalcopyrite, Chl-chlorite, Cv-Covellite, Dic-dickite, Dig-digenite, Eng-Enargite, Hem-hematite, Kao-kaolinite, lim-limonite, Mo-molybdenite, Py-pyrite, Q-quartz, Ser-sericite, Ten-tennantite, W-well crystallization, P-poor crystallization.

2 Results and Discussion

The diorite porphyry was intruded in the western of Tiegelongnan, as a concealed dike. Strong prophylic alteration and minor veinlet chalcopyrite, pyrite and/ or hematite are occurred in diorite porphyry, locally. Twenty LA-ICP-MS ages of zircons were used to determine the crystal age of diorite porphyry. Its weighted average age was 123.1 ± 1.7 Ma (MSWD=0.7) (Lin et al., 2017a), represented the initial magmatism in Tiegelongnan deposit.

The granodiorite porphyry was emplaced in the center of Tiegelongnan, showing the closely relationship with copper mineralization and potassic, phyllic and advanced argillic alteration. The LA-ICP-MS weighted average ages of three different granodiorite porphyry samples (4804, 3204 and 2404) were 121.5 ± 1.5 Ma ($n=27$, MSWD=0.8), 122.1 ± 1.0 Ma ($n=23$, MSWD=0.4) and 120.4 ± 1.3 Ma ($n=25$, MSWD=0.9), respectively. The SHRIMP weighted average age of another granodiorite porphyry sample

(4004) was 121.2 ± 2.4 Ma ($n=9$, $MSWD=1.3$), conceded with the LA-ICP-MS ages within the error.

The volcanic rocks, andesite and dacite of Meiriqiecuo Formation covered the intrusions obviously, indicated that they erupted later, as the end of magmatism in Tiegelongnan. The LA-ICP-MS weighted average ages of two samples of andesite (3220, 2404) were 111.8 ± 1.5 Ma ($n=21$, $MSWD=1.6$), 110.1 ± 0.7 Ma ($n=18$, $MSWD=2.3$) (Wang et al., 2015), respectively, which were conceded with the SHRIMP age of another sample (3204), 111.7 ± 2.1 Ma ($n=10$, $MSWD=1.3$).

The Re-Os ages of eight molybdenite samples from ore-bearing porphyry were in the range of 120.8 ± 1.7 Ma to 121.7 ± 1.7 Ma and a weighted averaged age of 121.2 ± 0.6 Ma ($MSWD=0.1$) (Lin et al., 2017a) in agreement with previously published dates of 119 ± 1.4 Ma (Fang et al., 2015). These data represented the porphyry mineralization age. Eight pyrite samples from the advanced alteration zone were used to do the Rb-Sr dating, and yielded an isochron age of 117 ± 1.8 Ma ($MSWD=1.3$), representing the age of high-sulfidation epithermal mineralization (Line et al., 2017b).

^{40}Ar - ^{39}Ar ages of biotite from potassic zone, sericite from phyllic zone were 121.1 ± 0.5 Ma, 120.8 ± 0.9 Ma, respectively (Lin et al., 2017b), which were coincided with Re-Os ages (121.2 ± 1.2 Ma) of molybdenite from the porphyry mineralization (Lin et al., 2017a). In addition, An ^{40}Ar - ^{39}Ar age of alunite from advanced argillic zone is 117.9 ± 1.6 Ma, which coincided with the Rb-Sr age (117.5 ± 1.8 Ma) of pyrite from epithermal mineralization (Fig. 3) (Lin et al., 2017b). These ages showed the delicate temporal framework of different alteration and mineralization, and were useful to reveal the ore-forming process of Tiegelongnan giant deposit.

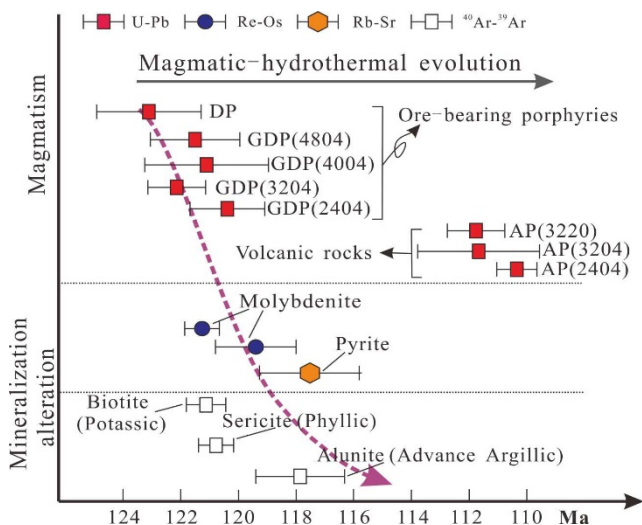


Figure 3. Metallogenic temporal framework of the Tiegelongnan deposit (Lin et al., 2017b)

3 Conclusion

In summary, the ore-forming process of the Tiegelongnan giant deposit can be divided into three stages: A) Porphyry mineralization (123 to 119Ma): diorite and

granodiorite porphyries intruded successively and formed the porphyry alteration and mineralization. B) Epithermal mineralization (118 to 117Ma): magmatic vapour and hydrothermal fluid mixed with groundwater, superimposed and reformed the early porphyry alterations and mineralization, and formed the advanced argillic alteration and high-sulfidation copper polymetallic mineralization. C) Post mineralization volcanic cover (111 to 110 Ma): the large volume of andesite and dacite were erupted after a significant period of erosion of the porphyry-epithermal ore-body (~7 Ma) (Fig. 4), and protected the deposit up to now..

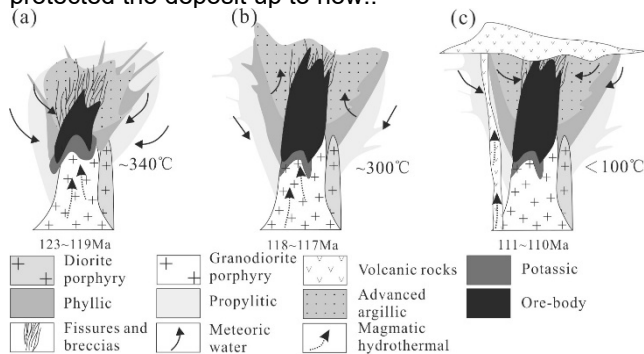


Figure 4. Ore-forming process of Tiegelongnan giant deposit (Lin et al. 2017b).

Acknowledgements

This work was jointly sponsored by the Public Science and Technology Research Funds Projects, National Key R&D Pro-gram of China, Deep Resources Exploration And Mining (project No.2018YFC0604101 and 2018YFC0604106).

References

Lin B, Tang JX, Chen YC., Baker M, Song Y, Yang HH, Wang Q, He W, Liu ZB (2019) Geology and geochronology of Naruo large porphyry-breccia Cu deposit in the Duolong district, Tibet. *Gondwana Res.* 66: 168-182

Lin B, Tang JX, Chen YC, Song Y, Hall G, Wang Q, Yang C, Fang X, Duan JL, Yang HH (2017a) Geochronology and Genesis of the Tiegelongnan Porphyry Cu(Au) Deposit in Tibet: Evidence from U-Pb, Re-Os Dating and Hf, S, and H-O Isotopes. *Resour Geol* 67: 1-21

Lin B, Chen YC, Tang JX, Wang Q, Song Y, Yang C, Wang, WL, He W, Zhang LJ (2017b) $^{40}\text{Ar}/^{39}\text{Ar}$ and Rb-Sr Ages of the Tiegelongnan Porphyry Cu-(Au) Deposit in the Bangong Co-Nujiang Metallogenic Belt of Tibet, China: Implication for Generation of Super-Large Deposit. *ACTA GEOLOGICA SINICA (English edition)* 91: 602-616

Wang Q, Tang JX, Fang X, Song Y, Wang YY, Yang HH, Yang C, Li YB, Wei LJ, Feng J, Li L (2015) Petrogenetic setting of andsites in Rongna ore block, Tiegelong Cu (Au -Ag) deposit, Duolong ore concentration area, Tibet: Evidence from zircon U-Pb LA-ICP-MS dating and petrogeochemistry of andsites. *Geology in China*, 42:1324-1336 (in Chinese with English abstract)

Fang X, Tang JX, Song Y, Yang C, Ding S, Wang YY, Wang Q, Sun XG, Li YB, Wei LJ, Zhang Z, Yang HH, Gao K, Tang P (2015) Formation epoch of the South Tiegelong supelarge epithermal Cu (Au-Ag) deposit in Tibet and Its Geological Implications. *Acta Geoscientica Sinica*, 36: 168-176 (in Chinese with English abstract)

Constraints of Re-Os-S-Pb isotopes and trace elements geochemistry on the genesis of the Larong W-Mo deposit, eastern Tibet

Jun Liu, Wenchang Li

Faculty of Earth Resources, China University of Geosciences, Wuhan, China

Wenchang Li, Xiangping Zhu, Baodi Wang

Chengdu Center of China Geological Survey, China

Fucheng Yang

Kunming University of Science and Technology, China

Abstract. The Larong W-Mo deposit is the first giant porphyry W-Mo deposit discovered in eastern Tibet. The W-Mo orebodies are mainly hosted in the monzogranite porphyry, the granodiorite porphyry and the surrounding quartz schist. Re-Os isotopic dating of six molybdenite samples yielded a weighted mean age of 91.8 ± 0.5 Ma. The results of in-situ trace elements analyses of pyrite, molybdenite and chalcopyrite are consistent with the mineralization characteristics of the Larong deposit, in which the main metallogenic elements are W and Mo, accompanied by Bi, Sn and Cu. The $\delta^{34}\text{S}_{\text{VCDT}}$ values of sulfides range from 0.25‰ to 6.37‰, with a mean of 2.15‰, suggesting a predominant magmatic sulfur origin. Molybdenite has high Pb isotopic composition ($^{208}\text{Pb}/^{204}\text{Pb} = 39.356\text{--}39.908$, $^{207}\text{Pb}/^{204}\text{Pb} = 15.747\text{--}15.928$, $^{206}\text{Pb}/^{204}\text{Pb} = 18.843\text{--}20.1$), but low Ni and Re contents, implying that the ore-forming materials in the Larong deposit were derived mainly from the upper crust. The W-Mo mineralization is genetically related to the Late Cretaceous monzogranite porphyry. With the decrease of temperature and oxygen fugacity of ore-forming fluid exsolved from magma, the mineralization of tungsten and molybdenum was formed successively.

1 Introduction

The Leiwuqi-Zogang metallogenic belt (LZMB) is an important non-ferrous metallogenic belt in Sanjiang area of southwestern China (Fig. 1). Previously discovered deposits in this belt mainly consist of Pb-Zn deposits and Fe deposits. The discoveries of the Saibeinong Sn deposit, Larong W-Mo deposit and Dongpulu Cu-W-Sn deposit in recent years indicate that the LZMB is expected to become another important W-Sn-Mo-Cu mineral resource base in southwest China. The Larong W-Mo deposit is situated in the southeastern part of the LZMB (Fig. 1). So far only a general study on the geological characteristics and metallogenic background of this deposit has been carried out. The formation age of the Larong deposit is unclear, the sources of ore-forming materials and the genesis of the deposit are not constrained.

Here Re-Os isotopic dating of molybdenite, in-situ sulfur and lead isotopic and trace elemental analyses of

sulfides from the Larong deposit are carried out in order to determine the mineralization age, reveal the sources of ore-forming materials and provide critical information for the metallogenic process of the Larong deposit.

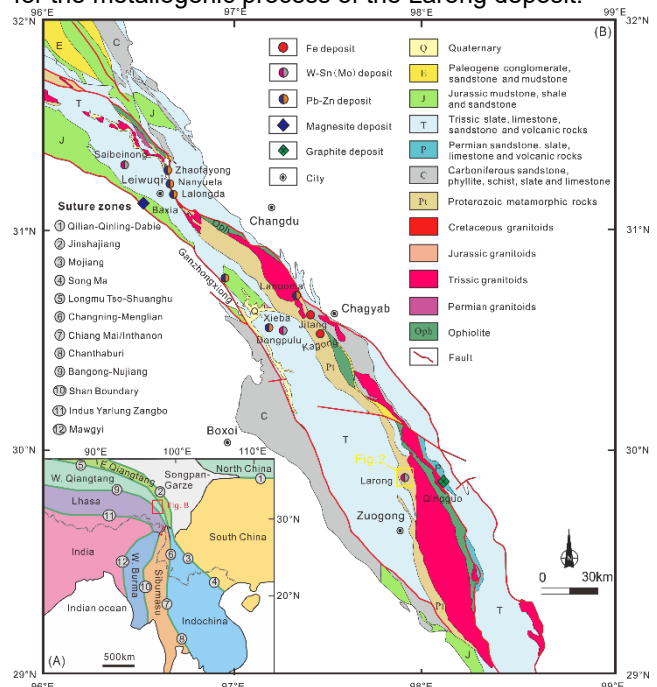


Figure 1. (A) Tectonic subdivision of the Tibetan Plateau-Sanjiang Region (Metcalf 2013); (B) Geological map of the Leiwuqi-Zogang belt in eastern Tibet.

2 Geology of the ore deposit

The Youxi Group is the main ore-bearing strata (Fig. 2), which predominantly comprises a set of quartz schist, and metamorphic quartz sandstone. The faults are well developed in this deposit, mainly consisting of two groups of fault structures in directions of NW and nearly W-E (Fig. 2). The magmatic rocks in the deposit are mainly hypabyssal intrusive rocks. The granodiorite porphyry is located in the shallow part of the deposit, the monzogranite porphyry is situated in the deep part of this deposit, and both of them are ore-bearing intrusions. LA-ICP-MS zircon U-Pb dating reveals that the Larong

granodiorite porphyry and monzogranite porphyry were emplaced at 213.8 ± 1.3 Ma and 93.9 ± 1.3 Ma, respectively.

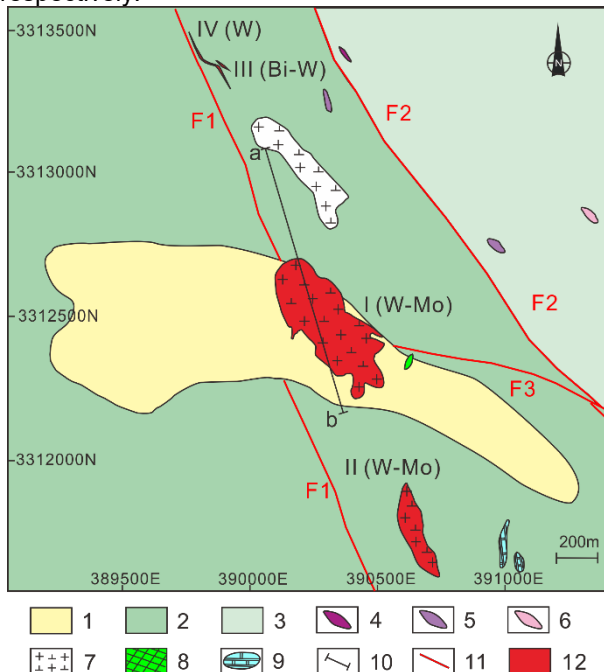


Figure 2. Geological map of the Larong W-Mo deposit. Abbreviations: 1–Quaternary; 2–Proterozoic Youxi Group; 3–Lower Carboniferous Kagong Formation; 4–granodiorite dike; 5–granite dike; 6–granite aplite dike; 7–granodiorite porphyry; 8–skarn; 9–limestone; 10–cross-section; 11–fault; 12–ore body.

The Larong W-Mo deposit includes four orebodies (Fig. 2) which occur as banded structures along the NW direction and holds more than 11.48 Mt WO_3 and 2.6 Mt Mo. The NO. I main orebody is mainly hosted in the monzogranite porphyry, the granodiorite porphyry and the surrounding quartz schist. The ore minerals mostly consist of scheelite, molybdenite, pyrite and a small amount of chalcocopyrite (Fig. 3). The gangue minerals are commonly composed of quartz, alkaline feldspar, sericite, muscovite, fluorite, chlorite, epidote and calcite. The Larong deposit has the alteration characteristics of typical porphyry W deposits. The alteration zonations from the inside to the outside can be roughly divided into potassium zone, strong quartz-sericite (muscovite) zone,

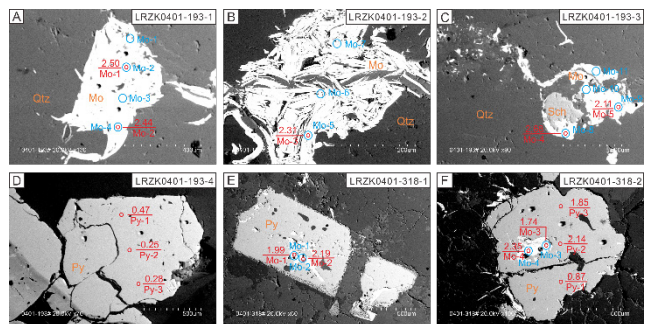


Figure 3. Representative SEM Photomicrographs showing $\delta^{34}S$ ‰ values for sulfides: (A)-(D) scheelite-molybdenite-chalcocopyrite-pyrite mineralization in quartz schist-hosted ore; (E) and (F) pyrite replaced by molybdenite in monzogranite porphyry-hosted ore. Note: The red line represents the analysed spot for in-situ S isotope; blue line represents in-situ Pb isotope analytical spot.

weak quartz-sericite-chlorite zone. The Larong W-Mo mineralization can be divided into three paragenetic stages: Stage I is the main W-mineralization stage, the main mineral assemblages are quartz, alkaline feldspar, scheelite and muscovite (sericite). Stage II (quartz-sulfide stage) is dominated by molybdenite, pyrite and chalcocopyrite, which have close relationships with silicidation, sericitization or muscovitization. This stage can be further subdivided into quartz + molybdenite + pyrite + chalcocopyrite + scheelite stage (Stage II-1), quartz + molybdenite + pyrite stage (Stage II-2) and pyrite + molybdenite stage (Stage II-3). The paragenetic Stage III (quartz vein stage) is dominated by the quartz veins, with no or little pyrite, and this stage is closely related to chloritization and carbonatization.

3 Analytical results

3.1 Molybdenite Re-Os ages

The concentrations of ^{187}Re and ^{187}Os of the molybdenite samples from the Larong deposit range from 33.33 to 54.14 ppb to 51.03 to 82.64 ppm, respectively. Six samples yielded restricted model ages of 91.5 to 92.3 Ma with a weighted mean age of 91.8 ± 0.5 Ma (Fig. 4B), which is consistent with the isochron age of 90.6 ± 2.1 Ma (Fig. 4A).

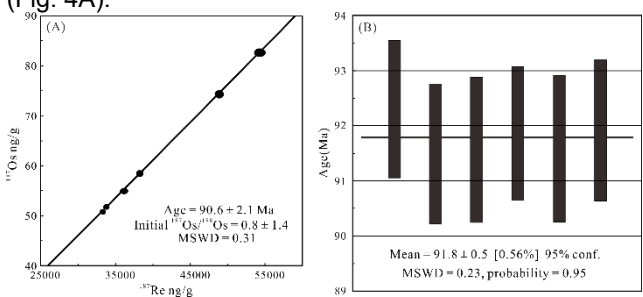


Figure 4. Molybdenite Re-Os isochron age (A) and weighted mean age (B) of the Larong deposit.

3.2 LA-ICP-MS trace element compositions

Upper crust-normalized trace element variation of sulfides are shown in Fig. 5.

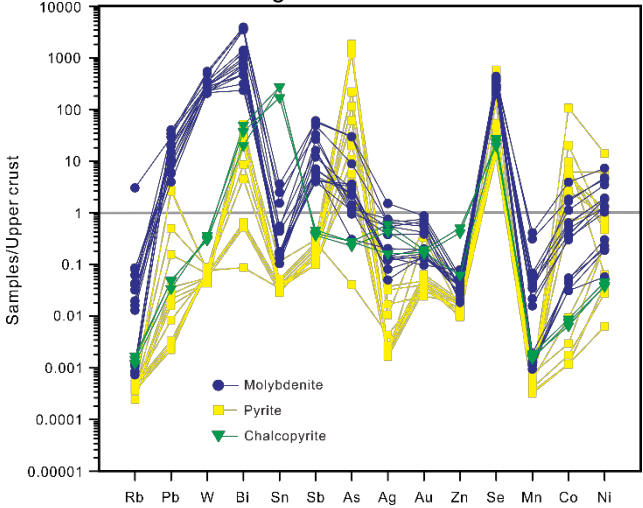


Figure 5. Upper crust-normalized trace element variation diagram of sulfides. Upper crust value is from Gao et al. 1998.

Pyrite in the Larong deposit is characterized by enrichment of As, Se, Co and Bi; Molybdenite is extremely rich in Pb, W, Bi, Sb, Se and Re; Chalcopyrite is characterized by enrichment in Se, Sn and Bi.

3.3 In-situ sulfur isotopic compositions

Except for individual grains of pyrite with higher values, the majority of $\delta^{34}\text{S}_{\text{VCDT}}$ values of sulfides are concentrated in the range of 0.25-2.68‰ and different sulfides are in the order: molybdenite (1.74-2.68‰, average 2.21‰) > pyrite (0.25-2.63‰, average 1.62‰) > chalcopyrite (0.46‰), indicating that sulfur isotopic fractionation had reached a balance between various sulfides and H_2S in hydrothermal ore-forming solution of the Larong deposit. Among them, $\delta^{34}\text{S}_{\text{VCDT}}$ values of the Stage II-1 pyrite are concentrated between 0.25‰ and 0.47‰, which are consistent with that of chalcopyrite (0.46‰); The Stage II-2 pyrite has $\delta^{34}\text{S}_{\text{VCDT}}$ values ranging from 0.72‰ to 2.5‰, which are basically consistent with those of molybdenum (1.74‰-2.68‰); The Stage II-3 pyrite has a wide range of $\delta^{34}\text{S}_{\text{VCDT}}$ values of 4.52‰-6.37‰.

3.4 In-situ lead isotopic compositions

All molybdenite samples have similar Pb isotopic compositions (Fig. 7) with $^{208}\text{Pb}/^{204}\text{Pb}$, $^{207}\text{Pb}/^{204}\text{Pb}$ and $^{206}\text{Pb}/^{204}\text{Pb}$ values of 39.356-39.908, 15.747-15.928 and 18.843-20.120, respectively. And they all have high μ , ω and Th/U values of 9.66-10.01, 35.26-40.90 and 3.47-3.97, respectively.

4 Discussion and conclusions

4.1 Timing the Larong W-Mo deposit

The Re-Os isochron age of 90.6 ± 2.1 Ma (Fig. 4A) is consistent with the weighted average age of 91.8 ± 0.5 Ma (Fig. 4B), indicating that the Larong W-Mo deposit was formed in the Late Cretaceous. This age is close to the K-Ar age of 99.16 Ma from the Saibeinong Sn deposit (Shentu and Wang 1991), suggesting that there exist a Late Cretaceous W-Sn-Mo metallogenic event in the LZMB.

4.2 Sources of ore-forming materials

The Larong deposit is free of sulphate minerals, and mainly composed of molybdenum, pyrite and chalcopyrite, indicating a relatively low oxygen fugacity, then the $\delta^{34}\text{S}$ values of the sulfides are roughly equivalent to the total $\delta^{34}\text{S}$ values of the hydrothermal fluid (Ohmoto 1972). The $\delta^{34}\text{S}_{\text{VCDT}}$ values of sulfides in the Larong deposit range from 0.25‰ to 6.37‰, with a mean of 2.15‰. Unlike sedimentary rocks, which usually have a negative or wide range of $\delta^{34}\text{S}_{\text{VCDT}}$ values, the $\delta^{34}\text{S}_{\text{VCDT}}$ values of sulfides in the Larong deposit are relatively concentrated, and slightly above the range of the mantle sulfur (0 ± 2 ‰), indicating a predominant magmatic sulfur origin. From Stage II-1, Stage II-2 to Stage II-3, the

average $\delta^{34}\text{S}$ values of pyrite change from +0.33‰, to 1.88‰ and to 5.34‰ (Fig. 6). It is possible that the increasing trend of $\delta^{34}\text{S}$ values may reflect the gradually decreasing of oxygen fugacity and temperature during the ore-forming process (Herlec. 2010).

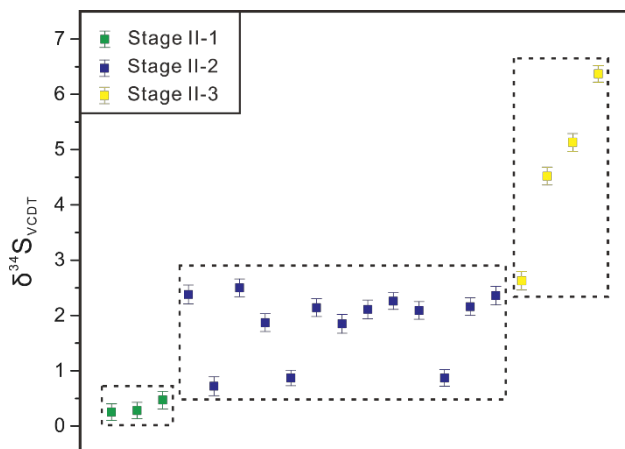


Figure 6. The $\delta^{34}\text{S}_{\text{VCDT}}$ values of pyrite from the Larong deposit.

The μ values of molybdenite in the Larong deposit are relatively concentrated (9.66-10.01), higher than the average value of upper crust (9.58), indicating a predominant upper crustal lead source. This argument is also supported by the fact that almost all molybdenite samples plot in the fields of the upper crust in the $^{207}\text{Pb}/^{204}\text{Pb}$ - $^{206}\text{Pb}/^{204}\text{Pb}$ diagram (Fig. 7A) and the $\Delta\beta$ - $\Delta\gamma$ lead parameters diagram (Fig. 7B). The ω values of molybdenite are between 35.26 and 40.90, and the great majority of them are higher than the average value of the upper crust (36.84). The Th/U ratios of molybdenite vary from 3.47 to 3.97, between the average values of the mantle (3.45) and the upper crust (3.88), and are closed to the upper crustal reservoir, indicating that the lead of the Larong deposit was mainly derived from the upper crust.

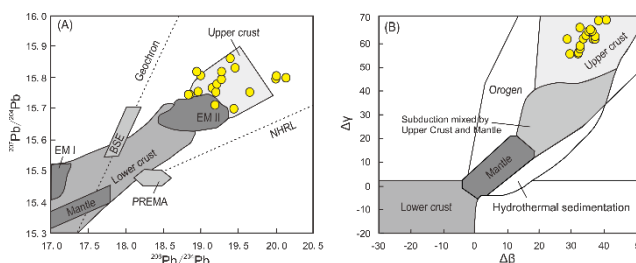


Figure 7. Diagram of lead isotope of metal sulfides from the typical deposits in the Bangonghu-Nuijiang belt. (A) $^{207}\text{Pb}/^{204}\text{Pb}$ versus $^{206}\text{Pb}/^{204}\text{Pb}$ plot (Zartman and Doe et al. 1981; Zindle and Hart 1986; Miller et al. 1999); (B) $\Delta\beta$ versus $\Delta\gamma$ plot (Zhu et al. 1998).

The Re-Os isotopic system can provide not only precise constraints on the age of metallic ore deposits, but also a highly sensitive monitor of the possible metal sources. The contents of Re decrease in molybdenite from several hundred ppm in the mantle source, to tens of ppm in the crust-mantle mixed source, and to several ppm in the crustal source (Mao et al. 1999). The Re contents of molybdenite from the Larong deposit range from 20.84 to 46.69 ppm, indicating a predominant crustal

source.

The Ni contents of pyrite can also provide important information for the sources of ore-forming materials. For example, the Ni contents in the mantle rocks can be up to 2200 ± 500 ppm (Palme and O'Neill 2003), therefore, if Ni in pyrite is derived from basic-ultrabasic rocks, then the Ni contents should be relatively high. In contrast, Ni in pyrite derived from felsic rocks such as highly differentiated granite usually has very low contents. In this study, the contents of Ni in most pyrites are less than the average value of continental crust (59 ppm; Rudnick and Gao 2003), indicating that the ore-forming materials were mainly derived from the continental crust.

4.3 Implications for ore-forming process

The Re-Os weighted average age (91.8 Ma) from the Larong deposit is consistent with the zircon U-Pb age (93.9 Ma) of the monzogranite porphyry, and high-temperature alteration and disseminated mineralization are well developed in the monzogranite porphyry. Hence, we propose that the Larong W-Mo deposit is genetically related to the monzogranite porphyry and the ore-forming processes are as below.

During the Later Cretaceous, fault-controlled emplacement of magma generated the Larong monzogranite porphyry, and it continued to cool and crystallize to form the W- and Mo-rich fluid.

2) In the ascending process, the fluid filtered through and reacted with the cooling porphyry rocks, causing K-silicate alterations. Then the alteration of plagioclase into K-feldspar released abundant Ca^{2+} , which combined with HWO_4^- or WO_4^{2-} to form scheelite during Stage I. However, the Stage I fluid was relatively high-temperature, oxidizing and poor in S^{2-} , thus unfavorable for sulfide deposition (Yang et al. 2012).

3) As the water-rock reaction continued, the fluid became more acidic, reducing, lower-temperature and rich in S^{2-} . This change facilitated the deposition of sulfides such as molybdenite, together with quartz, forming the Stage II quartz-molybdenite stockworks. Meanwhile, plagioclase was altered to sericite or muscovite and released abundant Ca^{2+} , then combined with remaining HWO_4^- or WO_4^{2-} to form a small quantity of scheelite.

4) Finally, after precipitation of scheelite and molybdenite, a small amount of pyrite was formed in the later stage (Stage III).

Acknowledgements

This research was supported by the Commonwealth Project from Yunnan Science and Technology Award-Outstanding Contribution Award (2017001), China Geological Survey (DD20179604 and DD20160016) and the International Megascience Research Program of Chengdu Center of China Geological Survey. We are grateful to Dr. Kaiyun Chen and Dr. Zhian Bao from the Continental Dynamics Laboratory of Northwest University for their help on in-situ sulfur and lead isotope analysis and Zhihui Dai from the Institute of Geochemistry,

Chinese Academy of Sciences for her assistance on the LA-ICP-MS trace element analysis of sulfides. We also appreciate the kind help of Wanhua Cheng from the Chengdu Center of China Geological Survey for his immense help on sample preparation.

References

- Gao S, Luo TC, Zhang BR, Zhang HF, Han YW, Zhao ZD, Hu YK (1998) Chemical composition of the continental crust as revealed by studies in East China. *Geochimica et Cosmochimica Acta* 62:1959–1975
- Herlec U, Spangenberg JE, Lavrič JV (2010) Sulfur isotope variations from orebody to hand-specimen scale at the Mežica lead–zinc deposit, Slovenia: a predominantly biogenic pattern. *Mineral Deposita* 45:531–547
- Mao JW, Zhang ZC, Zhang ZH, Du AD (1999) Re–Os isotopic dating of molybdenites in the Xiaoliugou W (Mo) deposit in the northern Qilian mountains and its geological significance. *Geochimica Et Cosmochimica Acta* 63:1815–1818
- Metcalfe I (2013) Gondwana dispersion and Asian accretion: Tectonic and palaeogeographic evolution of eastern Tethys. *Journal of Asian Earth Sciences* 66:1–33
- Miller CH, Schuster R, Klötzli U, Frank W, Purtscheller F (1999) Post-collisional potassic and ultrapotassic magmatism in SW Tibet: geochemical and Sr–Nd–Pb–O isotopic constraints for mantle source characteristics and petrogenesis. *Journal of Petrology* 40:1399–1424
- Ohmoto, H (1972) Systematics of sulfur and carbon isotopes in hydrothermal ore deposits. *Economic Geology* 67:551–578
- Palme H, O'Neill HSC (2007) Cosmochemical estimates of mantle composition *Treatise on Geochemistry*:1–38
- Rudnick R, Gao S (2003) Composition of the continental crust. *Treatise on geochemistry* 3:659
- Shentu B, Wang Z (1991) The characteristics and origin type of the Leiwuqi Saibeinong tin deposit, eastern. *Xizang Mineralogy and petrology* 11:74–82 (in Chinese with English abstract)
- Yang YF, Li N, Chen YJ (2012) Fluid inclusion study of the Nannihu giant porphyry Mo–W deposit, Henan Province, China: implications for the nature of porphyry ore- fluid systems formed in a continental collision setting. *Ore Geology Reviews* 46:83–94
- Zartman RE, Doe BR (1981) Plumbotectonics—the model. *Tectonophysics* 75:135–162
- Zhu BQ (1998) Theories and application of isotopic system in geoscience: crustal and mantle evolution in China continent. Beijing: Science Press:1–330 (in Chinese)
- Zindler A, Hart S (1986) Chemical geodynamics. *Annual Review of Earth and Planetary Sciences* 14:493–571

Geology and exploration of the Sinongduo Ag polymetallic low-sulfidation epithermal deposit in Tibet, China

Juxing Tang

MNR Key Laboratory of Metallogeny and Mineral Assessment, Institute of Mineral Resources, CAGS, Beijing, China

Zongyao Yang

Faculty of Geosciences and Environmental Engineering, Southwest Jiaotong University, Chengdu, China

Xinghai Lang, Chonghai Zhang

College of Earth Science, Chengdu University of Technology, Chengdu, China

Guyue Hu, Zhuang Li

MNR Key Laboratory of Metallogeny and Mineral Assessment, Institute of Mineral Resources, CAGS, Beijing, China

Abstract. Sinongduo Ag polymetallic deposit explored in recent years is considered to be the first discovery of the low sulfidation epithermal deposit type in the Linzizong Group volcanic rocks. It contains >0.5 Mt of Pb+Zn grading at about 8% and 500 tons of Ag grading at about 80 g/t. We take the Sinongduo as a type example to study the mineralization in the Linzizong Group volcanic rocks and based on the geological study of Sinongduo, we find another gold prospect area in Woruo, which is about 2 km to the north of Sinongduo. 6 orebodies were found on the surface of Woruo and the grades of Au and Ag are approximately 0.9 g/t and 90g/t respectively. Despite of the low grade of Au, we still believe there are potentially other high grade orebodies beneath the lithocap of Woruo.

1 Introduction

Tibet Plateau, is a result of the India–Eurasia collision, and is the Earth's largest ongoing orogen. There are two important metallogenic belts named Gangdese Metallogenic Belt and the newly delimited Bangong–Nujiang Metallogenic Belt, which are prospective. Benefit from the abundant resource exploration projects and basic geological surveys supported by the Chinese government and mining companies recently years, so many large or giant deposits have been found such as the Duolong (Lin et al. 2019), Jiama (Zheng et al. 2016) and Xiongcu (Lang et al. 2014; Tang et al. 2015; Yang et al. 2017). Although the amount of copper resources controlled at present is more than 60 Mt and the associated gold is more than 10 Mt, the prospective resources of copper is still more than 15 Mt (Tang et al. 2017).

The Linzizong volcanic rocks, which are widely distributed in the southern margin of Gangdese Metallogenic Belt in central Tibet, are the geological records of the India–Eurasia collision (Mo et al., 2008). It is mainly composed of a series of calc-alkaline subaerial volcanic rocks erupted from about 69 Ma to 40 Ma which are the main host rocks of the epithermal deposit around the world. Compared to the large number of epithermal

deposits found in the subaerial volcanic rocks of the Andean metallogenic belt in South America, however, there is rare report of epithermal deposits in the Tethyan metallogenic belt. We can't help asking that are these deposits denudated or even not exist? The answer is absolutely not, but those deposits just not have been found yet. Previous point is that the subaerial volcanic rocks of the Linzizong Group are with poor potential for prospect. However, the discoveries of the Sinongduo, Narusongduo, Luobuzhen, Lazong and Chagelei recently years which are related to the Linzizong volcanic rocks prove that it's controversial for prospecting. On the contrary, the erosion of the Linzizong volcanic rocks is slightly, and that means the preservation of the deposit is in good condition.

2 Geology

The research area is the central part of the south Gangdese Metallogenic Belt (Fig 1). There are many Pb–Zn deposits in this area, which include Sinongduo, S-Sinongduo (>0.6 Mt of Pb and Zn grading at 12%), Narusongduo (>1 Mt at 10% Pb and Zn), Woruo (potential of more than 30 t Au, 1000 t Ag and 1 Mt Pb and Zn), Lazong, Zhazhalong, Chagelei, Xuebie, Luobuzhen and Chazi. The controlled Pb and Zn metal resources are more than 3 Mt as so far and it has been predicted that there are still a large amount of deposits remain to be discovered.

The host rocks of Sinongduo Ag polymetallic deposit are volcanic breccia and crystal tuff. Vein and hydrothermal brecciated ore column are the main type orebodies. Particularly, there are independent Ag vein orebodies (grading from about 50 g/t to 6000 g/t) over the Ag–Pb–Zn orebodies different from other Pb–Zn deposits nearby. The main structures include veined structure, brecciated (Fig 2e), mesh-veined, banded and laminated, crustified, massive and disseminated structures, which show an open space environment. The ore textures of this deposit are developed on the basis of crystallization, metasomatism and exsolution.

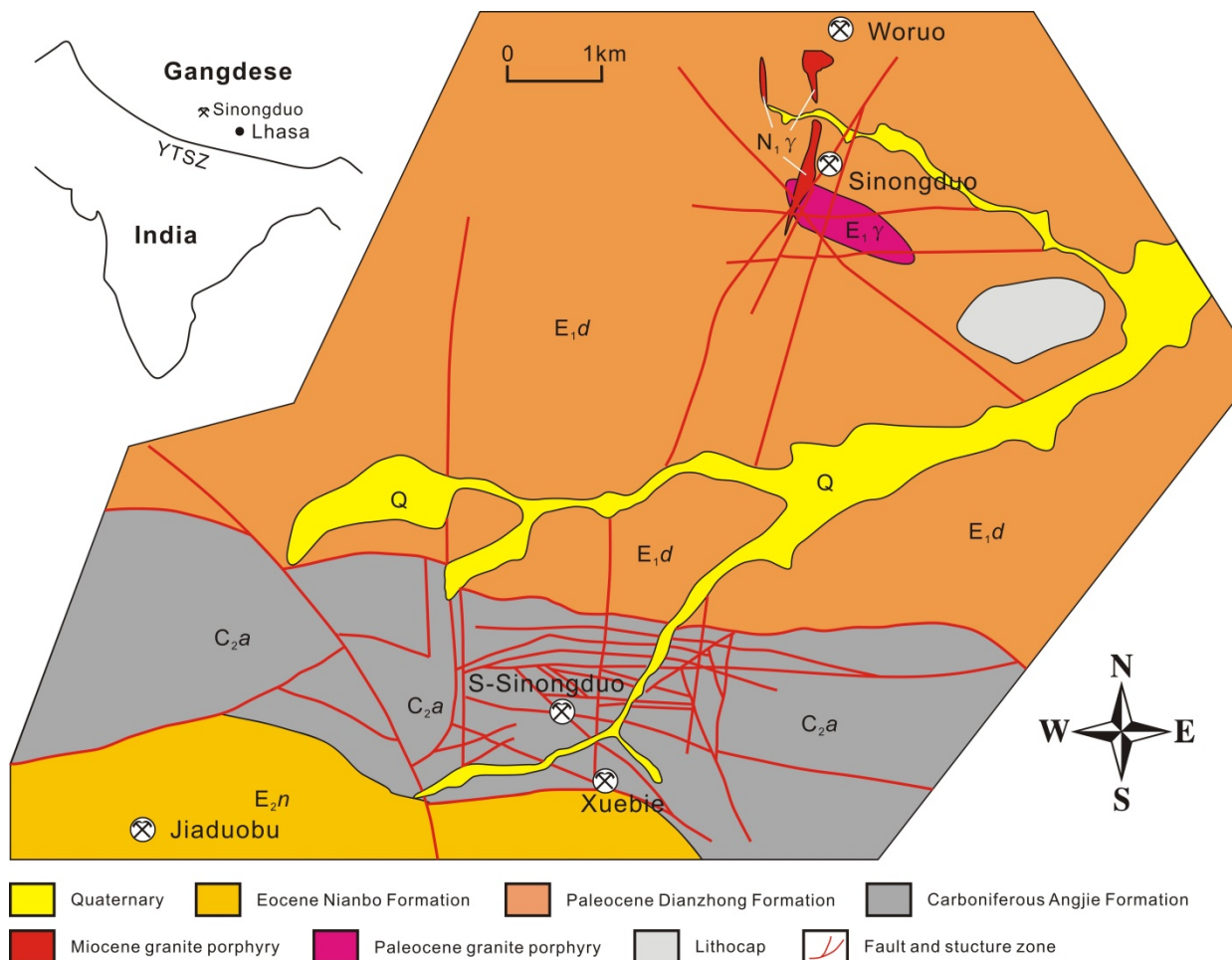


Figure 1. Geological map of the Sinongduo area showing the position of deposit.

The volcanic-intrusive rocks in Sinongduo area were formed in Paleocene 65-62 Ma (Ding et al 2017). The volcanic rocks belong to the high potassium peraluminous rocks and have the arc volcanoes geochemical characteristics. The ^{40}Ar - ^{39}Ar data of altered illite limited the deposit metallogenic age are about 62 Ma (unpublished yet), consistent with the eruption of volcanic rocks. The major metallic minerals are galena, sphalerite, and argentite, pearceite, and pyrite together with rare chalcopyrite. The silver minerals mainly include peacockite, argentite, pyrargyrite, akanthite and native silver, which occur in the fissures of the Fe-Mn carbonates, jasper and the early sulfides (Li et al 2017).

We first considered the Sinongduo Ag polymetallic as a low sulfidation epithermal deposit because of the typical alteration and its tectonic setting. The major altered minerals are illite (Fig 2c, 2d), chalcedony (Fig 2b), adularia (Fig 2a), sericite, fluorite and carbonates such as rhodochrosite, siderite and calcite (Fig 2c, 2f, 2g). After 4 years of exploration, we convince that it is the first discovery of low sulfidation epithermal deposit in Linzizong Group volcanic rocks according to the fluid inclusion (Li et al 2017), alteration, textures and ore mineralogy.



Figure 2. a. Adularia and carbonates vein. b. Chalcedony stockwork. c. Siderite in illite. d. Illite in volcanic breccia. e. Sulfides cemented breccia. f. Rhodochrosite cemented breccia. g. Quartz after bladed calcite in ore.

3 Exploration in Linzizong Group

In order to give some exploration advices for Zhongrui Mining, we chose rock and soil geochemical survey to study the metallogenic elements anomaly. A total of about 20 thousand samples (9235 samples are collected by our group members) were taken from the surface in Sinongduo area for prospecting. Based on the rock survey in Sinongduo area, we found that there are strong anomalies of Au, Ag, As, Sb, Pb, Zn and Mo. The strongest anomalous area is about 1 km² and 2 km to the north of Sinongduo Ag polymetallic low sulfidation epithermal deposit named Woruo (Fig 1). The level of Au range from 20×10⁻⁹ to 130×10⁻⁹, and Ag is 30×10⁻⁶ to 100×10⁻⁶. All these anomalous elements coordinate with each other completely in good zoning.



Figure 3. a. Vuggy quartz. b. Black sulfides-quartz cemented hydrothermal breccia. c. Hydrothermal breccia in drillhole WZK0001

In addition, geological survey helped us to circle out the rudiment of the gold orebodies. According to the geological survey, 5 main orebodies were found hosted in the tuff. The orebodies strike to the north and the dip is very high. Main orebodies are formed with echelon structure. The stockwork ore and vein ore are distributed on both sides of the 5 main ores. Black materials cement the tuff and chalcedony breccias forming the hydrothermal eruption breccia (Fig 3b, 3c). These kinds of black materials are composed of chalcedony, quartz, fine-grained pyrite and other sulfides, which is the cause of black based on the microscopic features. Furthermore, pyritohedron pyrite is always visible under the hand lens, which is considered to be the indicator of the ore-hunting

of gold. The crudely banded veins have many crystalized zonings which are black sulfides, quartz (chalcedony), fine-grained pyrite and quartz core from the external to the central. Siliceous veins, massive quartz and comb quartz are the most typical characteristics.

4 Discussion

The evolution of the Neo-Tethyan Ocean and the process of the India plate and Eurasia plate collision have been studied for decades. Although there are many patterns published, but the controversy still exist. Firstly, the ore-forming ages of Pb-Zn deposits in south Gangdese Metallogenic Belt are correspondence with the ages of Linzizong Group volcanic rocks (Wang et al. 2015). That could be an implication of the relationship between the Pb-Zn mineralization and Linzizong Group volcanic rocks, but not the Lhasa terrane basement. Secondly, the large amount of metal (more than 3 Mt Pb and Zn in our research area) also couldn't be remelted out from the Lhasa terrane basement. According to the possible tectonic setting during that time, our evidences (unpublished yet) tend to owe the metallogenic materials to the subduction of some micro-continents drift from India plate or even Gondwana, and continents subduction seems to be accepted by many researchers (Müller 2010; Capitanio et al. 2010; Ingalls et al. 2016).

In this case, the tectonic setting of Linzizong Group volcanic rocks needs to be discussed again. According to Mo et al. (2008), the Linzizong Group volcanic rocks represent a magmatic response to the India-Asia continental collision beginning at ~70-65 Ma, which means the south margin of Gangdese arc is a collisional background. However, we have evidences indicating that Dianzhong formation is subduction-related, and this let us have confidence in prospect especially of epithermal deposits in Linzizong Group volcanic rocks.

5 Exploration Implications

Geology and mineralization characteristics of the Woruo gold deposit indicate that it belongs to the epithermal deposit too. So far, studies about the genesis and geodynamic setting of this deposit have not been reported, and the exploration also at a primary level. Its powerful vein system indicates the stronger hydrothermal activity in depth. The exploration of Sinongduo and Woruo enable us to make conclusion that Linzizong Group volcanic rocks especially the Dianzhong formation show great potential for exploration of Au, Ag, Pb and Zn. We hope it can be a breakthrough of epithermal gold deposit prediction and exploration in Gangdese Metallogenic Belt.

Acknowledgements

This study was jointly supported by the National Key Research and Development Project of China (2018YFC0604101, 2018YFC0604105) and the National Science Foundation of China (No. 41772075).

References

- Capitanio FA, Morra G, Goes S, Weinberg RF, Moresi L (2010) India–Asia convergence driven by the subduction of the Greater Indian continent. *Nat Geosci* 3:136-139
- Ding S, Chen YC, Tang JX, Xie FW, Hu GY, Yang ZY, Shi S, Li YH, Yang HY (2017) Relationship between Linzizong volcanic rocks and mineralization: A case study of Sinongduo epithermal Ag-Pb-Zn deposit. *Miner Depos* 36(5): 1074-1092 (in Chinese with English abstract)
- Lang XH, Tang JX, Li ZJ, Huang Y, Ding F, Yang HH, Xie FW, Zhang L, Wang Q, Zhou Y (2014) U-Pb and Re-Os geochronological evidence for the Jurassic porphyry metallogenic event of the Xiongcu district in the Gangdese porphyry copper belt, southern Tibet, PRC. *J Asian Earth Sci* 79(2):608-622
- Li Z, Lang XH, Ding S, Li HF, Yang ZY, Shi S, Wang LQ, Li YH (2017) A study of the modes of occurrence of silver in the Sinongduo epithermal Ag-Pb-Zn deposit, Tibet. *Acta Geosci Sin* 38(5): 687-701 (in Chinese with English abstract)
- Lin B, Tang JX, Chen YC, Michael JB, Song Y, Yang HH, Wang Q, He W, Liu ZB (2019) Geology and geochronology of Naruo large porphyry-breccia Cu deposit in the Duolong district, Tibet. *Gondwana Res* 66:168-182
- Mo XX, Niu YL, Dong GC, Zhao ZD, Hou ZQ, Zhou S, Ke S (2008) Contribution of syncollisional felsic magmatism to continental crust growth: A case study of the Paleogene Linzizong volcanic succession in southern Tibet. *Chem Geol* 250(1–4): 49-67
- Müller RD (2010) Sinking continents. *Nat Geosci* 3:79-80
- Tang JX, Lang XH, Xie FW, Gao YM, Li ZJ, Huang Y, Ding F, Yang HH, Zhang L, Wang Q, Zhou Y (2015) Geological characteristics and genesis of the Jurassic No. 1 porphyry Cu-Au deposit in the Xiongcu district, Gangdese porphyry copper belt, Tibet. *Ore Geol Rev* 70(4):438-456
- Tang JX, Ding S, Meng Z, Hu GY, Gao YM, Xie FW, Li Z, Yuan M, Yang ZY, Chen GR, Li YH, Yang HY, Fu YG (2016) The first discovery of the low sulfidation epithermal deposit in Linzizong volcanics, Tibet: A case study of the Sinongduo Ag polymetallic deposit. *Acta Geosci Sin* 37(4):461-470 (in Chinese with English abstract)
- Tang JX, Wang Q, Yang HH, Gao X, Zhang ZB, Zou B (2017) Mineralization, exploration and resource potential of porphyry-skarn-epithermal copper polymetallic deposits in Tibet. *Acta Geosci Sin* 38(5):571-613 (in Chinese with English abstract)
- Wang LQ, Tang JX, Deng J, Kang HR, Lin X, Cheng WB, Li Z, Zhang Z (2015) The Longmala and Mengya'a skarn Pb–Zn deposits, Gangdese region, Tibet: evidence from U–Pb and Re–Os geochronology for formation during early India–Asia collision. *Int Geol Rev* 57(14):1825–1842
- Yang ZY, Lang XH, Tang JX, Zhang Z, Zhang JS, Gao YM, Huang Y, Xie FW, Fu YG, Wang Y (2017) Geochemical characteristics of the Jurassic sandstones in Xiongcu copper-gold deposit, Tibet: constraints on tectonic setting. *Acta Geol Sin* 91(9):1985-2003 (in Chinese with English abstract)
- Zheng WB, Tang JX, Zhong KH, Ying LJ, Leng QF, Ding S, Lin B (2016) Geology of the Jiama porphyry copper-polymetallic system, Lhasa region, China. *Ore Geol Rev* 74:151-169
- Ingalls M, Rowley DB, Currie B, Colman AS (2016) Large-scale subduction of continental crust implied by India–Asia mass-balance calculation. *Nat Geosci* 9: 848-853

Mineralogy and mineral chemistry of ore minerals in the Erdaohe skarn Pb-Zn-Ag deposit: implication for system evolution

Jun-Sheng Yang · Xin-Biao Lü

Geological Survey Institute, China University of Geosciences, China

Abstract. The Erdaohe Pb-Zn-Ag deposit is located in the central Great Xing'an Range, the eastern segment of the Central Asian Orogenic Belt. The Triassic monzodiorite is regarded the causative intrusion for the skarn formation and major mineralization in the deposit. The predominant calcic skarn and subordinate manganiferous skarn are developed and contain the majority of the ore body. Based on mineral composition and occurrence, five types of sphalerite and four types of galena are identified. Within the calcic skarn, sphalerite evolves from dark to red then yellow in color, combined with decrease of both Mn and Fe contents. Sphalerite in manganiferous skarn is characteristic of low molar Fe/Mn ratio (<10). Galena and associated exsolution proves a sequential consumption of Bi, Te, Ag and Sb in the system. Estimated fugacity of S_2 (g) and Te_2 (g) in the main sulfide stage went through an increase ahead of the later overall decrease.

1 Introduction

The Great Xing'an Range has witnessed amalgamations of micro-blocks (Erguna Block, Xing'an Block, Songliao – Xilinhot Block, etc.) and a prolonged magmatic activity throughout the Phanerozoic (Jahn et al. 2011; Li et al. 2013; Liu et al. 2017; Wu et al. 2011). This region is also famous for its immensity in metal resource and diversity in ore types (Ouyang et al. 2015; Wu et al. 2014). Somehow the central part of the Great Xing'an Range is sparse in deposits.

The Erdaohe Pb-Zn-Ag deposit is recently discovered, about 190 km southwest of Zhalantun. It contains more than 42 ore bodies and a reserve of 298,621 tons Pb, 1,175,518 tons Zn, 2,360 tons Ag and 1,226 tons Cu with average grades of 1.44% Pb, 5.56% Zn, 133.5 g/t Ag and 0.94% Cu, respectively. Due to its relatively short history, previous studies mainly aimed at its deposit geology and exploration (Wang et al. 2012; Cui et al. 2015). The present study is an attempt to clarify the evolution of related elements and some physical-chemical conditions, mainly based on its ore mineralogy.

2 Regional tectonics and deposit geology

The Great Xing'an Range lies in NE China, with the Siberia craton in the north and the North China craton in the south. The Xing'an Block is a NE-SW trending region bounded by the Xinlin-Xiguitu Suture and the Hegenshan-Heihe Suture. Through the Paleozoic to the

early Mesozoic, this region was controlled by the evolution of the Paleo-Asian Ocean, the evolution of the Mongol-Okhotsk Ocean since Mesozoic, and later the subduction of the western Pacific Ocean (Jahn et al. 2011; Li et al. 2013; Tang et al. 2016; Xu et al. 2013).

Exposed strata in the deposit are the Middle-Upper Permian Luohe Formation meta-siltstone, slate and carbonate rocks and the Middle Jurassic Tamulangou Formation to a lesser extent. A thrust fault strikes NE with a dip of 50° to 60°, controlling the distribution of strata and most intrusions. The monzodiorite is of the largest scale which intruded in Triassic. The other major intrusive rock is granite porphyry of Cretaceous age.

At present, mining as well as our study are merely carried out in the ore block I, which holds the majority of ore bodies, which are usually lenticular, banded or vein-like, along NE striking faults. Most ore bodies are hosted in skarn (Figure 1a and 1b), with a small proportion in the form of veins within distal strata. Both calcic skarn and manganiferous skarn developed. The massive calcic skarn displays well spatial relationship with the monzodiorite in a sequence of altered monzodiorite-garnet dominated skarn-pyroxene dominated skarn-altered marble. The manganiferous skarn always displays as rhodonite dominant veins cutting calcic skarn or carbonate strata, somehow limited at the northern verge of the contact.

Andradite-grossular garnet, pyroxene, apatite, local wollastonite and minor titanite are representative of prograde skarn. Retrograde skarn is dominated by an assemblage of epidote, amphibole, chlorite and minor quartz, hematite and magnetite. The relatively isolated manganiferous skarn minerals are considered posterior to retrograde stage due to lower temperature (unpublished data of fluid inclusion homogenization temperature from rhodonite). The following sulfide stage can be further divided into three stages. During the sulfide stage, mineral assemblage is complicated in form of different types of major sulfides, such as sphalerite and galena.

3 Mineralogy and mineral chemistry

3.1 Sphalerite

Sphalerite is a major ore mineral widely formed in the whole sulfide stage. In early sulfide stage, sphalerite is dark to almost opaque in association with pyrrhotite and chalcopyrite (Figure 1c). Red sphalerite starts to emerge in abundance later in sulfide stage, frequently accompanied by galena and pyrite (Figure 1d and 1e).

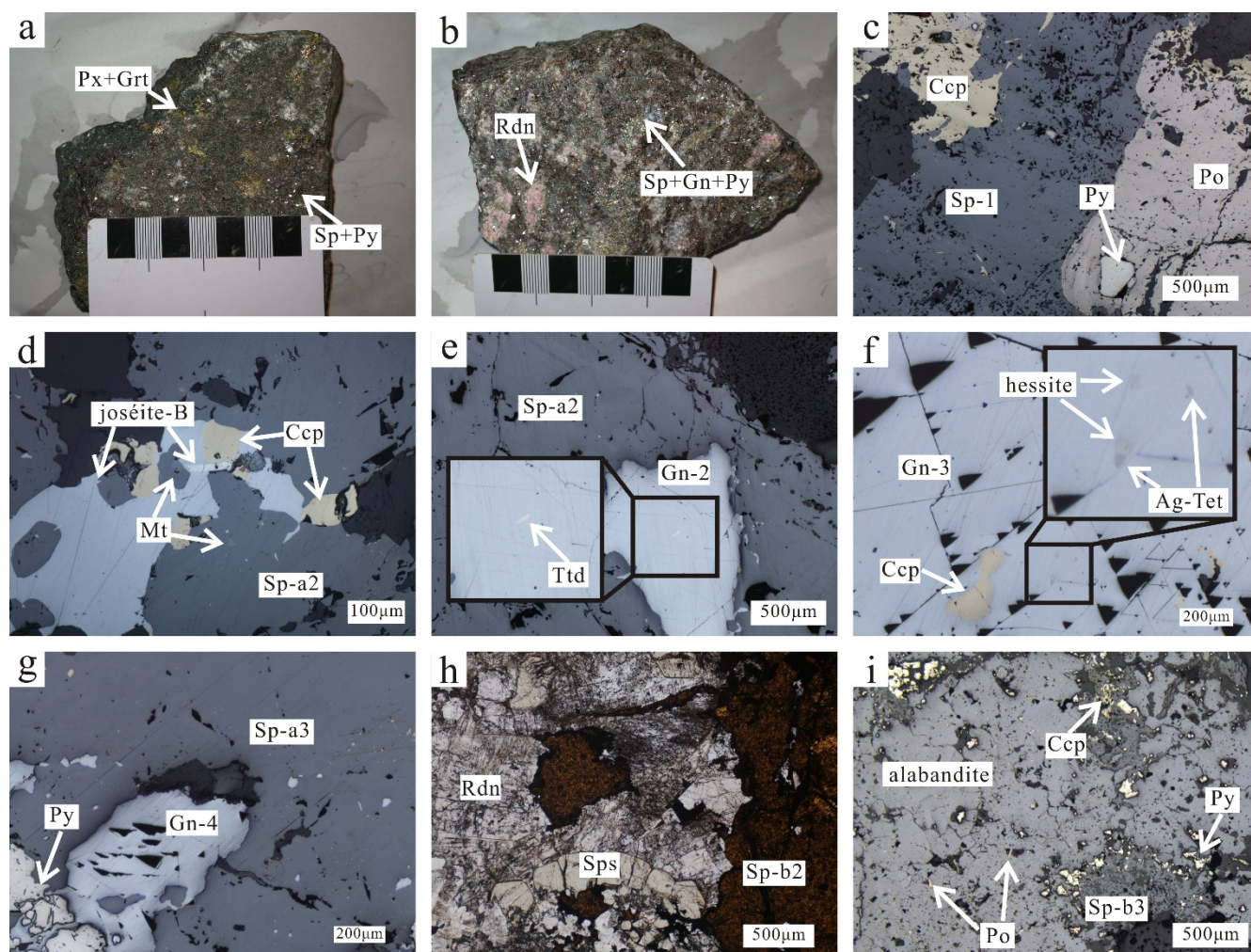


Figure 1. Representative photographs of skarn ores (a, b) and photomicrographs showing mineral relationships in the Erdaohe deposit. Detailed description (see text) is omitted here. *Px* pyroxene, *Grt* garnet, *Sp* sphalerite, *Py* pyrite, *Rdn* rhodonite, *Gn* galena, *Ccp* chalcopyrite, *Po* pyrrothite, *Mt* magnetite, *Ttd* tetradymite, *Ag-Tet* Ag-bearing tetrahedrite, *Sps* spessartine.

Sphalerite in the late stage is yellow, also coexisting with pyrite and galena (Figure 1g). Chalcopyrite is not always emulsion in sphalerite, instead, sometimes replacing sphalerite along grain boundary or cleavages as crystal growth or simply in an uneven pattern. Apart from the earliest opaque sphalerite, transparency of the mineral is mostly controlled by density of chalcopyrite.

Major composition variations in sphalerite are Fe and Mn contents (Figure 2). Earliest opaque sphalerite (Sp-1) is only observed in calcic skarn and contains significant amount of Fe (average 11.93 wt. %) and moderate amount of Mn (average 1.32 wt. %). Fe and Mn contents in sphalerite in later stages are influenced by different occurrence. Within calcic skarn, red sphalerite (Sp-2a) carries moderate Fe content (average 6.29 wt. %) and low Mn content (average 0.20 wt. %). In manganoan skarn, red sphalerite (Sp-2b, Figure 1h) is mainly seen replacing rhodonite or as interstitial mineral, which is the lowest in Fe content (average 1.05 wt. %) but relatively high in Mn content (average 3.42 wt. %). Yellow sphalerite (Sp-3a, Figure 1i) occurs in veins cutting carbonate strata, with the lowest Mn content (average 0.17 wt. %) and low Fe content (average 3.95 wt. %).

Another type of yellow sphalerite (Sp-3b), which occurs with alabandite in manganoan skarn, exhibit the highest Mn content (average 4.05 wt. %) with low Fe content (average 1.87 wt. %). A faint correlation between color and cadmium content may exist: yellow sphalerite contains higher Cd content compared to red and opaque variants (average 0.46 over 0.37 wt. %). The Fe/Mn molar ratio works well in recognizing sphalerite from different occurrence. Earliest sphalerite yield moderate Fe/Mn ratio of around 10. Later sphalerite has Fe/Mn molar ratios significantly deviate from 10 (Figure 2b).

3.2 Galena and associated exsolution

Galena is the most important mineral accommodating silver in the deposit, commonly found later in sulfide stage. Optically, no difference is observed in galena variants. Mineral assemblage and exsolution texture are considered to identify different types. Earliest galena (Gn-1, Figure 1d) occurs with Sp-B1 in proximal calcic skarn, replacing or enclosing magnetite. Anisotropic acicular minerals (joséite-B) are observed exclusively in galena, therefore considered as a result of exsolution.

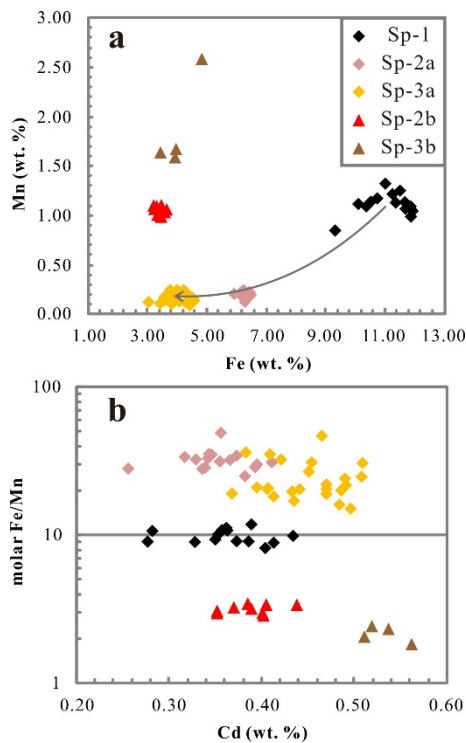


Figure 2. **a** Mn versus Fe concentration of sphalerite in the Erdaohe deposit. The grey curve suggests a gradual decrease trend for sphalerite in calcic skarn. **b** Fe/Mn molar ratio versus Cd concentration of sphalerite in the Erdaohe deposit.

The second type (Gn-2, Figure 1e) also has analogous exsolution mineral (tetradymite), but collected further away from the proximal skarn with no magnetite observed. At the manganoan skarn-marble contact zone, the third type (Gn-3, Figure 1f) is observed with tiny gray (hessite) and pale yellow (silver-bearing tetrahedrite) exsolution minerals. The last type (Gn-4, Figure 1g) is associated with yellow sphalerite (Sp-3a) with no exsolution at all. Major compositional variations are observed in Bi, Ag, Cd, Te and Sb contents (Figure 3).

Gn-2 contains the highest Ag (average 1.49 wt. %) and Bi (average 3.71 wt. %) contents among all types. Gn-1 has comparable Bi (average 2.96 wt. %) but slightly lower Ag (average 1.12 wt. %) contents with Gn-3. Gn-4 displays the lowest Bi (average 0.13 wt. %) contents with nearly no Ag concentration. Calculated molar percentage of Bi forms a distinct linear correlation with the one of Ag. Cd content in galena varies little. Only late type (Gn-4) carries slightly more Cd (Figure 3c). Sb concentration in galena is similar to Cd, yet lower overall concentration and more obvious trend (Figure 3d). Early tetradymite group minerals in galena carry little Ag (no more than 0.2 wt. %) but more Sb (average 0.2 wt. %) than their host. Their highly variable Pb contents are likely resulted from sub-micrometric galena inclusions instead of some Pb-rich variants (see dashed trends in figure 4). Ag-bearing tetrahedrite in Gn-3 contains average 18.47 wt. % Ag and only average 0.76 wt. % As, with average Ag/(Ag+Cu) molar ratio of 0.31 and Sb/(Sb+As) molar ratio of 0.96.

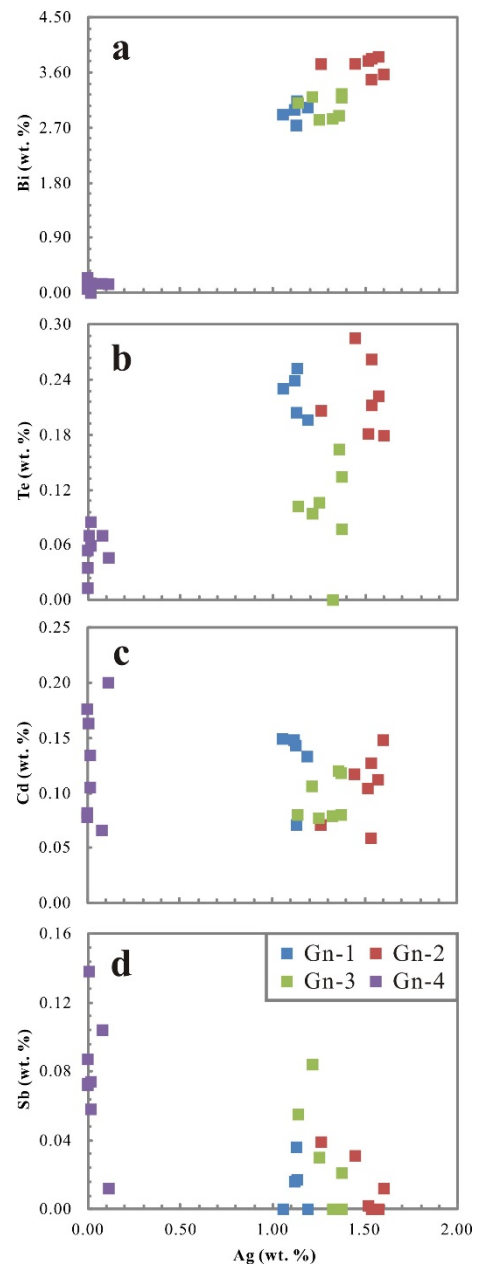


Figure 3. Bi, Te, Cd and Sb versus Ag concentration of galena.

4 Implication for system evolution

For Sp-1, Sp-2a and Sp-3a, decrease of both Mn and Fe concentration seems concordant with those in the hydrothermal system. Somehow, exceptionally high Mn concentrations of sphalerite in manganoan skarn display a reversed trend. As early Mn-rich minerals of rhodonite crystallize, accumulation of Mn in the hydrothermal is unlikely to be achieved. One possible explanation is that sphalerite obtains high Mn concentration via replacing Mn-rich minerals as rhodonite and alabandite.

Exsolution of joséite-B and tetradymite in early galena are indicative of the enrichment of Bi and Te. The Bi: Te (+S) ratio decrease from 1.27 (average of joséite-B, >1) to 0.64 (average of tetradymite, <1). According to the empirical redox indicator raised by Ciobanu et al. (2010),

the environment changes from a relatively reduced one to a relatively oxidized one, in accordance with the disappearance of magnetite inclusion in later galena. Compositional changes of galena and associated mineral assemblages indicate a sequential consumption of Bi-Te-Ag-Sb in the system.

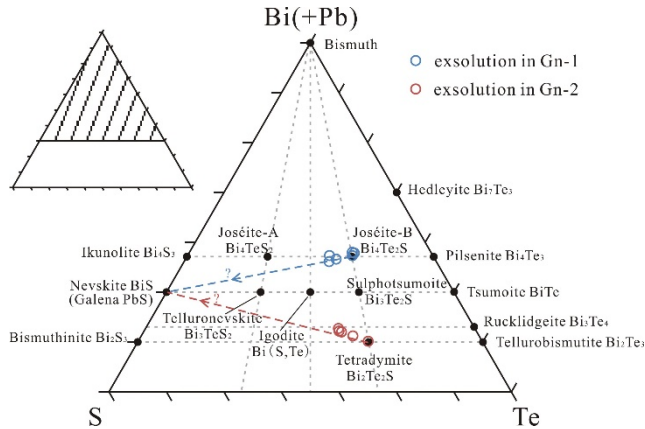


Figure 4. Schematic diagram comparing actual compositions to the ideal compositions of minerals in the system Bi (+Pb)-Te-S (modified after Cook et al. (2007)). Note the dashed lines indicative of possible mix of sub-micrometric galena inclusion.

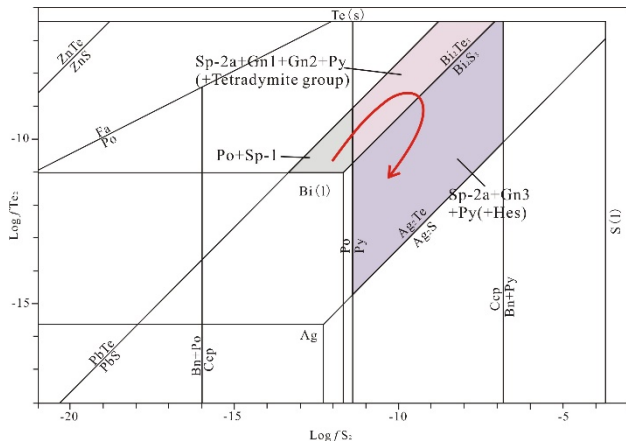


Figure 5. $\text{Log}f\text{Te}_2(\text{g})-\text{log}f\text{S}_2(\text{g})$ diagram showing relative stability of tellurides and sulfides at 300°C(modified after Afifi et al. (1988)). The shaded areas represents the estimated fugacity ranges of $\text{Te}_2(\text{g})$ and $\text{S}_2(\text{g})$ for different mineral assemblages in the deposit. *Fa* fayalite, *Po* pyrrhotite, *Sp* sphalerite, *Gn* galena, *Py* pyrite, *Ccp* chalcocopyrite, *Bn* bornite.

Temperature of the sulfide stage is constrained to 270~310°C by homogenization temperature of fluid inclusion of quartz, calcite and white fluorite (unpublished data). Combining with major ore mineral assemblages, a $\text{log}f\text{Te}_2(\text{g})-\text{log}f\text{S}_2(\text{g})$ diagram is presented (Figure 5). The inferred trend suggest a fugacity increase of both sulfur and tellurium due to early precipitation of silicate and oxide over sulfide, then followed by gradual fugacity decrease of both attributed to crystallization of both sulfide and Te-bearing minerals.

Acknowledgements

This contribution is financially supported by the Inner Mongolia Autonomous Region Geological Prospecting Fund Management Center (Grand NO. NMKD2014-23). We appreciated Tongliao Xinyuan Mining Co., Ltd. and Meijun Yang for assistance in the field work and electron microprobe analyses, respectively.

References

- Afifi AM, Kelly WC, Essene EJ (1988) Phase relations among tellurides, sulfides, and oxides: I. Thermochemical data and calculated equilibria. *Economic Geology* 83:377-394.
- Ciobanu CL, Birch WD, Cook NJ, Pring A, Grundler PV (2010) Petrogenetic significance of Au-Bi-Te-S associations: The example of Maldon, Central Victorian gold province, Australia. *Lithos* 116:1-17. doi: 10.1016/j.lithos.2009.12.004.
- Cook NJ, Ciobanu CL, Wagner T, Stanley CJ (2007) Minerals of the system Bi-Te-Se-S related to the tetradymite archetype: review of classification and compositional variation. *The Canadian Mineralogist* 45:665-708. doi: 10.2113/gscanmin.45.4.665.
- Cui X-W, Jiang S-H, Li H-B, Chang Y-H (2015) Integrated prospecting model of Erdaohe silver-lead-zinc deposit in the Zhilantun area, Inner Mongolia. *Mineral Exploration* 6:667-678 (in Chinese with English abstract).
- Jahn BM, Wu F, Chen B (2011) Granitoids of the Central Asian Orogenic Belt and continental growth in the Phanerozoic. *Transactions of the Royal Society of Edinburgh: Earth Sciences* 91:181-193. doi: 10.1017/s0263593300007367.
- Li S, Wang T, Wilde SA, Tong Y (2013) Evolution, source and tectonic significance of Early Mesozoic granitoid magmatism in the Central Asian Orogenic Belt (central segment). *Earth-Science Reviews* 126:206-234. doi: 10.1016/j.earscirev.2013.06.001.
- Liu YJ, Li WM, Feng ZQ, Wen QB, Neubauer F, Liang CY (2017) A review of the Paleozoic tectonics in the eastern part of Central Asian Orogenic Belt. *Gondwana Research* 43:123-148. doi: 10.1016/j.gr.2016.03.013.
- Ouyang H, Mao J, Zhou Z, Su H (2015) Late Mesozoic metallogeny and intracontinental magmatism, southern Great Xing'an Range, northeastern China. *Gondwana Research* 27:1153-1172. doi: 10.1016/j.gr.2014.08.010.
- Tang J, Xu WL, Wang F, Zhao S, Wang W (2016) Early Mesozoic southward subduction history of the Mongol-Okhotsk oceanic plate: Evidence from geochronology and geochemistry of Early Mesozoic intrusive rocks in the Erguna Massif, NE China. *Gondwana Research* 31:218-240. doi: 10.1016/j.gr.2014.12.010.
- Wang Z, Niu Y, Yao D (2012) Discovery and significance of Ag-polymetallic deposit in Inner Mongolia Erdaohe. *Journal of Shandong University of Technology(Natural Science Edition)* 26:46-49 (in Chinese with English abstract). doi: 10.13367/j.cnki.sdgc.2012.01.003.
- Wu FY, Sun DY, Ge WC, Zhang YB, Grant ML, Wilde SA, Jahn B-M (2011) Geochronology of the Phanerozoic granitoids in northeastern China. *Journal of Asian Earth Sciences* 41:1-30. doi: 10.1016/j.jseaeas.2010.11.014.
- Wu G, Wang GR, Liu J, Zhou ZH, Li TG, Wu H (2014) Metallogenic series and ore-forming pedigree of main ore deposits in northern Great Xing'an Range. *Mineral Deposits* 33:1127-1150 (in Chinese with English abstract).
- Xu WL, Pei FP, Wang F, Meng E, Ji WQ, Yang DB, Wang W (2013) Spatial-temporal relationships of Mesozoic volcanic rocks in NE China: Constraints on tectonic overprinting and transformations between multiple tectonic regimes. *Journal of Asian Earth Sciences* 74:167-193. doi: 10.1016/j.jseaeas.2013.04.003.

Complicated copper sulfides of the Zijinshan high sulfidation epithermal Cu-Au deposit in Fujian, China

Mei Lu, Rong Ye*, Yongkang Wang
China University of Geosciences (Beijing)

Abstract. Zijinshan high sulfidation epithermal Cu-Au deposit has attracted a number of studies due to its complicated mineral compositions, especially copper sulfides. Among copper-sulfur system, digenite, djurnite, covellite, anilite and chalcocite have been observed at Zijinshan ore deposit. Relationship of blaubleibender covellite and other Cu-S sulfides is reported at this deposit for the first time. Blaubleibender covellite is exsolved from anilite, indicating they experience very low temperature. The Zijinshan ore forming system experienced at least three possible stages: pyrite + enargite, digenite + bornite + covellite, fine grained covellite + anilite + djurnite + blaubleibender covellite.
Key words: Zijinshan epithermal deposit; copper sulfide; blaubleibender covellite

1 Introduction

The Zijinshan Orefield was discovered in the late 1970s in southeastern Fujian Province, China, including the Zijinshan high-sulfidation epithermal Cu-Au deposit, the Yueyang low-sulfidation epithermal Ag-polymetallic deposit, the Luoboling and Jingmei porphyry Cu-Mo deposits, the Wuziqilong, Longjiangting, and Ermiaogou Cu deposits, and several prospects. According to Zhang 2013, the proven reserves in the Zijinshan Orefield were 399.82 t Au, 6339 t Ag, 4.14 Mt Cu, and 110,000 t Mo. There are various types of mineralization in the giant Zijinshan Orefield, making it worthy of detailed studies. Zijinshan world-class high sulfidation epithermal Cu-Au deposit has attracted a number of studies since it was recognized the first high sulfidation epithermal deposit in mainland China, as well as the hypothesis of close spatial and temporal association between high sulfidation Cu-Au deposit and Luoboling or deep potential porphyry copper mineralization (Huang et al. 2018; Li and Jiang 2017; So et al. 1998; Zhong et al. 2018).

2 Zijinshan Cu-Au deposit

Zijinshan Cu-Au deposit is located near the center of the Zijinshan Orefield, hosted by Middle-Late Jurassic middle-fine grained granite (169-150Ma, Xu et al.,2017), Early Cretaceous dacite-porphyrity, and cryptoexplosive breccia (Figure 1).

The gold veins were concealed in the upper silicification zones. The lower copper ore bodies were mainly in the alunite-quartz alteration zone in various morphology of vein, capsule, and lenticule. The copper ore bodies usually contained economic concentrations of Au and Ag. It has been proven to have Cu reserve of over

five million tons (an average copper grade of 0.36 %) and Au reserve of 300 tons. In the year of 2017, Zijinshan deposit produced 3.875t gold and 75,850 t copper (from Zijin Mining).

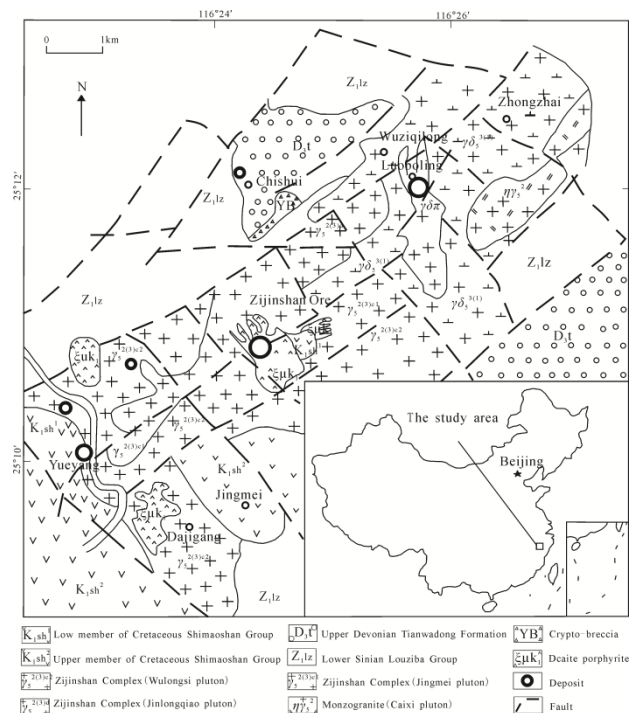


Figure 1. Generalized geology and deposits of the Zijinshan Orefield.

3 Mineral paragenesis

The uppermost deposit was oxidized intensely, and hematite was formed in this stage intergrown with the remaining quartz, containing the gold enrichment. Digenite is not commonly found as primary phase in ores (Vaughan and Craig 1997). However, the primary Cu-bearing minerals are digenite, covellite and bornite, making Zijinshan very special as a world-class high sulfidation epithermal Cu-Au deposit. Other Cu-bearing minerals have been identified, including pyrite, anilite, djurnite, enargite, chalcopyrite and some W or Sn bearing minerals (Liu 2015). The mineral assemblage of Zijinshan are indicative of an enrichment zone but massive and disseminated ores do not fit the nature of classic enrichment zone. With increasing depth, the main Cu-mineral assemblage varies from bornite-rich to digenite-rich to covellite-rich, representing higher sulfur and oxygen fugacity (Liu 2015).

Blaubleibender (a German word means blue remaining) covellite differs from normal covellite in their copper content and are easily distinguished optically because they keep blue in color of ordinary vibration in

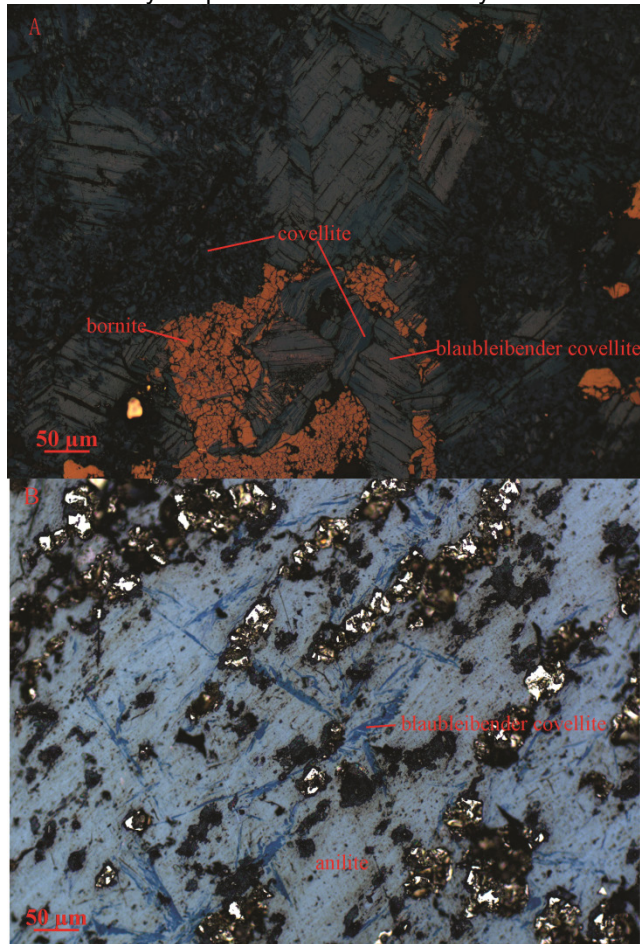


Figure 2. Copper sulfides at Zijinshan high sulfidation epithermal Cu-Au deposit. A. cracked bornite and striped covellite were surrounded by blaubleibender covellite and very fine covellite. B. blaubleibender covellite exsolution from anilite.

immersion oil. Natural blaubleibender covellite is usually intergrown with digenite, and their formation is due to low temperature oxidation of more copper rich phases (Putnis et al. 1977). Blaubleibender covellite are subdivided into yarrowite Cu_9S_8 (equal to $\text{Cu}_{1.125}\text{S}$) and spionkopite $\text{Cu}_{39}\text{S}_{28}$ (equal to $\text{Cu}_{1.4}\text{S}$). The formation of metastable phases such as blaubleibender covellites produced by the low-temperature replacement of other copper sulfides (Vaughan and Craig 1997). Paragenesis of Blaubleibender covellite and other copper sulfides is reported here in this ore deposit for the first time, indicating Zijinshan ore deposit experienced a very low temperature when forming primary sulfides.

4 Conclusion

At Zijinshan high sulfidation epithermal deposit, there are digenite, enargite, djurnite, covellite, anilite, bornite, pyrite, and blaubleibender covellite in ores. The Zijinshan ore forming system experienced at least three possible stages: pyrite + enargite, digenite + bornite + covellite,

fine grained covellite + anilite + djurleite + blaubleibender covellite. Complicated copper sulfides of this deposit are perhaps caused by the constant mixing of hydrothermal fluids and meteoric water.

Acknowledgements

Authors want to express their sincere appreciation for reviewers and the NSF of China (grant number: 41573037, 41273063).

References

- Huang WT, Liang HY, Wu L, Wu J, Li J, Bao ZW (2018) Asynchronous formation of the adjacent epithermal Au-Cu and porphyry Cu-Mo deposits in the Zijinshan orefield, southeast China. *Ore Geology Reviews* 102:351-367. doi: 10.1016/j.oregeorev.2018.09.023.
- Li B, Jiang SY (2017) Genesis of the giant Zijinshan epithermal Cu-Au and Luoboling porphyry Cu-Mo deposits in the Zijinshan ore district, Fujian Province, SE China: A multi-isotope and trace element investigation. *Ore Geology Reviews* 88:753-767. doi: 10.1016/j.oregeorev.2017.02.009.
- Liu WY (2015) Mineralogy of the Zijinshan porphyry-epithermal system, Fujian Province. Chinese Academy of Geological Sciences (in Chinese with English abstract).
- Putnis A, Grace J, Cameron W (1977) Blaubleibender covellite and its relationship to normal covellite. *Contributions to Mineralogy and Petrology* 60:209-217.
- So CS, Zhang DQ, Yun ST, Li DX (1998) Alteration-mineralization zoning and fluid inclusions of the high sulfidation epithermal Cu-Au mineralization at Zijinshan, Fujian Province, China. *Economic Geology and the Bulletin of the Society of Economic Geologists* 93:961-980. doi: 10.2113/gsecongeo.93.7.961.
- Vaughan D and Craig J (1997) Sulfide Ore Mineral Stabilities, Morphologies, and Intergrowth Textures. *Geochemistry of Hydrothermal Ore Deposits*, 3rd Edition.
- Xu C, Chen HY, Huang WT, Qi JP, Duan G, Zhang LJ, Wu C, Zhang S, Zhong WB (2017) Mesozoic multiphase magmatism at the Xinan Cu-Mo ore deposit (Zijinshan Orefield): Geodynamic setting and metallogenic implications. *Ore Geology Reviews* 88: 768-790. doi: 10.1016/j.oregeorev.2016.06.019
- Zhong J, Chen YJ, Chen J, Qi JP, Dai MC (2018) Geology and fluid inclusion geochemistry of the Zijinshan high-sulfidation epithermal Cu-Au deposit, Fujian Province, SE China: Implication for deep exploration targeting. *Journal of Geochemical Exploration* 184:49-65. doi: 10.1016/j.gexplo.2017.10.004.
- Zhang JZ (2013) Geology, exploration model and practice of Zijinshan ore concentrated area. *Mineral Deposits* 32: 757-766 (in Chinese with English abstract).

The Ryabinovoe Cu-Au-porphyry deposit (Southern Yakutia, Russia): geology, wallrock alteration, noble gases isotope systematics and isotopic dating of ore-forming processes

Shatova N.V., Shatov V.V., Molchanov A.V., Terekhov A.V., Sergeev S.A., Prasolov E.M.
A.P. Karpinsky All Russian Geological Research Institute (VSEGEI), St. Petersburg, Russia

Dvornik G.P.
Institute Geology and Geochemistry (IGG UB RAS), Yekaterinburg, Russia.

Leontev V.I.
St. Petersburg Mining University (SPbMU), St. Petersburg, Russia.

Abstract. In the Ryabinovoe Cu-Au-porphyry deposit, the ore mineralization is localized within multi-stage metasomatism fields, which were formed in two stages. In the first, pre-ore stage, high-temperature potassium-sodium metasomatites – aegirine feldspathites – were appeared whereas gumbaites of carbonate-sericite-muscovite-orthoclase composition - in the second, low/medium-temperature stage. The results of isotopic (U-Pb, Rb-Sr, Re-Os, $^{40}\text{Ar}/^{36}\text{Ar}$, $^3\text{He}/^4\text{He}$, ^{20}Ne) investigations of the above-mentioned metasomatites and ore mineralization are discussed in the paper.

1 The Ryabinovoe Ore Field

The Ryabinovoe ore field is associated with Mesozoic alkaline igneous rocks of the Ryabinovy stock and is situated in the Central Aldan Ore Region of South Yakutia. In the geological structure of the Ryabinovy stock, material and structural-textural features and the results of isotope geochronological studies using two independent U-Pb and Rb-Sr geochronometers, give two different groups of high potassium igneous rocks.

The early group, predominantly leucocratic rocks, is represented by aegirine-augite alkaline-feldspathic syenites, syenite-porphyrines and quartz syenites (nordmarkites) belonging to the Aldan Suite; the radiological age of magmatic crystallization of rocks is estimated to be 142-144 Ma. Syenite porphyry of the dyke series of the Aldan Suite showed a radiological age of 133 ± 5 Ma (Shatov et al. 2012).

The late group, melanocratic rocks of subordinate importance manifested in the form of small stock-shaped bodies and dykes intersecting the Aldan Suite syenites, is represented by alkaline gabbroids, monzonitoids, melanocratic aegirine-augite syenites, phlogopite-pyroxene lamprophyres (minette) and eruptive breccias with lamproitic cement, which belong to a later Tobuk Suite with a radiological age of 130-141 Ma (Shatova et al. 2017).

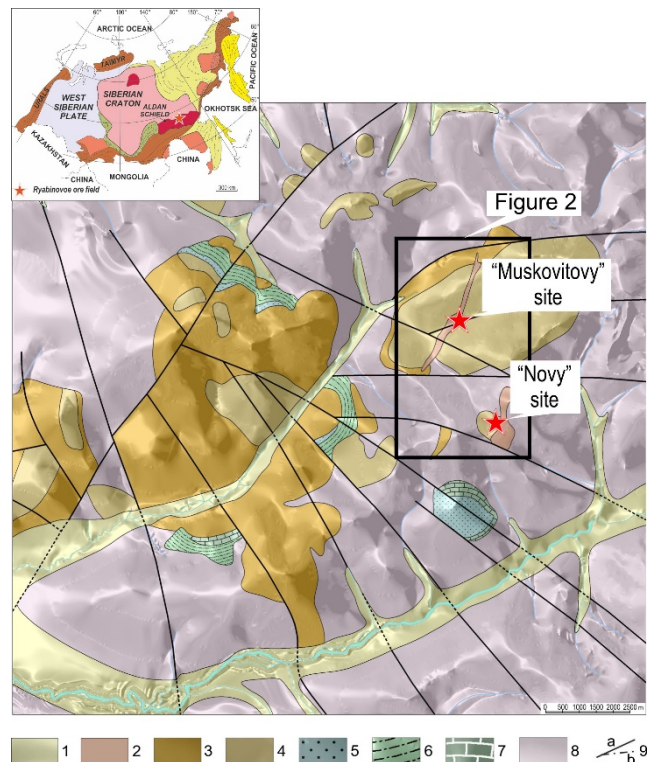


Figure 1. Geological map of the Ryabinovoe ore field. The frame shows location of Figure 2.

1 – Quaternary alluvial deposits; 2 – Tobuk Suite – Lower Cretaceous (gabbro-monzonite, monzodiorite, melanocratic syenite, alkaline phlogopite-pyroxene lamprophyre and eruptive breccias with lamproitic cement); 3-4 - Aldan Suite – Lower Cretaceous (3 – porphyritic alkali-feldspathic aegirine-augite syenite and nordmarkite, *the 1st phase*, 4 - alkali-feldspathic aegirine-augite syenite, nordmarkite and syenite-porphyry, *the 2nd phase*); 5 – Yukhtin Formation – Lower Jurassic (sandstone, siltstone, mudstone, conglomerate); 6-7 – Yudom Group – Middle Vendian-Lower Cambrian (6 – arenite, siltstone, dolomite, mudstone, conglomerate, 7 – dolomite, clay dolomite); 8 – Lower Proterozoic metamorphic rocks (amphibole, biotite and biotite-garnet granite-gneiss, gneissic granite, crystalline schist); 9 - faults (a - main, b - secondary).

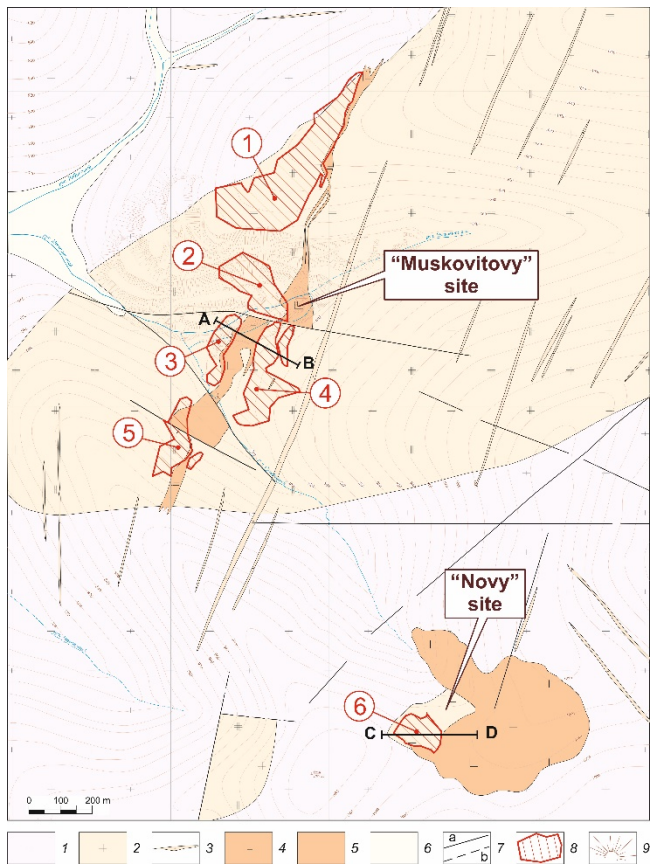


Figure 2. Geological map of the Ryabinovoe Cu-Au-porphyry deposit (modified after Kislyi et al. 2011). See location in Figure 1.

1 – gneiss and granite-gneiss of Proterozoic age; 2-3 – high potassium intrusive rocks of the Aldan Suite (2 - alkali-feldspathic aegirine-augite syenite and nordmarkite, 3 – syenite-porphyre), 4-5 – magmatic rocks of the Tobuk Suite (4 – gabbro-monzonite, monzodiorite, melanocratic syenite, phlogopite-pyroxene lamprophyre and eruptive breccias with lamproitic matrix, 5 - phlogopite-pyroxene lamprophyre and gabbro-monzonite), 6 – Quaternary alluvial deposits; 7 – faults (a – proven, b - proposed); 8 – projections of orebodies on the present day surface (*numbers in circles*): 1-5 – orebodies within the «Muskovitovy» ore site (1 – Northern, 2 – Central, 3 – Western, 4 – Eastern and 5 – Southern), 6 – orebody within the «Novy» ore site; 9 – bench and dump limits of the open pit carried out at the period from 1990 to 1994 years.

2 The Ryabinovoe Cu-Au-Porphyry Deposit

The Ryabinovoe deposit is confined to the northeast endocontact part of the Ryabinovy stock (Fig. 1). Ore mineralization of the deposit is localized within two ore sites, Muskovitovy and Novy, among the hydrothermally altered syenites of the Aldan Suite, containing vein-impregnated sulphide (to 3-5%) mineralization (Fig. 2-3).

In ores of the deposit, the main ore mineral is pyrite, the minor minerals are chalcopyrite, sphalerite, galena, molybdenite, and arsenopyrite. Native gold, electrum, native silver, acanthite, tellurides of silver and gold (hessite, petzite, calaverite), fahlores, enargite, digenite, djurleite, stannite, carrollite, moncheite, erlichmanite, etc. are rare (Kochetkov et al. 1989; Vetluzhskikh et al. 2002; Dvornik 2014).

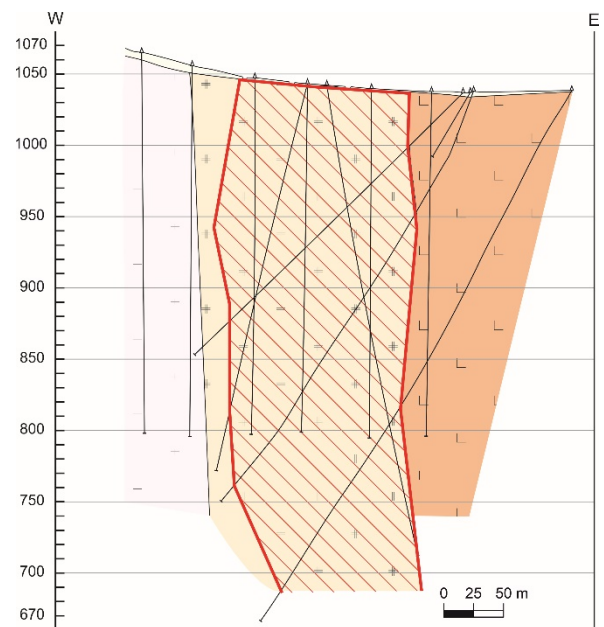
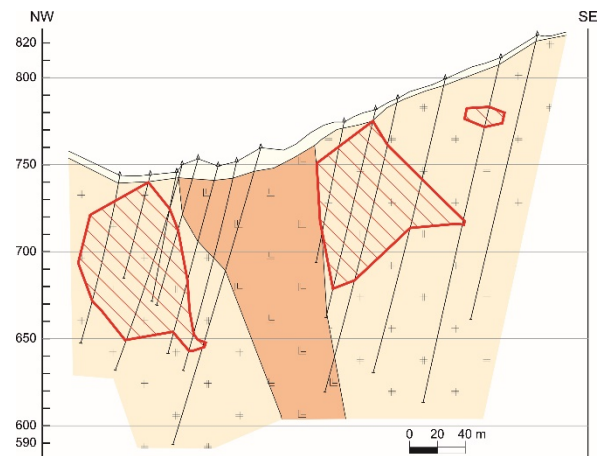


Figure 3. Cross-sections along lines AB (above) and CD (below). For captions see Figure 2.

Orebodies of the Ryabinovoe deposit form stockworks and mineralized zones with Au content varying from 1 to 4 g/t. Associated commercial components are Ag, Cu, Mo, and Pb. Copper content in ores of the Ryabinovoe deposit varies widely from 0.01% to 0.9% and is on average 0.13%.

Molybdenum and lead contents also vary widely: Mo - from 0.002 to 0.125% with an average content of 0.006-0.008%, and Pb - from 0.005 to 0.45% with an average content of 0.083%, that is, they are at levels below the minimum significant commercial values. Platinum ore mineralization is extremely rare and its distribution patterns in the orebodies are still not fully studied (Kovalenker et al. 1996).

As of June 1, 2011, the total Au reserves at the Ryabinovoe deposit with cut-off grade of 0.8 g/t are estimated at 26 t (with an average grade of 2.05 g/t), and silver, at 56 tons (with an average grade of 4.4 g/t). The above Au and Ag reserves are concentrated in six

orebodies, five of which (Central, Western, Southern, Eastern, and Northern) are found within the Muskovitovy ore site, and the sixth, within the Novy ore site (Kisly et al. 2011).

3 Alteration Control

A mineralogical and petrographic study and mapping of halos of hydrothermally altered rocks, conducted by the authors of the paper, made it possible to establish that the emplacement and long-term development of the Ryabinovy syenite stock was accompanied by the mineral alteration zonation of granite-related type.

Close to the syenite stock, near-contact halos of skarnification, fenitization, and alkaline-amphibole propylitization are widespread with a concentric-zonal structure, inherited largely from the ellipsoid shape of the Ryabinovy stock (Ugryumov and Dvornik 1984; Kochetkov et al. 1989).

In the inner parts of the stock, the zonation of mineral alteration is represented by halos of high-temperature aegirine-feldspathic alteration types - feldspathites and replacing them in time halos of medium-low-temperature wallrock gumbettes or carbonate-sericite-muscovite-orthoclase hydrothermally altered rocks.

Among the gumbettes, two facies varieties are distinguished: carbonate-sericite-muscovite-orthoclase (G1 facies), developed mainly among syenites of the Ryabinovy stock from 550 to 750 m, and quartz-carbonate-barite-adularia (facies G2), accentuated in rocks of the ore field at hypsometric marks from 750 to 1100 m and above.

Thus, the lateral row of hydrothermally altered rocks identified at the present level of erosion, in essence, reflects the vertical zonation of mineral alteration, manifested in the Ryabinovoe ore field.

Fig. 4 shows a model-reconstruction of the vertical zonation of mineral alteration, constructed by interpolating all the mineralogical and petrographic data obtained from the line intersecting the Novy and Muskovitovy ore sites of the Ryabinovoe deposit.

The established modern pattern in the distribution of the above-considered zones of hydrothermal alterations within the Muskovitovy and Novy sites is, on the one hand, a reflection of material and structural-tectonic heterogeneities in the structure of the Ryabinovy stock itself and its morphology, and on the other hand, under the conditions of a heavily dissected topography (600-1150 m), is a reflection of an uneven cut by the modern erosion surface of three subparallel zones of the "cover" type, replacing each other in the intra-intrusive space bottom-up (in the direction of the vector of maximum variability): *feldspathites* → *gumbettes of the carbonate-sericite-muscovite-orthoclase facies (G1)* → *gumbettes of the quartz-carbonate-barite-adularia facies (G2)*.

That is, in this series of hydrothermally altered rocks, gumbettes of the G2 facies occupy the uppermost link of the vertical column of mineral alteration (Terekhov et al. 2014).

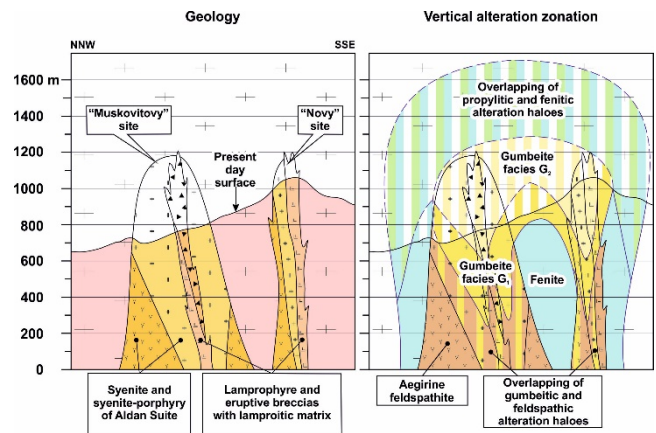


Figure 4. Reconstruction of the hydrothermal alteration system of the Ryabinovoe Cu-Au-porphyry deposit.

4 Results of Isotopic Dating of Wallrock Mineral Alterations

In order to date isotopically (U-Pb, Rb-Sr and Re-Os) hydrothermally altered formations associated with the emplacement of the Ryabinovy syenite stock, five representative samples of hydrothermally altered rocks were studied, of which two belong to the "pre-gumbette" aegirine feldspathites and three samples of wallrock gumbettes, replacing the Aldan Suite syenites.

Based on the use of three independent isotope geochronometers (U-Pb, Rb-Sr and Re-Os), it was found that the intra-intrusive altered rocks, aegirine feldspathites and wallrock gumbettes, were slightly separated in time from the final magmatic crystallization of the Aldan and Tobuk suites. High-temperature aegirine feldspathites formed in the interval of 132-143 Ma, and wallrock gumbettes replacing them in time ranged from 125-139 Ma (Fig. 5).

5 Geochemistry of Noble Gas Isotopes

This study used $^{40}\text{Ar}/^{36}\text{Ar}$, $^3\text{He}/^4\text{He}$, and ^{20}Ne in gas-liquid inclusions from altered rocks of the Muskovitovy and Novy ore sites and was carried out at VSEGEI Centre of Isotopic Research according to the method developed by Prasolov (1990).

Using the example of studying two samples of feldspathites and six samples of gumbettes of G1 and G2 facies, it was shown (Fig. 5) that the proportion of airborne argon in the vertical column of hydrothermally altered rocks from the Ryabinovoe deposit naturally increases from 70% in the sub-ore feldspathites (at hypsometric marks 600-650 m) to 87% in gumbettes of carbonate-sericite-muscovite-orthoclase facies G1 (at marks 700-800 m), reaching a maximum of 96% in gumbettes of quartz-carbonate-barite-adularia facies G2 (at marks above 950 m) within the Novy ore site (Fig. 5).

At the same time, the share of mantle helium in alteration types and ores remains extremely low ($\leq 2-3\%$) over the entire depth range of the vertical column of

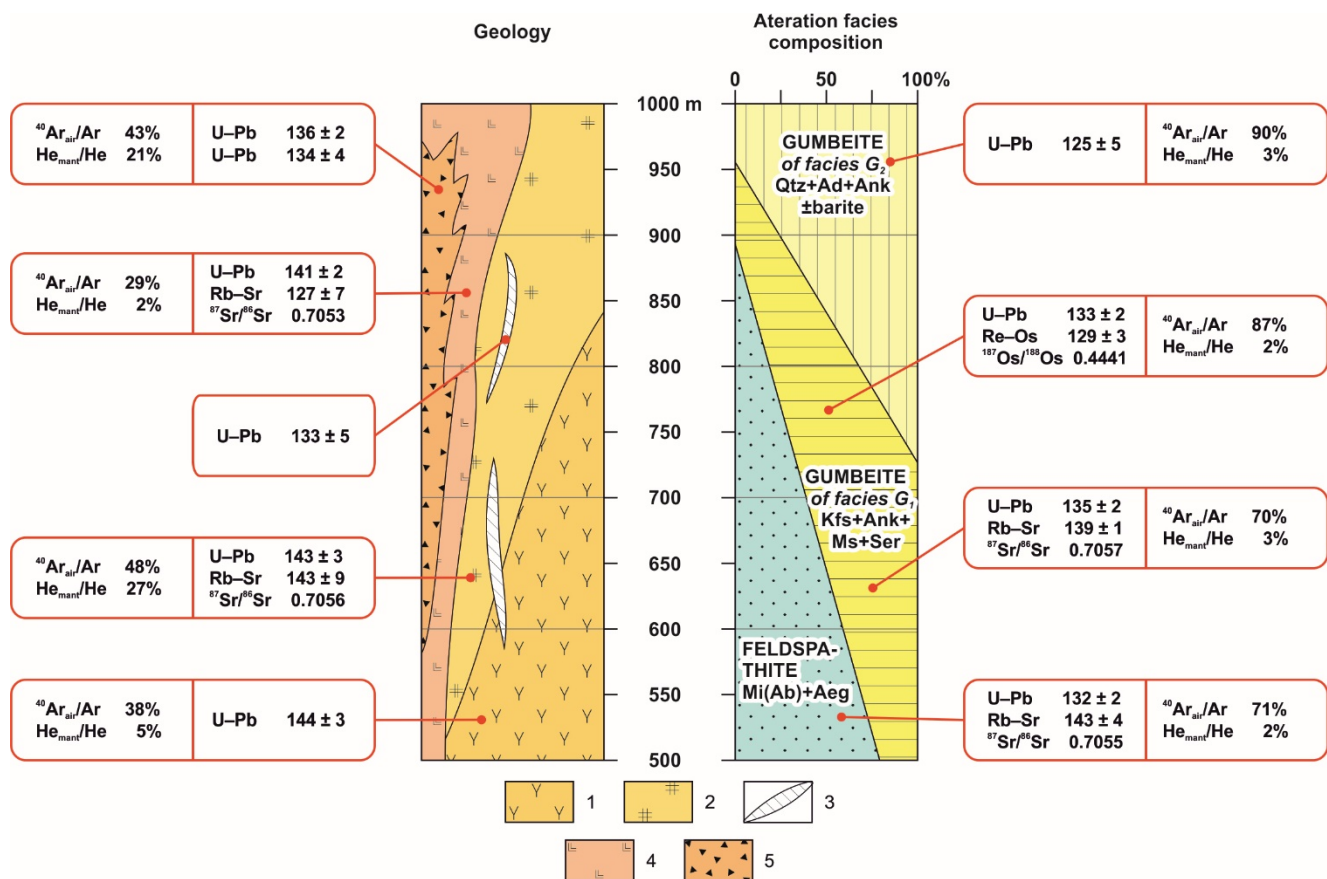


Figure 5. Summarized diagram, demonstrating change with depth of wallrock metasomatites' mineral composition and their isotope characteristics (U-Pb, Rb-Sr, Re-Os, $^{87}\text{Sr}/^{86}\text{Sr}$, $^{187}\text{Os}/^{188}\text{Os}$, $^{40}\text{Ar}_{\text{air}}/\text{Ar}$, $\text{He}_{\text{mant}}/\text{He}$) within the Ryabinovoe Cu-Au-porphry deposit. All isotope data, carried out by U-Pb, Rb-Sr и Re-Os methods, shown at Ma. 1-3 – magmatic rocks of the Aldan Suite (1 - porphyritic alkali-feldspathic aegirine-augite syenite and nordmarkite, the 1st phase, 2 - alkali-feldspathic aegirine-augite syenite and nordmarkite, the 2nd phase, 3 - syenite-porphry); 4-5 – magmatic rocks of the Tobuk Suite (4 – gabbro-monzonite, monzodiorite, melanocratic syenite and alkaline phlogopite-pyroxene lamprophyre, 5 - eruptive breccias with lamproitic matrix).

mineral alteration, which indicates active participation in the final stages of the ore formation in the Ryabinovoe deposit of predominantly vadose waters of the host rocks, altered in the thermogradient field of the Ryabinovy stock into hydrothermal solutions. Whereas the formation of pre-ore high-temperature feldspathites was most likely due to the effect on the host syenites of magmatogenic hydrothermal fluids of predominantly juvenile origin.

References

- Dvornik GP 2014 Metasomatites and gold mineralization of high potassium alkaline massifs (by example from the Central Aldan alkaline province). Yekaterinburg: URSMU Publishing House: 329 p. (In Russian).
- Kisly AV, Sotnikov OV, Utkina NE 2011 Report on the results of reserves assessment of the Ryabinovoe gold deposit, Aldan region, Yakutia. SPb: OOO «RJC Consulting», OOO «Ryabinovoe»: 250 p. (In Russian).
- Kochetkov AY, Pakhomov VN, Popov AB 1989 Magmatism and metasomatism of the Ryabinovy alkaline ore-bearing massif (Central Aldan). Magmatism of copper-molybdenum ore knots. Novosibirsk: Nauka: 79-110 (In Russian).
- Kovalenker VA, Myznikov IK, Kochetkov AY, Naumov VB 1996 PGE-bearing gold-sulphide mineralization in the Ryabinovy alkaline massif (Central Aldan, Russia). Geology of ore deposits 4:345-356 (In Russian).
- Prasolov EM 1990 Isotopic geochemistry and origin of natural gases. L.: «Nedra»: 280 p. (In Russian).
- Shatov VV, Molchanov AV, Shatova NV, Sergeev SA, Belova VN, Terekhov AV, Rad'kov AV, Soloviev OL 2012 Petrography, geochemistry and isotopic (U-Pb and Rb-Sr) dating of alkaline magmatic rocks of the Ryabinovy massif (South Yakutia). Region. Geol. and Metallogeny 51:62-78 (In Russian).
- Shatova NV, Skublov SG, Melnik AE, Shatov VV, Molchanov AV, Terekhov AV, Sergeev SA 2017 Geochronology of alkaline magmatic rocks and metasomatites of the Ryabinovy stock (South Yakutia) based on zircon isotopic and geochemical (U-Pb, REE) investigations. Region. Geol. and Metallogeny 69:33-48 (In Russian).
- Terekhov AV, Molchanov AV, Shatova NV, Belova VN 2014 Two types of ore-bearing gumbecite alteration from the Elkon gold and uranium ore knot (South Yakutia). Region. Geol. and Metallogeny 60:71-86 (In Russian).
- Ugryumov AN, Dvornik GP 1984 Ore-bearing alkaline metasomatites of the Ryabinovy massif (Aldan Shield). Sovetskaya Geologiya 9: 84-94 (In Russian).
- Vetluzhskikh VG, Kazansky VI, Kochetkov AY, Yanovsky VM 2002 Gold ore deposits of the Central Aldan region. Geol. ore deposits 6:467-499 (In Russian).

Geological position and structural control of ore mineralization of the Manukuyu-Varchatinsky ore cluster (the Polar Urals, Russia)

Julia N. Ivanova, Roman I. Vyhristenko, Ilya V. Vikentyev
Russian Academy of Sciences

Abstract. The Malouralsk volcano-plutonic belt (VPB) of the Polar Urals hosts the Toupugol-Khanmeyshorsky ore district and the Manukuyu-Varchatinsky ore cluster. The recent discoveries of the Novogodnee-Monto Au-Magnetite-skarn and the Petropavlovsk Au-porphyry deposits indicate that the belt is prospective for porphyry-style mineral systems. The comparative morphostructural and paleo-facial (paleovolcanic) analysis of Landsat 8 multispectral images demonstrates the relationship of annular and radial structures to gold mineralization. The identification of these structures in underexplored parts of the belt can be used as an aid to mineral exploration in this remote region.

1 Introduction

The Malouralsk VPB is located in the Polar Urals, to the East of the Main Uralian Fault zone and consists of a sequence of middle Silurian to lower Devonian volcanic rocks (Fig. 1a, b). The discovery of the Novogodnee-Monto gold-skarn-magnetite deposit, the Petropavlovsk gold-porphyry deposit and a number of other Au occurrences led to the identification of the Toupugol-Khanmeyshorsky ore district in the northern part of the Malouralsk VBP (Fig. 1b) (Soloviev et al. 2013; Ivanova et al. 2017; Vikentyev et al. 2017). These discoveries indicated the high perspectivity of the Malouralsk VBP. Further exploration work during the period 2010-2012 by Polyarnaya Partiya of Institute of mineralogy, geochemistry and crystal chemistry of rare elements (IMGRE) led to the discovery of the Polyarnaya Nadezhda, the Geokhimicheskoe, and the Blagodatnoye occurrences further to the South (Fig.1b). These discoveries were made through the multidisciplinary interpretation of geological, geochemical and geophysical data and the delineation of what became known as the Manukuyu-Varchatinsky ore cluster.

The Polyarnaya Nadezhda ore occurrence has an estimated resource of 20 tons contained gold (P2 category) (Kremenetsky, 2012). Multispectral images from the Landsat 8 program from the area surrounding Polyarnaya Nadezhda were processed and analyzed to identify key geological features and structures associated with the gold mineralization. A key focus of this analysis and interpretation was the identification of linear and concentric structures.

2 Geological setting

The geology of the Manukuyu-Varchatinsky ore cluster is

composed of a sequence volcanogenic and volcanogenic-sedimentary rocks of the Malouralskaya suite (middle Silurian – lower Devonian). In this sequence volcanic facies are dominant over the volcanogenic-sedimentary ones constituting and 60-80% of the total volume.

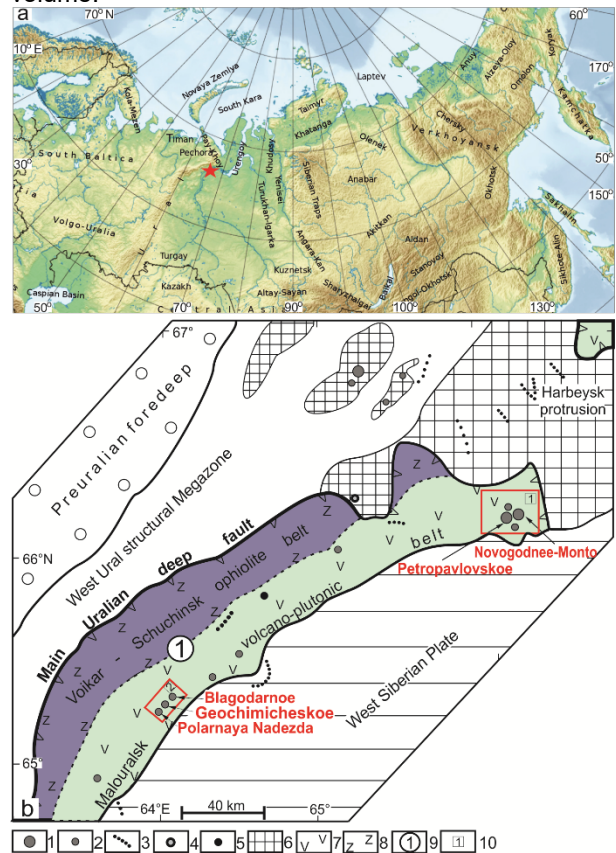


Figure 1. a Localization of the Manukuyu-Varchatinsky ore cluster and the Toupugol-Khanmeyshorsky ore district in within of the Russian Federation. **b** Position of the Manukuyu-Varchatinsky ore cluster in the Malouralskaya zone (structural basis was adopted after Chernyaev et al. 2005): 1 – gold deposit, 2 – gold occurrence, 3 – gold placer, 4 – V-Fe-Cu-(Au) occurrence, 5 – volcanogenic massive sulfide gold-bearing occurrence, 6 – the Central Uralian Megazone, 7 – basalt-andesite complex, 8 – ophiolites, 9 – the Malouralskaya zone, 10 – the Toupugol-Khanmeyshorsky ore district (1), the Manukuyu-Varchatinsky cluster (2).

Within the sedimentary facies present, bioherms are identified but rare and are composed of reef limestones. The Malouralskaya suite is subdivided into three series. The lower series is composed of subaerial agglomerates, bomb tuffs, tuff breccias, clastic flows, and lavas of andesitic composition. This series is interpreted as being

representative of the relicts of the Silurian volcanic centres, e.g. the Manyukuyu massif, the Dzolyavarchati range. The middle series is restricted to the area of the Elkoshor stream, the Elkoshorskoe and the Tret'ya Rudnaya Gorka ore occurrences, and is located on the right bank of the Tanyu River. The upper series is localized on the right bank of the Tanyu River. This series is composed of pyroclastic and volcano-sedimentary rocks and lavas. These are characterized by a wide development of coarse pyroclastics (bomb tuffs, tuff conglomerates and tuff gravelstones). In general, the petrogeochemical composition and lithological characteristics of the igneous and tuffaceous rocks of the suite indicate that these rocks were formed as a result of eruptive-explosive activity of central-type volcanoes formed in a subduction-related setting. The alternation of packs of volcanic and sedimentary rocks indicates that periodic activation of volcanic activity took place during the accumulation period of rocks.

This Malouralskaya suite is intruded by the Devonian to Eifelian Sobsky and the late Devonian to early Carboniferous Kongorsky plutonic complexes. The Sobsky complex is formed of large intrusions of gabbro, diorite and tonalite. This complex frame a band of volcanic rocks to the west. Minor intrusions and dikes belong to the Kongorsky complex. This complex includes gabbro, gabbro-diorites, diorites, and monzodiorites (Shishkin et al. 2007; Kremenetsky 2012).

The hydrothermal and metasomatic alteration type observed in the area include: skarnification, epidotization, silicification, albitization, beresitization, and sulfidization. The skarns contain both magnetite dominated and magnetite-sulfide bodies with the magnetite skarns at the Pervaya Rudnaya Gorka, the Tret'ya Rudnaya Gorka, the Magnetitovoye, and others occurrence being associated with contacts of the intrusions. Metasomatites and metamorphic rocks of the calcsilicate, sodium and magnesia series are genetically associated with gabbro-hyperbasite complexes.

Well-developed skarns are found near the contact of quartz diorites of the Sobsky complex with volcano-sedimentary rocks. An example of this type of mineralization is the ore body of the Novogodnee-Monto deposit (Soloviev et al. 2013). In the region, the skarn-type mineralization is considered as a highly prospective target for gold.

3 Methods

The data source for this study was NASA's earth observation platform Landsat 8 with the Operational Land Imager (OLI) and Thermal InfraRed Sensor (TIR) sensors. The spectral bands used were 7, 3, 5 from the OLI sensor and the band 10 from the TIR sensor. The scenes used were (LC08_L1TP_165013_20180820_20180829_01_T1; LC08_L1TP_166013_20170707_20170716_01_T1; LC08_L1TP_166014_20180827_20180911_01_T1; LC08_L1TP_166013_20180726_20180731_01_T1) which were 35,000m² in area and of a ground resolution ~30m² per pixel. The bands were composited in to two

RGB images, 7-5-3 and 10-7-3 for the purposes of analysis.

Hidden structures (arc, concentric, annular, and radial) were given out in the process of image analysis of multispectral satellite images. Lineaments are most clearly revealed in the regions adjacent to the border of the phototone and river drainage patterns.

The interpretation of the Landsat 8 was based on an integrated approach: paleo-facial and morphostructural analysis. Morphostructural analysis included the removal of informative structural indicators of the relief and hydrographic network from various images of the earth's surface; identification of the main morphostructural elements, scale 1:200000; comparison with geological and geophysical maps, cartographic materials (Shishkin et al. 2012). Geophysical maps used include the maps of magnetic and gravitational fields, scale 1:200000 for the studied and surrounding areas. Maps of magnetic and gravitational fields were used to confirm and refine the contours of morphostructurals.

4 Analysis of Landsat 8 Images

Image analysis of Landsat 8 Images and morphostructural analysis are widely used all the world for predictive perspective analysis for various types of minerals in different regions, including the Arctic (e.g., Pour 2012; Sarapää, Sarala 2013; Graham et al. 2017; Yousefi et al. 2018). Image analysis distinguished annular, arc, and radial lineaments within the ore cluster and adjacent territories. It should be noted that lineaments were less frequent in the southeastern part of the territory, than the adjacent area (Fig. 2). The structures are localized under a thick cover of Mesozoic sediments (about 1200 m) here, whereas the thickness is to 200 m in the southeastern part of the territory.

Two large oval structures are distinguished (Fig. 2b). Morphostructural № 1 has 54x44 km size. This morphostructural is complicated by smaller annular (about 10 km), arc, and radial lineaments. Most ore occurrences and mineralization points (Cu-Zn-pyrite, Cu, Cu-Zn, Fe-Ti-V, Cu-Pb-Au – on periphery part, Pt, Fe-Cu-Au – on the center part) are localized in this morphostructural. The Polyarnaya Nadezhda, the Geokhimicheskoe, and the Blagodatnoye ore occurrences belong to morphostructural № 1. Morphostructural № 2 is smaller (48x38 km size) than the morphostructural № 1. Annular, arc, and radial lineaments complicate this morphostructural too. Ore occurrences and mineralization points (Cu-Mo, Fe-Ti-V, Cu – inside, Fe-Cu, Mo-Cu, Cu-Au – near) belong to morphostructural № 2.

Image analysis identified the radial zones. These have north east (up to 40) and northwest (up to 22 km) directions. These probably are more ancient activated structures. These lineaments correspond to weakened areas of the earth's crust (decompression zones). These zones experienced periods of activation with the influx of mantle heat and focal crustal structures appeared. These controlled the placement of ore clusters. Thus, hydrothermal mineralization is localized in the

concentration points of the faults (the points of the intersection of lineaments near the center of large annular structures). Morphostructural № 1 and № 2 are volcano-plutonic heterogeneous structures of first order. They were probably formed under the influence of several geological processes and complicated by concentric structures of the second order (smaller diameter, morphostructural № 1). These structures with smaller diameters create feature of "telescoping" (Gornyi et al. 2014).

Khanmeyshorsky ore district. **b** Interpreted satellite imagery for the east part of the Main Ural Fault (the Malouralsk VPB): 1–3 – lineaments: 1 – arc; 2 – concentric (a), annular (b); 3 – radial; 4 – contours of ore cluster and district: the Manukuyu-Varchatinsky ore cluster (1) and the Toupugol-Khanmeyshorsky ore district (2); 5 – contours: a – morphostructurals № 1 and № 2, b – detected structure of the northeast direction; 6 – subvolcanic bodies: the Toupugol-Khanmeyshorsky ore district according Pryamonosov et al. 2001 for (a), the Manukuyu-Varchatinsky ore cluster according Shishkin et al. 2006 (b); 7–23 – ore deposits, ore occurrences, and points of mineralization: 20, 22 – ore deposit, 7–9, 11, 13, 15, 17–19, 21, 23 – ore occurrence, 10, 12, 14, 16 – mineralization point (7 – Fe-Cu-Au, 8 – Fe-Cu, 9, 10 – Fe-Ti-V, 11 – Cu-Au, 12 – Cu-Mo, 13 – Cu-Pd-Au, 14 – Cu-Zn-pyrite, 15 – Cu-Zn, 16, 17 – Cu, 18 – Mo-Cu, 19 – Pt, 20, 21 – gold-quartz/porphyry type, 22, 23 – skarn-magnetite type with gold).

The series of short closely parallel radial lineaments of the northeast directions were identified (Fig. 2b). These are concentrated in a strip to 25 km of wide and length to 105 km. This zone together forms structure of the northeast direction. Probably, this zone reflects the hidden structures and creates a complex block structure of the territory, and plays a controlling role in the placement of mineralization. This zone possibly has been formed later morphostructurals № 1 and № 2.

5 Comparative characteristics of the two territories

We compared morphostructural map with the more northern territory of the Toupugol-Khanmeyshorsky ore district (Ivanova et al. 2017; Vikentyev et al. 2017) (Fig. 2a) to identify similar structure features and localization of gold mineralization, as well as to develop a prediction and predictive features for gold type of mineralization.

1. These territories contain the tectonic-magmatic structures of a complex nature.
2. Ore districts and clusters are localized on the territory of intersection of tectonic disturbances in regional long-lived zones with the NE and the NW-trending. These zones control ore mineralization.
3. Intrusive formations are represented by polyphase and uneven-age complexes. Skarn-magnetite and gold ore mineralization is associated with these intrusive formations.
4. The internal structure of annular morphostructural was complicated by the intersection of concentric and (or) arc faults, radial faults of the NE and the NW-trending of various ranks, as well as zones of concentration of small annular structures.
5. Ore deposits and ore occurrences are localized within large annular structures of complex formation history and long-term evolution.

Differences:

1. The Novogodny morphostructural is smaller than morphostructural № 1 and № 2 (6x10 km, 54x44 km and 48x38 km, respectively).
2. The annular and arc structures are accompanied by less extensive radial lineaments (up to 20 for the Novogodny morphostructural and up to 50 km for morphostructurals № 1 and № 2).
3. The Novogodny morphostructural is volcano-plutonic monogenic structure of the second rank. This

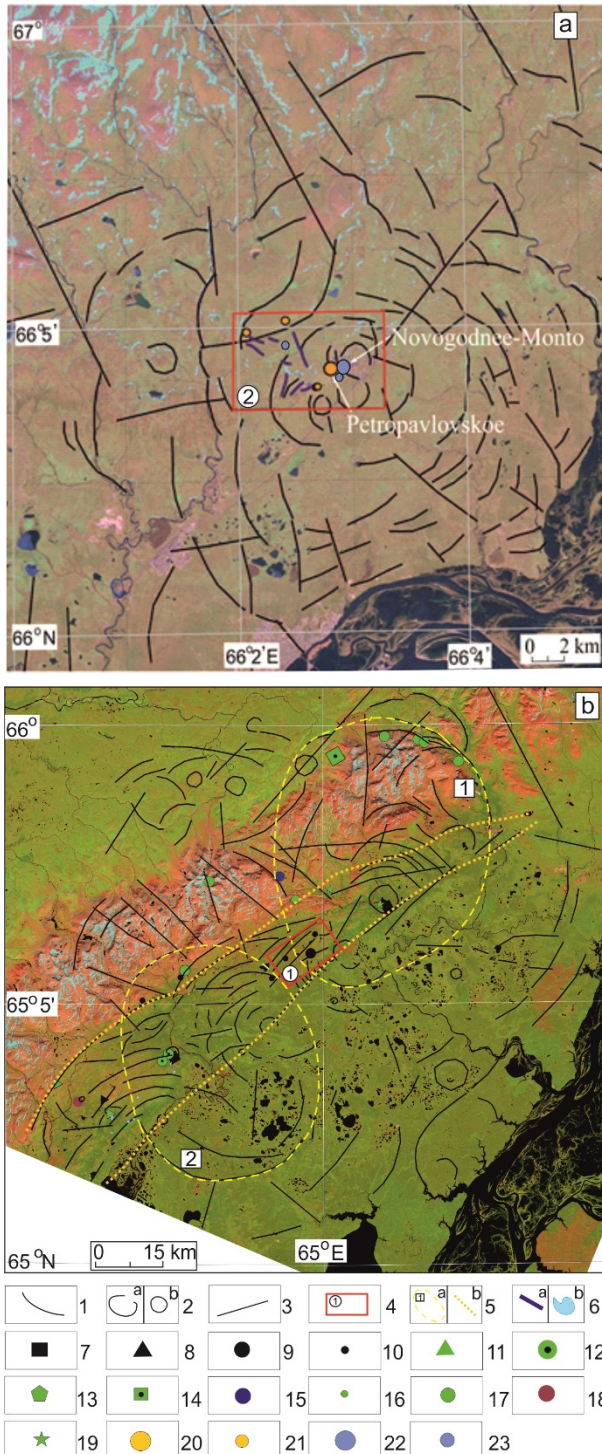


Figure 2. **a** Interpreted satellite imagery for the Toupugol-Khanmeyshorsky ore district. **b** Interpreted satellite imagery for the east part of the Main Ural Fault (the Malouralsk VPB).

morphostructural was probably formed under the influence of one leading geological process.

6 Why on this territory have not yet discovered deposits

1. Large faults up to hundred km of long absent in this territory that would cross-favourable horizons and structures. Because of, absent of renovation of these faults and took place their further “blockage”.
2. The period of stretching followed intrusion phase. Compressive forces decreased. Such conditions contributed of the intrusion and “retract” the hydrothermal solutions. The condition of ore formation is intrusion of hydrothermal solutions into cracks in the zone of large faults (Cox et al. 2001).
3. Hydrothermal deposits are formed in conditions of differentiated tectonic movements of small amplitude. Weak uplifts enliven hydrothermal solutions and favour their penetration into raised wings of the folds. The amplitudes of vertical movements (from 1 to 5 km) in compression conditions impede the penetration of fluids in the zone as a whole and, thus, ore formation does not develop (Perelman 1989).
4. The factor of poor knowledge of the territory should not be excluded from consideration.

7 Conclusions

The Malouralsk VPB is characterized by a wide evolution of radial and annular structures. These structures are clearly detected on the multispectral Landsat 8 Images. In the result of analysis of Landsat 8 Images two large oval-shaped morphostructurals compounded by annular, arc, and radial lineaments of smaller rank were decoded. These complicated morphostructurals indicate that multi-stage development. Ore deposits and ore occurrences are mainly localized in the periphery of these morphostructurals.

The northeast direction zone wide up to 25 km and length about 105 km was allocated in the process of analysis of multispectral images. This zone possibly may control the ore mineralization.

The mineralization zones (gold deposits, ore manifestations, and mineralization points) of the Malouralskaya zone belong to complexly-constructed systems of annular and radial structures. Large annular morphostructurals have great importance in ore localization.

In general, the ore districts on the eastern slope of the Urals correspond to the zone of intersection of faults of regional significance. They marked by the form of extending lineaments with a predominantly north-western orientation and large annular structures. Gold hydrothermal mineralization within these ore districts should be localised in areas of thickening faults and in the intersections of radial lineaments near concentrations of large annular morphostructural.

Acknowledgements

The authors gratefully thank: the Russian Foundation for Basic Research (grant № 18-05-70041) for financial support; R.N. Armstrong for helpful comments leading to improvement in this manuscript.

References

- Chernyaev EV, Chernyaeva EI, Sedelnikov AY, et al. (2005) Geological mapping and structural modeling of the Novogodnee–Monto deposit. Unpubl Prof Report. Geosphere, Tomsk (in Russian).
- Cox SF, Knackstedt MA, Braun J (2001) Principles of structural control on permeability and fluid flow in hydrothermal systems. *Soc Econ Geol Rev* 14:1–24.
- Gornyi VI, Kritsuk SG, Latypov IS, et al. (2014) Regularities of rock alteration assemblages of ore-magmatic systems containing quartz-vein manifestations of gold (by satellite spectrometry). *Modern prob of remote sensing of the Earth from space* 11(3):140–156 (in Russian).
- Graham GE, Kokaly RF, Kelley KD et al. (2017) Application of imaging spectroscopy for mineral exploration in Alaska: a study over porphyry Cu deposits in the Eastern Alaska Range. *Econ Geol* 113(2):489–510.
- Ivanova JN, Vikentyev IV, Sobolev ID, et al. (2007) Gold-porphyry mineralization of the Toupugol-Khanmeyshorsky ore district (the Polar Urals, Russia): geo-chronology and geological controls on ore genesis. 14th SGA Biennial Meeting, Quebec City, Canada. 1:363–366.
- Kremenetsky (2012) Justification of search and prediction and audit works on gold within the Manukuyu-Varchatinsky ore cluster (the Polyarnaya Nadezhda, the Geokhimicheskoe, and the Blagodatnoye ore occurrence). Scale 1: 10,000. Moscow: FSUC IMGRE. 45 p. (in Russian).
- Perelman AI (1989) *Geochemistry*. Moscow: High school. 528 p. (in Russian).
- Pour BA, Hashim M (2012) The application of ASTER remote sensing data to porphyry copper and epithermal gold deposits. *Ore Geol Rev* 44:1–9.
- Pryamonosov AP, Stepanov AE, et al. (2001) State geological map of the Russian Federation. Scale 1:200000 (second edition). The Polar Ural series. Q-41-XII Sheet. Explanatory note. Salekhard: natural resources committee for the Yamalo-Nenets autonomous district. 231 p (in Russian).
- Sarapää O, Sarala P (2013) Rare earth element and gold exploration in glaciated terrain: example from the Mäkärä area, northern Finland. *Geochem: Explor, Environ, and Anal* 13(2):131-143.
- Shishkin MA, Astapov AP, Kabatov NV, et al. (2007) State geological map of the Russian Federation. Scale 1: 1000000 (third generation). The Ural series. Q41 – Vorkuta sheet: Explanatory note. St. Petersburg: VSEGEI. 541 p. (in Russian).
- Soloviev SG, Kryazhev SG, Dvurechenskaya SS (2013) Geology, mineralization, stable isotope geochemistry, and fluid inclusion characteristics of the Novogodnee–Monto oxidized Au–(Cu) skarn and porphyry deposit, Polar Ural, Russia. *Miner Deposita* 48(5):603–627.
- Vikentyev IV, Ivanova YN, Tyukova EE, et al., (2017) Porphyry-Style Petropavlovskoe Gold Deposit, the Polar Urals: Geological Position, Mineralogy, and Formation Conditions. *Geol Ore Dep* 59(6):482–520.
- Yousefi T, Aliyari F, Abedini A, Asghar Calagari A (2018) Integrating geologic and Landsat-8 and ASTER remote sensing data for gold exploration: a case study from Zarshuran Carlin-type gold deposit, NW Iran. *Arabian J. Geosci* (11):1-19.

Mineralisation in the K1 vein-system, Kencana Epithermal Deposit, Gosowong Goldfield

Thomas Tindell, Kotaro Yonezu
Kyushu University, Japan

Syafrizal
Institute of Technology Bandung, Indonesia

Abstract. The Gosowong goldfield encompasses one of the most extraordinarily rich gold provinces in Indonesia, or indeed the western Pacific region. The depositional area lies on Halmahera Island, straddling a zone roughly equidistant to Sulawesi Island to the west and Papua Island to the east. Volcano-magmatic activity is related to the closure of the Molucca Sea, with an arc-arc subduction forming the Sangihe Thrust and the parallel Halmahera Thrust. The subsequent Halmahera Arc lies along the north-western arm of Halmahera Island and the north-south aligned volcanic islands chain to the south. The geology of Halmahera may be separated into two major domains; the eastern domain composed of Mesozoic ophiolite complexes and overlying Oligocene clastic sediments, with the western domain composed of Neogene to recent volcanic and pyroclastic rocks. Discovered through the major finding of the Gosowong low-sulfidation deposit in 1994, two further extremely rich epithermal deposits (Togarachi and Kencana) were subsequently discovered amongst numerous prospects. The Kencana deposit is located in the southeastern area of the Gosowong goldfield, and lies within the Gosowong Formation, principally composed of a large-scale andesite package with numerous interlayered sandstone mudstone volcanoclastic deposits.

1 Introduction

Epithermal gold mineralization and their often associated magmatic-arc porphyry affiliations are well recognized throughout the Indonesian archipelago. Much focus, with regard to research, has been on the significant and economical deposits situated along the Sunda-Banda arc system. Precious metal epithermal-type mineralization in the Indonesian Archipelago is significant, and with much of the major discoveries found on the westward largest islands of Sumatra and Java. High-grade precious metal deposits (low-sulfidation-type) are distributed throughout Java Island, for example the Cibaliung, Pongok and Trenggalek deposits. Large world-class porphyrys are well documented in the east, such as Batu Hijau on Sumbawa Island and the Grasberg deposit on Papua.

The Kencana deposit, located in the northern arm of Halmehera Island (Fig. 1), straddles a complicated grouping of plates, micro-plates, thrusts and subduction zones. Its north-eastern locality makes it far removed from the Sunda-Banda Arc and consequently a unique mineralization area. The deposit is a member of a group of epithermal deposits, prospects and porphyry systems, collectively referred to as the Gosowong Goldfield (Fig.

2). Within, there are three principle deposits; Gosowong, Toguraci and Kencana, all of which are classified as low-sulfidation epithermal-type and as yet encompass the richest precious metal deposits of Halmahera Island and indeed Indonesia. The Gosowong Goldfield was discovered in 1994, with mining commencing in the Gosowong deposit and subsequent discoveries at Toguraci and Kencana in 2000 and 2003 respectively.

The Kencana deposit has the highest precious metal endowment of the Gosowong mining area, with an average grade in excess of 23g/t Au and a total resource of 4Mt. Here we provide a summary of the mineralization patterns in successive zones is presented, with discussions eluding to the mechanisms to which this mineralization is attributed.

2 Geology

2.1 Regional geology

The geology of Halmahera Island is relatively straightforward, though it is a member of a tectonically complicated mosaic of microplates (Hakim and Hall 1991). The island is situated in the northern portion of the Sorong Fault, siting between the almost equidistant islands of Sulawesi to the west and New Guinea to the east. The Molucca Sea separates Halmahera Island from the northern Minahassa Peninsula of Sulawesi. The eastern most tip of the Minahassa Peninsula forms the Sangihe Arc, whilst the western edge of Halmahera (and the north-south chain of volcanic islands) forms the Halmahera Arc, forming an arc-arc collisional zone. The eastern domain of the island hosts the oldest rock units, comprising a basement of Late Cretaceous ophiolites and volcanic rocks attributed to development of the forearc sequence, collectively referred to as the Ophiolitic Basement Complex (Hall 1987; Hall et al. 1988; Hakim and Hall 1991). These are unconformably overlain by Miocene limestones. The Western domain is underlain by late Mesozoic volcanic rocks, which are unconformably covered by successive Paleogene-Quaternary volcanic and volcanoclastic rocks.

2.2 Local geology

The Gosowong Goldfield is situated in the lower neck of northern Halmahera Island, which is composed of Paleogene to Present volcanic-volcanoclastic and

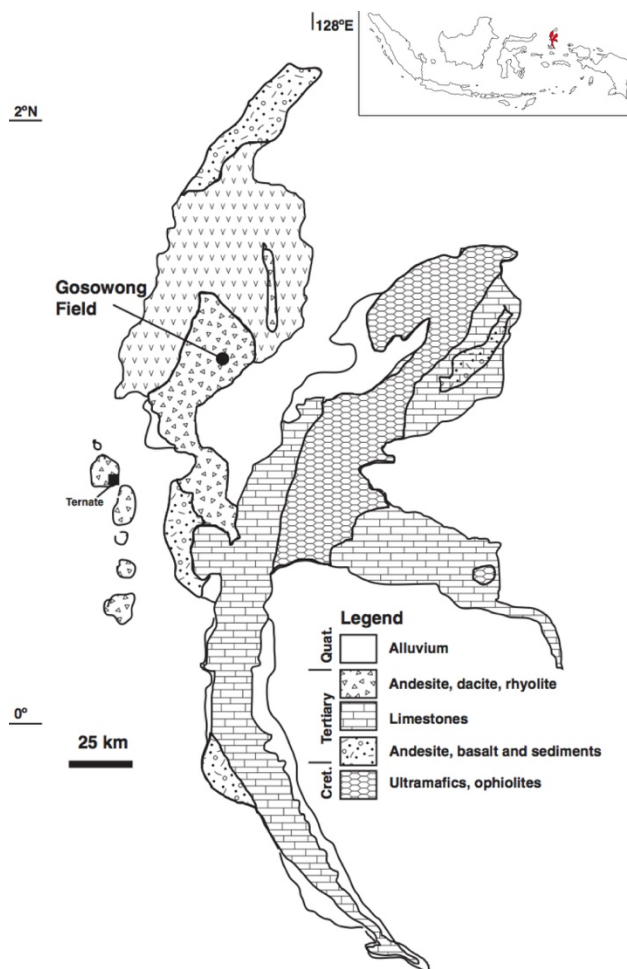


Figure 1. Geological boundaries of Halmahera Island and surrounding arc volcanism related islands. The southern and eastern limbs of the island host the Cretaceous ultramafic basement of obducted ophiolite sequences, whilst the northwestern limb is composed of the Paleogene to Present volcanogenic andesite packages. Inset (top right), Halmahera Island (red) in relation to wider Indonesian archipelago.

intrusive rocks.

The Gosowong district is composed of four formations: Bacan Formation (Paleogene), the Gosowong Formation (Neogene), Kayasa Formation (Pliocene) and Quaternary Volcanic Formation.

The Gosowong Formation consists of volcanic and volcanoclastic rocks, called as Gosowong volcanoclastics. Gosowong volcanoclastics are composed of basaltic group and andesitic group. Andesitic group is overlain by Basaltic group. The basaltic group consists of volcanoclastic conglomerate, basalt andesite, intrusive andesite, basalt lava and volcanoclastic sandstone. Andesitic group is composed of; diorite, andesite fragmental lava, volcanoclastic conglomerate, volcanoclastic sandstone, volcanoclastic mudstone and andesite lava (Gemmell 2007). $^{40}\text{Ar}/^{39}\text{Ar}$ ages of adularia from the epithermal mineralisation zone in Gosowong district ranged from 2.8Ma to 2.9Ma (Vansconcelos 1998) and from 2.4Ma to 2.9Ma (Olberg 2001). U-Pb isotopic age of host rock ranges from 3.1Ma to 3.7Ma (Steven and Daud 2011).

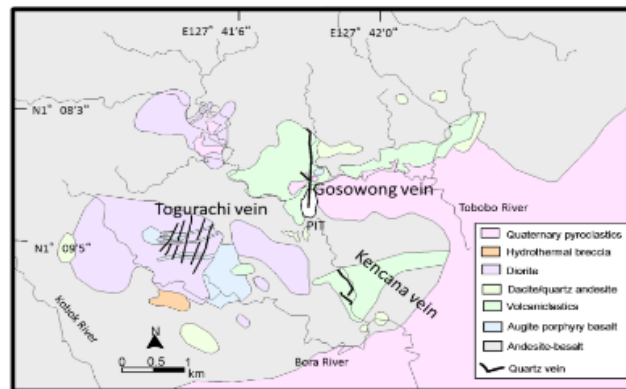


Figure 2. Local geology of the Gosowong district showing the principle vein systems of the respective epithermal deposits (Gosowong, Togurachi and Kencana).

3 Mineralisation

3.1 Kencana veining

There are three principle veins at Kencana; K1, K2 and K-LINK. The K1 vein system is exposed on the surface, but the main ore zone is located approximately 90m below the surface and the main focus of this study. The upper portion is composed of quartz-calcite, and high-grade ores present in the crustiform-colloform banding at 100-150m depth, with Au grades in excess of 1000g/t. Moderate to high-grades are encountered in the quartz-hematitic mudstone/volcanoclastics breccia at 150-200m depth. The K2 vein system is composed of quartz-calcite veins, breccia and stockworks. The K-Link system is largely brecciated with gingoro banding recognised as dismembered vein material in the breccia. Au grades of the deposit are extremely high, ranging from 5 to >1000g/t in the highest-grade zones. Mineral resources of the deposit are more than 2.2 Moz Au and 2.2 Moz Ag.

3.2 Ore mineralization

The K1 breccia system contains an early (Stage I) micro-crystalline quartz with chalcopyrite and electrum dissemination, with minor tellurides (hessite), this is followed by a later stage brecciation and resultant banded crustiform ore (Stage II), composed of; chalcopyrite, hessite, sylvanite, galena and sphalerite in order of abundance (Fig. 3). Analysis shows that there is a high Cd-composition in sphalerite and the extremely Cd-rich Zn sulfides recognised as zincian-greenockite.

3.3 Electrum

SEM-EDX measurements of electrum from Stages I and II show that broadly they have wide distribution from 15-44 At% Ag (Fig. 4). Stage-I electrum tends to exhibit higher Au compositions, with higher Ag compositions largely confined to Stage-II. The dominant trend for Ag composition from a suite of veins from K1, K2 and K-link ranges from 24 to 27 at%, indicative of extremely rich gold

grades.

This area hosts four subeconomic porphyries (Tabobo porphyry, Bora porphyry, Matat porphyry and Ngoali porphyry) and three main epithermal deposits (Gosowong deposit, Togurachi deposit and Kencana deposit).

K1 VEIN TEXTURE - SUB 12 AND 13

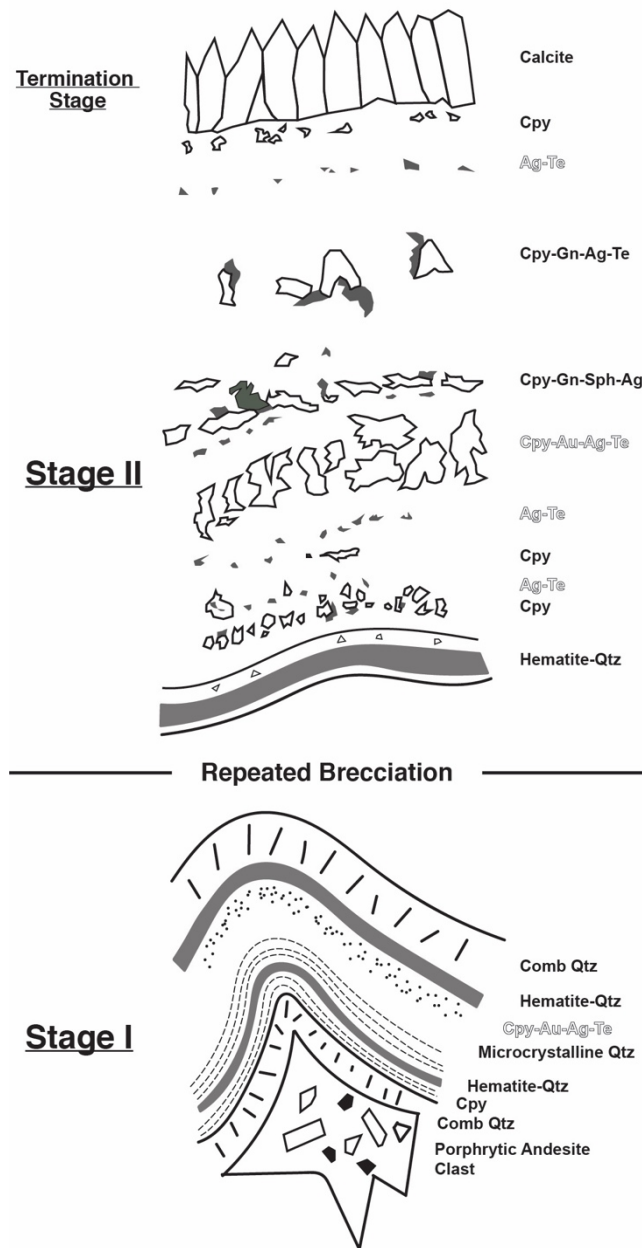


Figure 3. Brecciated vein textures and ore minerals of the K1 Sub 12 and Sub 13 ore drives. Abbreviations: Qtz – quartz, Cpy – chalcopyrite, Ag-Te – hessite, Cpy-Au-Ag-Te – (electrum, hessite, sylvanite, petzite, stuzite), Gn – galena, Sph – sphalerite (zincian Greenockite).

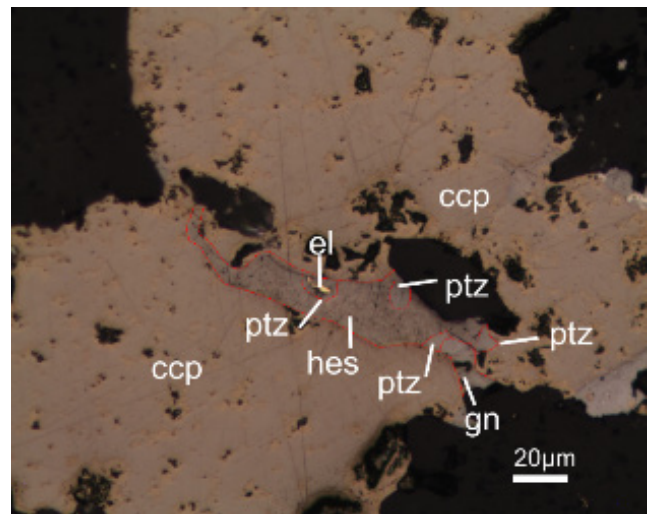


Figure 4. Representative microphotograph from K1 Sub 13, Stage-II mineralization (Cpy-Au-Ag-Te). Abbreviations: ccp – chalcopyrite, ptz – petzite, hes – hessite, gn – galena, el – electrum.

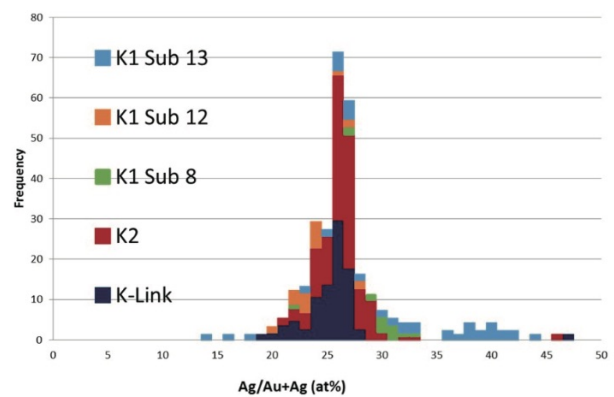


Figure 5. Ag ratio in electrum from the K1 vein and representative samples from the K2 and K-link vein systems. Results indicate that the electrum from Sub-12 and 13 have the widest range, with higher Au compositions largely attributed to Stage I and higher Ag composition largely confined to Stage II.

4 Short considerations

Although detailed geochemical mechanisms are yet to be established, general trends can be discerned from the available data. Preliminary microthermometry of the quartz gangue associated with Stage-II suggests a precipitation temperature of 200 to 250°C. Coupled with the precious metal compositions and related Au-Ag-Te minerals present, a higher temperature for Stage-I mineralization may be considered.

Acknowledgements

The authors thank all assistance from PT Nusa Halmahera mining for providing access and samples from the Gosowong goldfield.

References

- Gemmell BJ (2007) Hydrothermal alteration associated with the Gosowong epithermal Au-Ag deposit, Halmahera, Indonesia. *Econ Geol* 102:893-922.
- Hakim AS, Hall R (1991) Tertiary volcanic rocks from the Halmahera Arc, eastern Indonesia. *Journ Southeast Asian Earth Sci* 6:271-287.
- Hall R (1987) Plate boundary evolution in the Halmahera region, Indonesia. *Tectonophysics* 144:337-352.
- Hall R, Audley-Charles MG, Banner FT, Hidayat S, Tobing SL (1988) Basement rocks of the Halmahera region, eastern Indonesia: a late Cretaceous-early Tertiary arc and fore-arc. *Geol Soc* 145:65-84.
- Olberg D (2001) Ore shoot targeting in the Gosowong vein zone, Halmahera, Indonesia. MGeol thesis, 227.
- Steven M, Daud S (2011) Transient kinematic changes in epithermal systems: Toguraci deposit, Halmahera, unpublished
- Vansconcelos P (1998) $^{40}\text{Ar}/^{39}\text{Ar}$ analysis. Gosowong prospect area, Halmahera, PT Husa Halmahera Minerals, unpublished report.

The new discovered Tasikmadu porphyry copper-gold prospect in Watulimo sub-district, Southern Trenggalek, Java Island, Indonesia: characteristics and exploration challenges

Arifudin Idrus¹, Trifatama Rahmalia², Kresna Kustrianugroho¹

¹Department of Geological Engineering, Universitas Gadjah Mada, Yogyakarta, Indonesia

²Department of Geological Engineering, ITNY Yogyakarta, Indonesia

Abstract. This is a frontier study dealing with geology and key characteristics including hydrothermal alteration, quartz vein/veinlet system and ore mineralization of the new discovered Tasikmadu porphyry copper-gold prospect in the southern part of Trenggalek district, East Java province, Indonesia. Regionally, the studied area is a moderate undulating volcanoclastic terrain occupied by Mandalika formation (Tomm) intruded by a series of acidic to intermediate plutonic rocks (Tomi), which is dominated by dioritic intrusion (di). At least three intrusive diorite types are identified, i.e. fine-, medium- and coarse-grained diorite porphyries. NE-SW- and W-E- trending strike-slip faults might play an important role controlling the formation of the porphyry copper-gold prospect. Four hydrothermal alteration zones developed throughout the prospect including central potassic, proximal phyllic, distal propylitic and superimposed argillic alteration. Ore mineralization is characterized by high-density mineralized stockwork of quartz vein/veinlet system. Early A, center-line AB/B, transitional chalcopyritic C and late pyritic D vein/veinlet of a typical porphyry system are obviously observed. Chalcopyrite and pyrite are observed. Bornite, a typical high temperature copper sulfide in porphyry systems, is found as a minor phase. The Tasikmadu porphyry copper-gold prospect shares some similarities and few discrepancies of its key characteristics in comparison to other porphyry copper-gold deposits worldwide.

1 Introduction

Indonesian archipelago is controlled by the tectonic setting of the region, which is manifested by magmatic arcs from various ages from Late Mesozoic through the Cenozoic. Most of the hydrothermal mineralisation is derived from six major Neogene magmatic arcs including the Sunda-Banda, Aceh, Central Kalimantan, Sulawesi-East Minandau, Halmahera and Central Papuan fold and thrust belt (Carlile and Mitchell, 1994). The Sunda-Banda arc is the longest of the magmatic arcs in Indonesia. It extends nearly 4,000 km from northern Sumatra through Sumbawa (Sunda arc) and onwards through Flores to its terminus in the Banda Islands (Banda arc). Several porphyry copper-gold prospects in Java Island (Fig.1) were discovered along Sunda-Banda magmatic arc, for instance, Batu Hijau in Sumbawa (Idrus, 2007), Tumpang Pitu in East Java (Hellman, 2010; Maryono et al., 2012),

and Selogiri in Wonogiri (Imai et al., 2007). The study area, Tasikmadu is one of the porphyry copper-gold prospects situated in central segment of west-east trending Sunda Banda magmatic arc, which is administratively included East Java province of Indonesia. The prospect is a promising “new discovery” copper-gold mineralization in Java Island, which is proven by the occurrences of central potassic alteration in association with quartz vein/veinlet stockwork and an abundance of copper-bearing sulfides such as chalcopyrite, bornite, covellite, chalcocite and malachite. Detailed study of the prospect is still lacking. Therefore, this study is aimed to understand the deposit geology and some key characteristics of the deposit including hydrothermal alteration types and distribution, vein/veinlet system and ore mineralization. This would give a significant contribution for a better understanding of the deposit and future exploration strategy of the copper-gold mineralization in the region.

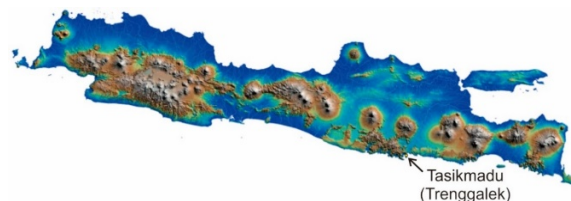


Figure 1. Research location (Tasikmadu prospect) plotted on the SRTM (Shuttle Radar Topography Mission) map of Java Island

2 Research methods

This study was conducted in four stages including literature, fieldwork, laboratory work, data processing and interpretation. Fieldwork includes mapping of surface geology, alteration and ore mineralization as well as sampling of representative rock types, altered rocks, quartz vein/veinlet stockwork and quartz vein in ore mineralization. Hydrothermal alteration mapping is focused on the type and distribution of the alteration halos from central potassic to proximal phyllic and distal propylitic types. Laboratory work includes vein textural and structural analysis, mineralogy (petrography, ore microscopy). A total of 22 samples were analysed at Department of Geological Engineering, Universitas Gadjah Mada.

3 Deposit geology

The studied area is categorized as a moderate undulating volcanoclastic terrain. The study area is underlain by a series of volcanic units, which from oldest to youngest are volcanic breccia, at least three phases of intrusive rocks mainly early fine-grained diorite, intermediate medium grained diorite and late coarse-grained diorite porphyries (Fig. 2). Those rock units are the members of Miocene Mandalika formation (Tomm). The youngest unit is a coastal deposit. The pre-mineralization rock unit i.e. volcanic breccia was intruded by the multiple series of diorite porphyries. The volcanic breccia is weakly altered to the distal propylitic domain. The causative mineralization intrusion is interpreted to be fine grained diorite porphyry, which is closely associated with quartz vein/veinlet stockwork occurrences. The fine grained diorite is spatially related to the distribution of central early potassic alteration, while the intermediate grained diorite is spatially associated with the occurrences of distal phyllic and early proximal propylitic alterations. Several structure patterns are recognized in the study area including NE-SW, N-S, NNW-SSE- and W-E-trending strike slip faults. However, NE-SW- and W-E- trending strike-slip faults are interpreted to be causative structure playing an important role controlling the formation of the porphyry copper-gold prospect.

4 Hydrothermal alteration

Four hydrothermal alteration zones developed throughout the prospect including central potassic, proximal phyllic, distal propylitic and superimposed argillic alteration (Fig. 3). Central potassic alteration is typified by fine-grained secondary biotite and magnetite. Phyllic alteration is typified by sericite-quartz-pyrite±chlorite, whereas propylitic alteration is characterized by chlorite+epidote+smectite±quartz, Argillic alteration is presented by illite-smectite-quartz-sericite-dickite±chlorite. Ore mineralization is closely associated with potassic alteration and high-dense quartz vein/veinlet stockwork. The potassic alteration is spatially and temporally distributed a whole of early fine-grained diorite porphyry. In comparison to other porphyry copper-gold deposits along Sunda-Banda magmatic arc such as Batu Hijau in Sumbawa, Selogiri in Wonogiri, Tasikmadu porphyry copper-gold shares similarity in alteration halos developed from central early potassic to distal phyllic and proximal propylitic which are superimposed by the late argillic alteration.

5 Vein/veinlet system and ore mineralization

Ore mineralization is characterized by high-density mineralized stockwork of quartz vein/veinlet system. Several typical quartz veins/veinlets in the porphyry systems such as early A, center-line AB/B, transitional chalcopiritic C and late pyritic D veins/veinlets are recognized and occurred throughout the prospect. The prospect area is centered on at least 1x1.5 km² of early potassic alteration, which is spatially (and potentially

coevally) associated with high-density mineralized vein/veinlet stockwork zone. Chalcopyrite and pyrite are ubiquitously observed. Bornite is present in the minor portion. Bornite is occasionally replaced by chalcopyrite in the rim and/or following cleavages forming lamellae texture. Microscopically Intergrown chalcocite and covellite replacing bornite are observed. Gold inclusion in copper-bearing sulphides. On the surface, the strongly mineralized host rock is clearly stained by colorful malachite, azurite and other supergene copper-bearing minerals.

6 Concluding remarks and implication for exploration

6.1 Concluding remarks

The Tasikmadu porphyry copper-gold prospect is centered on by multiple series of intrusive diorite porphyries. NE-SW- and W-E- trending strike-slip faults are interpreted to be causative structure playing an important role controlling the formation of the porphyry copper-gold prospect. Early fine-grained diorite porphyry is interpreted to be a causative mineralization intrusion. Early potassic, intermediate phyllic, early propylitic and late argillic alteration zones are well developed. Ore mineralization is closely associated with central potassic alteration and high-dense quartz vein/veinlet stockwork. The potassic alteration is spatially and temporally suffered the early fine-grained diorite porphyry, and associated with high abundances of copper bearing sulfides such as chalcopyrite, bornite, covellite, azurite, chalcocite and malachite.

6.2 Implication for exploration

Several porphyry copper-gold prospects were discovered along the mineralized Neogene Sunda-Banda magmatic arc, for instance, Batu Hijau in Sumbawa, Tumpang Pitu in East Java, and Selogiri in Wonogiri. The Tasikmadu is one of the best porphyry copper-gold prospects outcropping within central Java Island segment of the magmatic arc. The prospect is hosted by multiple series of intrusive diorite porphyries. Early fine-grained diorite porphyry is interpreted to be an intrusion that caused mineralisation. Early potassic, intermediate phyllic, early propylitic and late argillic alteration zones are centered on the fine-grained diorite porphyry stock. Thus, the Tasikmadu porphyry copper-gold meets the criteria of the Diorite porphyry model (after Hollister, 1978). The Tasikmadu prospect is a promising “new discovery” copper-gold mineralization in Java Island. Central early potassic alteration in association with quartz vein/veinlet stockwork and the abundances of copper bearing sulfides such as chalcopyrite, bornite, covellite, chalcocite and malachite is well exposed and preserved. The occurrence and discovery of the Tasikmadu porphyry copper-gold prospect may imply that other undiscovered porphyry copper-gold deposits along central to east segments of Java Island as a part of the mineralized Sunda-Banda magmatic arc may exist and could be discovered in the

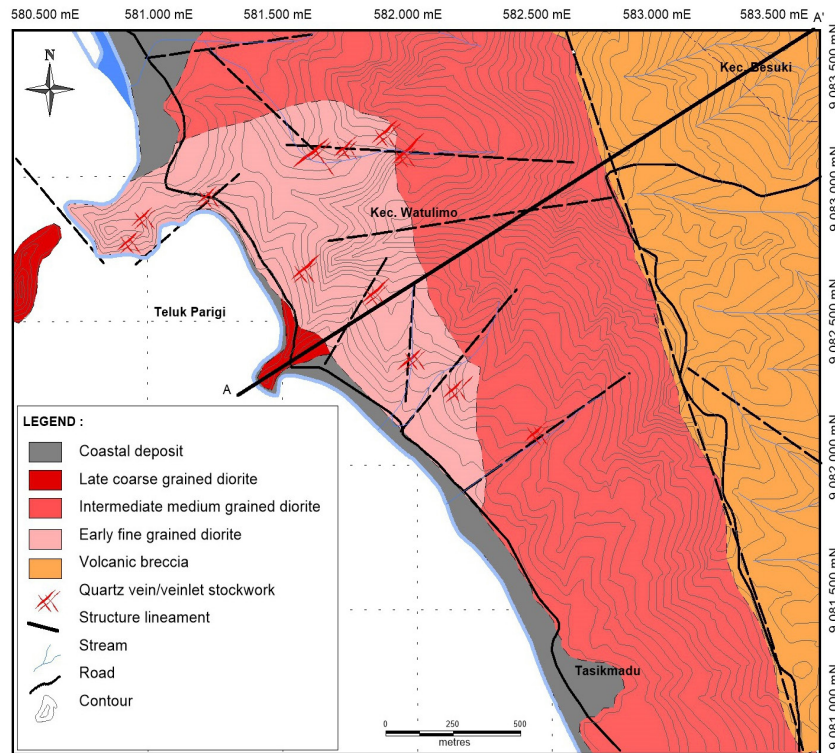


Figure 2 Geological map of the Tasikmadu porphyry copper-gold prospect, Trenggalek, Java Island

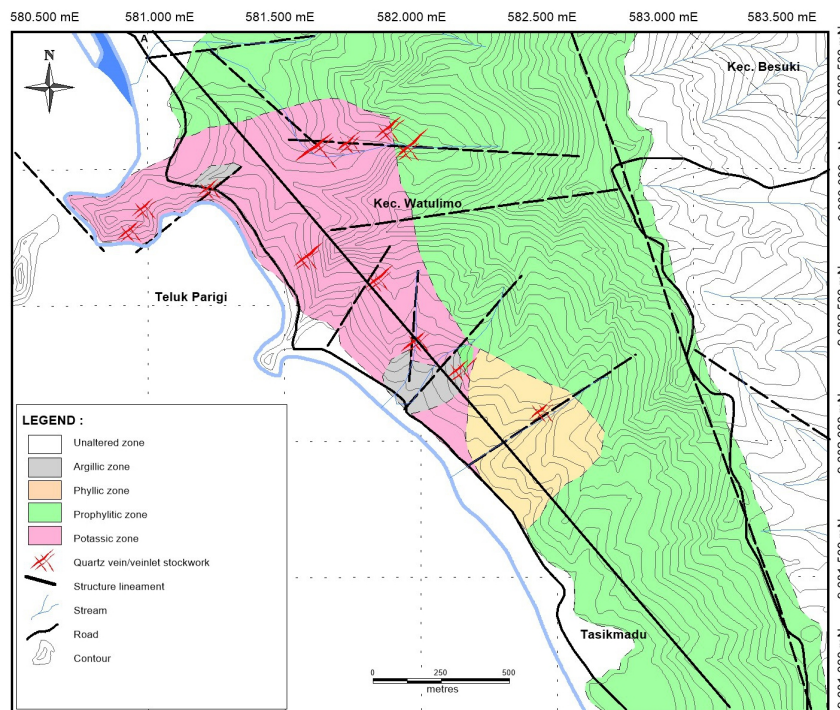


Figure 3 Hydrothermal alteration and mineralization map of the Tasikmadu porphyry copper-gold prospect, Trenggalek, Java Island.

future. Thus, it needs an effective and cost-benefit exploration model on the basis of the deposit genetic model.

Acknowledgements

Fieldwork and laboratory analyses funding was partly supported by PT. Erde Ressourcen and PT. Primata Batu Mulia. Therefore, we would like to express our sincere thanks and appreciation to the managements of both mining companies for their supports. We are also thankful to anonymous reviewer for the improvement of the manuscript.

References

- Carlile JC, Mitchell AHG (1994) Magmatic arcs and associated gold and copper mineralisation in Indonesia: in van Leeuwen TM, Hedenquist JW, James LP, Dow JAS (eds) Mineral Deposits of Indonesia, Discoveries of the Past 25 Years: Journal of Geochemical Exploration 50:91-142.
- Hellman, P.L., 2010. Tujuh Bukit Project Report on Mineral Resources, Located in East Java, Indonesia, Technical Report for Interpid Mines Limited.
- Hollister, V.F., 1978, Geology of the Porphyry Copper Deposits of Western Hemisphere. Am Inst Min Metall Pet Eng, 219 p.
- Idrus, A., Kolb, J. and Mayer, F.M. (2007) Chemical composition of rock-forming minerals in copper-gold-bearing tonalite porphyries at Batu Hijau deposit, Sumbawa Island, Indonesia: implication for crystallization condition and fluorine-chlorine fugacity. Resour.Geol., 57:102-113.
- Imai A, Shinomiya J, Soe MT, Setijadji LD, Watanabe K, Yoshikawa R, Warmada IW (2007) Porphyry-type mineralization at Selogiri area, Wonogiri regency, Central Java. Indonesia.
- Lubis, H., Prihatmoko, S., and James, L.P., 1994. Bulagidun prospect: a copper, gold and tourmaline bearing porphyry and breccia system in northern Sulawesi, Indonesia. Indonesian Mineral Deposit-Discoveries of the Past 25 Years, Journal Geochemical Exploration, 50:257-278
- Perello, J. A., 1994. Geology, Porphyry Cu-Au and Epithermal Cu-Au-Ag mineralization of the Tombulilato District, North Sulawesi, Indonesia. In: T.M. van Leeuwen, J.W. Hedenquist, L.P. James, and J.A.S. Dow (Editor), Indonesian Mineral Deposits-Discoveries of the Past 25 Years, J.Geochem. explor., 50:221-256.
- van Leeuwen, T.M. (1994) 25 Years of mineral exploration and discovery in Indonesia. J. Geochem. Explor., 50:13-90.

Contributions to the mineralogical and geochemical characterization of Fe-Sn-Zn-Cu-In skarn-type mineralization in the Schwarzenberg mining district, Germany

Malte Stoltnow

TU Bergakademie Freiberg, Institute of Mineralogy, Germany
 Deutsches GeoForschungsZentrum GFZ, Germany
 University of Potsdam, Inst. of Earth and Env. Science, Germany

Thomas Seifert, Tilman J. Jeske, Sabine Gilbricht

TU Bergakademie Freiberg, Institute of Mineralogy, Germany

Joachim Krause

Helmholtz Institute Freiberg for Resource Technology (HIF), Germany

Abstract. The Schwarzenberg mining district in the western Erzgebirge hosts numerous skarn-hosted tin-polymetallic deposits, such as Breitenbrunn. The St. Christoph mine is located in the Breitenbrunn deposit and is the locus typicus of christophite, an iron-rich sphalerite variety, which can be associated with indium enrichment. This study presents a revision of the paragenetic scheme, a contribution to the indium behavior and potential, and discussion on the origin of the sulfur. This was achieved through reflected light microscopy, SEM-based MLA, EPMA, and bulk mineral sulfur isotope analysis on 37 sulfide-rich skarn samples from a mineral collection. The paragenetic scheme includes: a pre-mineralization stage of anhydrous calc-silicates and hydrous minerals; an oxide stage, dominated by magnetite; a sulfide stage of predominantly sphalerite, minor pyrite, chalcopyrite, arsenopyrite, and galena. Some sphalerite samples present elevated indium contents of up to 0.44 wt%. Elevated iron contents (4-10 wt%) in sphalerite can be tentatively linked to increased indium incorporation, but further analyses are required. Analyzed sulfides exhibit homogeneous $\delta^{34}\text{S}$ values (-1 to +2 ‰ VCDT), assumed to be post-magmatic. They correlate with other Fe-Sn-Zn-Cu-In skarn deposits in the western Erzgebirge, and Permian vein-hosted associations throughout the Erzgebirge region.

1 Introduction

Situated in the western Erzgebirge, the Schwarzenberg mining district (Fig. 1) is well-known for both historic mining and being a target of active exploration of skarn-hosted Sn-polymetallic deposits. In addition to the promising Hämmerlein-Tellerhäuser and Pöhla-Globenstein deposits, the district also hosts the less investigated Breitenbrunn and Antonsthal deposits. The St. Christoph mine is located in the Breitenbrunn deposit and is the locus typicus of the iron-rich sphalerite variety christophite. Christophite has been shown to be associated with indium enrichment (Leutwein 1943). This study presents a revision of the paragenetic scheme, a contribution to the indium behavior and potential, and

discussion on the origin of the sulfur.

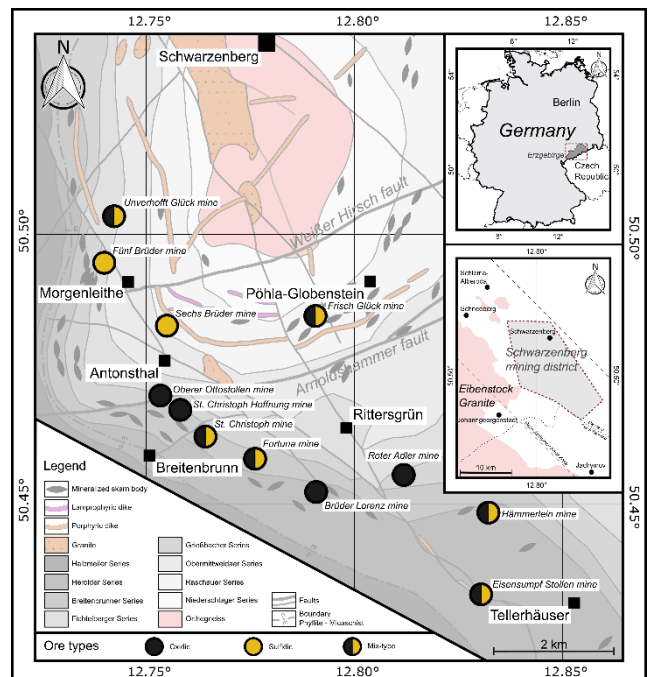


Figure 1. Simplified geological and tectonic map of the Schwarzenberg mining district, showing the occurrence of different classified mineralization types; modified after Baumann et al. (2000).

2 Geological setting

The Schwarzenberg mining district is located east of the Eibenstock granite massif and along the Schwarzenberg gneiss cupola, which is situated in the central part of the Gera-Jáchymov Zone, a large-scale transregional deep reaching lineament (Fig. 1).

The Schwarzenberger augengneiss is surrounded by a concentric complex of Cambrian metasedimentary rocks which comprise gneisses, schists, metacarbonates, metagreywackes, quartzites, metavolcanics, and phyllites. These units are transversed by major, ENE-WSE-trending (i.e. Weißer Hirsch and Arnoldshammer

faults) and minor, NW-SE-trending faults (Fig. 1).

Intrusions of the Schwarzenberg mining district comprise late-collisional granites and post-collisional porphyric and lamprophyric dikes (Fig. 1).

The district is host to numerous mineralized skarn bodies, which are arranged in a circle around the Schwarzenberg augengneiss and hosted by the Cambrian metasediments (Fig. 1). Baumann et al. (2000) subdivided the skarn bodies according to the spatial distribution of their mineralization style, into northern and southern zones of the cupola. The northern zone of the cupola (north of the Weißer Hirsch fault) is dominated by sulfide ores, whereas the southern zone (south of the Weißer Hirsch fault) is dominated by oxidic ores, or mixed sulfidic-oxidic type ores (Fig. 1).

3 Methods

For this study, a total of 37 sulfide-rich skarn samples were taken from the ore deposit collection (Lagerstättensammlung - LaSa) at the Institute of Mineralogy, TU Bergakademie Freiberg. Preparation steps comprised 25 mm embeddings and sulfide mineral concentrates. Methods conducted on the samples include reflected light microscopy, secondary electron microscopy (SEM)-based mineral liberation analysis (MLA lab TUBAF), electron probe microanalysis (EPMA lab HIF), and analysis of the mineral sulfur isotopic composition (stable isotope lab WWU Münster) and bulk sphalerite geochemistry (n=5) by ICP-MS (Actlabs).

4 Results

4.1 Paragenetic scheme

The revised paragenetic scheme (Fig. 2) is predominantly based on observations from this study, with integration of the observations of Wolf (1995) and Hösel et al. (2003) from studies on the sub-district Pöhla-Globenstein. The classified stages include a pre-mineralization stage and a mineralization stage.

4.1.1 Pre-mineralization stage

Early skarn minerals comprise anhydrous (i.e. pyroxene and early garnet; Fig. 3-D), in addition to hydrous minerals (e.g. epidote). Pyroxene, early garnet, and epidote never replace ore minerals. This stage is barren of oxidic and sulfidic mineral phases.

4.1.2 Mineralization stage

The mineralization stage describes a timespan where oxidic and sulfidic mineralization occurs, accompanied by less abundant arsenides and native metals, and is subdivided into an oxide and a sulfide stage.

4.1.3 Oxide stage

Early subhedral amphibole (Fig. 3F) and magnetite (Fig. 3A, B, D) are the dominant mineral phases of the

oxide stage. Both replace early skarn minerals and are replaced by oxide stage cassiterite (Fig. 3F) and later sulfides. Hematite occurs in form of martite in some cases, which is not replaced by later ore minerals.

4.1.4 Sulfide stage

Early pyrite, löllingite, sphalerite, chalcopyrite, and early arsenopyrite are roughly coincident. Chalcopyrite 1 (Fig. 3-C) is present as chalcopyrite disease in sphalerite. Patchy chalcopyrite 2 (Fig. 3-C, -E) can be differentiated from chalcopyrite 1 only by shape, as no age relationships are obvious. Pyrite 2, in most cases, forms laminated bird's eye aggregates with marcasite.

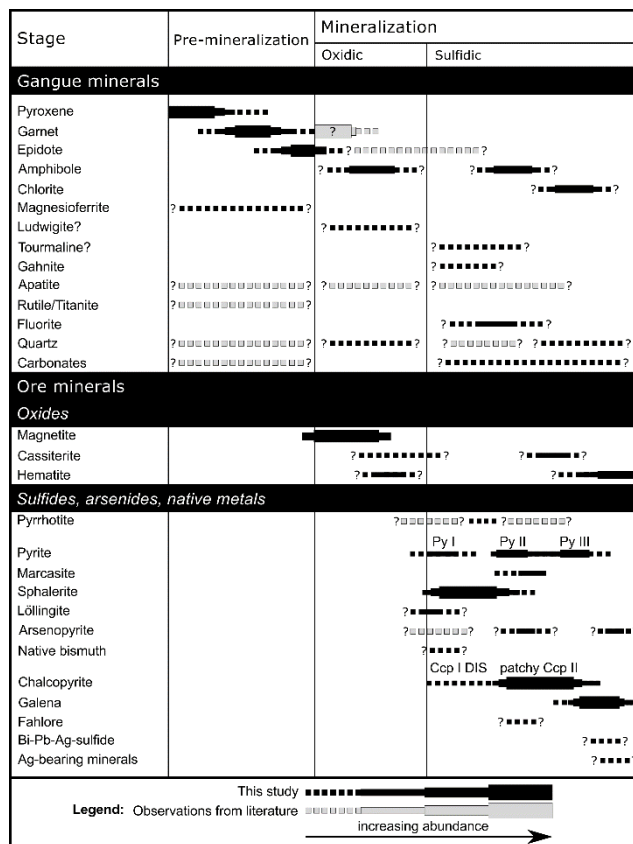


Figure 2. Paragenetic scheme of the Schwarzenberg mining district. The sequences are predominantly based on petrographic observations carried out during this study. Literature data (grey bars) from: Wolf (1995) and Hösel et al. (2003).

The late phase of the sulfide stage is characterized by the emplacement of fibrous chlorite which transverses, fractures, and intensely marginally corrodes earlier mineral phases. Late pyrite 3 (coarse euhedral, sieve-like blasts) and galena are roughly coincident with the chlorite and replace earlier sphalerite. Late cassiterite can be found as round crystals, related to late veinlets, as well as in the form of thin fringes around patchy chalcopyrite 2. Subsequently, pyrite 3 is surrounded by thin fringes of the youngest arsenopyrite.

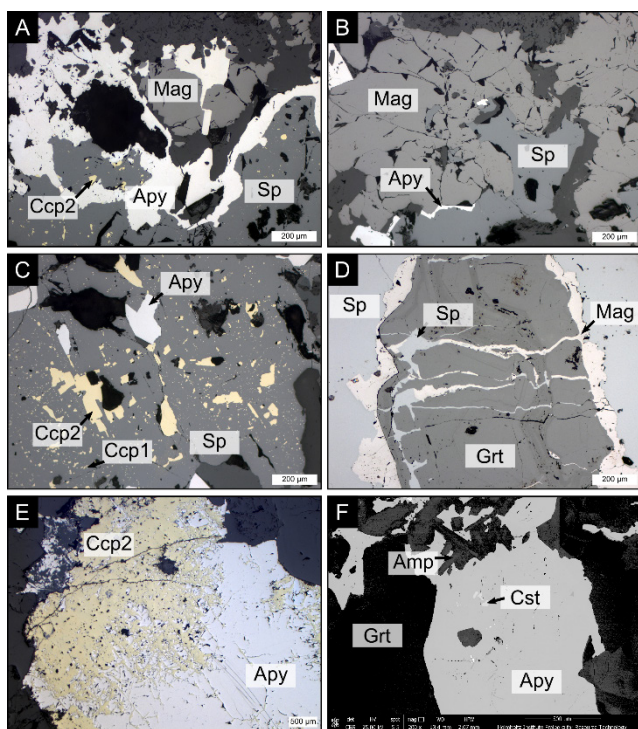


Figure 3. Photomicrographs and BSE images of the samples 64782 (St. Christoph mine, A, B, C), 65551 (Fortuna mine, D), 65600 (Oberer Ottostollen mine, E, F): A: Magnetite replaced by sphalerite; minor arsenopyrite is present; B: Magnetite and sphalerite replaced by arsenopyrite; minor chalcopyrite is present; C: Sphalerite replaced by arsenopyrite and chalcopyrite; D: Garnet replaced by magnetite and sphalerite; E: Arsenopyrite replaced by chalcopyrite; F: Cassiterite relicts in arsenopyrite; garnet and subhedral amphibole are also present; consider color code.

4.2 Sphalerite geochemistry

Indium is present in minor abundances (Fig. 4A), with three of twelve samples, 64782 (0.20-0.30 wt%, average = 0.27 wt%, $n = 10$), 65551 (0.02 wt%, $n = 11$), and 65600 (0.23-0.44 wt%, average = 0.36 wt%, $n = 11$) showing elevated indium contents.

Zn and Fe have a strong negative correlation (Fig. 4B). The overall range shows Zn values from 49.3 to 64.4 wt% with a mean value of 57.3 wt% (12 samples, $n = 272$ analyses) and Fe values from 1.5 to 15.6 wt%, with a mean value of 8 wt% (12 samples, $n = 272$ analyses). Bulk sphalerite ICP-MS analyses ($n = 5$) revealed concentrations of In 101-195 ppm, average 154 ppm, Cu with <0.05-1.55 wt%, average 0.66 wt%, and Fe 6.36-16.70 wt%, average 13.7 wt%.

According to the In content, samples can be divided into three groups. The first group comprises the samples with low Fe contents (0-4 wt%) and no detectable In, the second group with intermediate Fe contents (4-10 wt%) and partly detectable In, and the third group with high Fe contents (10-16 wt%) and no detectable In.

4.3 Sulfide sulfur isotopic compositions

Sulfur isotope compositions of sulfide minerals (sphalerite, chalcopyrite, and arsenopyrite) from 21 samples are shown in Fig. 5. They show $\delta^{34}\text{S}$ values

between -0.9 and 2.0 ‰ VCDT.

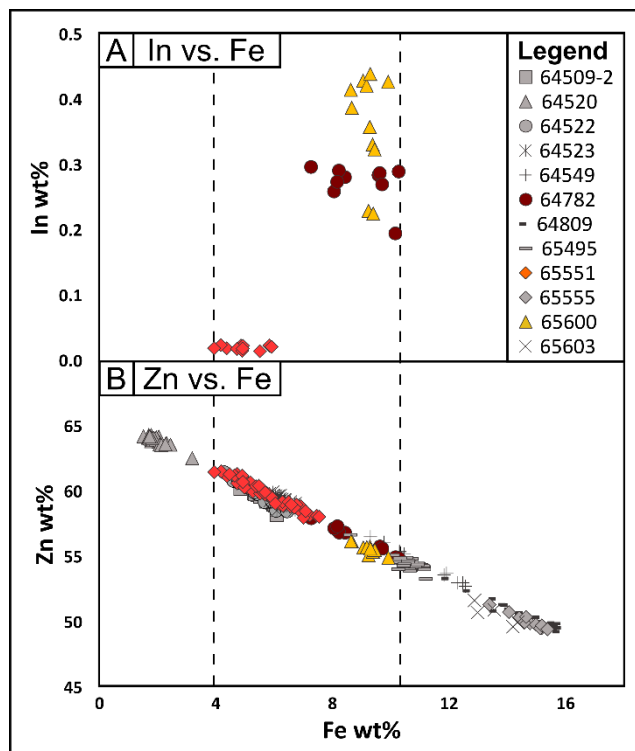


Figure 4. Binary plots of In, Fe, and Zn compositions in sphalerite (Schwarzenberg mining district; EPMA data); A: In vs. Fe; B: Zn vs. Fe; 3 of 12 analyzed samples (64782, 65551, and 65600 from the Breitenbrunn and Antonsthal deposits) with Fe contents between 4 and 10 wt% have elevated In contents.

The $\delta^{34}\text{S}_{\text{VCDT}}$ median is 0.8 ‰ and the average is 0.7 ‰ ($n = 21$). First quartile plots at 0.4 ‰ and the third quartile at $\delta^{34}\text{S}_{\text{VCDT}}$ 1.1 ‰. Therefore, with no large overall variation, the average measured $\delta^{34}\text{S}_{\text{VCDT}}$ composition is 0.7 ‰.

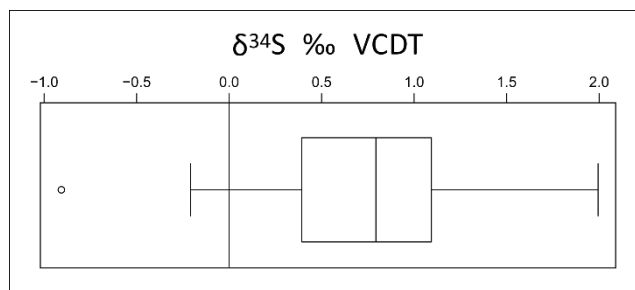


Figure 5. Boxplot with corrected sulfur isotope compositions of 21 sulfide mineral separates (EA-IRMS data; sphalerite, chalcopyrite and arsenopyrite) from the Schwarzenberg mining district; whiskers (-0.2 to +2.0 ‰ VCDT), minimum/outlier (-0.9 ‰ VCDT), box (+0.4 to +1.1 ‰ VCDT) and median (+0.8 ‰ VCDT) are shown.

5 Discussion

5.1 Indium behavior and potential

Three of twelve samples analyzed with EPMA confirmed the occurrence of elevated indium contents of the Breitenbrunn deposit, with up to 0.44 wt% In in sphalerite. However, the lack of detectable In in many samples

implies a heterogeneous In distribution in the ore bodies. Elevated Fe contents (>4 wt%) were tentatively linked with the incorporation of indium in sphalerite, but further analyses are required for confirmation. This also applies to the observation of indium concentrations below detection limit in samples with markedly high iron contents (>10 wt%).

5.2 Origin of the mineralizing fluids

Based on their petrographic observations, Wolf (1995) and Hösel (2003) distinguished several stages in the formation of mineralized ore bodies in this area, fitting to the genetic skarn formation model of Einaudi et al. (1981). This includes the early stage of sedimentation, a stage of regional metamorphic hornfels-skarnoid formation, a stage of contact metamorphic-prograde skarn mineral formation, a greisen stage, and a late stage related to a hydrothermal overprint of the skarns. Compared to observations made in this study, our identified stages include a pre-mineralization stage which is assumed to coincide with the prograde skarn-forming stages, and a mineralization stage. The latter presumably coincides with the greisen- and retrograde stages, or might represent a stage involving mineralizing fluids which are independent of the skarn development (Jeske and Seifert 2017). In the latter case, fertile fluids caused mineralization of the skarn bodies, which acted solely as geochemical barriers.

This is supported by the homogeneous sulfur isotopic composition (Fig. 6). The homogeneity of the values is confirmed by analyses of sulfides from the Hämmerlein Sn-Skarn deposit (Jeske and Seifert 2018) which is also situated in the study area. Late and postcollisional Li-F small intrusion granites and rhyolitic (Seifert and Kempe 1994) and lamprophyric dikes (Seifert 2008), could act as possible rare metal and sulfur sources.

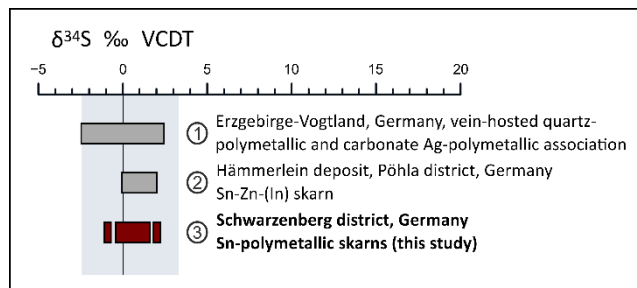


Figure 6. Comparison of sulfur isotopic compositions of sulfides from different skarn deposit and vein mineralization types; 1: Rösler et al. (1966), Seifert et al. (1992), Seifert (1994), Herrmann et al. (1995), Seifert (1995), and Bauer et al. (2018); 2: Jeske and Seifert (2018); 3: This study.

Acknowledgements

For the sample selection and documentation in the LaSa our sincere gratitude goes to C. Kehrer and B. Fritzke (both TUBAF). Furthermore, we are grateful for the high-quality sample preparation at the HIF ore lab. Finally, we would like to thank the TU Bergakademie Freiberg and the Federal Ministry of Education and Research (BMBF)

for promoting this thesis, through the “ResErVar” project, which is part of the “r4” funding program of Germany.

References

- Bauer ME, Burisch M, Ostendorf J, Krause J, Frenzel M, Seifert T, Gutzmer J (2018) Trace element geochemistry of sphalerite in contrasting hydrothermal fluid systems of the Freiberg district, Germany: insights from LA-ICP-MS analysis, near-infrared light microthermometry of sphalerite-hosted fluid inclusions and sulfur isotope geochemistry. *Miner Deposita* 54 (2):237–262
- Baumann L, Kuschka E, Seifert T (2000) Lagerstätten des Erzgebirges. Enke im Thieme-Verlag, Stuttgart
- Einaudi MT, Meinert LD, Newberry RJ (1981) Skarn deposits. *Econ Geol* 75th Anniversary Volume 75:317–391
- Herrmann S, Seifert T, Baumann L (1995) Zur Ausbildung von spätvariszischen Quarz-Polymetall-Mineralisationen im Lagerstättenrevier Schneeberg. *ZGW* 23:573–580
- Hösel, G., Büder, W., Fritsch, E., Schuppan, W., 2003. Die polymetallische Skarnlagerstätte Pöhla-Globenstein - Bergbaumonographie. Sächsisches Landesamt für Umwelt und Geologie Oberbergamt Sachsen, 'Bergbau in Sachsen' 8:143.
- Jeske TJ, Seifert, T (2017) Late-Variscan Sn-polymetallic overprinting of the Pöhla-Hämmerlein skarn zone, Erzgebirge, Germany. *Goldschmidt conference 2017, Paris*, p 1877
- Jeske TJ, Seifert T (2018) Sulfur isotopic composition of sulfides from the Hämmerlein deposit, Pöhla district, Germany. Project report – unpublished, TU Bergakademie Freiberg
- Leutwein F (1943) Vorkommen und Gewinnung von Indium. Forschungslaboratorium des Bergreviers Freiberg (Sächsisches Staatsarchiv, Bergarchiv Freiberg, 40030 Oberbergamt (neu) - staatliche Lagerstättenforschungsstelle, Nr. 1–0261), Freiberg, Germany
- Rösler HJ, Pilot J, Gebhardt R (1966) Schwefelisotopen-Untersuchungen an Magmatiten und postmagmatischen Lagerstätten des Erzgebirges und Thüringens. In: *Bergakademie* 18:266–273
- Seifert T (1994) Zur Metallogenie des Lagerstättendistriktes Marienberg (Osteil des Mittelerzgebirgischen Antiklinalbereiches). Dissertation, TU Bergakademie Freiberg
- Seifert T (1995) Zur metallogenetischen Charakteristik postpermischer Gangmineralisationen im Lagerstättendistrikt Marienberg-Lauta-Pobershau-Wolkenstein. (Zentralteil des sächsischen Erzgebirges). *Freiberger Forschungshefte* C460:136–162
- Seifert T (2008) Metallogeny and Petrogenesis of Lamprophyres in the Mid-European Variscides: Post-collisional Magmatism and its Relationship to Late-Variscan Ore Forming Processes in the Erzgebirge (Bohemian Massif). IOS Press, Amsterdam
- Seifert T, Baumann L, Jung D (1992) On the Problem of the Relationship Between Sn(-W) and Quartz-Polymetal Mineralizations in the Marienberg Deposit District. *ZGW* 20:371
- Seifert T, Kempe U (1994) Zinn-Wolfram-Lagerstätten und spätvariszische Magmatite des Erzgebirges. *Beih Eur J Mineral* 6 (2):125–172
- Wolf M (1995) Gesetzmäßigkeiten der Verbreitung und Erscheinung von Zinn- und Wolfram-Mineralisationen auf der Komplexlagerstätte Pöhla. *ZGW* 23 (5/6):609–618

Transition from porphyry to epithermal Cu-Au environments in Sardinia – Italy

Sandro Fadda, Maddalena Fiori, Carlo Matzuzzi

National Research Council

Institute of Environmental Geology and Geoengineering, Italy

Abstract. In Sardinia acidic fluids form argillic alteration halos and/or silicic lithocaps over Tertiary porphyry systems which may host subsequent mineralization. The spatial, geochemical and geophysical evidence suggests that the two systems may be genetically related and may help to determine the transition of a magmatic hydrothermal system from porphyry to epithermal environments. Tetrahedrite-tennantite series minerals occur extensively in hydrothermal deposits although in minor quantity as compared with other sulfides. At Furtei Au deposit available chemical data of these minerals and of the telluride-rich parts of drillcore samples, indicate direct magmatic inputs to the mineralizing solutions thus a transition of this system from porphyry to epithermal environments is envisaged and the relationship between mineral assemblages and sulfidation states may be assessed as well as evolution of ore solutions outlined. The Tertiary bodies occurring in the Siliqua sector display alteration and mineralisation patterns which can be referred to as a porphyry copper system consistent with a diorite model with the presence of epithermal silicapyrite alteration. Field observations and time and space relationships seem to suggest development of porphyry-style veining followed by several epithermal stage mineralised breccias which may be related to the adjacently outcropping porphyry system or telescoped to the periphery of some other stocks still buried at depth.

1 Introduction

Epithermal precious metal deposits may be distinguished in high-, intermediate- and low-sulfidation deposits based on the sulfidation state of their primary sulfide assemblage. A link between porphyry and epithermal mineralization is inferred especially in high-sulfidation (HS) systems where a single hydrothermal system, evolving over space and time would be responsible for forming the porphyry and HS ore body. The porphyry fluid may be related directly to the mineralization of the spatially associated epithermal system at proximal to distal positions relative to the quartz diorite dikes, with a continuum of mineralization styles associated with an evolving and migrating hydrothermal fluid. In a vertically zoned system, the epithermal top may have been eroded and/or the porphyry intrusive source is too deep to access. Te-bearing minerals and sulfosalts, as well as their mutual relationships in epithermal precious metal systems, offer potential for deciphering changes in temperature and sulfidation state (Cook and Ciobanu 2002). Their deposition is traditionally restricted to one or two stages that always follows initial sulfide deposition.

The Te-rich paragenetic assemblages may be examined to investigate the spatial variation in tetrahedrite chemistry (Wu and Peterson 1977) and sulfidation states in the evolving hydrothermal column from plutonic to epithermal zones.

2 The Furtei epithermal Au deposit

The Furtei Au deposit is the only example of HS mineralization in Sardinia (Fig.1). It is typically acid-sulfate in style (Fiori et al. 2001).

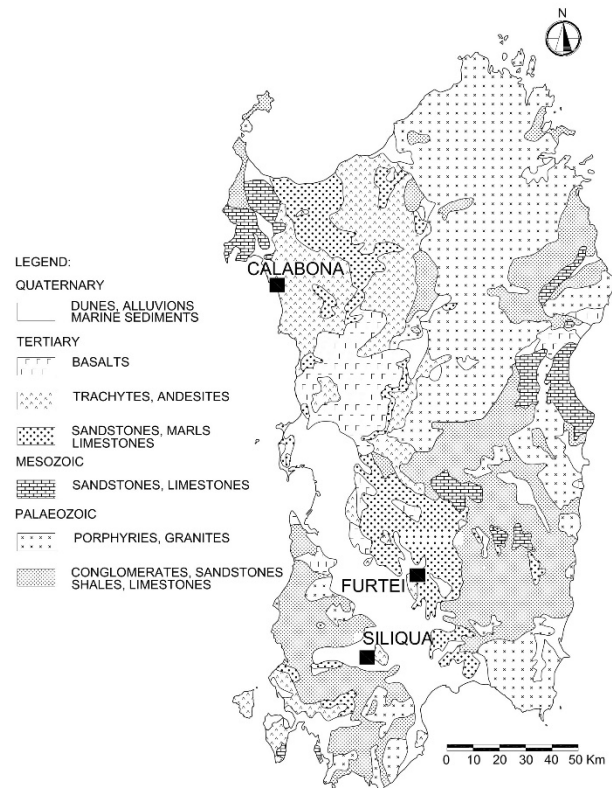


Figure 1. Geological map of Sardinia with the sites under study.

Under the surficial oxidized zone of supergene nature, the primary sulfide zone is largely hosted by diatreme breccia and characterized by a vertical zoning of the mineral assemblage, dominated by pyrite-energite-luzonite-gold at higher levels, whereas in the deep zone tetrahedrite, minor base metal sulfides and Te-rich minerals are present, especially in the deeper parts of the orebodies. Gold mostly occurs as high-fineness native metal and within some tellurides. A quantitative approach

to the study of hydrothermal zoning was pursued by systematic, detailed microanalytical and high-magnification investigations of the telluride-rich samples and sulfosalts from different parts of the ore-bodies of the mine. Several samples were selected from drill cores from economic and non-economic parts of the mine to establish the continuity of the zones and the spatial association among the deposits. The lateral distribution of minerals allows for the exposure of a cross-section of the mineralised column, at the present level of erosion, from porphyry to peripheral veins having epithermal characteristics. Samples for analysis were selected from open pits and drill cores chosen to represent the stages of ore formation over the vertical and lateral extent of the mine.

Table 1 shows the three main ore mineral assemblages in the deposit.

Table 1. Mineral assemblages in the Furtei deposit.

	Mineral assemblages
Oxidized surface (shallow)	Jarosite (with native Au max 1-2% Ag), gypsum, Fe-Mn-hydroxides, digenite, covellite, scorodite.
Sulfide (shallow)	enargite-luzonite, pyrite, chalcopyrite, sphalerite, covellite, digenite, galena, arsenopyrite, native Au (max 1-2% Ag), bornite in enargite.
Sulfide (deep)	Tennantite-tetrahedrite, Te-bearing tetrahedrite up to goldfieldite, pyrite, calaverite, krennerite, coloradoite, native Te, enargite, aikinite, native Au (max. content 6% Ag), chalcopyrite, stannite and native tin in enargite-luzonite.

The As-sulfosalt assemblage grades into the telluride assemblage with increasing depth. In the deeper parts of the system the paragenesis evolves into a Te- and Sb-rich assemblage with the presence of increasing tetrahedrite and Te-rich tetrahedrite up to goldfieldite, calaverite and krennerite, sometimes associated with native Te. Native Au in drillcore samples always appears as blebs within enargite. It is ubiquitous and fairly pure, with a maximum Ag content around 6%. Minerals of the tetrahedrite series, ranging from tetrahedrite, $Cu_{12}Sb_4S_{13}$, to tennantite, $Cu_{12}As_4S_{13}$, occur in minor amounts in all ore types often including gold and tellurium phases such as native tellurium and tellurides. Other varieties are due to substitutions of Te for (Sb, As). However the most abundant and ubiquitous ore minerals are enargite and luzonite, pyrite sphalerite and arsenopyrite are also of importance. Chalcopyrite can be fairly common in places, but is always present in the upper levels with covellite and sulfosalts. Tetrahedrite commonly appears as veinlets and swarms disseminated in chalcopyrite, or occurs as interstitial grains with the other sulfides or fills the interstices of pyrite and chalcopyrite; some tetrahedrite grains grew in the holes of porous vuggy silica.

Geophysical evidence for the presence of a relatively shallow intrusion at 1 to 1.5 km present depth is reported by Meloni (1994). Volumes of high temperature fluids may have been rapidly flushed upwards from the already emplaced porphyry into a ready network of fractures, breccias and channel ways. Fluid inclusion data (Ruggieri

et al. 1997) are similar to those found in many porphyry Cu deposits, including Calabona (Fig.1) where a minerographic study on ore samples included petrographic and fluid inclusion studies to characterize alteration, mineralization, and fluid phase circulation in the dacite porphyry system. The alteration pattern and assemblages at Calabona reflect the style shown by several studies on porphyry copper deposits and three major generations of mineralizations were distinguished: early, intermediate, and late (Frezzotti et al. 1992). Fluids associated with late stages of hydrothermal circulation have significantly lower salinities and are characterized by a progressive cooling (500°- 90°C) and dilution throughout the shallow and peripheral zones of the intrusions and with late quartz-pyrite veins. These fluids are interpreted to be responsible for the argillic alteration, which was possibly facilitated by the extensive fracturing and influx of meteoric water. The similarity of the fluid inclusion data from the Calabona deposit suggests that epithermal mineralization at Furtei may be associated with a porphyry system with a fluid of magmatic derivation circulating at deeper level followed by the mixing of the high-temperature magmatic hypersaline brine with cooler low-salinity meteoric water at shallow depth. The epithermal mineralization of Furtei can be divided into two stages postdating the silicic, and much of the advanced argillic alteration and was characterized by a distinct zoning with depth: the HS-state sulfosalts, enargite and luzonite are the principal Cu minerals in the orebody and occur at a shallow level, with abundant euhedral pyrite and gold. At depth tennantite-tetrahedrite, chalcopyrite, stannite, Au, Ag-tellurides including coloradoite, petzite, hessite are present. Ruggieri et al. (1997) estimated fS_2 and fTe_2 for the formation of Is Concas sector deep mineral assemblages in the Furtei site. The construction of fS_2 - fTe_2 diagrams at 100°C and 300°C (Afifi et al. 1988b) has shown that the topologies of these diagrams are essentially constant with changing temperature making these diagrams useful for comparison of telluride assemblages in low-temperature (<350°C) hydrothermal deposits.

The commonly observed dominant telluride mineral assemblages stable at the deep levels of Furtei ore bodies allows a narrow domain to be constrained in fTe_2 - fS_2 space (Fig. 2). Deposition of sulfide-gold mineralization at shallow depth occurred under comparatively high fS_2 , whereas deep assemblages were characterized by lower fS_2 . Gold mineralization is associated with tennantite and chalcopyrite which partially replaces enargite; luzonite appearing paragenetically later. Because Te solubilities are predicted to be low in auriferous chloride waters (Cooke et al. 2001), deposition of tellurides and native tellurium in intermediate-/low-sulfidation (IS/LS) environments may result from condensation of magmatically-derived $H_2Te(g)$ and $Te_2(g)$ into deep-level chloride waters.

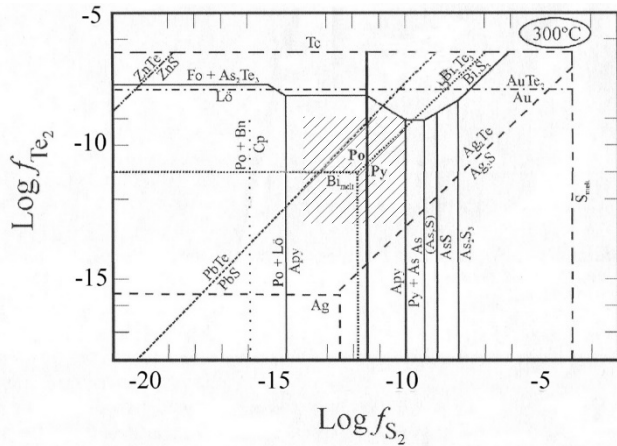


Figure 2. Telluride-sulfide stability diagram at 300°C in f_{Te_2} - f_{S_2} space, after Afifi et al. (1988b). The shaded domain corresponds to the mineral assemblages of Is Cocas sector, Furtei mine.

Such magmatic input into the hydrothermal system is later than the input of sulfur, since telluride deposition is always preceded by that of sulfides. The fugacity of Te_2 is very important and is controlled by the supply of this element from the source, and also locally controlled by reactions between the fluid and rock minerals or changes in fluid chemistry. Whether gold occurs in the native form, in petzite or in sylvanite is influenced by variations of this parameter. The relative stabilities of hessite and calaverite depend on the initial tellurium concentration and Ag: Au ratio in the water. However, minor amounts of Te can dissolve into chloride waters and could precipitate into lower temperature surficial acid sulfate waters by cooling or fluid mixing producing geochemical anomalies only or Te-rich mineralizations. Study of the mineral assemblages in the Furtei ore bodies demonstrates that introduction of gold in HS ores is related to IS assemblages, indicating an evolution from an IS towards HS environment. This implies that HS-style epithermal mineral assemblages may be precipitated from Au-bearing LS/IS waters with a distinct vertical zonation of electrum and Te-bearing species. In fact, the deeper part of the ore is characterized by tetrahedrites, Te-rich minerals, including precious metal tellurides, Te-tetrahedrite and native tellurium evolving in shallow level to enargite-luzonite, Cu-Fe-sulfides and native gold. The ore minerals also indicate that a part of gold introduction (in native form and in sulfosalts) has taken place contemporaneously with deposition of the HS assemblage, thus suggesting a genetic link between the two sulfidation states in the same ore deposition environment. There is a strong suggestion that the magmatic-hydrothermal system at Furtei underwent an evolution from an earlier IS porphyry-style mineralization, to IS-HS mineralizations in porphyry related, base-metal and epithermal precious-metal veins. Tellurium was introduced by both HS and IS solutions in a succession of phases of progressively lower Te content until the establishment of the observed paragenesis. The initial increase in f_{Te_2} from the magmatic source led to saturation, with the appearance of native Te and di-

tellurides (sylvanite, calaverite, krennerite), followed in turn by altaite, coloradoite, hessite, petzite and finally gold with gradual decreasing f_{Te_2} values. Condensation of Te-bearing magmatic volatiles may be essential for the formation of Te-rich mineral assemblages at depth, thus consuming the major part of the initial available tellurium. For aqueous tellurium species, cooling and mixing of fluids are predicted to be an effective, temperature dependent depositional mechanism. During multistage boiling, sufficient tellurium may be transported in the gas phase through the epithermal environment up to the shallow zones where it could condense back into groundwater leading to the observed vertical zonation from goldfieldite at depth to Te-free tetrahedrites in the outer zones. This chemical zonation suggests a component of vertical migration for the mineralising fluids progressing away from the pluton which seems to have acted not only as a heat source but provided material input. The relationship between the proportion of Te and (Sb+As) in tetrahedrite-goldfieldite from deep to shallow level ore bodies of the Furtei mine verifies the substitution of (Sb+As) by tellurium until the end-member goldfieldite is reached (Fig. 3).

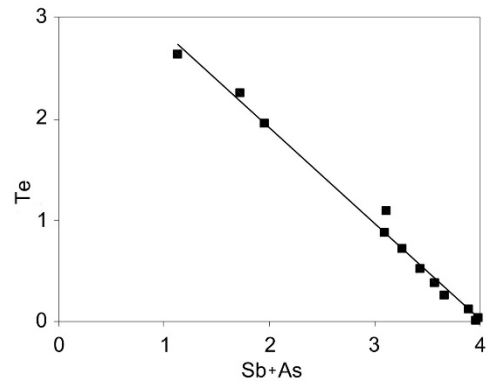


Figure 3. Relationship between Te and (Sb+As) in goldfieldite-tetrahedrite from Furtei mine.

However, mixing of different fluids at shallow levels seems to have been important in controlling the chemistry of tetrahedrite series, and late stage fluids may have been oxidized as indicated by the presence of barite in the epithermal assemblage. In the ore assemblage, the presence of arsenopyrite indicates that the mineralising fluids had a generally low sulfidation state. For tetrahedrite and chalcopyrite to have followed this mineral in the paragenetic sequence, a slight increase in f_{S_2} and/or decrease in temperature would have been necessary (Fig. 4). In conclusion, the chemical composition of tetrahedrite can record some of the chemical variables of the hydrothermal fluids at the time of mineralisation. The correlation of compositional variations of this mineral series through the Furtei deposit can delineate a zoning pattern in which Te decreases away from a presumable, porphyry-style center of the hydrothermal system.

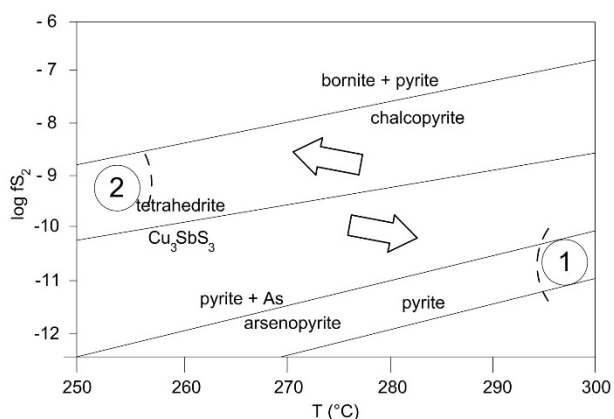


Figure 4. Transition between paragenesis of arsenopyrite evolving to tetrahedrite-bearing assemblage. Thermodynamic data are taken from Craig and Barton (1973).

3 A Porphyry-copper in the Siliqua volcanic complex

The andesitic and dioritic bodies occurring in the Siliqua sector (Fig.1), formed during the Tertiary calc-alkaline magmatic cycle, display alteration and mineralisation patterns which can be referred to as a porphyry copper system consistent with a diorite model. In the northern part of this sector an exploration drilling campaign showed high gold contents, strong silicification and the presence of epithermal silica-pyrite alteration. The field observations and time and space relationships between the porphyry and epithermal styles of mineralisation and host rocks seem to suggest successive development of alternating porphyry-style veining and igneous and/or hydrothermal breccias, followed by several epithermal stage mineralised breccias within previously advanced argillic-altered subvolcanic and volcanic rocks (Fiori et al. 1999). The epithermal occurrences may be considered to be related to the adjacently outcropping porphyry system or telescoped to the periphery of some other stocks still buried at depth. Detailed petrographic studies for the reconstruction of such a complex scenario are in progress. Perhaps the best geotectonic conditions for the formation of porphyry ore systems, i. e. such as to permit a rapid and easy access of magmas to the shallow crust, were limited in time and space. Excellent exposures provide good opportunity to study spatial, temporal, and possibly genetic links between porphyry and epithermal stages of the continuous development of a complex magmatic-hydrothermal-epithermal activity. The epithermal occurrences in the study area may be considered to represent the upper parts of porphyry bodies still buried at depth. But the existence of such a magmatic contribution, genetically connected, may be only speculated as yet. Alternatively, the close space and time relationships between possibly multiple intrusion phases and different epithermal fluids along the same or different plumbing systems, may support a genetic connection if erosion and tectonism in the province are taken into account. Systematic exploration will provide further data for a correct interpretation of previous detailed field and petrographic studies; this interpretation

may form the basis for reconstructing the chemical, spatial and temporal evolution of the events. Chemical analyses of fluid inclusions from both the porphyry and the epithermal parts of the system, combined with electron microprobe analyses of magmatic phenocrysts and hydrothermal minerals, are currently in progress and will be of primary interest in understanding magmatic factors controlling the mineralisation. Microthermometry, isotopic geochemistry and tracing, as well as high-precision (U-Pb and Ar-Ar) dating of the different magmatic and hydrothermal regimes will also be of help to study the connection between these two mineralisation styles and possibly to trace the porphyry to epithermal transition, if present.

Acknowledgments: The research has been supported by the CNR - IGAG, Cagliari, Italy.

References

- Afifi AM, Kelly WC, Essene EJ, (1988b). Phase relations among tellurides, sulfides, and oxides: II. Applications to telluride bearing ore deposits. *Econ. Geol.* 83:395-404
- Cook NJ, Ciobanu CL, (2002). Tellurides: more than mineralogical curiosities, but also markers of fS_2 - fO_2 evolution in zoned hydrothermal systems. IMA, 18th General Meeting, Edimburg, Programme with Abstracts: 283
- Cooke DR, McPhail DC, 2001. Epithermal Au-Ag-Te mineralization, Acupan, Baguio District, Philippines: numerical simulations of mineral deposition. *Economic Geology*, 96:109-131.
- Craig, JR, Barton, PB, 1973. Thermochemical approximations for sulfosalts. *Economic Geology*, 68:493-506
- Fiori M, Grillo SM, 2001. The Furtei high-sulfidation epithermal gold deposit (Sardinia, Italy): mineral assemblage and its evolution. In: A. Piestrzynski et al. (Eds), *Mineral Deposits at the beginning of the 21st Century*, Swets and Zeitlinger, p. 739-742.
- Meloni P, 1994. Metodologie di prospezione geomineraria e geofisica di mineralizzazioni sepolte tipo porphyry copper. Studio del settore di Serrenti-Furtei (Sardegna Meridionale): Unpublished PhD thesis, University of Cagliari (English abstract in *Plinius* 13:145-148).
- Ruggieri G, Lattanzi P, Luxoro S, Dessì R, Benvenuti M, Tanelli G, 1997. Geology, Mineralogy, and Fluid Inclusion Data of the Furtei High-Sulfidation Gold Deposit, Sardinia, Italy. *Economic Geology*, 92:1-19.
- Wu I, Peterson U, 1977. Geochemistry of Tetrahedrite and Mineral Zoning at Casapalca, Perú. *Economic Geology*, 72, 993-1016.
- Fiori M, Granizio F, Grillo SM 1999, Hydrothermal breccias in the southern sector of the Tertiary volcanogenic Cu-Au-Ag province of Sardinia, Italy. Proceeding of the fifth biennial SGA meeting and the tenth quadriennial IAGOD meeting: Mineral deposits: Processes to processing, 491-494
- Frezzotti ML, Ghezzi C, Stefanini B, 1992. The Calabona Intrusive complex (Sardinia, Italy): Evidence for a Porphyry Copper System. *Econ. Geology*, 87:425-436

Geological setting and lithological controls of breccia-hosted Cu-Au ore at the Late Cretaceous Kvemo Bolnisi prospect, Bolnisi, Lesser Caucasus, Georgia

Nino Popkhadze

A. Janelidze Institute of Geology of Iv.Javakhishvili Tbilisi State University, Georgia

Greg Corbett

Corbett Geological Services Pty. Ltd., Australia

Jason Cunliffe

International Mineral Exploration Consultants LTD., UK

James Royall, Simon Cleghorn, Mikheil Chokhanelidze, Jack Davies, Ryan Hampton, John Newman, Leqso Gelashvili, Koba Khmaladze, Taniel Tedliashvili

Georgian Mining Corporation (GCG mining); GCG Mining, Bolnisi, Georgia

Robert Moritz

Department of Earth Sciences, University of Geneva, Switzerland

Abstract. Detailed field mapping and drill core description was undertaken at the Kvemo Bolnisi prospect located in the Bolnisi ore district, of the Lesser Caucasus, in Southern Georgia. This study facilitated the distinction between the main host rock facies units and understanding of the lithological control to copper-gold mineralization. The base of the oxidation zone controls the distribution of supergene gold and underlying copper mineralization in upper non-welded permeable ignimbrite, while the lower welded fiamme ignimbrite hosts mostly copper ore mostly within the cross cutting the polymictic breccia pipe. The columnar jointed, post-ore dacite body represents the final volcanic event in this area.

1 Introduction

The Bolnisi ore district belongs to the renowned 10,000 km-long Tethyan Eurasian Metallogenic Belt (TEMB; Fig.1; Jankovic 1997). The Kvemo Bolnisi Cu-Au mineral deposit is part of the Artvin-Bolnisi unit of the TEMB located in the northern part of the Lesser Caucasus. The Bolnisi district host numerous producing Late Cretaceous ore deposits, including the Madneuli, Sakdrisi, Beqtakari Cu-Au and polymetallic deposits. Kvemo Bolnisi breccia-hosted Cu-Au deposit is located at a distance of 6 km from the Madneuli deposit, which produced approximately 85 Mt of copper and gold bearing ore, at a reported grade of 1.0g/t Au and 1.0% Cu, over a period of 30 years. At Kvemo Bolnisi, the resources have been estimated as 947,000 tonnes at an average grade of 0.93 Cu and 0.15 g/t Au. (https://polaris.brighterir.com/public/georgian_mining_corporation/news/news_rns/story/w0eq36r).

New exploration programs are going on in Georgia and new prospective ore zones are investigated by RMG

(Rich Metals Group) company, including Bnelikhevi, David Gareji, and Mushevani. The Kvemo Bolnisi prospect represents the highest priority target for exploration by the Georgian Mining Corporation, which

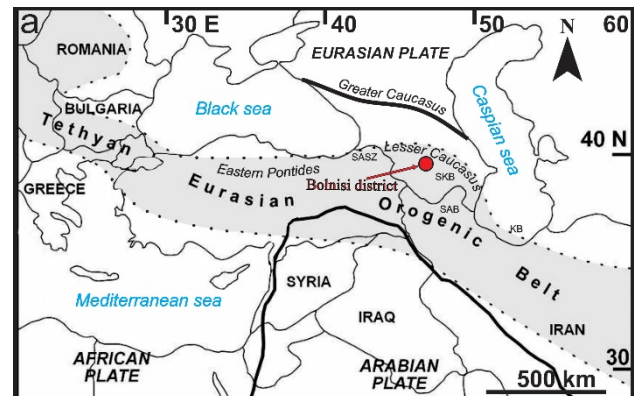


Figure 1. Location of the Bolnisi district within the Tethyan orogenic belt (modified from Yigit, 2012). Abbreviations: SAB – South Armenian block; SASZ - Sevan-Akera suture zone; SKB – Somkheto-Karabagh belt; KB - Kapan Block.

also has the Dambludi, Tsiteli Sopeli, Tamarisi and Balichi prospects under investigation. The main aims of our work are to understand the lithological and structural controls for the development of the main ore zones in order to understand the distribution and anatomy of the Cu-Au mineralization.

2 Regional geology and stratigraphy

The Kvemo Bolnisi prospect is located in Artvin-Bolnisi zone, which belongs to the Lesser Caucasus. The Lesser Caucasus extends over the territories of Armenia, Azerbaijan and Georgia. It consists of three

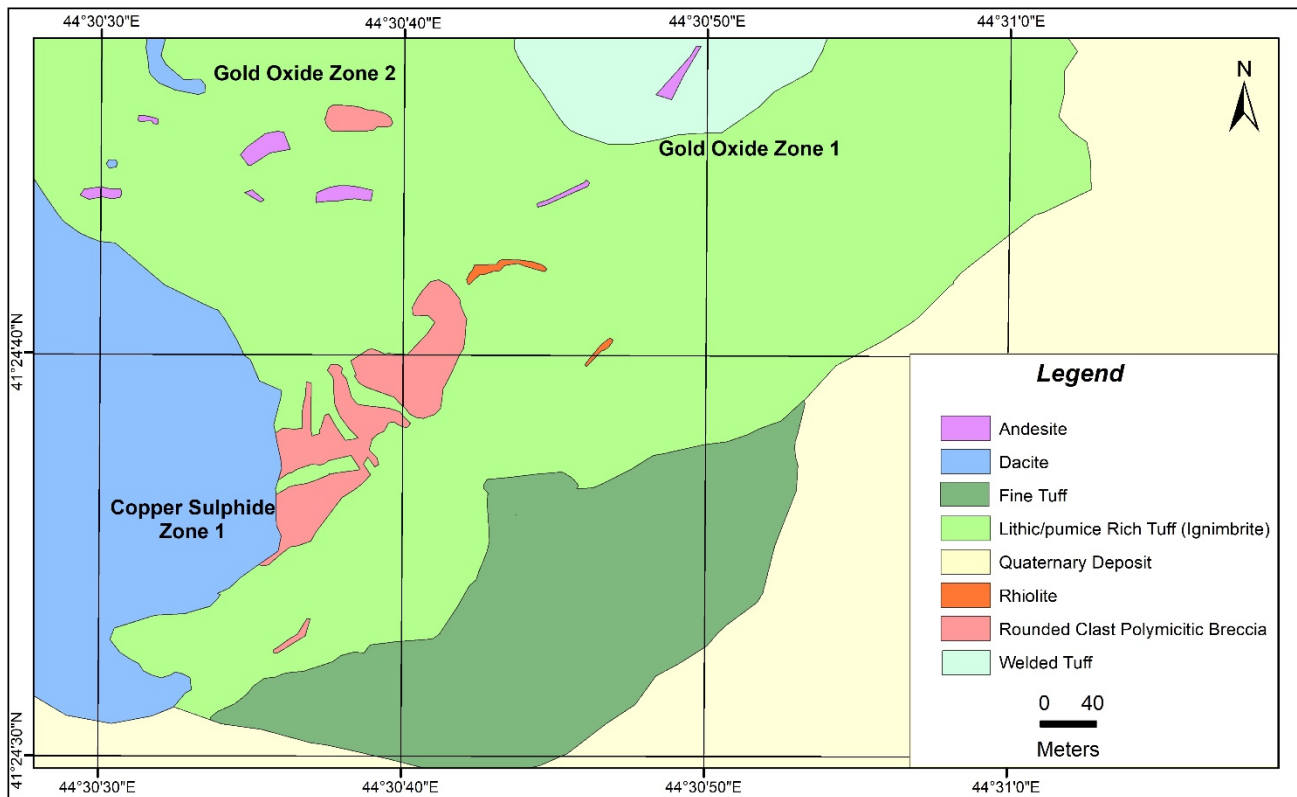


Figure 2. Simplified geological map of the Kvemo Bolnisi prospect. Modified from Davies (2017), Georgian Minong Corporation) (unpublished material)

tectonic zones (Sosson et al. 2010), which are from SW to NE: (1) the South Armenian Block (SAB), (2) the Amasia-Sevan-Akera suture zone (ASASZ) and (3) the southern Eurasian plate margin consisting of the Somkheto-Karabagh belt (SKB) and the Kapan block (KB) (Fig. 1). The Somkheto-Karabagh belt is known in Georgia as the Artvin-Bolnisi zone (Yilmaz et al. 2000). The host rocks for the ore deposits and prospects in the Bolnisi district are composed of Late Cretaceous volcanic and volcano-sedimentary rocks emplaced into a depression between the basement rocks of the Khrami and Loki massifs (Zakariadze et al 2007). Predominant Late Cretaceous volcanic and pyroclastic rocks in this region include rhyodacitic ignimbrite, ash fall and density current deposits with a phreatomagmatic origin (Popkhadze et al 2017). The distribution of rhyodacitic to basaltic lava domes has led to speculation that a central caldera may have played a role in the localization of the Cu-Au exploration prospects in the vicinity of Kvemo Bolnisi. Based on lithological and paleontological data, Late Cretaceous volcanic and volcano-sedimentary rocks in this region are subdivided into six volcanogenic suites, and are Cenomanian to Campanian and Maastrichtian in age (Gambashidze 1984). Ore deposits in this region are associated with Late Cretaceous explosive volcanic events in different stratigraphic levels. According to Gugushvili (2004), deposits/prospects from the eastern part of the district, including: Madneuli, Kvemo Bolnisi, Tseli Sopeli, Mushevani and David-Gareji are hosted by stratigraphically older rocks of the late Turonian to early

Santonian Mashavera suite. A second group of ore deposits/prospects, including: Sakdrisi, Darbazi, Imedi, Beqtakari, Bnelikhevi and Samgereti are hosted by stratigraphically younger rocks of the Campanian Gasandami suite.

3 Geology of Kvemo Bolnisi

3.1 Host rock facies architecture of the Kvemo Bolnisi prospect

This study has focused upon the physical volcanology and facies analyses during a mapping program, together with detailed drill core logging and interpretations. The complete data set including correlation of outcrop and drill core samples allows us to distinguish the following facies types in Kvemo Bolnisi area: lithic/pumice-rich tuff or non-welded ignimbrite, fine-grained tuff, columnar-jointed dacite dome, polymictic breccia, a bedded volcano-sedimentary sequence and welded ignimbrite. The detailed description and interpretation of the Kvemo Bolnisi east polymictic breccia pipe, allow us to constrain the stratigraphy of the host rocks of this area (Fig.2). The stratigraphically upper lithic/pumice tuff is strongly oxidized, fractured and in some areas silicified. The highly porous, permeable and glassy pumice/lithic tuff was affected by pervasive argillic (illite) alteration (Fig 3a). During the petrographic investigation, it was difficult to recognize pumice or lithic clasts in the tuff, as they are affected by argillic alteration. In some places, remnants

of pumice clasts were identified. The lower stratigraphic unit consists of welded (fiamme) ignimbrite (Fig.3b). In some cases, this fiamme might be considered as a fiamme in secondary welded pumice-rich facies, produced by secondary welding of pumice-rich clastic facies. The formation of such fiammes is possible in contact with hot lava or an intrusion. Sometimes, fiamme produced by secondary welding of fiamme-rich clastic facies are virtually indistinguishable from fiamme in conventional primary welded pyroclastic facies (McPhie and Hunns, 1995).



Figure 3. The host rock architecture from KB area: a - lithic/pumice-rich tuff; b - welded (fiamme) ignimbrite; c - fine and medium-grained, bedded volcano-sedimentary tuff, with classical slide-slump units; d - mineralized polymictic breccia; e - margin of breccia pipe showing the mixture of wall rock - with breccia clasts.

The fine- and medium-grained, bedded volcano-sedimentary tuff, with classical slide-slump unit crop out at the contact with non-welded ignimbrite and might be interpreted as an older stratigraphically unit in this sequence (Fig.3c). The mineralized polymictic breccia pipe is cross-cutting all previously mentioned host rock sequences, including felsic dikes (Fig.3d). While a columnar-jointed post-ore dacite dome represents the last volcanic event in the Kvemo Bolnisi area (Fig.3e). The polymictic breccia pipe crops out in the western part of the Kvemo Bolnisi prospect, as a matrix-rich to clast-supported breccia of well rounded, milled clasts of fine tuff, less silicified ignimbrite, and also clasts of felsic dikes and other silicified clasts. In the Kvemo Bolnisi the polymictic breccia pipe margin is discernible in outcrop and drill hole intercepts as a mixture of wall rock – lithic/pumice tuff (ignimbrite) with breccia clasts (Fig.3f).

3.2 Ore zones and lithological controls at Kvemo Bolnisi

The Kvemo Bolnisi project includes different ore zones, including (Fig.4): Kvemo Bolnisi west, which is the gold zone 3 characterized by polymetallic-gold-silver mineralization; Kvemo Bolnisi south, which includes the copper zone 1, where the breccia pipe and other structures are identified. Gold zones 1 and 2 represent the gold oxide ore, developed from the surface to the base of the oxidation zone, between a depth of 40 and

70m (<https://www.georgianmining.com/projects/>).

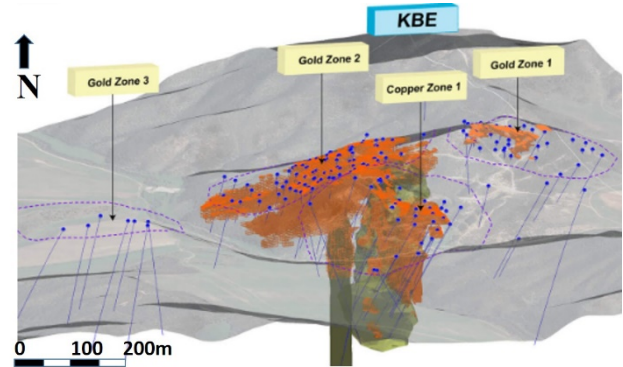


Figure 4. Model of the Kvemo Bolnisi prospect, including different copper and gold mineralized zones (Source: Georgian Mining corporation).

The gold zones 1 and 2 represent the upper stratigraphic level, consist of strongly oxidized lithic/pumice tuff (non-welded ignimbrite) with shallow supergene Au mineralization (Fig. 5a, b).

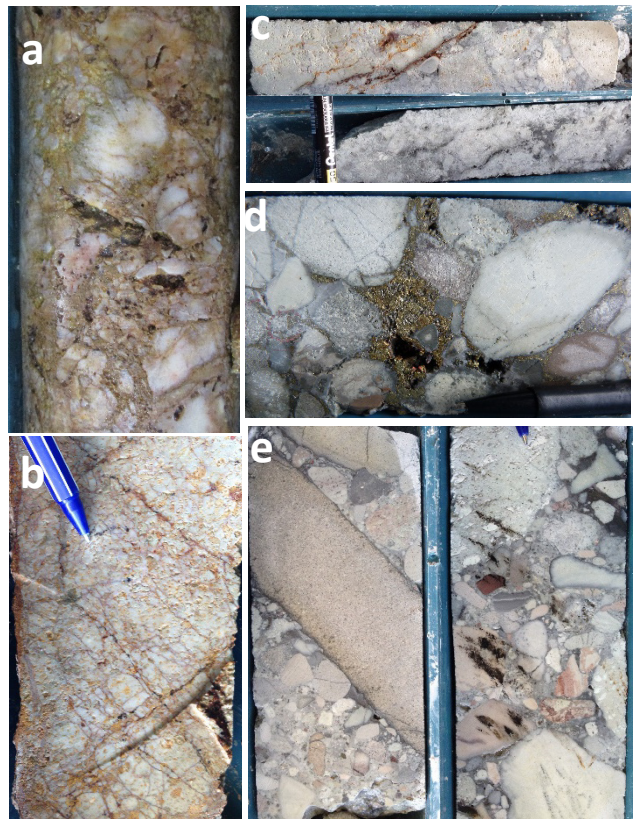


Figure 5. Characteristic features of ore at the Kvemo Bolnisi copper-gold prospect: a,b strongly silicified, crackle fractured lithic/pumice tuff cross cut by quartz-iron oxide veinlets; c – iron oxide veinlet above the redox boundary zone with chalcocite in the transition zone; d – clast-supported open space polymictic breccia filled with quartz-pyrite-chalcopyrite; e – clast-supported subrounded to rounded breccia. Pyrite and chalcopyrite are in the matrix.

This zone extends down to the base of the oxidation zone, which is clearly identified in nearly all drill holes. Chalcocite is present coating pre-existing sulphides and

veinlets in the transition zone below the base of oxidation (Fig.5c). The copper zone 1 includes the welded ignimbrite of the lower stratigraphic unit, below the redox boundary, with copper-gold and mostly with copper mineralization and the mineralized polymictic breccia (Fig. 5d,e). The breccia (Fig. 5d) contains rounded to sub-rounded, mostly silicified and mineralized clasts of pumice tuff. Some clasts host vein mineralization formed prior to brecciation which does not extend in the matrix. The open space in the polymictic breccia between the clasts is filled by a magmatic hydrothermal ore assemblage including quartz, pyrite and chalcopyrite. Relationships in outcrop suggest there is a transition from the central polymictic breccia with rounded clasts, to a matrix-rich portion, followed by a contact with the silicified pumice tuff host rock (Fig.6).

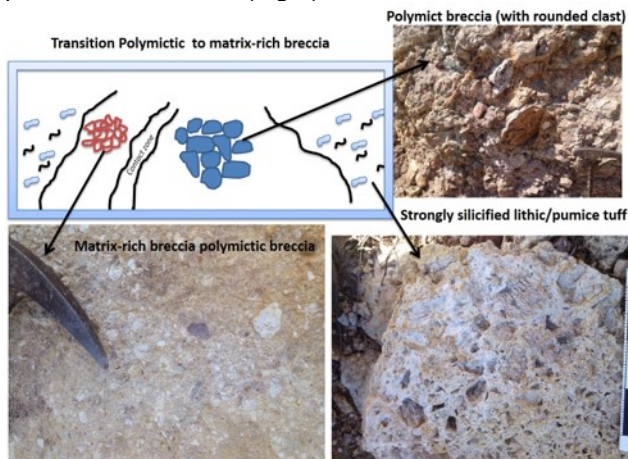


Figure 6. The scheme showing the transition zone from clast-rich to matrix-rich polymictic breccia and contacts with lithic/pumice tuff.

The transitional breccia is less silicified and more affected by argillic alteration, and it contains a juvenile clast.

4 Conclusions

The permeability of host rock units in the Bolnisi district, including: non-welded ignimbrite, lithic/pumice tuff and different types of breccia, provides a favorable environment for fluid migration and ore formation. The existence of mineralized polymictic breccia in the Kvemo Bolnisi area provides an attractive exploration target. Different stages of ore formation and fluid migration are overprinted in polymictic breccia. Most of the clasts in this breccia are mineralized, which indicates there has been an early stage of ore formation which is overprinted by a later breccia infill mineralization. The breccia pipe is interpreted to have evolved from a magmatic hydrothermal to a more phreatomagmatic nature with an associated change in mainly breccia matrix-hosted mineralization low sulphidation Cu-rich quartz-sulphide Au±Cu style to Au rich carbonate-base metal Au mineralization, as typical of these types of breccia deposits. The key controls on the mineralization is the breccia pipes, which are mineralized with hypogene auriferous pyrite and chalcopyrite. In the supergene environment the sulphides are oxidized giving rise to a

classic sequence of oxidized and enriched gold mineralization where copper mineralization is mobilized and redeposited at the base of oxidation giving rise to strongly enriched chalcocite mineralization overprinting primary sulphides.

Acknowledgements

The authors would like to thank: the members of staff of the Georgian Mining Corporation and Rich Metals Group (RMG) company for the collaboration and sharing the information; SGA, SEG, and IAVCEI organizations and the Shota Rustaveli National Science Foundation in Georgia for attending many international conferences, where the work and results from the Bolnisi district were presented. The Swiss National Science Foundation (grant 200020_168996) is also thanked for support.

References

- Gambashidze R (1984) Geological development history of Georgia during the Upper Cretaceous period. Metsniereba: Al.Janelidze Institute of Georgian Academy of Sciences. Proceedings, New Series, 82:1-111 (in Russian)
- Gugushvili V (2004) Two types of gold mineralization in the Bolnisi mining district related to Cretaceous volcanism: Proceedings of the Geological Institute of the Georgian Academy of Science, New Series, 119: 749-755
- Jankovic S (1997) The Carpatho-Balkanides and adjacent area: a sector of the Tethyan Eurasian metallogenic belt. Mineralium Deposita 32:426-433
- McPhie J and Hunns S (1995) Secondary welding of submarine, pumice-rich breccia at Mount Chalmers, Queensland, Australia. Bulletin of Volcanology. 57(3):170-178
- Popkhadze N, Moritz R, Natsvlishvili M, Bitsadze N (2017) First evidence of phreatomagmatic breccia at the Madneuli Polymetallic Deposit, Bolnisi district, Lesser Caucasus, Georgia. In: proceedings of the 14th SGA Biennial Meeting: Mineral resources to discovery, 1:323-326; 20-23 August Quebec City, Canada
- Sosson M, Rolland Y, Muller C, Danelian T, Melkonyan R, Kekelia S, Adamia Sh, Babzadeh V, Kangarli T, Avagyan A, Galoyan G, Mosar J (2010) Subductions, obduction and collision in the Lesser Caucasus (Armenia, Azerbaijan and Georgia), new insights. Geological Society London, Special publication, 340:329-52
- Yigit O (2012) A prospective sector in the Tethyan Metallogenic Belt: Geology and geochronology of mineral deposits in the Biga Peninsula, NW Turkey, Ore Geology Review, 45:118-148
- Yilmaz A, Adamia Sh, Chabukiani A, Chkhotua T, Erdogan K, Tuzcu S, Karabilykoclu M (2000) Structural correlation of the southern Transcaucasus (Georgia)-Eastern Pontides (Turkey)-Tectonics and magmatism in Turkey and the surrounding area. Geological Society of London Special Publication. 173:171-182
- Zakariadze G, Dilek Y, Adamia Sh, Oberhansli R, Kaepenko S, Bazulev B and Soloyeva N (2007) Geochemistry and geochronology of the Neoproterozoic Pan-African Transcaucasian Massif (Republic of Georgia) and implications for island arc evolution of the late Precambrian Arabian-Nubian shield. Gondwana Research. 11:92-108

Regional-scale mapping of mineral potential for porphyry Cu-Au deposits in southeastern Europe

Felix Camenzuli and Hartwig E. Frimmel
University of Würzburg, Germany

Adam Wooldridge
Vardar Minerals

Abstract. The Balkan Peninsula is probably Europe's most famous region for porphyry Cu(-Au) deposits thanks to the collision between Eurasia and Gondwana and preceding subduction of the Tethyan oceanic lithosphere. A complex plate tectonic history left behind magmatic arcs which are known for porphyry and related epithermal deposits. To better assess the potential for discovering new such deposits, especially in areas covered by younger strata, we followed a GIS-based mineral potential mapping approach using exclusively ESRI ArcMap. For this purpose, geological data from eight Balkan countries were combined. The results revealed a particularly high probability of porphyry Cu(-Au) mineralization in arc-related rocks of Tertiary age and not only in Cretaceous arc rocks, which have been the centre of past mining activities.

1 Introduction

Porphyry Cu deposits account for some 80% of the global Cu resources and can contain also several other metals at economic grades (Sillitoe 2014). Europe's largest porphyry Cu deposits are located on the Balkan Peninsula – a region that has seen mining of ores since antiquity. Extraction of gold and copper there is thought to have had a major influence on the cultural and economic development of early Europe (Kaiser Rohrmeier et al. 2013).

Today's exploration faces the problem that most of the bigger deposits that have a surface expression have been found and mined already (Hronsky and Groves 2008; Huston et al. 2016). The challenge is to discover new deposits under cover. The Balkan Peninsula is no exception in this regard. Prior to cost-intensive local geological mapping as well as geophysical and geochemical surveying and eventually drilling, identifying prospective target areas on a larger scale based on available geological, geochemical and geophysical information and a solid genetic model has become standard practice. This is readily achieved by GIS, in which a number of different kinds of data can be combined and spatially overlain resulting in mineral potential maps (Bonham-Carter 1994). Such a modelling approach can be data-driven or knowledge-driven. The latter is preferred when the amount of input data, such as known mineral deposits/occurrences, geochemical anomalies, etc., is limited. In that case, existing empirical models for the genesis of the deposit type of interest form the base of the modelling as they determine the weight of

each layer of information, that is, each layer represents a major factor controlling the formation and spatial distribution of ore (Bonham-Carter 1994). The combination of all these factors has become known as mineral system approach, first used by Wyborn et al. (1994) for hydrothermal deposits. Modelling is scale-dependent. If scale increases, number of relevant factors, and thus complexity of the system decreases (Hronsky and Groves 2008).

Similar to the work by Billa et al. (2004), who examined the porphyry and epithermal deposits of the central Andes on a continental scale, this study aims at conducting large-scale predictive modelling of the exploration potential for porphyry and related epithermal Cu-Au deposits in the Balkan Peninsula using fuzzy logic and a knowledge-driven model. The studied area of interest (AOI) covers $\sim 1 \cdot 10^6$ km² as illustrated in Figure 1.

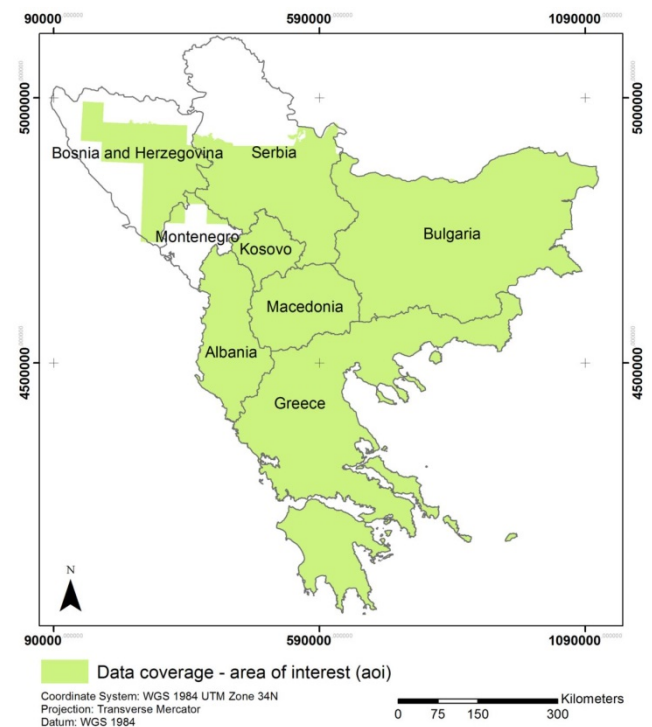


Figure 1. Map of the studied area showing the extent of data coverage.

2 Geological background

The AOI forms part of the Tethyan Eurasian metallogenic belt and extends L-shaped from Romania to Bulgaria. The subduction and collision events that shaped the convergent margin of Eurasia in the Balkan Peninsula are a consequence of closure of the Paleotethys and from the Cretaceous on the Neotethys (Stampfli and Borel 2004). As a result, magmatism and mineralization occurred in different parts of the AOI during three major periods: a Cretaceous, a Paleocene to Oligocene, and a Miocene magmatic arc can be distinguished (Marton et al. 2013).

The Cretaceous arc, referred to as Banatitic Magmatic and Metallogenic Belt (BMMB; Ciobanu et al. 2002), was formed due to the subduction of the Vardar oceanic lithosphere beneath the Serbo-Macedonian continent, which started in the late Jurassic. The Vardar Ocean filled one of the back-arc basins that were closed between the Jurassic and the Cretaceous in the region of the Balkans and Carpathians. This was followed by the accretion of microcontinents and island-arcs, resulting in syn-collisional calc-alkaline magmatism around the Cretaceous-Tertiary boundary (Richards 2015; Ciobanu et al. 2002). Porphyry Cu and high-sulfidation Cu-Au mineralization affected mainly andesitic-dacitic rocks and was limited to belt-parallel basins.

The BMMB hosts the famous deposits Majdanpek, Veliki Krivelj and Bor located in the Serbian Timok ore district (Timok Magmatic Complex), as well as Elatsite and Assarel of the Bulgarian Panagyurishte ore district. The timing of mineralization in these districts varied as the position of the subduction zone shifted. Whereas mineralization in the Panagyurishte ore district took place between 92 and 86 Ma, it was around 86-84 Ma in the Timok ore district (Fig. 2; Quadt et al. 2007, Richards 2015).

Historical mining activity has focused on the Cretaceous arc. Active subduction was long believed to be indispensable for fertile magmatism and porphyry mineralization and indeed, the Cretaceous deposits of the Balkan Peninsula can be explained by subduction-related mineralization processes. There are, however, some major deposits that have been formed later, e.g. the Buchim and Skouries deposits (Fig. 2).

As summarized by Richards (2015), porphyry Cu deposits occur scattered in both space and time within the Tethyan Belt, reflecting different settings of formation. When the subduction zone shifted in the Paleogene to the Hellenic Trench, porphyry and epithermal mineralization took place again in the Balkans and the eastern Rhodopes. This has been explained by Richards (2015) who suggested that the formation of the younger porphyry Cu-Au and epithermal Au deposits was initiated by remelting of subduction-metasomatized subcontinental lithospheric mantle or lower crustal hydrous cumulate zones. Thus, the bulk of Cenozoic deposits of the Tethyan Belt can be considered to be of either back-arc, post-subduction or collisional origin. In the case of the Balkan Peninsula, the formation of these deposits was related to the closure of Vardar Ocean. Consequently, collisional orogens can be regarded as

being as attractive for porphyry mineralization as subduction settings (Richards 2015).

3 Methodology

The genetic model underlying this study assumed four critical factors that have to be satisfied in order to form a porphyry/epithermal Cu-Au system: (i) mineralization is primarily tectonically controlled; (ii) it is spatially and genetically related to felsic to intermediate porphyry intrusive bodies; (iii) these intrusions occurred in root zones of volcanoes in subduction-related, continental ridge/arcs and/or island arc settings; and (iv) they are limited in age to Cretaceous and Eocene-Miocene times.

Geological data was used as primary data source. That data was originally taken from 1:200000 to 1:500000 geological maps. Prior to modelling, that data was unified due to strong country-specific differences in extent and quality of data. Lithological and age data were simplified in a classification scheme, respectively. From the processed data three predictor maps or layers were prepared: a "lithology" layer, representing lithology suitable for hosting porphyry Cu mineralization, that is, intrusive and extrusive magmatic rocks of felsic to intermediate composition.

The second layer, "subvolcanic level", reflects the assumption that porphyry Cu deposits are located in volcanic root zones and was obtained from mapped contacts of extrusive and intrusive igneous rocks. Those areas were ascertained from the distance of both intrusive and extrusive rocks to points of a grid, having a cell length of 1 km. The smaller the distance the higher the value of representing the contact. Both the "lithology" and "subvolcanic level" layers were prepared for each time window known to be critical for mineralization. Due to data inconsistencies and lack of necessary age resolution on many of the available geological maps, only two periods could be distinguished: Cretaceous and Tertiary.

The third layer, "Cu-anomalies", is based on point data of locations from which anomalously high Cu concentrations have been reported. Only those anomalies were considered further, which occur within or nearby areas of rock types typical of porphyry/epithermal environments in order to exclude genetically unrelated mineralization. The proximity of those anomaly point data was implemented by circled polygons of different radii representing the decrease of Cu enrichment with distance. Smallest radii were 250 m and 500 m, which are the expected size of porphyry stocks (Sillitoe 2014). The probability values were set to decrease away from the anomalies. This layer was used for modelling mineral potential maps for both Cretaceous and Tertiary times. Tectonic control was not considered in a separate layer because it is effectively represented by the lithology layer as the magmatic rocks of interest tend to be emplaced along the same large-scale structures (crustal-scale lineaments) as the associated mineralization.

Mineral potential mapping of this study was carried out with a knowledge-driven model and the usage of Fuzzy logic, using a Fuzzy gamma operator with a value of 0.98,

following a recommendation by An et al. (1991). For each period, a separate mineral potential map was modelled. Highest probability of porphyry Cu mineralization is expressed by a value of ~1, and no probability by a value of ~0. The results obtained for both the Cretaceous and Tertiary time slices were validated by 72 locations of known Cu deposits or occurrences as given in the USGS database “Global assessment of undiscovered copper resources” (Dicken et al. 2016), by comparing modelled probability values and the location of the deposits/occurrences as point data. In a second step, the vicinity (5 km radius) of the point data was included and the highest value was taken from this circular surrounding. For better comparison, the probability values were classified as low ($0.25 \geq x$), medium ($0.25 < x \leq 0.75$) and high ($x \geq 0.75$).

4 Results

The modelled mineral potential maps for the Cretaceous and Tertiary periods (Fig. 2) show several differences regarding the spatial distribution of areas with high and medium probability for porphyry Cu mineralization. In comparison to the Cretaceous, the potential map for Tertiary deposits reveal a number of differences: (i) high and medium probability areas are more abundant, (ii) they are bigger in extent, (iii) more widely distributed, and (iv) they are spatially separated from the potentially mineralized Cretaceous areas. The areas of Cretaceous age are arranged in an arc-shaped zone extending from central-eastern Serbia via central- and southwestern Bulgaria to central, southeastern Bulgaria. The zone has its smallest extent in the north, and becomes wider to the south and southeast, where it continues as two small separated bands. In contrast, areas of Tertiary age are mostly located further to the south and west, appear as a funnel-shaped zone extending from the northwestern to the southwestern parts of the AOI. The zone broadens in extent from the area of Macedonia onwards. In regard to (iv) it is necessary to note that there are parts of the AOI where areas of high a medium probability of both periods exist. These are mainly central-eastern Serbia and central and southern Bulgaria. The areas of highest probability values for the Cretaceous and Tertiary differ, however, in geographic position.

The results show that the areas with the highest probability values are restricted to small domains in central-eastern Serbia in the case of Cretaceous age, whereas those of Tertiary age are somewhat further north. The other centers of highest probability of Tertiary deposits are arranged linearly from eastern and southern Serbia to western and southwestern Bulgaria.

The validation of the mineral potential maps showed that 36 % of the known deposits/occurrences lie directly in areas of high probability, 7 % in areas of medium probability. If the surroundings of the known locations are included in the validation, 67 % of the locations lie within, or in ≤ 5 km proximity of, an area of high probability. Using the same method on areas of medium probability, 1% of the locations lie within or in proximity of those areas. Combining areas of high and medium probability, the

mineral potential map based on known deposits/occurrences as point data, explains 43 % of the existing locations. If one includes the vicinity around known deposits/occurrences, this percentage increases to 68%.

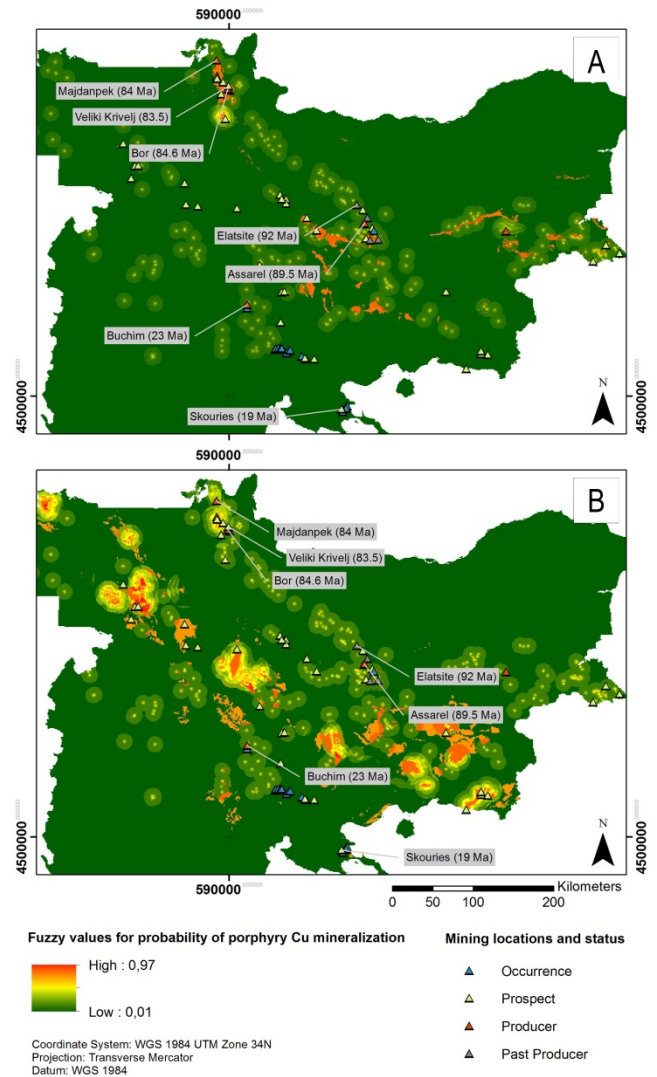


Figure 2. Mineral potential maps showing suitable areas for copper mineralization of Cretaceous (A) and Tertiary (B) age. Both maps were produced by using a Fuzzy Gamma operator with a value of 0.98. Additionally, the existing mining locations and their status after USGS database - Dicken et al. (2016) are shown as well as the names and age data of selected deposits (after Richards 2105).

5 Interpretation and discussion

Modelled mineral potential maps are typically validated with known deposits. Previous studies illustrate a strong dependence of the model's accuracy on the spatial scale, as proposed by e.g. Hronsky and Groves (2008). Mutele et al. (2017) did prospectivity mapping of granite-related polymetallic mineralization of an area on the scale of 10^5 km² area in the Bushveld Igneous Complex. The validation of their study showed that all known mineral occurrences are within areas of modelled high and medium probability. In contrast, the study by Billa et al.

(2004) on predicting epithermal and porphyry systems in the Andes at a continental-scale of 10^6 km² found only ~64 % of known deposits lying within areas of modelled high and medium probability (excluding the vicinity of known deposits). Similarly, our results (68 %, including vicinity of known deposits), referring to an AOI on the scale of 10^6 km², fall short of a 100 % coverage and illustrate the importance of scale for the accuracy of mineral potential maps. Without doubt, applying a more complex model should lead to a mineral potential map that can explain a higher number of deposits/occurrences.

Furthermore, our results, being strongly dictated by the spatial distribution of the different magmatic arcs (Marton et al. 2013), provide information on the relative fertility of these arcs. While historic mining activities focused on the Cretaceous arc, this study attests to a considerable potential also in the Tertiary arc. The latter area shows a higher number and greater extent of areas with high and medium probability.

6 Conclusions

Regional-scale mineral potential mapping has shown its ability to delineate regions of elevated probability for hosting porphyry Cu (and related epithermal Au) deposits as exemplified here for the Balkan Peninsula. The usefulness of the model is supported by its ability to predict known deposits in spite of simple input data. Overall the results show a much higher probability for porphyry Cu mineralization in the Tertiary arc than in the Cretaceous one. Thus, the Tertiary arc could become an even more important target for future exploration as the Cretaceous arc has been already.

Acknowledgements

We thank Vardar Minerals Ltd. for providing the regional databases.

References

- An P, Moon WM, Rencz A (1991): Application of fuzzy set theory for integration of geological, geophysical and remote sensing data. *Canadian Journal of Exploration Geophysics* 27:1-11.
- Billa M, Cassard D, Lips, AL et al (2004) Predicting gold-rich epithermal and porphyry systems in the central Andes with a continental-scale metallogenic GIS. *Ore Geology Reviews* 25:39-67.
- Bonham-Carter GF (1994) *Geographic Information Systems for Geoscientists: Modelling with GIS*. Pergamon, Oxford.
- Ciobanu CL, Cook NJ, Stein H (2002) Regional setting and geochronology of the Late Cretaceous Banatitic Magmatic and Metallogenic Belt. *Miner Deposita* 37:541-567.
- Dicken CL, Dunlap P, Parks HL, Hammarstrom JM, Zientek ML (2016) Spatial database for a global assessment of undiscovered copper resources. In: U.S. Geological Survey (ed) U. S. Geological Survey Scientific Investigations Report 2010-5090-Z and GIS data. doi: <http://dx.doi.org/10.3133/sir20105090Z>.
- Hronsky JMA, Groves DI (2008) Science of targeting: definition, strategies, targeting and performance measurements. *Australian Journal of Earth Sciences* 55:3-12.
- Huston DL, Mernagh TP, Hagemann SG et al (2016) Tectono-metallogenic systems - the place of mineral systems within

- tectonic evolution, with an emphasis on Australian examples. *Ore Geology Reviews* 76:168-210.
- Kaiser Rohrmeier M, Von Quadt A, Driesner T et al (2013) Post-orogenic extension and hydrothermal ore formation. High-precision geochronology of the Central Rhodopian Metamorphic Core Complex (Bulgaria-Greece). *Economic Geology* 108:691-718.
- Marton I, Dragić D, Djordjević B et al (2013) Intrusion-Alteration-Mineralization Relationships from the Porphyry Cu-Au Deposit at Kiseljak, Serbia. 12th Biennial SGA Meeting 2013, Uppsala. *Proceedings, Vol 2:837-840*.
- Mutele L, Billay A, Hunt JA (2017) Knowledge-Driven Prospectivity Mapping for Granite-Related Polymetallic Sn-F-(REE) mineralization, Bushveld Igneous Complex, South Africa. *Natural Resources Research* 26:535-552.
- Quadt A von, Peytcheva I, Heinrich CA, Cvetkovic V et al (2007) Upper Cretaceous magmatic evolution and related Cu-Au mineralization in Bulgaria and Serbia. 9th Biennial SGA Meeting 2007, Dublin: 861-864.
- Richards JP (2003) Tectono-Magmatic Precursors for Porphyry Cu-(Mo-Au) Deposit Formation. *Economic Geology* 98:1515-1533.
- Richards JP (2015) Tectonic, magmatic, and metallogenic evolution of the Tethyan orogen: from subduction to collision. *Ore Geology Reviews* 70:323-345.
- Stampfli GM, Borel GD (2004) The TRANSMED transects in space and time: constraints on the paleotectonic evolution of the Mediterranean domain. In: Cavazza W, Roure F, Spakman W et al (ed): *The TRANSMED Atlas. The Mediterranean Region from Crust to Mantle*, Springer, Berlin: pp 53-80.
- Stampfli GM, Kozur HW (2006) Europe from the Variscan to the Alpine cycles. In: Gee DG, Stephenson RA (ed) *European lithosphere dynamics. Memoir of the Geological Society*, London, 32: pp 57-82.
- Wyborn LAI, Heinrich CA, Jacques AL (1994) Australian Proterozoic mineral systems: essential ingredients and mappable criteria. *AusIMM Publication Series* 5:109-115.

Mineralogical characterization of Te-Au porphyry-epithermal California prospect in Tolima, Colombia

Iván Mateo Espinel Pachón, Juan Carlos Molano Mendoza, Juan David Alarcón Rodríguez, Mónica Ágreda López
Universidad Nacional de Colombia

Andrés Felipe González Durán
CDTEC Gemlab

Abstract. The California prospect is located 200 km west from Bogotá, Colombia and only 8 km SE from La Colosa Au-rich porphyry. The mineralization is associated with two porphyritic dacites that intruded muscovite-quartz-graphite schists of Palaeozoic age. The ore minerals are accompanied by a strong phyllic alteration which affects both the host rock and the hypabyssal bodies. Using clay minerals and Ga, Ge, In, Mn and Fe concentrations in sphalerite (GGIMFis) geothermometer, it was possible to differentiate two areas. In the hottest area, tetradymite was reported for the first time and it is related to structural gold concentration in pyrites.

1 Introduction

A gold-rich porphyry deposit was defined as a porphyry copper deposit that contains more than 0.4 g/t Au (Sillitoe 1979). Few Au-rich porphyry deposits have been found worldwide; there are some examples in the Maricunga Belt in Chile (Vila and Sillitoe 1991), Cajamarca in Perú (Teal and Benavides 2010) and Luzon in Philippines (Cooke et al. 2011). Sillitoe (2008) defined the Middle Cauca Belt according to the occurrence of Miocene gold rich deposits (porphyry and epithermal); Leal (2011) defined the Cajamarca-Salento district where a series of gold deposits occur associated with hypabyssal intrusions. In 2006 the AngloGold Ashanti greenfields exploration team discovered the world's largest gold-rich porphyry deposit, La Colosa. It is located within the Cajamarca-Salento district and they inferred a mineral resource of 470 Mtonnes with an Au content of 0.9 g/t (Gil-Rodríguez 2010).

The California prospect is located about 8 km southeast from La Colosa (Fig. 1). In 1960's there was gold exploitation but, a couple of years later the mine closed due to Colombian armed conflict. Gold was extracted from quartz veins and loads, using mercury amalgamation.

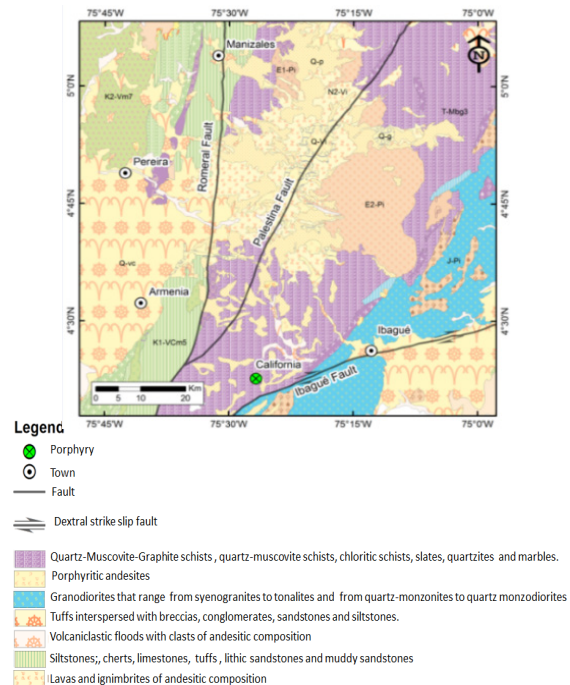


Figure 1. Regional geological map of the area between Ibagué, Armenia, Pereira and Manizales.

2 Geological framework

The Central Cordillera of Colombia is limited at east from Romeral Fault System and west from the Otú-Pericos fault. It is divided in four lithodemic megaunits (Maya and Gonzalez 1995): Cajamarca Complex, Quebradagrande Complex, Arquía Complex and Mesozoic oceanic vulcanites (Amaime Formation). There are some reported ages, using $40\text{Ar}/39\text{Ar}$ and $238\text{U}/206\text{Pb}$, for the Cajamarca Complex revealing an average age of 236.2 ± 6.3 Ma (Villagomez et al. 2011). Villagomez et al. (2010) proposed a synchronous exhumation process occur during 117-107 Ma for Arquía Complex.

Villagomez et al. (2011) reported an age on zircons from a metatuff in Quebradagrande Complex, yielding an age of 114.3 ± 3.8 Ma; in (Sinton et al. 1998) and average age of 77 Ma was given for Amaime Formation.

A seven-stage genetic model for the Central Cordillera was proposed by Villagomez and Spikings (2013), explaining the subduction model and the accretion of terrains over the Paleozoic and Triassic basement, following the chronological order exposed before.

In the Central Cordillera, an important gold belt had

been reported The Middle Cauca Belt is a structure that starts at north in the Antioquia Batholith with deposits like Titiribí ending at south in El Poma (Bissig et al. 2017).

It was formed in a transtensional tectonic setting and the gold mineralization is associated with Miocene magmatism (Sillitoe 2008). Another important gold region is the Cajamarca-Salento district, which is located at the southeast of the Middle Cauca Belt. The most important deposit in this district is La Colosa, a gold-rich porphyry deposit associated to the intrusion of andesitic to dacitic porphyries, hosted by black schists and quartzites from the Cajamarca Complex (Gil-Rodriguez 2010).

3 Methodology

Thirty rock samples were collected during several field trips through series of outcrops on “Las Hormas” creek. Respective macroscopic descriptions were done, characterizing the hydrothermal alteration and the types of veinlets. Ten significant samples were selected for petrographic and metallographic studies using polished thin sections. Raman spectroscopy was used to verify metallographic and petrographic observations.

Furthermore, some points were analyzed using TerraSpec with the aim to identify alteration minerals. Data was taken with an equipment model 350-2500 ASD inc© and it was analyzed with the softwares SpecMin-Pro-3.1. Version and The Spectral Geologist (TSG). In order to verify and complement the previous data, X-ray Diffraction was done in all samples using a Brucker D2 phaser Diffractometer, the data was analyzed with the software DIFFRAC.EVA.

Finally, WDS points were measured over sphalerites, pyrites and tellurides using an electronic microprobe JEOL JXA-8230.

4 Results

In the creek three different rocks were identified. The hypabyssal bodies were classified using the QAPF triangle for volcanic rocks of Streckeisen (1980):

-Dacite 1: Dacite with a green matrix product of chloritization. (Fig. 2).



Figure 2. Outcrop of Dacite 1 composed mainly by quartz and plagioclase. The green color of the rock is related with the chloritic alteration.

-Dacite 2: Dacite with a whitish color, with quartz, sericite and disseminate pyrite, hints for a phyllic alteration (Lowell 1970). Also, some sulphide veinlets were observed (Fig. 3).

Field observations show that Dacite 1 cuts Dacite 2

and that both have different grain size. In muscovite-quartz schists with graphite, a phyllic alteration was recognized by the presence of quartz and sericite. Additionally, some veinlets of sulphides clearly cut the foliation planes of the rock (Fig. 4).

The last event identified in the area was quartz-veins with disseminated sulphides, cutting the foliation of the schists.

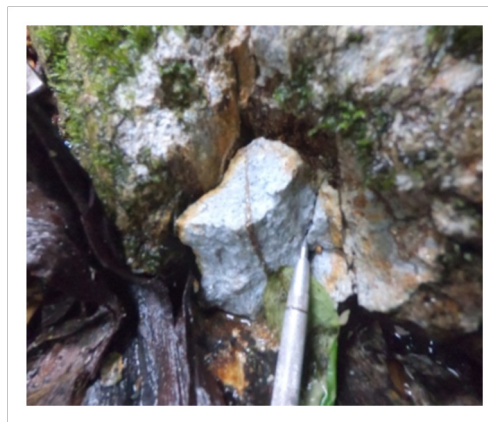


Figure 3. Outcrop of Dacite 2. Whitish color due to phyllic alteration, presence of a sulphide veinlet.



Figure 4. Muscovite-quartz schists with graphite. Phyllic alteration in different areas. Veinlets of sulphides are clearly observed.

4.1 Structural control

In La Colosa, the deposit is affected by Palestina fault, which allows the ascent and the emplacement of the porphyries that initiated the mineralization. A similar geological control exists in California due to the interactions of Ibague and Palestina faults, considering that Cauca-Romeral faults system, Ibague fault and Palestina fault is a conjugate dextral-fault set.

4.2 Mineralization

The mineralization was divided in two zones, according to alteration and mineral assemblage:

Zone 1: Lithologies with phyllic alteration, sulphides veinlets, tetradymite and structural gold.

Zone 2: Quartz veins with disseminated sulphides cutting the foliation of the schists.

In the first zone, the mineral assemblage is: Quartz+Pyrite+Chalcopyrite+Arsenopyrite+Sphalerite+Galena+Marcasite+Pyrrhotite+Tetradymite+High

crystallinity illite+Jarosite (Fig 5 and 6).

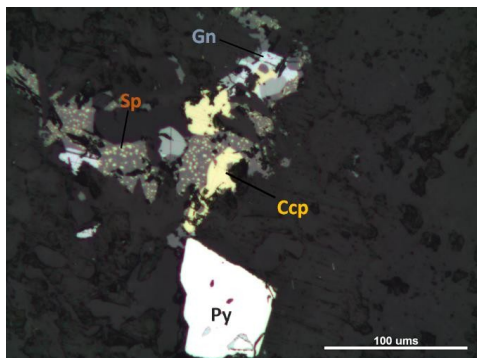


Figure 5. Reflected light photomicrograph with crossed nicols of Dacite 1. Note chalcopyrite disease in sphalerite. Pyrite (Py), Chalcopyrite (Ccp), Sphalerite (Sp) and Galena (Gn).

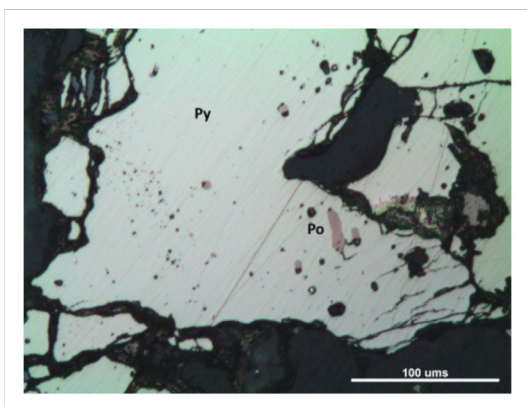


Figure 6. Reflected light photomicrograph with crossed nicols of a veinlet in a muscovite-quartz schist with graphite. Pyrite (Py), Pyrrhotite (Po).

According to Table 1, the high crystallinity illite was determined using X-ray diffraction and the relation $(\text{ALOH}/\text{H}_2\text{O}) > 1$ (Pontual 1997). Steiner (1968) and Reyes (1990) established that when illite has a high crystallinity the temperatures should be over 300 °C. This information fits with the presence of >250 °C minerals like pyrrhotite and arsenopyrite.

Table 1. Data and relations obtained using The Spectral Geology (TSG).

Sample	ALOH	H2O	ALOH/H2O	Mineral	Temperature
AFG-003 (schist)-no alteration	0,147	0,0311	4,734	MUSCOVITE	<300°C
AFG-004 (schist)-S.phyllic alteration	0,23	0,0588	3,907	ILLITE	220°C-300°C
AFG-004 (schist)-S.phyllic alteration	0,147	0,0482	3,047	ILLITE	220°C-300°C
AFG-002 (schist)-L.phyllic alteration	0,214	0,0943	2,275	ILLITE	220°C-300°C
AFG-005 (dacite)-S.phyllic alteration	0,279	0,134	2,084	ILLITE	220°C-300°C
AFG-002 (schist)-L.phyllic alteration	0,429	0,23	1,866	ILLITE	220°C-300°C
AFG-005 (dacite)-S.phyllic alteration	0,338	0,182	1,861	ILLITE	220°C-300°C
AFG-005 (dacite)-S.phyllic alteration	0,295	0,165	1,787	ILLITE	220°C-300°C
AFG-006 (dacite)-S.phyllic alteration	0,533	0,313	1,703	ILLITE-SMECTITE?	220°C-300°C
AFG-006 (dacite)-S.phyllic alteration	0,531	0,317	1,674	ILLITE-SMECTITE?	220°C-300°C
AFG-004 (schist)-phyllic alteration	0,333	0,2	1,662	ILLITE-SMECTITE?	220°C-300°C
AFG-008 (tectonic breccia)	0,321	0,227	1,412	ILLITE-SMECTITE?	220°C-300°C
AFG-006 (dacite)-S.phyllic alteration	0,445	0,319	1,394	ILLITE-SMECTITE?	220°C-300°C
AFG-021 (dacite)-Chloritic alteration	0,198	0,149	1,334	ILLITE	220°C-300°C
AFG-008 (tectonic breccia)	0,174	0,131	1,333	Phengite	220°C-300°C
AFG-020 (schist)-S.phyllic alteration	0,298	0,233	1,279	ILLITE	220°C-300°C
AFG-020 (schist)-S.phyllic alteration	0,123	0,109	1,125	ILLITE	220°C-300°C
AFG-005 (dacite)-S.phyllic alteration	0,187	0,234	0,796	ILLITE	220°C-300°C
AFG-004_Supergene	0,165	0,248	0,667	SMECTITE-ILLITE	220°C-300°C

Structural gold values of 250 ppm were found in the pyrites of this area. This high concentration of gold in pyrites is related with shearing processes in the area that

allow tellurium to enter in the lattice of pyrite as small inclusions. These inclusions create an empty space where gold can enter (Cook et al. 2009).

The GGIMFis geothermometer proposed by Frenzel et al. (2016) was applied. In this area, sphalerites show temperatures of ~253 °C. This geothermometer fits properly with the temperatures shown by the clay minerals (Table 2).

Table 2. Concentrations (%wt) of different elements in sphalerites. The temperatures were obtained replacing values of Ga, Ge, In, Mn and Fe on the equation published in Frenzel et al. (2016).

SAMPLE	AFG020-6,1	CAM5-4,2	CAM5-6,1	CAM5-6,2
Ga	0,053	0,104	0,104	0,132
Zn	42,879	60,158	63,291	59,211
S	37,753	33,369	33,258	33,419
Mn	0,243	0,158	0,085	0,139
Fe	18,965	2,222	1,716	2,945
Cd	0,678	0,818	1,042	0,819
Ge	0,019	0,036	0,01	0,033
In	0,007	0,001	0,014	0,005
ZONE	1	2	2	2
T (°C)	253,012	164,400	183,572	176,491

In the second zone, the mineral assemblage is: Pyrite+Sphalerite+Galena+Chalcopyrite+Carbonates+Quartz (Fig 7 and 8).

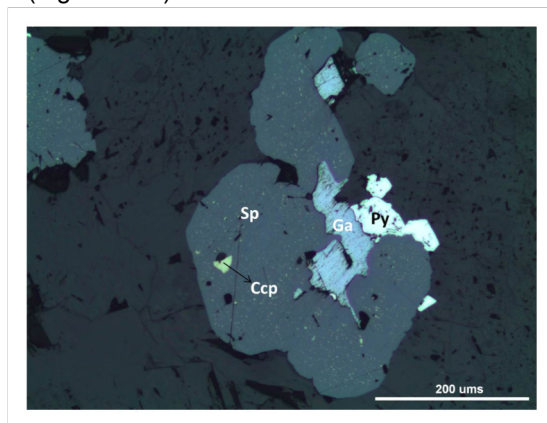


Figure 7. Reflected light photomicrograph with crossed nicols of a quartz vein. Pyrite (Py), Chalcopyrite (Ccp), Sphalerite (Sp) and Galena (Ga).

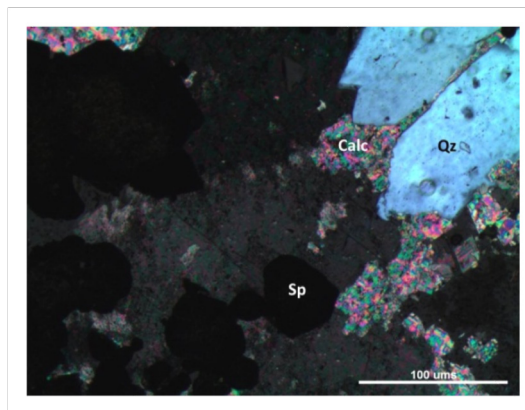


Figure 8. Reflected light photomicrograph with crossed nicols of a quartz vein. Quartz (Qz), Carbonates (Calc) and Sphalerite (Sp).

The temperatures in this area using the GGIMFis geothermometer are ~ 174 °C which are consistent with

the mineral assemblage. Note that the sphalerite crystals are bigger and euhedral in this area.

5 Conclusions

The mineral occurrence is divided in two main zones. The first one shows phyllic alteration with temperatures ~253 °C and the mineral assemblage of pyrite, marcasite, pyrrhotite, sphalerite, chalcopyrite, galena, tetradymite, high crystallinity illite and jarosite. The second zone presents a simple mineralogy of quartz, sphalerite, chalcopyrite, galena and carbonates with temperatures of ~174 °C.

The occurrence of structural gold in pyrite is associated with the presence of tellurium in the area.

The disseminated mineralization accompanied by phyllic alteration produced by the intrusion of hypabyssal bodies, may suggest the existence of an unroofed porphyry system with an epithermal overprint. However, more field, geochemical and isotopic evidence is needed to confirm this supposition.

Tetradymite is a good pathfinder, due to its relation with gold mineralization within the area. In Colombia, there are only few articles and investigations where tellurides systems are reported and studied. California is a good prospect for gold greenfield exploration due to the structural setting, mineralogy, temperatures and gold mining history.

Acknowledgements

Thanks to the Universidad Nacional de Colombia for all the support and equipments that make possible this work. To the Professors Dr rer nat. Ana Elena Concha Perdomo, M.Sc. Jimmy Fernández Lamus, B.Sc Gloria Inés Rodríguez, Ph.D. Analia Del Valle Pantorilla, M.Sc Germán Bonilla Osorio and Ph.D. Thomas Kramer. To the geologists M.Sc. Ruben Gaitán, M.Sc. Carolina Jimenez, M.Sc. Natalia Guerrero, M.Sc. Leonardo Santacruz and M.Sc. Milton Linares.

References

- Bissig T, Leal-mejía H, Stevens RB, Hart CJR (2017) High Sr / Y Magma Petrogenesis and the Link to Porphyry Mineralization as Revealed by Garnet-Bearing I-Type Granodiorite Porphyries of the Middle Cauca Au-Cu Belt, Colombia. *Soc Econ Geol* 112:551–568
- Cooke DR, Deyell CL, Waters PJ, et al (2011) Evidence for Magmatic-Hydrothermal fluids and Ore-Forming Processes in Epithermal and Porphyry deposits of the Baguio District, Philippines. *Econ Geol* 106:1399–1424
- Cook NJ, Ciobanu CL, SPRY PG, Voudouris P (2009) Mineral Deposits. *Essentials Miner Explor Eval* 32:.. doi: 10.1016/B978-0-12-805329-4.00009-0
- Frenzel M, Hirsch T, Gutzmer J (2016) Gallium, germanium, indium, and other trace and minor elements in sphalerite as a function of deposit type - A meta-analysis. *Ore Geol Rev* 76:52–78. doi: 10.1016/j.oregeorev.2015.12.017
- Gil-rodríguez J (2010) Igneous petrology of the Colosa Gold-rich System (Tolima, Colombia). University of Arizona
- Leal-Mejía H (2011) Phanerozoic Gold Metallogeny in the Colombian Andes: A Tectono-Magmatic Approach. Dissertation, Universitat de Barcelona
- Lesage G, Richards JP, Muehlenbachs K, Spell TL (2013)

- Geochronology, Geochemistry, and Fluid Characterization of the Late Miocene Buriticá Gold Deposit, Antioquia Department, Colombia. *Econ Geol* 108:1067–1097
- Maya M, González H (1995) Unidades litodémicas en la Cordillera Central de Colombia. *Boletín Geológico, Ingeominas* 11
- Muntean JL, Einaudi MT (2000) Porphyry Gold Deposits of the Refugio District, Maricunga Belt, Northern Chile. *Econ Geol* 95:1445–1472
- Santacruz L (2011) Microtermometria de inclusiones fluidas aplicada al depósito de Marmato. Dissertation, Universidad Nacional de Colombia, Sede Bogotá
- Sillitoe RH (1979) Some Thoughts on Gold-Rich Porphyry Copper Deposits. *Miner Depos* 14:161–174
- Sillitoe RH (2000) Gold-Rich Porphyry Deposit: Descriptive and Genetic Models and Their Role in Exploration and Discovery. *SEG Rev* 13:315–345
- Sillitoe RH (2008) Special paper: Major Gold Deposits and belts of the North and South American Cordillera: Distribution, Tectonomagmatic Settings, and Metallogenic Considerations. *Econ Geol* 103:663–687
- Sillitoe RH, Tolman J, Van Kerkvoort G (2013) Geology of the Caspiche Porphyry Gold-Copper Deposit, Maricunga Belt, Northern Chile. *Econ Geol* 108:585–604
- Sinton CW, Duncan R a., Storey M, et al (1998) An oceanic flood basalt province within the Caribbean plate. *Earth Planet Sci Lett* 155:221–235
- Steiner A (1968) Clay minerals in hydrothermally altered rocks at Wairakei, New Zealand. *Clays Clay Miner* 16:193–213. doi: 10.1346/CCMN.1968.0160302
- Streckeisen A (1980) Classification and nomenclature of plutonic rocks recommendations of the IUGS subcommission on the systematics of Igneous Rocks. *Geol Rundschau* 69:194–207.
- Pontual (1997) Spectral Analysis Guides for Mineral Exploration
- Reyes AG (1990) Petrology of Philippine geothermal systems and the application of alteration mineralogy to their assessment. *J Volcanol Geotherm Res.* doi: 10.1016/0377-0273(90)90057-M
- Teal L, Benavides A (2011) History and Geologic Overview of the Yanacocha Mining District, Cajamarca, Peru. *Econ Geol* 105:1173–1190
- Toussaint JF, Restrepo JJ (1982) Magmatic Evolution of the Northwestern Andes of Colombia. *Earth Sci Rev* 18:205–213
- Vila T, Sillitoe RH (1991) Gold-Rich Porphyry Systems in the Maricunga Belt, Northern Chile. *Econ Geol* 86:1238–1260.
- Villagómez D (2010) Thermochronology, Geochronology and Geochemistry of the Western and Central Cordilleras and Sierra
- Villagómez D, Spikings R (2013) Thermochronology and tectonics of the Central and Western Cordilleras of Colombia: Early Cretaceous-Tertiary evolution of the Northern Andes. *Lithos* 160–161:228–249
- Villagómez D, Spikings R, Magna T, et al (2011) Geochronology, geochemistry and tectonic evolution of the Western and Central cordilleras of Colombia. *Lithos* 125:875–896
- White NC, Hedenquist JW (1995) Epithermal Gold Deposits: Styles, Characteristics and Exploration. *SEG News* 23:9–13

Geology setting and metallogensis of the Alta Floresta Province, southern Amazon Craton (Brazil)

Veronica Trevisan, Roberto Xavier

Institute of Geosciences, University of Campinas, Brazil

Steffen Hagemann, Anthony Kemp, Robert Loucks

Centre for Exploration Targeting, The University of Western Australia, Australia

Jian-Feng Gao

State Key Laboratory of Ore Deposit Geochemistry, Chinese Academy of Sciences, Guiyang, China

Abstract. The Alta Floresta Province consists of Paleoproterozoic plutonic-volcanic sequences (2.01-1.75 Ga) originated from a series of successive magmatic arcs that accreted to the southwestern margin of the Central Amazon Province. The geologic framework of the eastern sector of the province is organized into: 2.8-1.97 Ga deformed metamorphic and metamorphosed granitic basement; 1.97-1.78 Ga I-type plutonic-volcanic and volcano-sedimentary sequences; 1.78-1.77 Ga post-orogenic and anorogenic plutonic-volcanic units; and Mesoproterozoic (~1.3 Ga) to Quaternary sedimentary sequences. The ore deposits are clustered into four main groups: (i) disseminated Au-Cu-Mo; (ii) structurally-controlled vein-type Au-Cu-Mo; (iii) disseminated Cu-Mo; and (iv) structurally-controlled vein-type Au-Zn-Pb-Cu. Groups (i) to (iii) are characterized by pyrite-chalcopyrite-molybdenite, whereas group (iv) consists of pyrite-sphalerite-galena-chalcopyrite-digenite. In most deposits, mineralization is contained within muscovite-chorite-quartz-rich or silica-rich zones. The fluid regime of groups (i) and (ii) is mainly represented by CO₂-rich fluids, whereas group (iv) by two-phase aqueous fluids with heterogeneous degree of filling. Re-Os on pyrite and molybdenite and Pb-Pb on pyrite geochronology systematics constrain the mineralization age between 1.84 - 1.77 Ga. This overlaps with the ages of porphyritic granitoids, and in a regional scale with ages of the Colíder and Teles Pires suites. These deposits represent magmatic-hydrothermal systems and are considered to share broad similarities with porphyry-epithermal deposits.

1 Introduction

The Alta Floresta Province (AFP) is located in the southern sector of the Amazon Craton, between the Tapajós-Parima (2.03 - 1.88 Ga) and Rondônia-Juruena (1.82 - 1.54 Ga) tectonic provinces (Santos et al. 2006) in the Mato Grosso state, Brazil. The province outlines a NW-SE to E-W-striking belt of 500 km extent and 30 km wide containing plutonic-volcanic sequences generated in continental arc to post-collisional settings during the Paleoproterozoic (2.01 – 1.75 Ga; Souza et al. 2005; Paes de Barros 2007, Assis 2015) (Fig. 1). This province has historically been an important gold-producing region in Brazil (~4 Moz from 1990 and 1999), especially its

eastern segment, where the number of mining sites totals over a hundred placer and medium to high-grade and low-tonnage (< 5t) “hard rock” gold deposits, mainly exploited by local artisanal prospectors (garimpeiros; Paes de Barros 2007). However, since the 1980’s, junior companies, and more recently (2015 to today) major companies, have been exploring and discovering large-scale “hard rock” polymetallic deposits. The scarcity of outcrops, the Mesoproterozoic to Quaternary sedimentary cover over the plutonic-volcanic sequences, and poor understanding of geological controls for the mineralization have made exploration challenging in this region.

Based on the metallic association and mineralization style, the deposits are clustered into four main groups (Xavier et al. 2011; Trevisan et al. 2017): (i) disseminated Au-Cu-Mo mineralization (e.g. Luizão, Pé Quente, X1 and Serrinha deposits); (ii) structurally-controlled vein-type Au-Cu-Mo mineralization (e.g. Paraíba, Pezão, and Peteca deposits); (iii) disseminated Cu-Mo mineralization (e.g. Ana, Jaca and Paraíba deposits); and (iv) structurally-controlled vein-type Au-Zn-Pb-Cu mineralization (e.g. Francisco, Bigode, Carrapato and Luiz deposits).

This work provides an overview of the regional geology and main characteristics of these deposits based on host rocks, structures and vein textures, hydrothermal alteration, ore associations, fluid regime, and U-Pb, Pb-Pb and Re-Os geochronology. These deposits have been considered (Moura et al. 2006; Xavier et al. 2011; Trevisan et al. 2017; Assis et al. 2017; Xavier et al. 2011; Trevisan et al. 2017; Assis et al. 2017) to represent magmatic-hydrothermal systems that display broad similarities to Au-Cu-Mo, Cu-Mo porphyry and Au-Zn-Pb-Cu epithermal systems.

2 Regional geology

In the eastern sector of the AFP, basement rocks of Orosirian age (2.8 – 1.97 Ga) rarely crop out and include tonalitic-to-granitic gneiss and migmatite intruded by calc-alkaline foliated and nondeformed monzogranite to tonalite (Paes de Barros 2007; Assis et al. 2017). The previous units are crosscut by Orosirian non-deformed I-type granitoids including the Aragão granite (1.99 – 1.93 Ga; Miguel-Jr 2011), Novo Mundo granite

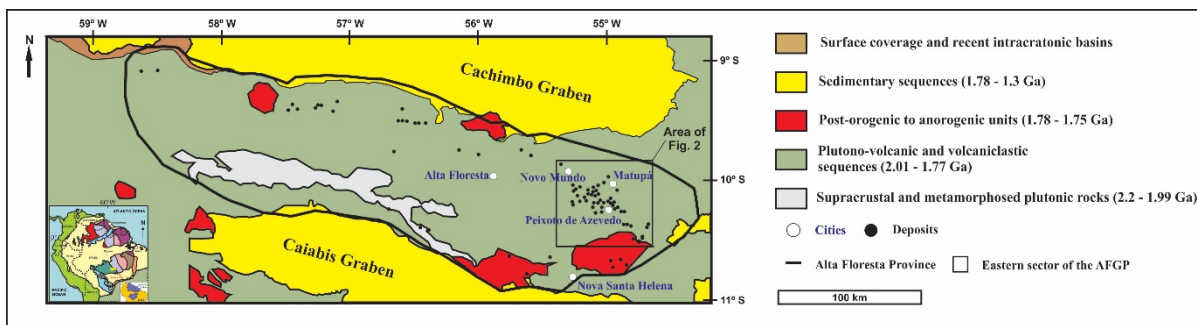


Figure 1. Simplified geological map of the AFP showing the distribution of the mineral occurrences (Modified from Paes de Barros 2007).

(Paes de Barros 2007) that varies from monzogranite (1.97 Ga) to syenogranite (1.96 Ga), Pé Quente Intrusive Suite composed of monzonite (1.97 Ga; Miguel-Jr 2011) and biotite tonalite (1.9 Ga; Assis 2015), Nhandu granite (1.88 – 1.84 Ga; Silva and Abram 2008), Matupá Intrusive Suite (1.87 – 1.86 Ga; Moura et al. 2006), Flor da Mata granite (1.87 Ga; unpublished data), União do Norte granodiorite (1.85 Ga; Miguel-Jr 2011), undifferentiated granite (1.8 Ga; unpublished data), and Peixoto granite (1.79 – 1.78 Ga; Paes de Barros 2007; Silva et al. 2014). Except for the Flor da Mata, undifferentiated and Peixoto granites, all other units host mineralization. Collectively, these plutonic-volcanic sequences show affinities to oxidized I-type, calc-alkaline, medium to high-K, metaluminous to slightly peraluminous granites originated in continental arc settings. Also, volcanoclastic sediments represented by immature feldspathic-sandstone, feldspathic-wacke, lithic-sandstone, and conglomerate rocks from the Serra Formosa Formation overlie an unknown basement (~2.0 Ga; Miguel-Jr 2011).

These units are often crosscut by dikes and rocks that vary in composition from basalt-diorite-gabbro to andesite-dacite. According to Duarte (2015), this ~1.82 – 1.77 Ga mafic-intermediate magmatism episode may belong to the Colíder suite, which also hosts mineralization.

Units listed above are intruded by post-orogenic and anorogenic felsic plutonic-volcanic units represented by the Teles Pires Intrusive suite (1.78 – 1.75 Ga; Silva and Abram 2008), which includes the União do Norte porphyry (1.77 Ga; Miguel-Jr 2011) and the Braço Sul tuffs (unknown age; Paes de Barros 2007).

Overlying all the units listed above are Mesoproterozoic rocks of the Caiabis group (Dardanelo Formation), composed of sandstone, arkose, siltstone, mudstone, volcanic greywackes and basal conglomerate (maximum ages ~1.3 Ga; Leite and Saes 2003). The Mesozoic and Cenozoic are represented by detritus-lateritic covers, whereas the Quaternary by alluvial deposits (Souza et al. 2005) (Fig. 2).

Despite the lack of consensus regarding the regional tectonic framework of the AFP, Assis (2015) correlates the units to three tectono-magmatic events: (stage 1) 2.1 to 1.95 Ga, coeval with the Cuiú-Cuiú magmatic arc defined by the Tapajós-Parima tectonic province; (stage 2) 1.88 to 1.82 Ga, Juruena magmatic arc evolved within

the Rondônia-Juruena tectonic province; and (stage 3) 1.78 to 1.75 Ga, the post-orogenic and anorogenic felsic magmatism of the Juruena magmatic arc.

3 Features of the deposits

3.1 Host rocks

The deposits in the AFP are mainly hosted by tonalitic to syeno-monzogranitic intrusions (1.98, 1.90 and 1.87 Ga), quartz-feldspar porphyries (1.98, 1.97 and 1.77 Ga), and, to a lesser degree, basement rocks (2.0 to 1.98 Ga) and volcanic/volcanoclastic sequences (2.0 Ga) (Moura et al. 2006, Paes de Barros 2007, Silva and Abram 2008, Assis et al. 2017). In some deposits, aplitic and mafic to intermediate rocks of unknown ages frequently contain mineralization (e.g. Luiz and Pé Quente deposits).

3.2 Structures and vein textures

The vein-type deposits are controlled by NNW, NW and E-W-striking shear zones or faults. The veins commonly display massive to banded, open-space filling (e.g. comb, crustiform, zonal, colloform, cockade, mini geodes), recrystallization (e.g. flamboyant or feathery), platy (e.g. bladed calcite and quartz), and vuggy textures. Stockwork veins and hydrothermal breccias are also found in these deposits (Trevisan 2015).

3.3 Hydrothermal alteration and mineralization

In all deposits, the mineralization occurs within and/or enveloped by pervasive muscovite-quartz-sulfides-carbonate-magnetite (phyllitic alteration), orthoclase-quartz-hematite-sulfides-microcline or biotite-quartz-magnetite-carbonate-sulfides (potassic alteration) halos or silicification represented by fronts of replacement or aggregates and quartz infill alteration (e.g. quartz veins, stockwork zones, fracture-fill, and hydrothermal breccias). However, disseminated gold mineralization associated with early pervasive albite-quartz-coarse-grained pyrite (sodic alteration) is also recognized at Pé Quente deposit. Outwards from the ore zones, carbonatization, silicification, potassic (K-feldspar),

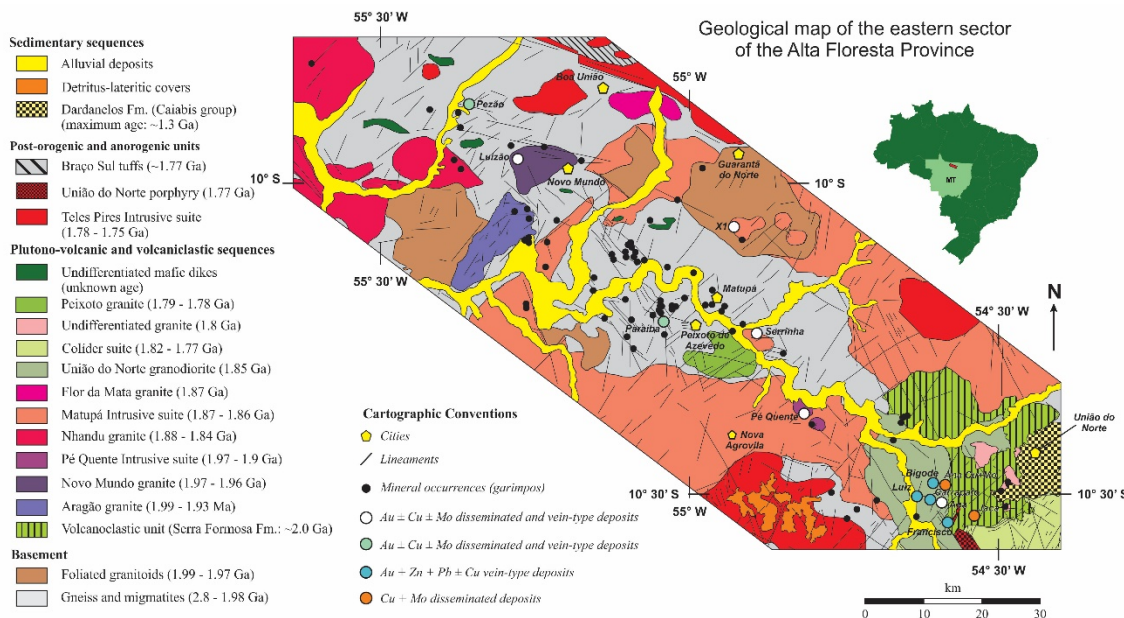


Figure 2. Geological map of the eastern sector of the Alta Floresta Province (Modified from Assis *et al.* 2017)

epidote-clinozoisite-chlorite-calcite-apatite-rutile-magnetite-hematite-pyrite assemblage (propylitic alteration) and late veinlets with variable composition (carbonate, quartz, quartz-carbonate, epidote, sericite and chlorite) are important hydrothermal alteration types, whereas kaolinite-sericite-quartz-hematite assemblage (argillic alteration) is also found in distal zones at the Francisco and Bigode deposits.

The ore paragenesis in groups (i), (ii) and (iii) consists mainly of pyrite-chalcopyrite-molybdenite-magnetite, whereas in the group (iv) is represented by pyrite-sphalerite-galena-chalcopyrite-digenite. In all groups, gold occurs as inclusions mainly in pyrite and, to a lesser extent, in galena or as free gold. (Assis 2015, Trevisan 2015, Trevisan *et al.* 2017, Assis *et al.* 2017).

3.4 Fluid characteristics

Fluid inclusion studies in quartz from the ore zones of the deposits belonging to groups (i) and (ii) reveal the presence of three types of fluids: (i) two-phase aqueous with variable salinity (2.1 – 26.1 wt.% eq. NaCl) and homogenization temperature between 126.5°C and 268.4°C; (ii) aqueous-carbonic fluids of low salinity (6.1 to 8.9 wt.% eq. NaCl) and homogenization temperatures between 251.6°C and 334.6°C; and, more subordinately, (iii) high saline (33.6 to 37 wt.% eq. NaCl) aqueous fluid represented by halite-bearing fluid inclusions with homogenization temperatures between 98.9 and 211.9°C and dissolution temperature of halite between 200.2 and 280.3°C (Assis 2015, Trevisan *et al.* 2017). In contrast, fluid inclusions in group (iv) deposits are represented by aqueous fluids of low to moderate salinity (up to 24 wt.% eq. NaCl) and variable homogenization temperatures between 85.3°C and 373.2°C (Assis 2015; Trevisan *et al.* 2017).

Oxygen, deuterium, and sulfur isotope data (Assis

2015) point to a predominant contribution of magmatic water for the formation of groups (i) and (ii) deposits, whereas external fluids (meteoric) may have strongly interacted with magmatic fluids in the case of group (iv) deposits. There is no fluid inclusions or stable isotopes data available in the literature for group (iii) so far.

3.5 Timing of mineralization

The Re-Os ages obtained in pyrite and molybdenite from groups (i) and (ii) deposits yielded weighted average model ages at 1786.7 ± 3.2 Ma (MSWD = 0.96; molybdenite, X1 deposit; Assis *et al.* 2017), 1787 ± 6.2 Ma (MSWD = 2.2; pyrite, Luizão deposit; Assis *et al.* 2017), 1787 ± 5.5 Ma (MSWD = 0.99; pyrite, Pé Quente deposit; Assis *et al.* 2017), and 1787 ± 17 Ma (molybdenite, Paraíba deposit; unpublished data). Conventional Pb-Pb geochronometry yielded an age of 1841 ± 22 Ma (MSWD = 1.6; Santos 2011) in pyrite from the Paraíba deposit. The Re-Os analyses in sulfides from group (iii) deposits are still under progress.

Sericite ^{40}Ar - ^{39}Ar plateau ages from the phyllic alteration halo of the Francisco deposit (group iv) yielded ages between 1779 ± 6.3 and 1777 ± 6.3 Ma (Assis 2015), very similar to the Re-Os ages obtained for groups (i) and (ii).

4 Conclusions and future work

The continental arc setting attributed to the AFP plutonic-volcanic units, the close spatial relationship between the mineralization and granitic plutons, structures and vein textures, types and distribution of the hydrothermal alteration and ore paragenesis, collectively suggest that the Au-Cu-Mo, Cu-Mo and Au-Zn-Pb-Cu deposits may be genetically linked to the emplacement of magmatic-hydrothermal systems. This is further corroborated by the

pyrite and molybdenite Re-Os and sericite ^{40}Ar - ^{39}Ar ages described above that closely overlap the crystallization ages of the quartz-feldspar porphyries at the X1 (1.78 Ga; Assis 2015) and Paraíba (1.79 Ga). A similar age interval has also been obtained for other intrusion-hosted deposits in the province: Re-Os model ages of pyrite of ~1.78 Ga for the Luizão and Pé Quente deposits; Re-Os model age of 1.8 Ga in ore-related molybdenite at the Juruena gold district (Paranaíta suite) in the northern sector of the province (Serrato 2014). Nevertheless, quartz-feldspar porphyry outcrops or interception by drill cores have not been reported so far in these cases. Hence, the interval of 1.77 to 1.84 Ga seems to mark an important regional metallogeny episode in the Alta Floresta Province. The regional felsic magmatism in the province that displays a broad temporal association with this 1.77 – 1.84 Ga event includes volcanics and granitic intrusions that belong to the Colíder (1.82 – 1.77 Ga), Paranaíta (1.81 – 1.79 Ga) and Teles Pires (1.78 – 1.75 Ga) intrusive suites.

At the deposit scale, exsolution of aqueous-carbonic fluids from crystallizing quartz-feldspar porphyries in the deposits belonging to groups (i) and (ii) may have triggered the magmatic-hydrothermal system. The CO₂-rich nature of these magmatic fluids suggest that emplacement of the causative porphyries likely occurred at deep crustal levels, since the solubility of volatiles in magma is controlled dominantly by pressure (Lowenstern 2001). Heterogeneous entrapment by fluid phase separation (immiscibility processes) accompanied by progressive mixing with externally-derived fluids (meteoric) causing CO₂ dilution and cooling may have caused the lowering of the solubility of gold and other metals. In contrast, in the case of group (iv), boiling process may have driven precipitation of metals in a shallower crustal level.

Based on the geotectonic setting, combined with the geological characteristics of the mineralization and their temporal relationship with the porphyritic rocks, we argue that ore-forming processes at the deposits from the eastern sector of the Alta Floresta Province were similar to those observed in Mesozoic-Cenozoic Au-Cu-Mo and Cu-Mo-Au porphyry systems, but emplaced at deeper crustal levels, and Au-Zn-Pb-Cu epithermal systems.

Future work will include dating of granitoids via SHRIMP U-Pb on zircon, which will potentially provide crystallization ages that can help to better constrain the magmatic framework of the eastern sector of the province. Whole-rock geochemical analyses, and Lu-Hf, trace elements and O isotopes analyses on the same zircons will be applied in order to constrain the chemistry, source/contamination, evolution and fertility potential of the magmas.

Acknowledgements

This research was funded by CNPq/Brazil (grant 142061/2016-6) and SKLODG/Chinese Academy of Sciences (project number 201507).

References

- Assis RR (2015) Depósitos auríferos associados ao magmatismo félsico da Província de Alta Floresta (MT), Cráton Amazônico: litogeoquímica, idade das mineralizações e fonte dos fluidos. Thesis, University of Campinas.
- Assis RR, Xavier RP, Creaser RA (2017) Linking the Timing of Disseminated Granite-Hosted Gold-Rich Deposits to Paleoproterozoic Felsic Magmatism at Alta Floresta Gold Province, Amazon Craton, Brazil: Insights from Pyrite and Molybdenite Re-Os Geochronology: *Economic Geology*, 112:1937-1957.
- Duarte TB (2015) Geologia, geoquímica e geocronologia do domínio vulcânico do arco magmático Juruena, SW do Cráton Amazônico. Dissertation, University of Campinas.
- Leite JAD and Saes GS (2003) Geocronologia Pb/Pb de zircões detríticos e análise estratigráfica das coberturas sedimentares proterozóicas do Sudoeste do Cráton Amazônico. *Geologia USP: Série Científica*, 3(10):113-127.
- Lowenstern JB (2001) Carbon dioxide in magmas and implications for hydrothermal systems, *Mineralium Deposita*:36(6):490-502.
- Miguel-Jr E (2011) Controle Estrutural das mineralizações auríferas e idades U-Pb das rochas encaixantes ao longo do Lineamento Peru-Trairão: Província Aurífera de Alta Floresta, Mato Grosso. Dissertation, University of Campinas.
- Moura MA, Botelho NF, Olivo GR, Kyser TK (2006) Granite-related Paleoproterozoic, Serrinha gold deposit, Southern Amazonia, Brazil: hydrothermal alteration, fluid inclusion and stable isotope constraints on genesis and evolution. *Economic Geology*, 101:585-605.
- Paes de Barros AJ (2007) Granitos da região de Peixoto de Azevedo – Novo Mundo e mineralizações auríferas relacionadas – Província Aurífera Alta Floresta (MT). Thesis, University of Campinas.
- Santos JOS, Hartmann LA, Faria MSG, Riker SR, Souza MM, Almeida ME, McNaughton NJ (2006) A compartimentação do Cráton Amazonas em províncias: avanços ocorridos no período 2000–2006, in *Sociedade Brasileira de Geociências, Núcleo Norte (SBG-NO)*, Simpósio de Geologia da Amazônia, 9, Belém, CD-Rom.
- Santos AC (2011) Petrografia e isótopos de chumbo e enxofre de depósitos auríferos da Província Alta Floresta (MT): Implicações Metalogenéticas. Undergraduate thesis, Rio de Janeiro State University.
- Serrato AAA (2014) Geocronologia e evolução do sistema hidrotermal do depósito aurífero de Juruena, Província Aurífera de Alta Floresta (MT), Brasil. Dissertation, University of Campinas.
- Silva MG and Abram MB (2008) Projeto Metalogenia da Província Aurífera Juruena-Teles Pires, Mato Grosso. Goiânia, Serviço Geológico Brasileiro, CPRM.
- Souza JP, Frasca AAS, Oliveira CC (2005) Geologia e Recursos Minerais da Província Mineral de Alta Floresta. Relatório Integrado. Brasília, Serviço Geológico Brasileiro, CPRM.
- Trevisan VG (2015) Estudo comparativo entre mineralizações filonares de Au ± Cu e Au + metais base do setor leste da Província Aurífera de Alta Floresta (MT), Cráton Amazônico. Dissertation, University of Campinas.
- Trevisan VG, Xavier RP, Rodrigues RM, Assis RR, Bartolomeu JO, Matos JHSN, Mesquita MJ (2017) Paleoproterozoic porphyry-related Au ± Cu (± Mo) systems in the Alta Floresta Gold Province, southern Amazonian Craton, Brazil: the case of the X1 and Paraíba deposits. In: 14th SGA Biennial Meeting, Quebec City.
- Xavier RP, Assis RR, Miguel-Jr E, Santos TJS, Paes de Barros AJ (2011) Gold ± copper and gold-base metal deposits associated with granitic systems in the eastern sector of the Alta Floresta Province. In: 12° Simpósio de Geologia da Amazônia, Boa Vista, Roraima. CD-ROM.

Trace element variation in ore minerals from the Iron Cap deposit (KSM), British Columbia, Canada: Implications for fluid evolution in porphyry-epithermal gold systems

Hugh Graham, Daniel Morgan, Robert Chapman, and David Banks

University of Leeds, UK

Abstract. Trace amounts of elements such as As, Sb, Se, Te, Pd, Hg and Au are commonly identified in porphyry and epithermal mineral deposits. Investigating variations in the concentration, distribution and hosting of these elements in an ore mineral suite has the potential to enable elucidation of the specific characteristics of discrete fluids throughout the evolution of a mineralizing magmatic-hydrothermal system. The Iron Cap deposit in the Kerr-Sulphurets-Mitchell (KSM) district, British Columbia, Canada, provides an opportunity to interpret the characteristics of hydrothermal fluids from an early porphyry stage, through transition, to a late epithermal stage. A suite of 60 core samples are characterized by petrographic methods to constrain the sequence of vein formation at Iron Cap, and identify deposit mineralogy. The results of initial trace element analysis of ore minerals by SEM-EDX analysis has shown that pyrite growth zones are Cu- or As-bearing, and arsenopyrite growth zones have a variable Fe:As:S ratio. Galena commonly contains Se, ranging in concentration from ~2 wt. % to clausthalite (PbSe). Additionally, gold in the deposit contains between 2-42 wt. % Ag. These initial discoveries will allow a methodology to be developed to interpret fluid conditions with trace element variations.

1 Introduction

Trace element studies are now increasingly applied to a range of mineral deposits, including porphyry, epithermal, volcanogenic massive sulphide, and orogenic gold (e.g., Huston et al. 1995; Reich et al. 2013; Zhang et al. 2018; Augustin and Gaboury 2019). Sulphides such as pyrite may be analyzed by electron microprobe (EMP) or laser ablation-inductively coupled plasma-mass spectrometry (LA-ICP-MS) to measure the concentration and distribution of elements within a single crystal (e.g., Large et al. 2009). The trace element composition of a crystal can be used to assist the understanding of mineral paragenesis, identify relative element abundances in mineralizing fluids throughout ore formation, enable speculation of fluid conditions (e.g., temperature), and improve mineralization vectoring (e.g., Sykora et al. 2018). However, few studies use trace element data to consider the wide range of factors that could be influential in enrichment or depletion of an element at a given site, such as fluid chemistry (e.g., pH, phase, salinity, fO_2 , fS_2 , ligand availability), trace element mineral incorporation mechanisms (lattice substitution vs. inclusion), fluid-mineral partition coefficients, and the effect of post-deposition remobilization, recrystallization or diffusion

(e.g., Grant et al. 2018). Furthermore, there remains a paucity of research investigating trace elements in an ore mineral suite, where sulphides (e.g., galena, sphalerite, molybdenite, arsenopyrite), sulphosalts (e.g., tetrahedrite-tennantite), tellurides (e.g., hessite, altaite), selenides (e.g., clausthalite, naumannite) and metal alloys may together exhibit a trace element partitioning signature that might better constrain the nature of mineralizing fluids at certain points in time and space, taking into account the above factors.

Porphyry- and epithermal-style mineral deposits are often spatially, temporally and genetically linked as they form from magmatic-hydrothermal systems at convergent tectonic margins (Sillitoe 2010). These magmatic-hydrothermal systems are complex, and comprise multiple stages. As such, there is significant variability in mineralizing fluid characteristics throughout their evolution, with the transitional period from porphyry to epithermal conditions remaining a key topic of discussion (e.g., Gammons and Williams-Jones 1997; Hedenquist et al. 1998; Heinrich 2005; Pudack et al. 2009; Maydagán et al. 2015). The application of a comprehensive trace element study to a porphyry-epithermal system has the potential to elucidate the sequential transitions in physico-chemical conditions of hydrothermal fluids at different stages of deposit formation.

The Iron Cap deposit, in the Kerr-Sulphurets-Mitchell (KSM) district, British Columbia, Canada, exhibits features of both porphyry and epithermal mineralization, and is being investigated as a case study for this research. To date, a suite of 60 core samples have been collected from the deposit, encompassing deep porphyry through to shallow epithermal environments. Here, we present the initial results of petrographic and trace element analyses, and suggest potential methods for interpreting the characteristics of hydrothermal fluids at Iron Cap.

2 Geological setting

The KSM district hosts four Cu-Au, predominantly porphyry-style deposits: Kerr, Sulphurets, Mitchell and Iron Cap. Together, they host proven and probable reserves of 38.8 Moz Au, 4.63 Mt of Cu, 0.09 Mt of Mo and 183 Moz of Ag, at grades of 0.55 g/t Au, 0.21% Cu, 42.6 g/t Mo and 2.6 g/t Ag, making KSM one of the

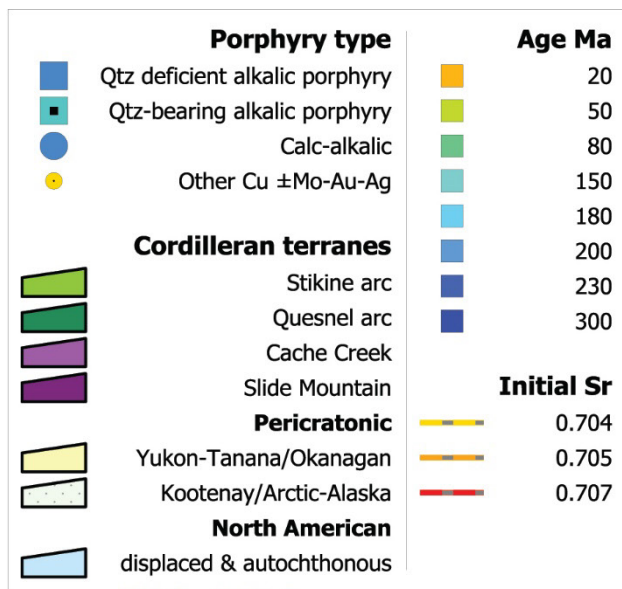


Figure 1. Location of the Kerr-Sulphurets-Mitchell (KSM) district in northwestern British Columbia (modified from Logan and Mihalynuk 2014). Other porphyry deposits of the Canadian Cordillera are also shown, with porphyry type represented by symbol shape, and the age of deposits depicted by colour.

largest undeveloped Cu-Au districts in the world and particularly one of the most gold-rich in terms of total contained metal (Seabridge Gold 2018). KSM is situated in the porphyry-endowed Stikine arc terrane of the Canadian Cordillera, with most deposits in the region having formed during a prolific ~15 m.y. period of mineralization at the Triassic-Jurassic boundary (Fig. 1; Febbo et al. 2015).

A series of Early Jurassic diorite to syenite intrusions are the magmatic source for the KSM deposits, with adjacent wall rocks comprising volcanoclastic and sedimentary units. Mineralization at Iron Cap is

predominantly hosted within porphyritic monzonite and unclassified quartz vein-rich intrusions. The plunging orebody exhibits potassic alteration at depth, zoning outward to peripheral propylitic in the wall rocks, and phyllic alteration that is largely restricted to shallower parts of the deposit (Campbell and Dilles 2017). Deposit margins partially outcrop at surface, with the remainder buried beneath the barren hanging wall of a thrust fault. Post-mineralization deformation occurred in the Middle Cretaceous, with metamorphism reaching lower greenschist facies (Aldrick 1993).

3 Vein generations

Ongoing petrographic analysis of core samples has so far discriminated at least 8 vein stages at Iron Cap (Table 1, Fig. 2). Further work is required to fully characterize all vein generations, ascertain variation in vein mineralogy and confidently determine the relative timing of veins. Additional generations may also be characterized with further petrography.

Table 1. Initial assessment of vein types and order of emplacement in the Iron Cap deposit. Note that not all veins have been analyzed by scanning electron microscopy (SEM) to identify minor phases.

Vein generation	Mineralogy
1	Magnetite-quartz-chalcopyrite ± galena
2	Quartz-pyrite-chalcopyrite-molybdenite ± galena
3	Pyrite-quartz ± chalcopyrite ± galena
4	Chlorite-quartz-chalcopyrite ± galena ± gold
5	Quartz-tennantite/tetrahedrite-chalcopyrite ± galena ± altaite ± Ag-Hg alloy ± hessite ± petzite
6	Quartz-pyrite-chalcopyrite-sphalerite-chlorite-carbonate
7	Quartz-pyrite-arsenopyrite-sphalerite-carbonate ± gold
8	Carbonate

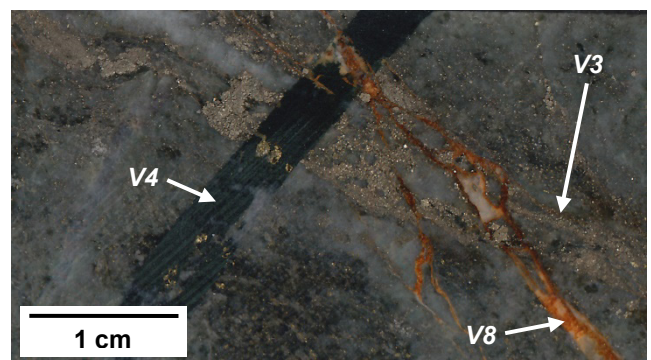


Figure 2. Type occurrences of vein generations 3, 4 and 8, as outlined in Table 1.

4 Initial results and discussion

4.1 Sulphide zonation

Scanning electron microscopy (SEM) has identified a number of trace element variations within pyrite and in arsenopyrite growth zones. Different pyrite generations observed in type 3 vein show variance in Cu, with an increased abundance of galena inclusions in the Cu-bearing pyrite (Fig. 3). This may indicate that boiling was influential in the formation of the Cu-bearing pyrite, owing to the chemistry and inclusion abundance (Román et al. 2018). The chalcopyrite rim grown around the first pyrite generation (Py1) may have sourced the Cu for incorporation into the adjacent Cu-rich pyrite; possibly with recrystallization of chalcopyrite into pyrite, and excess Cu distributed elsewhere. Diffusion of Cu from the chalcopyrite into Py2 may have also occurred, before growth of Py3, as the euhedral crystal shape is preserved, which would likely not be the case if diffusion occurred post-Py3.

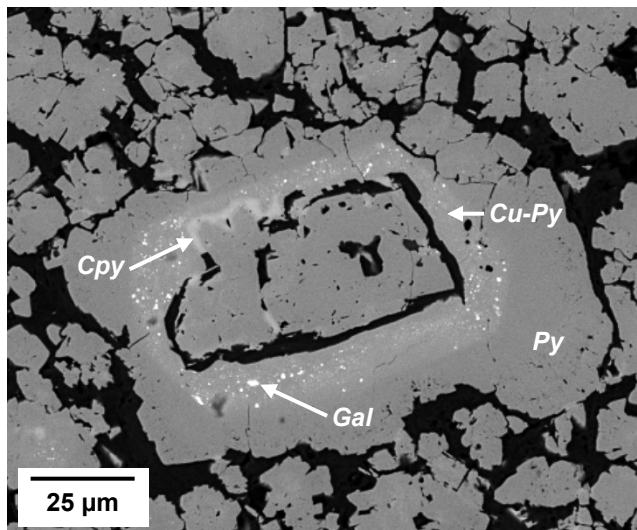


Figure 3. Back scattered electron (BSE) image of a Cu-zoned pyrite crystal with galena inclusions. Py: pyrite, Cpy: chalcopyrite, Gal: galena, Cu-Py: Cu-bearing pyrite.

Arsenic is abundant (> 1% As) in at least two phyllic-altered near-surface samples, both hosting vein type 7. These exhibit zonation in pyrite, with variable As content depicting the generally euhedral growth of crystals, and informing changes in As incorporation. These As-rich zones may represent an increase in the fluid-pyrite partitioning of As related to changing fluid chemistry, with the As content of the fluid probable being a major factor. Arsenopyrite growth on the rims of the As-zoned pyrites suggests that fluid conditions changed significantly post-Py3 to allow deposition of arsenopyrite. However, variation in the composition of arsenopyrite is evident, with changes in the Fe:As:S ratio depicting growth zones (Fig. 4). Of particular interest are certain arsenopyrite zones hosting small (~5 µm or less) gold grains. These provide a specific time constraint on the local deposition of gold.

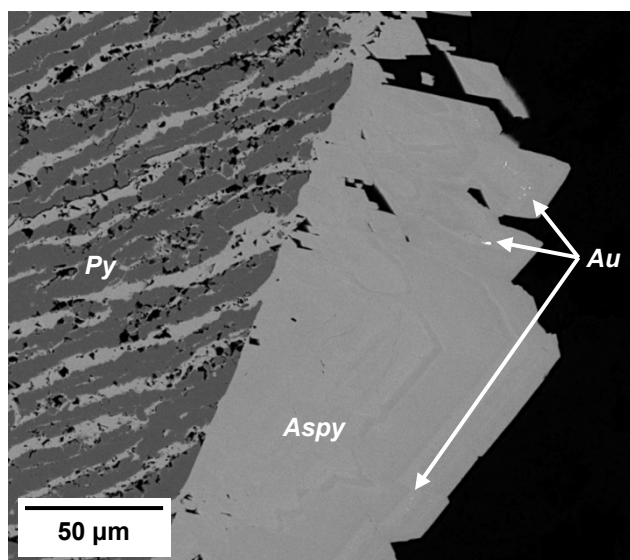


Figure 4. Gold observed in zoned arsenopyrite by BSE imaging. Py: pyrite, Aspy: arsenopyrite, Au: gold.

4.2 Galena-clausthalite series

A solid solution series exists between galena (PbS) and clausthalite (PbSe; Shiga and Urashima 1989). Core samples from different depths and alteration zones in the Iron Cap deposit host galena as a minor phase (including vein types 1-5), and often show the presence of Se in SEM-energy dispersive X-ray (EDX) analysis. When quantitatively measured, variance in the Se content of galena crystals is evident, with some samples having galena of comparable S:Se ratios throughout, and others having variable ratios relating to different vein types or alteration. Rare clausthalite grains also occur. Both Se-bearing galena and clausthalite are commonly found with, or included in chalcopyrite and/or tennantite/tetrahedrite, suggesting similar solubility, transport and deposition controls between Cu and Se. Understanding the controls on the Se:S ratio of the galena-clausthalite series may allow changes in the physico-chemical characteristics of the fluid to be tracked over time and through space. For example, temperature is often proposed to be a key control on the abundance of Se in mineral deposits and, if a similar control exists when incorporating Se into galena, then the temperature evolution of a fluid phase could be constrained by measuring the Se:S ratio of galena crystals throughout the paragenesis (e.g., Auclair et al. 1987; Keith 2016).

4.3 Metal alloys

Gold at Iron Cap is present as inclusions in chalcopyrite, pyrite, arsenopyrite, and also found within cracks in pyrite and rarely free in altered groundmass or vein carbonate. Differences in the Au:Ag ratio of grains between samples, veins and host site have been recognized by SEM-EDX. The range in measured Ag content of gold grains across all the analyzed samples is 2-42 weight % Ag. One sample hosting vein type 5 also contains multiple occurrences of a Ag-Hg alloy, indicating that this vein-forming fluid may have been relatively Au-poor;

additionally suggested by the rare presence of petzite (Ag_3AuTe_2) instead of native gold. Differences in the physico-chemical conditions of the fluids are likely to be a key control on the Au:Ag ratio of native gold (e.g., Gammons & Williams-Jones 1995), and thus investigating metal alloy compositions along with the trace element composition of the ore mineral suite at Iron Cap may provide further constraints on fluid conditions.

5 Conclusions and future work

Initial petrography and SEM has characterized at least 8 vein generations at Iron Cap, knowledge of which are essential to investigate the change in hydrothermal fluid conditions over time, as each vein type relates to a separate or transitioning fluid. Trace element variations have been recognized, with pyrite exhibiting Cu- or As-bearing growth zones, and arsenopyrite showing variable Fe:As:S ratios between zones, with specific zones hosting gold. Galena contains variable amounts of Se, with clausthalite rarely present, and gold exhibits changes in Au:Ag ratio, with a Ag-Hg alloy observed instead of gold in one vein phase. Further analytical work, chiefly EMP and LA-ICP-MS, will quantitatively measure the concentration of trace elements in each vein type, while additional petrography and SEM will fully characterize vein mineralogy and paragenesis, and highlight differences in trace element distribution that can be investigated further. Modelling of fluid conditions using the acquired data will follow, providing insight to the transition from porphyry to epithermal conditions at Iron Cap.

Acknowledgements

This project is funded by the NERC. The lead author thanks Geoscience BC for funds provided through the scholarship program, and the Society of Economic Geologists is acknowledged for financial support provided through a Graduate Student Fellowship. Seabridge Gold Inc. is gratefully acknowledged for access to the KSM project, and for logistical support and accommodation provided during sample collection.

References

Alldrick DJ (1993) Geology and metallogeny of the Stewart mining camp, northwestern BC. BC Min of Energy and Mines, BCGS Bulletin 85:105.

Auclair G, Fouquet Y, Bohn M (1987) Distribution of Selenium in high-temperature hydrothermal sulfide deposits at 13° North, East Pacific Rise. *Can Mineral* 25:577–587.

Augustin J, Gaboury D (2019) Multi-stage and multi-sourced fluid and gold in the formation of orogenic gold deposits in the world-class Mana district of Burkina Faso – Revealed by LA-ICP-MS analysis of pyrites and arsenopyrites. *Ore Geol Rev* 104:495–521.

Campbell ME, Dilles JH (2017) Magmatic History of the Kerr-Sulphurets-Mitchell Copper-Gold Porphyry District, Northwestern British Columbia (NTS 104B). *Geosci BC Sum of Activ* 2016:233–244.

Febbo GE, Kennedy LA, Savell M, Creaser RA, Friedman RM (2015) Geology of the Mitchell Au-Cu-Ag-Mo porphyry deposit, northwestern British Columbia, Canada. *Geol Fieldwork* 2014,

BC Min of Energy and Mines, BCGS paper 2015-1:59–86.

Gammons CH, Williams-Jones AE (1995) Hydrothermal Geochemistry of Electrum: Thermodynamic Constraints. *Econ Geol* 90:420–432.

Gammons CH, Williams-Jones AE (1997) Chemical Mobility of Gold in the Porphyry-Epithermal Environment. *Econ Geol* 92:45–59.

Grant HLJ, Hannington MD, Petersen S, Frische M, Fuchs SH (2018) Constraints on the behavior of trace elements in the actively-forming TAG deposit, Mid-Atlantic Ridge, based on LA-ICP-MS analyses of pyrite. *Chem Geol* 498:45–71.

Hedenquist JW, Arribas A Jr, Reynolds TJ (1998) Evolution of an Intrusion-Centered Hydrothermal System: Far Southeast-Lepanto Porphyry and Epithermal Cu-Au Deposits, Philippines. *Econ Geol* 93:373–404.

Heinrich CA (2005) The physical and chemical evolution of low-salinity magmatic fluids at the porphyry to epithermal transition: a thermodynamic study. *Miner Deposita* 39:864–889.

Huston DL, Sie SH, Suter GF, Cooke DR, Both RA (1995) Trace Elements in Sulfide Minerals from Eastern Australian Volcanic-Hosted Massive Sulfide Deposits. *Econ Geol* 90:1167–1196.

Keith M, Smith DJ, Jenkin GRT, Holwell DA, Dye MD (2017) A review of Te and Se systematics in hydrothermal pyrite from precious metal deposits: Insights into ore-forming processes. *Ore Geol Rev* 96:269–282.

Large RR, Danyushevsky L, Hollit C et al (2009) Gold and Trace Element Zonation in Pyrite Using a Laser Imaging Technique: Implications for the Timing of Gold in Orogenic and Carlin-Style Sediment-Hosted Deposits. *Econ Geol* 104:635–668.

Logan JM, Mihalynuk MG (2014) Tectonic Controls on Early Mesozoic Paired Alkaline Porphyry Deposit Belts (Cu-Au ± Ag-Pt-Pd-Mo) Within the Canadian Cordillera. *Econ Geol* 109:827–858.

Maydagán L, Franchini M, Rusk B et al (2015) Porphyry to Epithermal Transition in the Altar Cu-(Au-Mo) Deposit, Argentina, Studied by Cathodoluminescence, LA-ICP-MS, and Fluid Inclusion Analysis. *Econ Geol* 110:889–923.

Pudack C, Halter WE, Heinrich CA, Pettko T (2009) Evolution of Magmatic Vapor to Gold-Rich Epithermal Liquid: The Porphyry to Epithermal Transition at Nevados de Famatina, Northwest Argentina. *Econ Geol* 104:449–477.

Reich M, Deditius A, Chryssoulis S et al (2013) Pyrite as a record of hydrothermal fluid evolution in a porphyry copper system: A SIMS/EMPA trace element study. *Geochim Cosmochim Acta* 104:42–62.

Román N, Reich M, Leisen M et al (2019) Geochemical and micro-textural fingerprints of boiling in pyrite. *Geochim Cosmochim Acta* 246:60–85.

Seabridge Gold (2018) Mineral reserves and resources, February 2018. <http://seabridgegold.net/resources.php>. Accessed March 2019.

Shiga Y, Urashima Y (1989) Isomorphous Compounds; Galena, Clausthalite, and Altaite from the Kushikino Gold-Silver Ore Deposit, Japan – Possible Substitutional Limits. *Mining Geol* 39:253–260.

Sillitoe, RH (2010) Porphyry Copper Systems. *Econ Geol* 105:3–41.

Sykora S, Cooke DR, Meffre S et al (2018) Evolution of Pyrite Trace Element Compositions from Porphyry-Style and Epithermal Conditions at the Lihir Gold Deposit: Implications for Ore Genesis and Mineral Processing. *Econ Geol* 113:193–208.

Zhang B, Li N, Shu S et al (2018) Textural and compositional evolution of Au-hosting Fe-S-As minerals at the Axi epithermal gold deposit, Western Tianshan, NW China. *Ore Geol Rev* 100:31–50.

An integrated accessory mineral approach to understanding post-subduction magmatism and mineralisation

Jessica Berry, Andrew J. Miles, David A. Holwell

School of Geography, Geology, and the Environment, University of Leicester, UK

Shaun Graham

Carl Zeiss Ltd., UK

C. Johan Lissenberg

School of Earth and Ocean Sciences, Cardiff University, UK

Chiara M. Petrone

Natural History Museum, UK

Abstract. Post-subduction and predominantly alkaline magmas are commonly associated with gold (Au) and tellurium (Te) mineralisation. By contrast, calc-alkaline subduction-related magmas are more often associated with copper mineralisation. Amphibole and sulfide-bearing cumulates formed in the lower crust during active subduction are an important repository for water and gold during the passage of calc-alkaline magmas through the crust. However, these cumulates also have the potential to act as a fertile source of Au and Te during later episodes of post-subduction magmatism when remobilized. A suite of accessory minerals have been analyzed from variably mineralized syn- and post-subduction plutons associated with the Laramide Orogeny in the Colorado Mineral Belt. The common occurrence of inherited zircons in plutonic rocks means they provide a potentially valuable opportunity to assess the role of lower crustal cumulates in the formation of mineralized post-subduction magmas. Spatial and temporal characteristics of syn- and post-subduction intrusions in Colorado are considered. Gold mineralisation is closely associated with post-subduction magmas. Further analysis of barren and fertile syn- and post-subduction suites using Zeiss' Automated Mineralogic system has shown that zircon, apatite, titanite, and magnetite are present in all samples. Apatite hosted within zircon, and sulfides (pyrite, chalcopyrite) hosted within titanite are also present.

1 Introduction

During subduction, the break-down of hydrous minerals in the down-going slab liberate water and metals, and cause partial melting of the overlying mantle wedge. Magma differentiation occurs during intrusion of these partial melts into the lower crust.

Arc magmas commonly exhibit cryptic evidence for significant amphibole fractionation despite the common absence of amphibole phenocrysts in erupted magmas (Davidson et al. 2007). This is thought to reflect the formation of amphibole-rich cumulates in the lower crust

via basaltic underplating. These cumulates behave as a "sponge" and filter for water. Further evidence also suggests that these cumulates contain significant amounts of metal-enriched sulfides that may act as effective filters for highly chalcophile elements such as Cu, Au and Te during magmatic differentiation (Richards 2011).

Sulfide saturation in the lower crust during subduction may limit the formation of Au-Cu porphyry deposits. However, these sulfides may act as fertile sources of Au and Te if they become remobilized during later magmatic events, resulting in the formation of younger Au-bearing porphyry-epithermal systems (Richards 2009). Post-subduction, or post-collisional tectonic settings commonly enable remelting and remobilization of lower crustal cumulates due to slab roll-back or breakoff (Richards 2009).

In many cases, these Au-Te porphyry-epithermal systems are accompanied by completely barren systems that are apparently part of the same magmatic events. The cause of this is unknown. Understanding the gateways that magma must pass through to become either fertile (able to generate mineral deposits) or barren (unable to generate mineral deposits) is critical for exploration.

2 The use of accessory minerals in tracing ore forming processes

Whole-rock data is often limited in its use; rocks are susceptible to alteration and represent homogenised compositions that reflect the cumulative effect of multiple magmatic processes (Miles et al. 2013; Bruand et al. 2016). It is therefore difficult to isolate individual magmatic events that are critical for reconstructing mineralisation processes using whole-rock data alone.

Accessory minerals, such as zircon, titanite, and magnetite, by contrast, are generally robust and often host inclusions of otherwise less-robust minerals (Miles et al. 2013; Wilkinson et al. 2017), which may include sulfides (Simpson 2014).

Zircon chemistry and isotopic signatures, when coupled with high precision U-Pb geochronology, can be useful when assessing successive stages of magmatic history. An increasing number of studies are showing that many zircons are antecrysts; they may contain cores that crystallised during earlier stages of magmatism, and were inherited from different parts of the magmatic system (Miller et al. 2007; Barboni et al. 2013; Miles et al. 2013). The inheritance of zircons from deeper parts of the crust is a critical method for accessing the role of cumulates, and may record protracted magmatic histories (Jackson et al. 2018).

Apatite, titanite (sphene), and magnetite can also be useful fertility indicators. Apatite has an affinity for REE and can be used to determine fluid and volatile exsolution and composition (Boyce and Hervig 2009; Bruand et al. 2016). Apatite geochemistry compared to whole-rock may also be used to determine magmatic histories over different lengths of time (Miles et al. 2013).

3 The Colorado Mineral Belt

The Colorado Mineral Belt spans an area more than 500 km in length, and 20 – 40 km in width in central – western Colorado, USA. Many igneous centres are associated with extensive and predominantly epithermal Au and Te mineralisation with occasional porphyry gold deposits. Most importantly, the region hosts both subduction-related, and post-subduction-related magmas, with both barren and fertile intrusive complexes.

Subduction-related magmatism in the region began during the Laramide Orogeny, when the Farallon plate was subducted beneath the North American plate. Arc-type magmatism occurred from 75 Ma to 45 Ma, during which time subduction of the Farallon slab was shallow. Magmatism at this time was predominantly calc-alkaline, silica oversaturated and silica saturated (Cunningham et al. 1994; Chapin 2012).

The cessation of subduction at 45 Ma was rapid, and post-subduction magmas, predominantly calc-alkaline to alkaline, were generated between 45 Ma and 25 Ma, during steepening and westward roll-back of the Farallon slab (Cunningham et al. 1994; English et al. 2003; Chapin 2012).

The world class Cripple Creek Au-Te deposit formed at ~ 30 Ma (Kelley and Ludington 2002) on the margin of the northward propagating Rio Grande Rift and during continued slab roll-back. The deposit is associated with a phonolite and alkali basalt diatreme complex and hosts an estimated 1,000 t of Au-Te as native gold, gold-tellurides in quartz veins, and disseminated gold (Saunders 1986; Jensen and Barton 2007).

3.1 Spatial and temporal characteristics

Spatial and temporal characteristics of syn- and post-subduction intrusions in Colorado are evidence of significant influence from previous magmatic events. Proterozoic intrusions (1.8 Ga, 1.4 Ga, 1.1 Ga; Whitmeyer and Karlstrom 2007) show controls on the spatial dynamics of successive magmatism, and are

found to define pathways for successive magmatism, blocking pathways in areas where Proterozoic intrusions are present. Gold occurrences are occasionally associated with these Precambrian granite intrusions, suggesting some metallogenic potential for them.

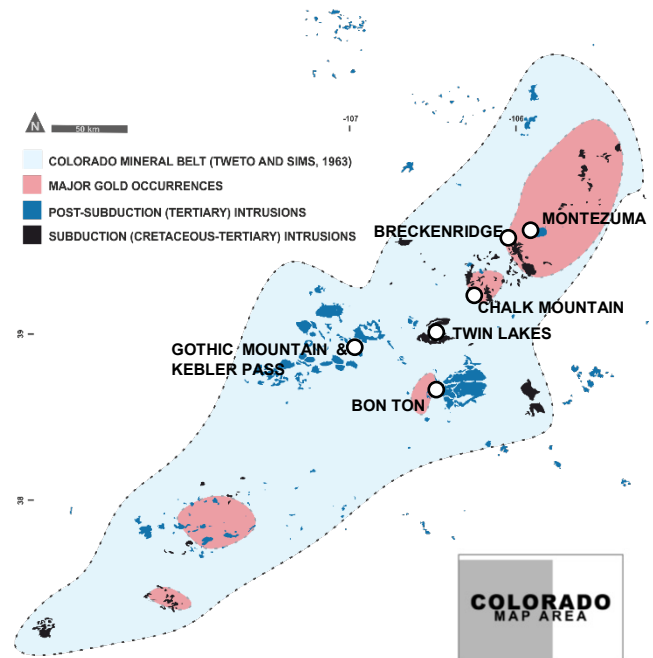


Figure 1. Spatial and temporal associations of syn- and post-subduction intrusions of the Colorado Mineral Belt. The light blue depicts the bounds of the Colorado Mineral Belt (Tweto and Sims 1963). The red ovals show areas with high concentrations of gold occurrences. Gold occurrences from MRDS.

Laramide-age, subduction-related intrusions are poorly exposed at the surface (~ 700 km²). These are shown as the black intrusions in Figure 1. Post-Laramide, post-subduction intrusions show a larger surface area (~ 3,500 km²) compared to subduction-related intrusions. This may suggest a higher volume of intrusion during post-subduction magmatism. Spatially, these post-subduction intrusions fill voids where no subduction-related magmas have intruded.

Subduction-related plutons comprise 17% of the total syn- and post-subduction intrusions in the Colorado Mineral Belt (based on area). 83% are post-subduction intrusions (blue outcrops on Figure 1). 33% of gold occurrences are associated with syn-subduction intrusions. 67% of the gold occurrences are associated with post-subduction intrusions. Red ovals in Figure 1 represents an area with a high density of gold occurrences.

Post-subduction intrusions are associated with approximately twice as many gold occurrences than with syn-subduction intrusions. This is suggestive of a concentration of gold in a post-subduction setting. Whilst gold is found in occurrence with subduction-related intrusions, it is more commonly found in post-subduction settings. This is perhaps a function of the volumes of magma that are present for both syn- and post-subduction.

3.2 Automated Mineralogy

Four suites of rocks from the Colorado Mineral Belt have been assessed, covering a selection of barren and fertile samples from both subduction-related and post-subduction intrusions.

Two barren subduction-related samples and three barren post-subduction samples were collected from Twin Lakes (granite, granodiorite), and Gothic Mountain, Kebler Pass, and Chalk Mountain (dacite, rhyolite), respectively. One fertile subduction-related sample and two fertile post-subduction samples were collected from Breckenridge (granite), and Montezuma and Bon Ton (granites), respectively.

These samples were mapped using Zeiss' Automated Mineralogic Element Mapping instrument. A bright phase search (BPS) was set to capture zircon, apatite, titanite, and magnetite, and any sulfide phases, and a dilute threshold was applied to provide textural and contextual information for each accessory phase. Samples were mapped at a resolution of 5 μm .

By gathering automated mineralogy information from these samples we can texturally constrain the associations and paragenesis of accessory minerals, in order to give spatial context for any subsequent isotopic work. Already, this mapping has shown that zircon, apatite, titanite, and magnetite are present in each sample from barren and fertile, syn- and post-subduction systems. The uniform presence of these minerals across all samples means a direct comparison can be made of each accessory phase.

Acknowledgements

This PhD is funded by NERC, with additional funding from Carl Zeiss Ltd as CASE partner. Thanks to Carl Zeiss Ltd. for access to facilities, and training with Automated Mineralogic software. Additional thanks to Tom Knott at the University of Leicester.

References

- Barboni M, Schoene B, Ovtcharova M, et al (2013) Timing of incremental pluton construction and magmatic activity in a back-arc setting revealed by ID-TIMS U/Pb and Hf isotopes on complex zircon grains. *Chemical Geology* 342:76–93. doi: 10.1016/j.chemgeo.2012.12.011
- Boyce JW, Hervig RL (2009) Apatite as a monitor of late-stage magmatic processes at Volcán Irazú, Costa Rica. *Contributions to Mineralogy and Petrology* 157:135–145. doi: 10.1007/s00410-008-0325-x
- Bruand E, Storey C, Fowler M (2016) An apatite for progress: Inclusions in zircon and titanite constrain petrogenesis and provenance. *Geology* 44:91–94. doi: 10.1130/G37301.1
- Chapin CE (2012) Origin of the Colorado Mineral Belt. *Geosphere* 8:28–43. doi: 10.1130/GES00694.1
- Cunningham CG, Naeser CW, Marvin RF, et al (1994) Ages of Selected Intrusive Rocks and Associated Ore Deposits in the Colorado Mineral Belt. USGS, Washington DC
- Davidson J, Turner S, Handley H, et al (2007) Amphibole “sponge” in arc crust? *Geology* 35:787–290. doi: 10.1130/G23637A.1
- English JM, Johnston ST, Wang K (2003) Thermal modelling of the Laramide orogeny: testing the flat-slab subduction hypothesis. *Earth and Planetary Science Letters* 214:619–632. doi: 10.1016/S0012-821X(03)00399-6

- Holwell DA, McDonald I (2010) A Review of the Behaviour of Platinum Group Elements within Natural Magmatic Sulfide Ore Systems. *Platinum Metals Review* 54:26–36. doi: 10.1595/147106709X480913
- Jackson MD, Blundy J, Sparks RSJ (2018) Chemical differentiation, cold storage and remobilization of magma in the Earth's crust. *Nature* 564:405–409. doi: 10.1038/s41586-018-0746-2
- Jensen EP, Barton MD (2007) Geology, petrochemistry, and time-space evolution of the Cripple Creek district, Colorado. In: *GSA Field Guide 10: Roaming the Rocky Mountains and Environs: Geological Field Trips*. Geological Society of America, pp 63–78
- Kelley KD, Ludington S (2002) Cripple Creek and other alkaline-related gold deposits in the southern Rocky Mountains, USA: influence of regional tectonics. *Mineralium Deposita* 37:38–60. doi: 10.1007/s00126-001-0229-4
- Miles AJ, Graham CM, Hawkesworth CJ, et al (2013) Evidence for distinct stages of magma history recorded by the compositions of accessory apatite and zircon. *Contributions to Mineralogy and Petrology* 166:1–19. doi: 10.1007/s00410-013-0862-9
- Miller JS, Matzel JEP, Miller CF, et al (2007) Zircon growth and recycling during the assembly of large, composite arc plutons. *Journal of Volcanology and Geothermal Research* 167:282–299. doi: 10.1016/j.jvolgeores.2007.04.019
- Richards JP (2011) Magmatic to hydrothermal metal fluxes in convergent and collided margins. *Ore Geology Reviews* 40:1–26. doi: 10.1016/j.oregeorev.2011.05.006
- Richards JP (2009) Postsubduction porphyry Cu-Au and epithermal Au deposits: Products of remelting of subduction-modified lithosphere. *Geology* 37:247–250. doi: 10.1130/G25451A.1
- Saunders JA (1986) *Petrology, Mineralogy, and Geochemistry of Representative Gold Tellurium Ores from Colorado*. PhD, Colorado School of Mines
- Simpson R (2014) Sulfide inclusions in zircon and their significance to understanding the evolution of copper porphyries in the Macquarie Arc, New South Wales. Bachelor of Science (Hons.), School of Earth and Environmental Sciences, University of Wollongong
- Tweto O, Sims PK (1963) Precambrian Ancestry of the Colorado Mineral Belt. *Geological Society of America Bulletin* 74:991–1014
- Whitmeyer SJ, Karlstrom KE (2007) Tectonic model for the Proterozoic growth of North America. *Geosphere* 3:220–259
- Wilkinson JJ, Cooke DR, Baker MJ, et al (2017) Porphyry indicator minerals and their mineral chemistry as vectoring and fertility tools. In: *Application of indicator mineral methods to bedrock and sediments*. Geological Survey of Canada, Ottawa, pp 67–77

Trace element chemistry, polytypes, isotopic composition and Re-Os dates of molybdenite from the Bingham Canyon Cu-Au-Mo porphyry deposit, Utah

Simon Kocher^{1,2}, Jamie J. Wilkinson^{1,2}, Robin N. Armstrong¹, Iain McDonald³, Mark Rehkaemper², Robert A. Creaser⁴, Jens Najorka⁵

¹LODE, Department of Earth Sciences, Natural History Museum, London, United Kingdom;

²Department of Earth Sciences & Engineering, Imperial College London, London, United Kingdom;

³School of Earth and Ocean Sciences, Cardiff University, Cardiff, United Kingdom;

⁴Department of Earth and Atmospheric Sciences, University of Alberta, Edmonton, AB;

⁵Core Research Laboratories, Natural History Museum, London, United Kingdom

Abstract. The controls on the formation of Mo-rich porphyry mineralization remain poorly constrained. By characterizing molybdenite from well constrained samples with Re-Os dating it is possible to trace the processes controlling Mo mineralization at one of the world's most prolific Cu-Au-Mo porphyry deposits at Bingham Canyon. Petrographic observations indicate three major modes of occurrence of molybdenite, two different types of quartz veins and molybdenite disseminated in porphyritic matrix. Molybdenite trace element compositions are a function of their respective magmatic sources and are capable of recording hydrothermal overprints. In deeper parts of the deposits, Mo isotopes correlate with depth, and are interpreted to be the result of Rayleigh distillation during molybdenite precipitation from a hydrothermal fluid. Polytype compositions show no systematic variations across the deposit. High precision Re-Os dates indicate that molybdenum mineralization formed between 37.62 - 38.22 Ma during a late hydrothermal event coinciding with the emplacement of the youngest porphyry phase. The decoupled deposition of Mo and Cu at Bingham is attributed to the preferential early extraction of Cu from the underlying, less evolved magma chamber, followed by Mo extraction from a more evolved magma.

1 Introduction

99% of molybdenum is recovered from porphyry deposits (Sillitoe 2010) where it is concentrated by 2-3 orders of magnitude relative to the magmatic source, making it the metal with the single strongest affinity to a single deposit type. Due to the economic significance of porphyry-type deposits, considerable research has been undertaken to constrain the behavior of Cu and Au from the generation of a hydrous magma through the precipitation of ore minerals from a hydrothermal fluid (e.g. Williams-Jones and Heinrich 2005). Molybdenum, generally being a co- or by-product, has received less attention even though it has important uses in metallurgy.

To better understand the controls on and timing of Mo mineralization in porphyry deposits, molybdenite samples from Bingham Canyon were analyzed for trace elements, polytypes and isotopic compositions and Re-Os dates.

2 Deposit geology and mineralization

The Bingham Canyon deposit is located 45 km southwest of Salt Lake City, Utah. It is related to Eocene, I-type, shallow-level intrusions emplaced into a thick sequence of shallow marine sedimentary rocks, including quartzite and limestone (Fig. 1).

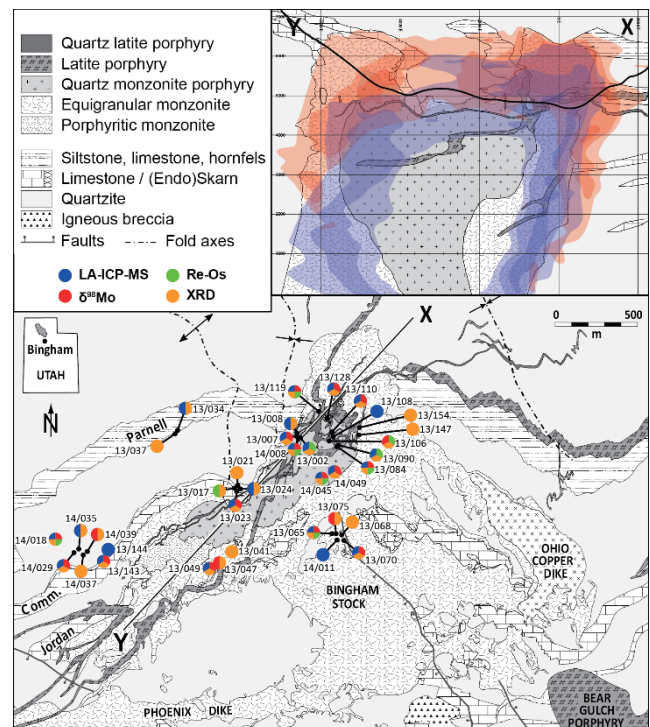


Figure 1. Simplified geological map of the Bingham Canyon mine displaying projected sample locations and analytical techniques. Labels represent sample numbers. The cross section (inset) shows the spatially separated Cu (red) and Mo (blue) ore bodies centered over a "barren" core. Modified after Landtwing et al. (2005).

Mineralization is present as spatially separated Cu and Mo ore bodies hosted by a series of felsic-intermediate intrusions, comprising equigranular monzonite, quartz monzonite porphyry, latite porphyry, and quartz latite porphyry (Fig. 1; e.g. Redmond and Einaudi 2010).

Molybdenite occurs as disseminated aggregates in quartz latite porphyry and predominantly in two different

types of quartz veins as fine or coarse-grained flakes (Fig. 2). Molybdenite-bearing quartz veins are generally late-stage and cross cut all porphyry intrusions and Cu mineralization.

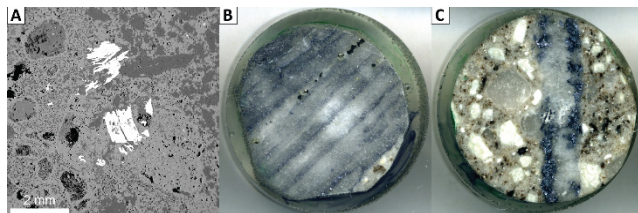


Figure 2. Types of molybdenite mineralization at Bingham Canyon. **(A)** BSE image of disseminated molybdenite in K-spar, biotite and quartz-rich groundmass; **(B)** Typical example of type 1 vein with multiple bands of fine-grained molybdenite; **(C)** Type 2 quartz-molybdenite with abundant coarse-grained molybdenite along vein margins.

3 Trace element chemistry

Laser ablation inductively-coupled-plasma mass spectrometry was used to analyze concentrations of major and trace elements in 25 polished molybdenite samples. All measurements were carried out on a New Wave Research UP213 UV laser system attached to a Thermo X Series ICPMS at Cardiff University. Quantitative calibration was achieved using a set of synthetic Ni-Fe-S quenched sulfide standards, natural molybdenite and galena.

Within individual samples most trace element concentrations are mostly homogeneous. Rhenium concentrations in Molybdenite records large variations ranging from <10 to >1000 ppm sometimes even within individual mineral grains. Some elements, including Te, Pb, and Au are concentrated in discrete mineral inclusions, mainly galena and tellurides with a metal/Te ratio of 2/1.

In a ternary Re-(Zn+Pb+As)-(Bi+Te+Au) plot (Fig. 3) data from various deposits plot in discrete fields, suggesting that molybdenite has the potential to record important information on mineralizing processes. In a Re-Se diagram, data from most deposits show no systematic variation on a deposit-scale, thus suggesting that the Re-Se concentrations in molybdenite are controlled by their magma sources. This is consistent with elevated Se concentrations in molybdenites at Bingham, Hilltop and Boddington, which display a stronger mantle component as indicated by higher Re content.

4 Molybdenite polytypes

Molybdenite naturally occurs as two different polytypes, most commonly as hexagonal (2H) and less abundantly as rhombohedral (3R) polytype. The controls on polytype formation are poorly constrained, but likely the result of trace element concentrations (mainly Re) and formation temperatures (e.g. Newberry 1979).

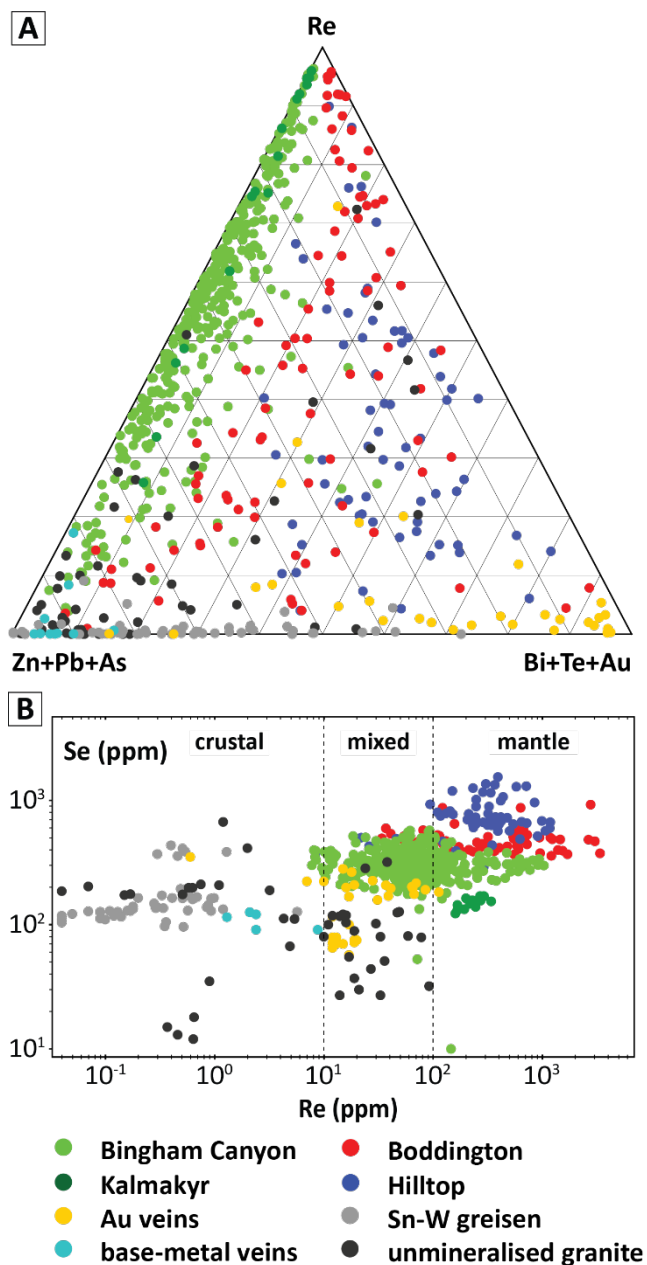


Figure 3. (A) Ternary Re-(Zn+Pb+As)-(Bi+Te+Au) plot. Data from Bingham and Kalmakyr show a large spread in Re concentrations. Base metal, greisen and Au deposits generally have low Re. Au deposits plot in the Bi+Te+Au corner, Greisen and base metal molybdenite displays higher Pb+Zn+As values; **(B)** Bivariate plot of Re vs. Se showing two different groups. Greisen, base metal and some barren data display low Re and Se concentrations and plot in the crustal field (Mao et al. 2013). Data from Bingham, Hilltop, Boddington and some Au deposits plot in the mixed and mantle fields. Ciobanu et al. (2013), Pašava et al. (2016).

Twenty-six molybdenite-bearing vein samples were selected for polytype analysis (Fig. 1). Samples were crushed, hand-picked and the pure molybdenite concentrates ground into a fine powder prior to analysis. To counteract the effects of preferred orientation, measurements were carried out in transmitted mode on a Panalytical X-Pert Pro MPD X-ray scanning diffractometer equipped with an X-Celerator position

sensitive detector. Relative abundances of polytypes were quantified following the Rietveld method using the GSAS program (Larson and Von Dreele, 2005).

Results indicate that the majority of molybdenite at Bingham crystallized as the 2H polytype and contains no detectable 3R polytype component. Only three samples were found to contain the 3R polytype in varying proportions from 5% to a maximum of 23%. 3R abundance appears to be unrelated to host rock lithology, vein type and mineral association; however, the 3R-bearing samples tend to be located the furthest from the unmineralized center of the deposit. No obvious correlations were found between trace element concentration and polytype abundance, however, the sample with the highest proportion of 3R polytype contains the highest Re concentrations.

5 Isotopic composition

Molybdenum has seven stable isotopes and in order to assess isotope fractionation under hydrothermal conditions, molybdenite from 20 different hand specimens (Fig. 1) were analyzed for inter-sample $\delta^{98}\text{Mo}$ variations. The measurements were performed on a Nu Instruments Nu Plasma HR MC-ICP-MS at the Imperial College London MAGIC Laboratory.

$\delta^{98}\text{Mo}$ values of molybdenite range from -0.82‰ to $+1.14\text{‰}$ with a median of $-0.23\text{‰} \pm 0.02$ (Table 1). Disseminated molybdenite measured from two samples range from -0.11‰ to -0.01‰ . Isotopic composition of vein-hosted molybdenite follows a trend towards lighter values (Fig. 4). No correlation is seen between Re concentration and isotopic composition.

Table 1. Mo isotopic compositions of Bingham molybdenite.

Sample	Lith.	Type	$\delta^{98}\text{Mo}$	$\pm 2\sigma$
BC13SK007	QLP	diss.	-0.11	0.02
BC13SK023	QLP	2a	-0.19	0.03
BC13SK047	EN	1	1.14	0.03
BC13SK049	MZ	2b	-0.82	0.02
BC13SK065	MZ	2b	-0.61	0.03
BC13SK070	SK	1	-0.45	0.01
BC13SK075	EN	1	0.38	0.03
BC13SK084	QMP	2a	-0.69	0.05
BC13SK106	MZ	2a	-0.22	0.03
BC13SK110	QZ	1	0.22	0.03
BC13SK119	QMP	2b	-0.40	0.02
BC13SK128	LP	2b	-0.68	0.02
BC13SK143	MZ	1	0.09	0.02
BC14SK008	QLP	diss.	-0.01	0.03
BC14SK018	MZ	2a	0.16	0.02
BC14SK029	QMP	2b	-0.16	0.03
BC14SK039	QMP	1	-0.25	0.02
BC14SK045	SK	2b	-0.35	0.02
BC14SK049	MZ	2b	-0.46	0.02
BC11JW1	QMP	2a	-0.45	0.03

On a plot showing sample elevation versus $\delta^{98}\text{Mo}$, two populations are observed (Fig. 4). Deeper samples follow a trend from heavier $\delta^{98}\text{Mo}$ values in Type 1 veins at greater depth to lighter values in slightly shallower Type 2 veins. This is interpreted to be the result of Rayleigh distillation. The shallow population shows no clear trend.

Samples analyzed in this study record the widest range of $\delta^{98}\text{Mo}$ to date (Mathur et al. 2009; Greber et al. 2014; Shafiei et al. 2014; Wang et al. 2015; Yao et al. 2016), casting doubt on the suitability of Mo isotopes as tracer for magma origin (Wang et al. 2015).

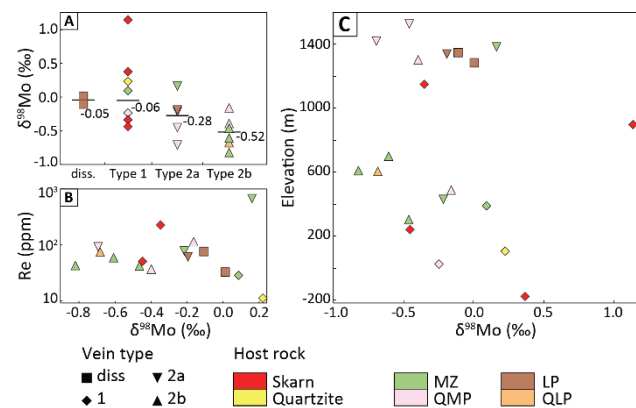


Figure 4. (A) Average molybdenum isotope compositions show a trend towards lighter values from disseminated to Type 2b molybdenite. (B) No correlation exists between Re content of molybdenite and $\delta^{98}\text{Mo}$. (C) Sample elevation vs. $\delta^{98}\text{Mo}$ plot illustrating two different groups. Deeper samples follow a trend towards lighter values with increasing elevation. Shallower molybdenite samples show no clear trend.

6 Re-Os dates

Ten samples were selected for Re-Os dating (Fig. 1) and were prepared and analyzed at the University of Alberta Radiogenic Isotope Facility, Canada, using the method of Selby and Creaser (2001). Prior to processing, samples were examined microscopically to identify molybdenite of interest and to make sure only one generation of molybdenite was selected for analysis. Isotope dilution and negative thermal ion mass spectrometry (ID-NTIMS) isotope measurements were performed on N-TIMS using a Thermo Triton mass spectrometer fitted with Faraday Collectors.

Ten samples from molybdenite-bearing veins were analyzed and the main population yield dates that range from 37.97 ± 0.17 and 37.62 ± 0.17 Ma (Fig. 5). One sample, BC14SK018 yielded an older date of 38.22 ± 0.17 Ma and is considered to represent an earlier molybdenite generation. The main population records crystallization over 350 ka and is consistent with U-Pb zircon dates ($38.10 - 37.78$ Ma) obtained from porphyritic intrusions (von Quadt et al. 2011). No clear trends are observed between Re-Os molybdenite dates and vein type, elevation, distance to unmineralized center of the deposit or host rock.

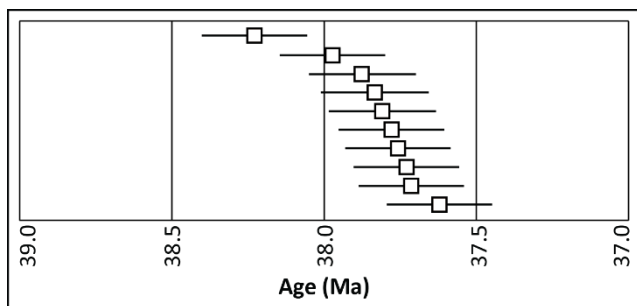


Figure 5. Re-Os ages of 10 molybdenite samples from Bingham Canyon.

7 Conclusions

- Molybdenite at Bingham occurs in two different types of hydrothermal veins and is disseminated in a magmatic-hydrothermal breccia.
- Selenium, W and Re are incorporated into the molybdenite structure. Pb, Pd and Te are present in nano-scale mineral inclusions.
- Molybdenites from different deposit types vary in their trace element chemistry, thus highlighting their importance as a potential tracer for mineralizing processes.
- At Bingham, Re concentrations range from 1-1000 ppm. These relatively low values might be attributed to crustal assimilation.
- Analyzed molybdenite is predominantly of the 2H polytype. Mixed 2H-3R molybdenite were found distal to the barren core of the deposit.
- Hydrothermal molybdenite yields $\delta^{98}\text{Mo}$ between -0.82‰ and 1.14‰, recording the widest range in any porphyry deposit to date.
- Magmatic molybdenite yields an average $\delta^{98}\text{Mo}$ of -0.06, which is in the range of values reported for the mantle.
- $\delta^{98}\text{Mo}$ values correlate with vein-type and depth which is interpreted to be caused by Rayleigh distillation.
- Ten new high-precision Re-Os ages indicate that the main population crystallized over 350 ka.
- Re-Os ages overlap with U-Pb ages (von Quadt et al. 2011) for porphyry intrusions, suggesting that Cu-Au-Mo mineralization at Bingham formed within ~480 ka.
- Sample BC14SK18 is Re-rich, contains abundant 3R polytypes and yielded the oldest Re-Os date, and is therefore thought to represent an early molybdenite generation.

Acknowledgements

I would like to thank Imperial College London, Department of Earth Science and Engineering, for a Janet Watson Ph.D. scholarship. Fieldwork and laboratory analyses were made possible through the financial support of Rio Tinto, The Institute of Materials, Minerals and Mining bursary scheme (2013-2014), the Society of Economic Geologists Hugh E. McKinstry Fund (2014-2015), and the Society of Economic Geologists travel bursary scheme (2014).

At Bingham, I would like to thank Kim Schroeder and

other members of the geology team, in particular Rudy Ganske, Nate Bishop, Jenny Lutz, Jeff Hoggan and Greg Sayer for sharing their expert knowledge.

References

- Ciobanu CL, Cook NJ, Kelson CR, Guerin R, Kalleske N, Danyushevsky L (2013) Trace element heterogeneity in molybdenite fingerprints stages of mineralization. *Chem. Geol.*, 347:175-189.
- Greber ND, Pettke T, Nögler TF (2014) Magmatic-hydrothermal molybdenum isotope fractionation and its relevance to the igneous crustal signature. *Lithos*, 190-191:104-110.
- Landtwing M, Pettke T, Halter WE, Heinrich CA, Redmond PB, Einaudi MT, Kunze K (2005) Copper deposition during quartz dissolution by cooling magmatic-hydrothermal fluids: The Bingham porphyry. *EPSL*, 235(1-2):229-243.
- Larson AC and Von Dreele RB (2005), General Structure Analysis System (GSAS), Los Alamos National Laboratory Report LAUR 86-748.
- Mathur R, Brantley S, Anbar A, Munizaga F, Maksaev V, Newberry RJ, Vervoort J, Hart G (2009) Variation of Mo isotopes from molybdenite in high-temperature hydrothermal ore deposits. *Mineralium Deposita*, 45(1):43-50.
- Mao Z, Cheng Y, Liu J, Yuan S, Wu S, Xiang X, Luo X (2013) Geology and molybdenite Re-Os age of the Dahutang granite-related veinlets-disseminated tungsten ore field in the Jiangxin Province, China. *Ore Geol. Rev.*, 53:422-433.
- Newberry RJ (1979a) Polytypism in molybdenite (I); A non-equilibrium impurity-induced phenomenon. *AM*, 64(7-8):758-767.
- Pašava J, Svojtka M, Veselovský F, Ďurišová J, Ackerman L, Pour O, Drábek M, Halodová P, Haluzová E (2016) Laser ablation ICPMS study of trace element chemistry in molybdenite coupled with scanning electron microscopy (SEM) - An important tool for identification of different types of mineralization. *Ore Geol. Rev.*, 72:874-895.
- Redmond, P.B. and Einaudi, M.T., 2010. The Bingham canyon porphyry Cu-Mo-Au deposit. I. Sequence of intrusions, vein formation, and sulfide deposition. *Econ. Geol.*, 105(1):43-68
- Selby D and Creaser RA (2001) Re-Os geochronology and systematics in molybdenite from the Endako porphyry molybdenum deposit, British Columbia, Canada. *Econ. Geol.*, 96(1):197-204.
- Shafiei B, Shamanian GH, Mathur R, Mirnejad H (2014) Mo isotope fractionation during hydrothermal evolution of porphyry Cu systems. *Mineralium Deposita*, 50(3):281-291.
- Sillitoe RH (2010) Porphyry copper systems. *Econ. Geol.*, 105(1):3-41.
- von Quadt A, Erni M, Martinek K, Moll M, Peytcheva I, Heinrich CA (2011) Zircon crystallization and the lifetimes of ore-forming magmatic-hydrothermal systems. *Geology*, 39(8):731-734.
- Wang Y, Zhou L, Gao S, Li J-W, Hu Z-F, Yang L, Hu Z-C (2015) Variation of molybdenum isotopes in molybdenite from porphyry and vein Mo deposits in the Gangdese metallogenic belt, Tibetan plateau and its implications. *Min. Dep.*, 51(2):201-210.
- Williams-Jones AE and Heinrich CA (2005) 100th Anniversary special paper: vapor transport of metals and the formation of magmatic-hydrothermal ore deposits. *Econ. Geol.*, 100(7):1287-1312
- Yao J, Mathur R, Sun W, Song W, Chen H, Mutti L, Xiang X, Luo X (2016) Fractionation of Cu and Mo isotopes caused by vapor-liquid partitioning, evidence from the Dahutang W-Cu-Mo ore field. *Geochemistry, Geophysics, Geosystems*, 17(5):1725-1739.

Salinity of magmatic fluid: experiments, phase equilibrium models, and implications for ore formation

David Dolejš

Institute of Earth and Environmental Sciences, University of Freiburg, Germany

Abstract. Chlorine concentration, often determined as the salinity of a hydrothermal fluid, is the most important control on the solubility and transport efficiency of metals during ore-forming processes. We provide new experimental data and design a comprehensive phase-equilibrium model of magmatic crystallization and fluid exsolution that predicts variations in fluid salinity and alkali ratio as a function of magma composition, temperature and pressure throughout the magmatic-hydrothermal transition. In isothermally decompressing systems, granitic or rhyolitic, near-eutectic melt exsolves vapor with negligible changes in salinity; exsolution of a brine is only encountered at the solidus. In isobarically cooling systems, fluid exsolution is often suppressed until significant crystallization occurs, then continues by simultaneous exsolution of vapor and brine. In non-eutectic melt compositions, which progressively crystallize upon cooling, the nature, salinity and the amount of fluid phase are strongly pressure-dependent. At 100 MPa, the magma exsolves vapor first, rapidly followed by vapor-and-brine saturation. At 200 MPa, the magma exsolves brine first, with its salinity decreasing and nearly continuously evolving to low-salinity vapor. These scenarios elucidate fundamental control mechanisms on the relative timing of brine or vapor saturation and their production rates, thus delineating intervals of efficient metal sequestration into hydrothermal fluids.

1 Introduction

The salinity of magmatic-hydrothermal fluid, or more specifically the total Cl and HCl concentrations, are the most important controls on partitioning of elements from silicate magmas and subsequent metal transport in hydrothermal systems (e.g., Audétat et al. 2008; Harlow and Aranovich 2018). Concentrations of elements, particularly the chalcophile and transition metals in aqueous fluids, directly correlate with the fluid chlorinity, and subsequent breakdown of metal-chloride complexes dictates efficiency of ore precipitation (e.g., Wood & Samson 1998; Heinrich & Candela 2014). From intrusive to shallow epithermal settings, salinity and composition of hydrothermal fluids change dramatically and this is only partly due to subcritical phase separation in the H₂O-NaCl system. It is still unclear: (1) what controls the salinity of magmatic fluids; (2) whether one or two fluid phases can simultaneously separate from magmas; and (3) how analytical data from melt inclusions can be linked to fluid chemistry or be used to monitor the course of the magmatic-hydrothermal transition.

From a theoretical viewpoint, the chlorine

concentration in aqueous fluid exsolving from a silicate melt is a complex function of the chlorine solubility in the parental silicate melt, temperature and pressure. Previous experimental studies have addressed these dependencies in a variety of simple or multicomponent systems (e.g., Webster 2004; Dalou et al. 2015; Webster et al. 2015; see Dolejš & Zajacz 2018 for review). Phase-equilibrium and spectroscopic approaches indicate that chlorine in silicate melts is preferentially complexed by alkalis (e.g., Sandland et al. 2004; Baesner et al. 2014; Grousset et al. 2015), thus these components and their variation (e.g., melt aluminosity or alkalinity) should exert first-order control on chlorine behavior. This observation has motivated our new experimental work in the system Na₂O-Al₂O₃-SiO₂-NaCl.

As hydrous magmas evolve through the magmatic-hydrothermal transition by decompression or cooling, fluid salinity is not only a function of instantaneous values of chlorine partition coefficients but is also subject to mass balance and mass conservation between crystals, residual melt and hydrothermal fluid. This restrictive principle has led us to develop a comprehensive phase-equilibrium model for predicting crystallization and fluid exsolution quantitatively, as a function of magma composition and under any ambient gradients in temperature and/or pressure.

2 Chlorine solubility in peraluminous to peralkaline silicic melts

We have experimentally determined chlorine solubility in five anhydrous Na₂O-Al₂O₃-SiO₂ melts at 1100–1600 °C and up to 2.0 GPa. The starting compositions were albite-quartz eutectic (Ab₅₉Qz₄₁ = NaAlSi₆O₁₄), albite (NaAlSi₃O₈), and their peralkaline and peraluminous derivatives with nominal alumina saturation index, ASI = 0.6, 0.8 and 1.2, respectively. Experiments were performed in quenching furnaces (1100–1575 °C and 1 atm) and piston cylinder apparatus (1400 °C and 0.5–2.0 GPa). All starting glasses were doped with 5 wt% NaCl as a chlorine source and were found to saturate with molten NaCl which formed an immiscible phase.

In all compositions, chlorine solubility in the melt is independent of temperature but it significantly increases with pressure. Therefore, the dissolution of NaCl into the silicate network is purely entropic and it implies that NaCl remains associated as passive molecular species in the melt network. At 1400 °C the chlorine solubility in the NaAlO₂-SiO₂ system increases with decreasing SiO₂ concentration as a result of competition of chloride species for free volume in the silicate tetrahedral

framework. In the quartz-albite eutectic melts ranging from peralkaline to peraluminous composition the chlorine solubility exhibits a minimum near the subaluminous composition where molar Al/(Na-Cl) ~ 1. The chlorine solubility increases in both peralkaline and peraluminous melts, in a ratio of 2.8–2.9 that is comparable to a charge ratio of $Al^{exc}/Na = 3$.

3 Phase equilibrium model for crystallization and fluid exsolution from granitic and rhyolitic melts

We use experimental data on chlorine solubility in granitic melts at 800–1060 °C and 50–200 MPa to devise and calibrate a thermodynamic model for silicate melt in the system Qz-Or-Ab-H₂O-Cl₂O₋₁. Properties of H₂O-NaCl-KCl fluids are described by the Kosinski-Anderko-Pitzer equation of state, and phase equilibria in the SiO₂-Al₂O₃-Na₂O-K₂O-H₂O-Cl₂O₋₁ system were calculated by Gibbs energy minimization. This setup enables predictions of fluid saturation during equilibrium or fractional crystallization or decompression and instantaneously calculates proportions and compositions of coexisting solid, melt and fluid phases.

We have modelled fractional devolatilization during isothermal decompression and isobaric crystallization of a minimum haplogranitic melt (QZ₃₈Ab₃₃Or₂₉) with Cl/H₂O = 0.02 (3.7 wt% H₂O, 740 ppm Cl) from 800 °C and 100 MPa (Fig. 1a) in which a melt isothermally rises to lower pressures. Fluid release is continuous and the fluid composition corresponds to low-salinity vapor (1.4 to 0.7 wt% NaCl + KCl). This process is solely driven by decompression (first boiling), and significant crystallization only occurs 5 MPa above the solidus. Nearly invariant crystallization implies loss of all volatiles (H₂O and Cl) from the magma, which is accommodated by formation of brine, in addition to the vapor, at the solidus. The vapor-brine composition is dictated by the solvus in the H₂O-NaCl-KCl system (0.9 vs. 83.8 wt% NaCl + KCl, respectively) but is expected to further change as the fluids migrate towards lower pressure.

In Fig. 1b, an identical initial melt evolves by isobaric cooling. In this case, a positive dependence of H₂O solubility with temperature leads to fluid undersaturation, hence inducing discontinuous devolatilization events. The magma remains fluid-undersaturated until significant crystallization occurs near the solidus (~740 °C). Here, fluid saturation is related to second boiling and the vapor and brine exsolve simultaneously. As in the previous scenario, their composition is invariantly dictated by the solvus in the H₂O-NaCl-KCl system (0.3 vs. 70.6 wt% NaCl + KCl). When the fluids are retained at their formation level ($P = 100$ MPa) and cool, the solvus shape is negligibly sensitive to temperature and the vapor and brine salinities remain essentially constant. These scenarios are applicable to behavior of near-eutectic or minimum melts in highly evolved plutons. The saturation with brine at the solidus allows for incompatible enrichment of ore and other minor elements in late stage, residual melt, and these elements are then efficiently

sequestered by the high-salinity brine at the solidus.

In order to explore the consequences of continuous magmatic crystallization on fluid exsolution, we have performed additional cooling and crystallization simulations starting with feldspar-saturated haplogranitic melt (QZ₁₅Ab₄₉Or₃₆) with Cl/H₂O = 0.02 at fluid saturation. In Fig. 2a, a feldspar-saturated melt cools isobarically at 100 MPa. This path is analogous to that in Fig. 1b, where the melt composition is a minimum one. However, in this case, cooling leads to continuous feldspar crystallization (~10 % solids per 10 °C) and induces continuous fluid saturation. The separating fluid is a vapor (~1.7 wt% NaCl + KCl) until the increasing Cl/H₂O ratio in the residual melt reaches simultaneous saturation with a brine. Brine (~71 wt% NaCl + KCl) and vapor exsolve simultaneously above and at the solidus. The fluid production increases rapidly (approximately doubles) at the solidus, as a consequence of magma composition.

In Fig. 2b, a feldspar-saturated melt has been emplaced at 200 MPa and allowed to isobarically cool. This approach illustrates the effect of depth on hydrothermal systems, which significantly affects the size of the vapor-brine solvus in the H₂O-NaCl-KCl system. Upon cooling, an initial melt with Cl/H₂O = 0.02 saturates first with a brine, with rapidly decreasing salinity (from 57.2 to 46.1 wt% NaCl + KCl). At 770 °C, the fluid composition reaches the vapor-brine solvus and invariantly switches to the vapor (19.4 wt% NaCl + KCl). Upon further crystallization, the vapor remains the only exsolving fluid and its salinity decreases to 0.3 wt% NaCl + KCl.

These simulations are applicable to crystallizing plutons after final emplacement. When the magma is already crystal-saturated, accumulation of volatiles in the residual melt generally promotes earlier or exclusive saturation with a high-salinity brine. Such systems will experience early sequestration of metals into hydrothermal fluids, possibly precluding incompatible enrichment of metals in residual melt. Systems that are emplaced at shallow level (~100 MPa) will eventually exsolve two fluids – vapor and brine – simultaneously, and their composition is only dictated by the extent of the fluid solvus in the H₂O-NaCl-KCl system. The amounts of vapor and brine, and the Cl/H₂O ratio in the melt are buffered by the vapor-brine coexistence and remain invariant. Therefore, the composition of melt inclusions at this stage cannot be a useful monitor of the devolatilization process. Systems that are emplaced at deep level (~200 MPa) exsolve one fluid only because the extent of fluid miscibility is large or even complete. The initial fluid is a highly saline brine, which evolves rapidly and continuously decreases in salinity towards lower salinity vapor. The early fluids will rapidly exhaust the metal budget of their parental magma. The lack of a wide vapor-brine solvus, together with the mass balance effect, causes large changes (dramatic decrease) in the Cl/H₂O ratio of the residual melt. Therefore, melt inclusions in deep-seated devolatilizing intrusions are likely to capture the progress of devolatilization and mirror the concomitant changes in fluid salinity.

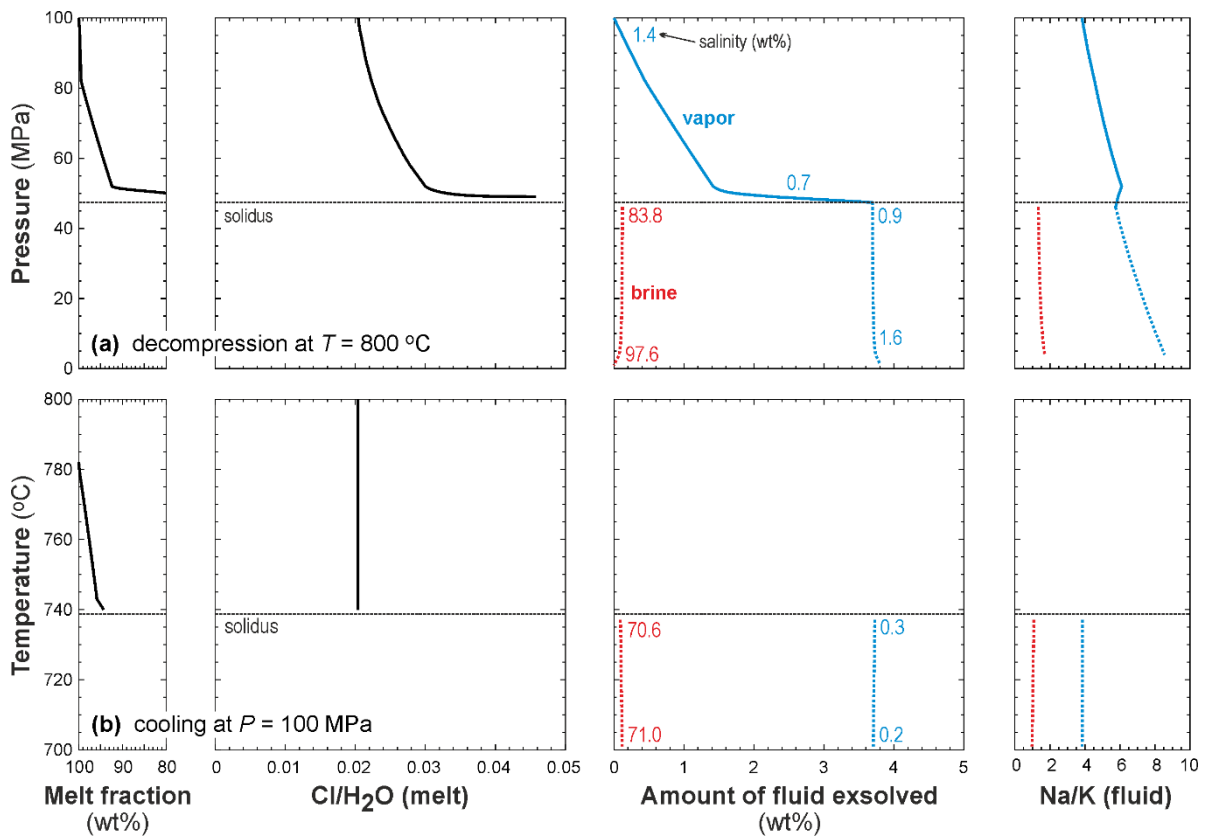


Figure 1. Crystallization and fluid exsolution from minimum haplogranitic melt ($Qz_{38}Ab_{33}Or_{29}$) with $Cl/H_2O = 0.02$ at fluid saturation: (a) isothermal decompression at $T = 800$ °C; (b) isobaric cooling at $P = 100$ MPa.

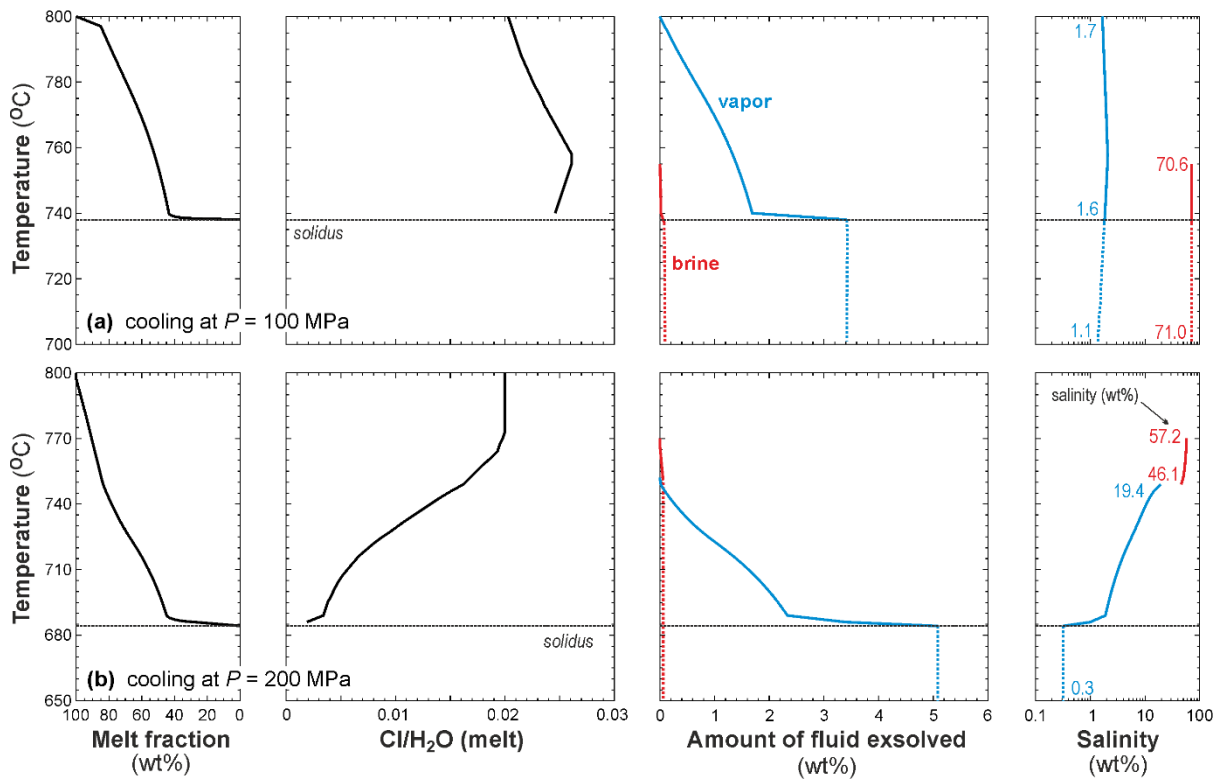


Figure 2. Isobaric crystallization and fluid exsolution from feldspar-saturated haplogranitic melt ($Qz_{15}Ab_{49}Or_{36}$) with Cl/H_2O at fluid saturation: (a) isobaric cooling at $P = 100$ MPa; (b) isobaric cooling at $P = 200$ MPa.

4 Implications for ore-forming processes

We have devised solubility experiments and phase equilibrium models that allow us to calculate chlorine solubility in peraluminous to peralkaline silicic magmas and to quantitatively predict and assess exsolution and composition of hydrothermal fluids during magma cooling, crystallization and/or decompression.

Our experimental results indicate that chlorine solubility in silicate melts strongly decreases with decreasing pressure. This leads to increasing chloride activity and general promotion of halide saturation during magma ascent. By contrast, temperature has no significant effect on chlorine solubility in silicate melts.

Variations in the alumina saturation index, that is, the peralkaline or peraluminous nature of the melt, have a substantial effect on chlorine solubility. The chlorine solubility rises proportionally with excess alkalis or aluminum in the melt. Consequently, the activity of the chloride species, the partition coefficient of chlorine between fluid and melt, and fluid salinity are predicted to increase in subaluminous systems. Since chlorine is preferentially associated with alkalis in the silicate melt structure, variations in melt alkalinity or aluminosity are likely to affect the onset of fluid saturation and fluid salinity in compositionally heterogeneous or evolving magmatic systems.

Fluid saturation, fluid salinity and simultaneous saturation with vapor and brine are all strongly dependent on ambient magmatic conditions (cooling vs. decompression) and progress of crystallization (magma composition), and are in detail controlled by the miscibility gap in the H₂O-NaCl-KCl system. In general, crystallizing magmas saturate with vapor, brine or both, depending on the pressure-temperature path and degree of crystallization. In melts that have near-eutectic or minimum composition, fluid saturation is dictated solely by the H₂O solubility. Upon cooling, these melts become fluid-undersaturated until second boiling is encountered at the solidus. Hence fluid exsolution is discontinuous and episodic. By contrast, during decompression, fluid exsolution is driven by falling H₂O solubility in the melt and manifested by continuous release of low-salinity vapor. In both cases, rapid crystallization at the solidus induces invariant co-exsolution of vapor and brine, with salinities dictated by the H₂O-NaCl-KCl solvus (1–2 vs. 70–84 wt% NaCl + KCl in our simulations).

Magmas that are solid-saturated and steadily crystallize promote transfer of volatiles from diminishing amount of residual melt to fluid(s). This “continuous second boiling” is universally responsible for early or exclusive saturation with high-salinity brines. In low-pressure systems (~100 MPa), fluid exsolution will occur early on conjugate sides of the solvus and continue so until the solidus is reached. In high-pressure systems (~200 MPa), the brine quasi-continuously evolves to low-salinity vapor.

Chlorine and water concentrations in evolving melts vary according to the devolatilization path. The decompressing melts have lowered H₂O contents, whereas the cooling magmas show chlorine depletion.

However, the magnitude of the chlorine depletion increases and becomes analytically traceable only when magmas simultaneously crystallize solid phases. Fluid salinities do not vary appreciably in several evolutionary scenarios, therefore the information from fluid inclusions may not be useful for tracking the progress of devolatilization. However, the salinity of conjugate vapor and brine is a sensitive pressure indicator.

In systems where pre-enrichment of metals by incompatible accumulation in residual melts is required, high metal concentrations in hydrothermal fluids can only be reached if brine exsolution occurs late and close to the solidus. This is mainly fulfilled at low pressures and in near-eutectic melts. By contrast, magmas with early mineral saturation and/or evolving at high pressures are unlikely to produce economic mineralization.

Acknowledgements

The assistance of Vincenzo Stagno with laboratory experiments and electron microprobe analyses at the Bayerisches Geoinstitut, University of Bayreuth (Germany) is gratefully acknowledged. I appreciate careful and detailed review by Jamie Wilkinson.

References

- Audétat A, Pettke T, Heinrich CA, Bodnar RJ (2008) The composition of magmatic-hydrothermal fluids in barren and mineralized intrusions. *Econ Geol* 103:877-908
- Baasner A, Hung I, Kemp TF, Dupree R, Schmidt BC, Webb SL (2014) Constraints on the incorporation mechanism of chlorine in peralkaline and peraluminous Na₂O-CaO-Al₂O₃-SiO₂ glasses. *Am Mineral* 99:1713-1723
- Dalou C, Le Losq C, Mysen BO, Cody GD (2015b) Solubility and solution mechanisms of chlorine and fluorine in aluminosilicate melts at high pressure and temperature. *Am Mineral* 100:2272-2283
- Dolejš D, Zajac Z (2018) Halogens in silicic magmas and their hydrothermal systems. In Harlov DE, Aranovich L (eds) *The role of halogens in terrestrial and extraterrestrial geochemical processes*. Springer, Cham, p 431-543
- Grousset L, Pili E, Neuville DR (2015) Incorporation and role of halogens in silicate melts and glasses. *Mater Techn* 103:402
- Harlov DE, Aranovich L (eds) *The role of halogens in terrestrial and extraterrestrial geochemical processes*. Springer, Cham, 1030 p
- Heinrich CA, Candela PA (2014) Fluids and ore formation in the Earth's crust. *Treatise Geochem* 13:1-28
- Sandland TO, Du LS, Stebbins JF, Webster JD (2004) Structure of Cl-containing silicate and aluminosilicate glasses: A ³⁵Cl MAS-NMR study. *Geochim Cosmochim Acta* 68:5059-5069
- Webster JD (2004) The exsolution of magmatic hydrosaline melts. *Chem Geol* 210:33-48
- Webster JD, Vetere F, Botcharnikov RE, Goldoff B, McBirney A, Doherty AL (2015) Experimental and modeled chlorine solubilities in aluminosilicate melts at 1 to 7000 bars and 700 to 1250 °C: Applications to magmas of Augustine Volcano, Alaska. *Am Mineral* 100:522-535
- Wood SA, Samson IM (1998) Solubility of ore minerals and complexation of ore metals in hydrothermal solutions. *Rev Econ Geol* 10:33-8